




ADVERTIMENT. L'accés als continguts d'aquesta tesi queda condicionat a l'acceptació de les condicions d'ús establertes per la següent llicència Creative Commons:  <https://creativecommons.org/licenses/?lang=ca>

ADVERTENCIA. El acceso a los contenidos de esta tesis queda condicionado a la aceptación de las condiciones de uso establecidas por la siguiente licencia Creative Commons:  <https://creativecommons.org/licenses/?lang=es>

WARNING. The access to the contents of this doctoral thesis it is limited to the acceptance of the use conditions set by the following Creative Commons license:  <https://creativecommons.org/licenses/?lang=en>

Preparation of all-oxide heterostructures based on cation engineered photoferroelectric BiFeO_3 thin films by cost-effective methodologies

Pamela Machado da Silva Rattín

Supervisor: Dr. Mariona Coll

Tutor: Dr. Eva Pellicer

Universitat Autònoma de Barcelona (UAB)
Institut de Ciència de Materials de Barcelona
(ICMAB-CSIC)

Thesis submitted for the degree of Doctor of Philosophy
PhD programme in Materials Science

June, 2023



Acknowledgements

To begin, I would like to express my heartfelt gratitude to my supervisor, Dr. Mariona Coll. This doctoral thesis would not have been possible without the unwavering support she has provided me since my arrival at ICMAB. Thanks to her, I have gained a more critical perspective on science, improved my laboratory skills, developed the ability to interpret results, and notably enhanced my writing abilities. Despite her tireless insistence on being brief, I will take the liberty of elaborating in these lines, as she truly deserves it (some things never change). There are countless reasons to thank you, Mariona: for imparting your knowledge to me, for never giving up and teaching me how to redirect situations that sometimes seemed lost while keeping a positive outlook, for all the endless cycles of corrections that have taught me so much (truly!), but above all, for your closeness, your commitment and your time. You have always been deeply involved in this thesis, finding any free moment to discuss and answer my questions. For sure, one of the best things of this thesis has been learning together about this fascinating research area. I will always remember our meetings with great affection.

My sincere acknowledgements go to our many collaborators who provided meaningful analysis for this thesis. Dr. Roger Guzmán and Prof. Wu Zhou from the University of Chinese Academy of Sciences, China, for the STEM characterization. Dr. Claudio Cazorla from Universitat Politècnica de Catalunya (UPC) and Dr. César Menéndez from The University of New South Wales, Australia, for first-principle studies based on density functional theory. Dr. Carlos Escudero and Dr. Massimo Tallarida from ALBA for XAS measurements. Dr. Joaquim Puigdollers and Eloi Ros from UPC for providing access to the experimental facilities and interesting discussions about photovoltaic systems. Prof. Christian Hagendorf, Alexander Müller and Stefan Lange from Fraunhofer Center for Silicon Photovoltaics CSP for ToF-SIMS and STEM analysis of compositional gradient thin films. Dr. Joe Briscoe and Chloe Forrester for hosting me at Queen Mary University of London and for the fruitful discussions on recombination. Prof. Andreas Klein from Technical University of Darmstadt for assistance on energy band

alignment determination and Dr. Guillaume Sauthier from Institut de Nanociència i Nanotecnologia (ICN2) for the support in the XPS measurements. Also, all our collaborators from ICMAB: Prof. Josep Fontcuberta who provided access to his facilities for ferroelectric and photoresponse characterization as well as instrumental discussions on photoferroelectrics, Dr. Ignasi Fina and Huan Tan for the PFM measurements, Prof. Mariano Campoy for helping me with spectroscopic ellipsometry, Jordi Alcalà and Dr. Anna Palau for the electrical resistivity measurements, Dr. Gabriele de Luca for his help to deposit ITO electrodes and Prof. Gustau Catalán (ICN2) for providing access to the sputtering equipment. Dr. Carles Frontera for guidance on XRD interpretation.

I also want to deeply thank the members of our research group at ICMAB. Pol (Dr. Pol Sallés now, sorry), thank you so much for your contribution with thin film deposition by ALD, for sure a big part of this thesis could not have happened without your help. I really appreciate all the hours that you have dedicated on it during your PhD thesis. Recognition also goes to Alexander Frebel, for his sound contribution in energy band alignment determination during his stay at ICMAB in the scope of his Master thesis. Also, Ivan Caño who worked in the study of cation engineering of BFO in his Master thesis and Ramon J. Morera for his involvement on the synthetic route for transparent LSCO thin films during his short stay as undergraduate student. Finally, I would also like to acknowledge Dr. Pengmei Yu, for all the discussions in group meetings and for always being available for helping me in the laboratory.

Acknowledgements also go for all the technicians at ICMAB. Mariona de Palau, thank you for showing me around when I first arrived to ICMAB, you have always been so kind to me, thank you for your predisposition to make sure that everything is safe and ready-to-work at the laboratories. Also, thanks to the XRD lab team, Anna, Joan and Xavi, for your help in data interpretation and for the infinite measurements that you have performed, sometimes even in a rush but always with a good mood. To the NANOQUIM clean room team, Marta, Luigi, Neus and Rosa, thank you for your flexibility when I unexpectedly needed to use any equipment and for your trainings, I have learned a lot from you. Finally, I would also like to acknowledge the scientific service of electron microscopy, Anna Esther and Judith for their help with SEM equipment, the scanning probe microscopy lab for providing AFM images, Raul Solanas from the thin films laboratory for sputtering deposition and Vega from the spectroscopic techniques laboratory. My gratitude goes to each and every one of you because to a greater or lesser extent, you have contributed to this thesis and you have taught me during my stay at ICMAB.

I also want to especially mention all those people with whom I have had the pleasure of meeting over the years at ICMAB. I have worked closer with some of you than with others, but we have shared countless memorable moments together. Alex, Juri, Artur, Mathieu, Ziliang, Pedro, Jordi, Francesco, Lavinia, Coco, Roxana, Yunwei, Ma, Joshua, Irene... thank you for sharing lunch times, breaks, coffees, beers and laughs. My stay at ICMAB would not have been the same without you and I take a beautiful friendship from many of you. I would also like to express my gratitude to the entire SUMAN group, especially Prof. Teresa Puig, Prof. Xavier Obradors, and Dr. Mar Tristany.

I acknowledge financial support from *Ministerio de Ciencia, Innovación y Universidades* for their funding through FPI fellowship program (PRE2018-084618) inside the project Severo Ochoa Programme for Centers of Excellence (SEV-2015-0496-18-1). We also acknowledge MICIN/AEI/10.13039/501100011033/FEDER through the projects Severo Ochoa FUNFUTURE CEX2019-00917-S, FREEOXIDES PID2020-114224RB-I00, CHEMOX-MAT2017-83169-R and the project TED2021-130402B-I00 funded by MICIN/AEI/10.13039/501100011033 and European Union NextGeneration EU/PRTR. Financial support from the 2020 Leonardo Grant for Researchers and Cultural Creators and the i-link A20346-CSIC project is acknowledged.

Por otro lado, y para concluir, mis agradecimientos más íntimos van para mi familia, por apoyarme desde el principio de este proyecto. Quienes nos hemos dedicado a este mundo de la investigación, sabemos que son muchas las horas invertidas en experimentos, artículos, documentación..., muchas de esas horas incluso a expensas de tiempo personal. Les agradezco a todos por haber sido siempre comprensivos y por ayudarme a mantener el foco en mis objetivos, cuando hasta yo lo había perdido. Gracias mamá, porque siempre me has mostrado tu amor y respaldo incondicional. Sin toda tu ayuda jamás habría llegado hasta aquí y hoy sé, que todo lo que soy es gracias a todos los valores que me has transmitido siempre. Nico, has sido sin duda el apoyo más fuerte en este camino, has estado a diario, dándome palabras de aliento y de cariño, has aguantado muchas horas de frustraciones, de ordenadores, de reuniones, de laboratorio, muchos "*lo siento, al final llego 3 horas tarde...*" Aún así, siempre me has recordado que soy capaz de todo lo que me proponga. A mi padre, mi hermano, mis abuelos y mis tías y a toda esa familia que se elije y que uno tiene la suerte de encontrar.

Abstract

Photoferroelectric perovskite oxides offer singular opportunities to be used as stable and lead-free light-absorbers in front of traditional semiconductors. Owing to their unconventional photovoltaic (PV) mechanism, the bulk PV effect, they are attractive to be integrated as an homogeneous-single phase photo-active material in simple PV devices. In addition, they can potentially modulate the photore-sponse by taking benefit of their ferroelectric polarization switching.

Over the past years, the study of photoferroelectrics in PVs has been mainly focused on BiFeO_3 (BFO) due to its relatively narrow bandgap at 2.7 eV and its high ferroelectric polarization at room tempera-ture, which is maximized in epitaxially grown thin films. However, its PV performance is still far from ideal. In order to exploit its full potential there are at least two key aspects that need investigation.

The first one is to engineer the BFO layer itself to further improve light absorption and the photocurrent. The use of cation engineering is very attractive and recent investigations provided evidence that the sub-stitution of Fe by Co in epitaxial BFO ($\text{BiFe}_{1-x}\text{Co}_x\text{O}_3$, BFCO) can introduce a bandgap modulation towards the visible with improved ferroelectricity. Nonetheless the stabilization of this phase is limited to Co loads $< 30\%$ due to the formation of parasitic secondary phases, limiting additional bandgap narrowing. Better understanding of the role and the control of cation substitution is required to tackle this bottleneck.

The second aspect is to design an adequate device architecture to improve the extraction of the photo-generated carriers and this study is missing for epitaxial BFO films. It is essential to dedicate efforts towards identifying compatible materials from structure, chemistry and optoelectronic standpoints that can be integrated in the BFO device, i.e. perform interface engineering, and investigate how they affect the device properties. The versatility of oxides can facilitate this task and the use of economical depo-sition techniques can be an attractive approach.

With a focus on these crucial aspects, in this PhD thesis we first investigate the frontiers of cation nanoengineering in BFO targeting the challenging task to perform two simultaneous cation substitution, $\text{Bi}_{1-y}\text{Ln}_y\text{Fe}_{1-x}\text{Co}_x\text{O}_3$ (Ln-BFCO, with $\text{Ln} = \text{Ce}, \text{La}$), to prepare pure phase and epitaxial films. Spe-cial emphasis is placed to comprehend the effects of compositional engineering on the structure, optical, electronic and electrical properties of the system. Noteworthy, this demanding study is assessed by using chemical solution deposition (CSD) owing its strong versatility to perform compositional changes while being a cost-effective methodology.

Then, it is studied the design of an appropriate architecture based on all-oxide components to facilitate both material integration and promote the extraction and collection of the photogenerated carriers. In order to shed light on the unexplored epitaxial BFO PV system, it is aimed a simple and stable architecture consisting of an epitaxial $\text{La}_{0.7}\text{Sr}_{0.3}\text{MnO}_3$ (LSMO) *p*-type bottom electrode grown on SrTiO_3 (STO) single crystal, epitaxial BFCO-based photoabsorber and completed with a *n*-type Sn-doped In_2O_3 (ITO) transparent top electrode. In this basic system it is investigated the role of interface engineering with ZnO transport layer (ITO/ZnO/BFCO/LSMO//STO). Optimization of the deposition conditions and film thickness is first performed to subsequently evaluate the influence of interface engineering with ZnO on ferroelectricity and photoresponse. To help unraveling the role of ZnO on short circuit current density (J_{sc}) and open circuit voltage (V_{oc}) parameters, the energy band alignment is extracted. The photo- and ferroelectric response is also evaluated, providing the opportunity to learn the complex interplay of ferroelectricity with the photogenerated currents. Additionally, the performance of double-site cation substituted La-BFCO films is examined. Then, as an alternative approach to improve the light absorption and extraction of the photogenerated carriers in BFCO, it is explored for the first time the preparation of a vertical gradient composition of Co. In an attempt to control and drive the cobalt distribution throughout the BFO film thickness, atomic layer deposition (ALD) and CSD have been adopted along with performing meticulous examination of the thermal process. Next, the optical and photoferroelectric properties are studied and compared to those of BFCO thin film with homogeneous Co composition.

Finally, aiming to further engineer the PV performance of the epitaxial photoferroelectric perovskite oxide device, it is investigated the development of a synthetic process for a *p*-type transparent conducting oxide with compatible structure, which are rather scarce. The use of these oxides is of utmost importance to provide structure compatibility and a more effective collection of holes in the device. Nevertheless, achieving *p*-type conductivity in perovskite oxides is intrinsically complex and the use of chemical deposition routes adds a new challenge. In this thesis, we perform an exhaustive and systematic study to develop a pioneering CSD-based synthesis route to prepare of epitaxial Sr-doped $\text{La}_{0.75}\text{Sr}_{0.25}\text{CrO}_3$ (LSCO) thin films. We examine the influence of different solution chemical formulations and processing conditions on the surface morphology and crystallinity of the films. The optical transparency and electrical resistivity are studied for the optimized epitaxial LSCO thin films. Moreover, a detailed structure

and electronic analysis allows understanding the influence of Sr-doping on the resulting physical properties.

Overall, in this thesis it is presented an extensive study beyond the state of the art to explore the opportunities of solution processing to tune the composition of the photoferroelectric epitaxial BFO to make it more suitable as photo-active material. Also, a strong effort has been placed to identify and synthesize compatible oxide materials to build a stable all-oxide PV device based on cation engineered BFO and provide insights of the key role of interface engineering on the device performance.

Resumen

Los óxidos de perovskita fotoferroeléctricos ofrecen oportunidades singulares para ser utilizados como materiales foto-absorbentes estables y sin plomo frente a los semiconductores tradicionales. Debido a su mecanismo fotovoltaico (FV) no convencional, el efecto FV masivo (*bulk PV effect*), son atractivos para integrarse como capa activa homogénea en dispositivos fotovoltaicos simplificados. Además, podrían ofrecer la posibilidad de modular la fotorrespuesta aprovechando su conmutación ferroeléctrica.

En los últimos años, el estudio de fotoferroeléctricos en FV se ha centrado principalmente en BiFeO_3 (BFO) debido a que posee una banda prohibida relativamente estrecha (2.7 eV) y una alta polarización ferroeléctrica a temperatura ambiente, que puede ser maximizada en capas delgadas con crecimiento epitaxial. Sin embargo, su rendimiento fotovoltaico aún está lejos de ser el ideal. Para explotar todo su potencial, hay al menos dos aspectos clave que necesitan ser investigados.

El primero es modificar la capa BFO para mejorar aún más la absorción de luz y la fotocorriente en la misma. Para este propósito, el uso de la ingeniería de cationes resulta muy atractivo. De hecho, investigaciones recientes han demostrado que la sustitución de Fe por Co en capas de BFO epitaxial ($\text{BiFe}_{1-x}\text{Co}_x\text{O}_3$, BFCO) puede introducir una modulación de la banda prohibida hacia el visible, dando lugar además a propiedades ferroeléctricas mejoradas. No obstante, la estabilización de esta fase se limita a concentraciones de Co $< 30\%$, valores en los que tiene lugar la formación de fases secundarias no deseadas, limitando así la posibilidad de continuar estrechando la banda prohibida. Un mejor control y comprensión sobre el papel de la sustitución catiónica es necesario para superar este reto de estabilización.

El segundo aspecto es diseñar un dispositivo con arquitectura adecuada para mejorar la extracción de los portadores fotogenerados. Sin embargo, este estudio ha sido poco explorado, especialmente para capas epitaxiales de BFO. Es esencial dedicar esfuerzos hacia la identificación de materiales compatibles desde el punto de vista estructural, químico y optoelectrónico para su integración en el dispositivo basado en BFO, así como investigar cómo afectan estos materiales en las propiedades del dispositivo. Esta estrategia se conoce como ingeniería de interfaz. La versatilidad de los óxidos puede facilitar esta tarea y el uso de técnicas de depósito económicas puede ofrecer una ruta atractiva.

Teniendo en mente estos objetivos cruciales, en esta tesis primero investigamos las posibilidades de la nanoingeniería catiónica en BFO y nos centramos en la desafiante tarea de realizar dos sustituciones catiónicas de manera simultánea para la preparación de capas epitaxiales con pureza de fase,

$\text{Bi}_{1-y}\text{Ln}_y\text{Fe}_{1-x}\text{Co}_x\text{O}_3$ (Ln-BFCO, siendo Ln = Ce, La). Se pone especial énfasis en comprender los efectos de la ingeniería de composición en la estructura, las propiedades ópticas, electrónicas y eléctricas del sistema. Cabe destacar que este exigente estudio se evalúa mediante métodos de deposición química por soluciones (del inglés, CSD) debido que ofrecen una gran versatilidad para realizar cambios composicionales además de un bajo coste.

A continuación, se estudia el diseño de una arquitectura basada en componentes óxidos, para facilitar tanto la integración del material como promover la extracción y recolección de los portadores de carga fotogenerados. Con el fin de arrojar luz sobre el sistema fotovoltaico basado en capas epitaxiales de BFCO, se propone una arquitectura simple y estable que consiste en: un electrodo inferior epitaxial de tipo p ($\text{La}_{0.7}\text{Sr}_{0.3}\text{MnO}_3$, LSMO) crecido sobre SrTiO_3 (STO), el fotoabsorbente BFCO y un electrodo superior transparente de tipo n ($\text{Sn-In}_2\text{O}_3$, ITO). En este sistema básico se investiga el papel de la ingeniería de interfaz al añadir una capa de transporte selectivo, ZnO, (ITO/ZnO/BFCO/LSMO//STO). Primero se realiza la optimización de las condiciones de depósito y el espesor de la capa ZnO. A continuación, se evalúa su influencia en la ferroelectricidad y la fotorrespuesta. Para comprender qué función tiene la capa de ZnO en los parámetros de densidad de corriente de cortocircuito (J_{sc}) y voltaje de circuito abierto (V_{oc}), se extrae el diagrama de alineación de bandas energéticas. De forma paralela se evalúa la respuesta foto- y ferroeléctrica de estos sistemas, con el objetivo de aprender sobre el complejo rol de la ferroelectricidad en las corrientes fotogeneradas. Además, se examina la fotorrespuesta de dispositivos con capas de doble sustitución catiónica, La-BFCO. Luego, como un enfoque alternativo para mejorar la absorción de luz y la extracción de los portadores fotogenerados en BFCO, se realiza un estudio pionero para evaluar la fabricación de una composición de gradiente vertical de Co. Con el propósito de controlar e impulsar la distribución de Co a lo largo de la película de BFO, se adoptan técnicas de deposición de capas atómicas (del inglés, ALD) y CSD y se evalúa meticulosamente el proceso térmico. Las propiedades ópticas y fotoferroeléctricas son analizadas y comparadas con las de una capa de BFCO con composición homogénea.

Finalmente, con el objetivo de continuar explorando el diseño de dispositivos fotovoltaicos basados en óxidos de perovskita fotoferroeléctricos epitaxiales, se investiga el desarrollo de una ruta sintética para un óxido conductor transparente de tipo p que aporte compatibilidad estructural. Actualmente, el desarrollo de estos materiales está en su infancia. Además de la compatibilidad estructural, el uso de estos óxidos es

de suma importancia para ayudar a promover una recolección más efectiva de agujeros en el dispositivo. Sin embargo, lograr una conductividad de tipo p en óxidos de perovskita es intrínsecamente complejo y el uso de rutas químicas para su preparación agrega un nuevo desafío. En esta tesis, realizamos un estudio exhaustivo y sistemático para desarrollar por primera vez una ruta basada en CSD que permita preparar capas delgadas epitaxiales con composición $\text{La}_{0.75}\text{Sr}_{0.25}\text{CrO}_3$ (LSCO). Examinamos la influencia de diferentes formulaciones químicas de solución y condiciones de procesamiento en la morfología de la superficie y la cristalinidad de las películas. La transparencia óptica y la resistividad eléctrica se estudian para las capas de LSCO epitaxial preparadas a partir de la ruta química optimizada, y un análisis electrónico y estructural detallado permite comprender la influencia del dopaje con Sr en las propiedades físicas finales.

En líneas generales, en esta tesis se presenta un estudio exhaustivo que va más allá de la investigación actual. Se pretende explorar las oportunidades que ofrece el procesamiento de soluciones para ajustar la composición de capas epitaxiales del material fotoferroeléctrico BFO y hacerlo más adecuado para su uso como material fotoactivo. Además, se realiza un gran esfuerzo para identificar y preparar materiales óxidos con compatibilidad para construir un dispositivo fotovoltaico "totalmente óxido" y estable basado en BFCO. Se intenta proporcionar información sobre el importante papel que juega la ingeniería de interfaces en el rendimiento del dispositivo.

Resum

Els òxids de perovskita fotoferroelèctrics ofereixen oportunitats singulars per a ser utilitzats com a materials foto-absorbents estables i sense plom enfront dels semiconductors tradicionals. A causa del seu mecanisme fotovoltaic (FV) no convencional, l'efecte FV “massiu” (*bulk PV effect*), són atractius per integrar-se com a capa activa homogènia en dispositius FVs simplificats. A més, podrien oferir la possibilitat de modular la fotoresposta aprofitant la seva commutació de polarització ferroelèctrica.

En els últims anys, l'estudi de fotoferroelèctrics en fotovoltaica s'ha centrat principalment en BiFeO_3 (BFO) a causa de la seva banda prohibida relativament estreta de 2.7 eV i la seva alta polarització ferroelèctrica a temperatura ambient, que es maximitza en capes primes epitaxials. Tot i això, el seu rendiment FV encara està lluny de ser l'ideal. Per explotar tot el seu potencial, hi ha almenys dos aspectes clau que necessiten ser investigats.

El primer és modificar la capa BFO per millorar encara més l'absorció de llum i el fotocorrent al sí de la capa. Amb aquest propòsit, l'ús de l'enginyeria de cations resulta molt atractiu. De fet, investigacions recents han demostrat que la substitució de Fe per Co en capes de BFO epitaxial ($\text{BiFe}_{1-x}\text{Co}_x\text{O}_3$, BFCO) pot introduir una modulació de la banda prohibida cap al visible amb propietats ferroelèctriques millorades. No obstant això, l'estabilització d'aquesta fase es limita a concentracions de Co $< 30\%$, valors en els quals té lloc la formació de fases secundàries no desitjades, limitant així la possibilitat de continuar baixant els valors de banda prohibida. Un millor control i comprensió sobre el paper de la substitució catiònica és necessari per superar aquest repte d'estabilització.

El segon aspecte és dissenyar un dispositiu amb arquitectura adequada per a millorar l'extracció dels portadors fotogenerats. Aquest estudi ha estat poc explorat, especialment per a capes epitaxials de BFO. És essencial dedicar esforços cap a la identificació de materials compatibles des del punt de vista estructural, químic i optoelectrònic que puguin ser integrats al dispositiu basat en BFO, així com investigar com afecten aquests materials en les propietats del dispositiu. Aquesta estratègia es coneix com a enginyeria d'interfície. La versatilitat dels òxids pot facilitar aquesta tasca i l'ús de tècniques de deposició econòmiques ofereix un enfocament atractiu.

Enfocant-nos en aquests aspectes crucials, en aquesta tesi doctoral primer investiguem les possibilitats de la nanoenginyeria catiònica a BFO i ens centrem en la tasca desafiant de realitzar dues substitucions catiòniques de manera simultània per a la preparació de capes epitaxials amb puresa de fase, $\text{Bi}_{1-y}\text{Ln}_y\text{Fe}_{1-x}\text{Co}_x\text{O}_3$ (Ln-BFCO, on Ln = Ce, La). Es posa especial èmfasi a comprendre els

efectes de l'enginyeria de composició en l'estructura, les propietats òptiques, electròniques i elèctriques del sistema. Cal destacar que aquest exigent estudi s'avalua mitjançant mètodes de deposició química per solucions (de l'anglès, CSD) degut que ofereixen una gran versatilitat per a fer canvis composicionals a més d'un baix cost.

A continuació, s'estudia el disseny d'una arquitectura basada en components totalment òxids i compatibles, per facilitar tant la integració del material com per promoure l'extracció i la recollida dels portadors de càrrega fotogenerats. Per tal de generar coneixement sobre el pràcticament desconegut sistema FV basat en capes epitaxials de BFCO, es proposa una arquitectura simple i estable que consisteix en: un elèctrode inferior epitaxial de tipus p ($\text{La}_{0.7}\text{Sr}_{0.3}\text{MnO}_3$, LSMO) crescut sobre SrTiO_3 (STO), el fotoabsorbent basat en BFCO i un elèctrode superior transparent de tipus n ($\text{Sn-In}_2\text{O}_3$, ITO). En aquest sistema bàsic s'investiga el paper de l'enginyeria d'interfície en afegir una capa de transport selectiu, ZnO, (ITO/ZnO/BFCO/LSMO//STO). Primer es realitza l'optimització de les condicions de deposició i el gruix de la capa de ZnO. A continuació, s'avalua la seva influència en la ferroelectricitat i la fotoresposta. Per ajudar a comprendre el paper del ZnO en els paràmetres de densitat de corrent de curtcircuit (J_{sc}) i voltatge de circuit obert (V_{oc}), s'extreu el diagrama d'alineació de bandes energètiques. De manera paral·lela, s'avalua la resposta foto- i ferroelèctrica, aportant l'oportunitat d'aprendre sobre el complex rol de la ferroelectricitat en els corrents fotogenerats. A més, s'examina la fotoresposta de dispositius amb capes de doble substitució catiònica, La-BFCO. Després, com un enfocament alternatiu per millorar l'absorció de llum i l'extracció dels portadors fotogenerats a BFCO, es realitza un estudi pioner per a avaluar la fabricació d'una composició de gradient vertical de Co. Amb la intenció de controlar i impulsar la distribució de cobalt al llarg de la pel·lícula, s'adopten les tècniques de deposició de capes atòmiques (ALD) i CSD, juntament amb la realització d'un meticulós estudi del procés tèrmic. Les propietats òptiques i fotoferroelèctriques són analitzades i comparades amb les d'una capa prima de BFCO amb composició homogènia.

Finalment, amb l'objectiu de continuar explorant el disseny de dispositius FVs basats en òxids de perovskita fotoferroelèctrics epitaxials, s'investiga el desenvolupament d'una ruta de síntesi per un òxid conductor transparent de tipus p que aporti compatibilitat estructural. La disponibilitat d'aquests òxids és actualment prou escassa. A més de la compatibilitat estructural, l'ús d'aquests òxids és de gran importància per a ajudar a promoure una recollida més efectiva de forats en el dispositiu. No obstant

això, assolir una conductivitat de tipus p en òxids de perovskita és intrínsecament complexe i l'ús de rutes químiques per a la seva preparació afegeix un nou repte. En aquesta tesi, realitzem un estudi exhaustiu i sistemàtic per desenvolupar per primera vegada una ruta de síntesi basada en CSD que permeti preparar capes primes epitaxials amb composició $\text{La}_{0.75}\text{Sr}_{0.25}\text{CrO}_3$ (LSCO). Examinem la influència de diferents formulacions químiques de solució i condicions de processament en la morfologia de la superfície i la cristal·linitat de les capes. La transparència òptica i la resistivitat elèctrica s'estudien per a les pel·lícules de LSCO epitaxial preparades a partir de la ruta química optimitzada. A més, un estudi electrònic i estructural detallat permeten comprendre la influència del dopatge amb Sr en les propietats físiques finals.

En línies generals, en aquesta tesi es presenta un estudi exhaustiu que va més enllà de la investigació actual. Es pretén explorar les oportunitats que ofereix el processat de solucions per ajustar la composició de capes primes epitaxials del material fotoferroelèctric BFO, fent-lo així més adequat per el seu ús com a material foto-actiu. A més, es realitza un gran esforç per identificar i sintetitzar materials òxids compatibles per construir un dispositiu FV "tot òxid" i estable basat en BFCO. S'intenta proporcionar informació sobre l'important paper que juga l'enginyeria d'interfícies en el rendiment del dispositiu.

List of abbreviations

α : Absorption coefficient
 ϵ_{xx} : In-plane strain
 ϵ_{zz} : Out-of-plane strain
 κ : Extinction coefficient
 λ : Wavelength
 ρ : Resistivity
 a : in-plane lattice parameter
AA: Acetylacetone
AcA: Acetic acid
AFM: Atomic Force Microscopy
ALD: Atomic Layer Deposition
AZO: Al-doped ZnO
BFO: BiFeO₃
BFCO: BiFe_{1-x}Co_xO₃
BFCO10: BiFe_{0.9}Co_{0.1}O₃
BFCO20: BiFe_{0.8}Co_{0.2}O₃
BFCO30: BiFe_{0.7}Co_{0.3}O₃
 c : out-of-plane lattice parameter
c-Si: Crystalline silicon
CA: Citric acid
CB: Conduction Band
CBM: Conduction Band Minima
CBO: Conduction Band Offset
Ce-BFCO: Bi_{1-y}Ce_yFe_{1-x}Co_xO₃
Ce-BFCO30: Bi_{0.9}Ce_{0.1}Fe_{0.7}Co_{0.3}O₃
CIGS: Copper Indium Gallium Selenide (solar cell)
CSD: Chemical Solution Deposition
 d : Thickness
DEA: Diethanolamine
DFT: Density Functional Theory

DMF: Dimethylformamide

DLCC: Dynamic Leakage Current Compensation

DSC: Differential Scanning Calorimetry

EDX: Energy Dispersive X-ray

EELS: Electron Energy-Loss Spectroscopy

E: Electric field

E_c : Coercive electric field

E_f : Fermi Energy

E_g : Bandgap energy

ETL: Electron Transport Layer

FE: Ferroelectric

FTO: F-doped SnO_2

GIXRD: Grazing Incidence X-Ray Diffraction

HAADF: High-Angle Annular Dark-Field

HIT: Heterojunction with Intrinsic Thin Layer

HTL: Hole Transport Layer

IPCE: Incident Photon to Current Efficiency

ITO: Sn-doped In_2O_3

J: Current density

J_{sc} : Short circuit current density

m : Lattice mismatch

MoE: 2-methoxyethanol

n : Refractive index

NREL: National Renewable Energy Laboratory

La-BFCO: $\text{Bi}_{1-y}\text{La}_y\text{Fe}_{1-x}\text{Co}_x\text{O}_3$

La-BFCO10: $\text{Bi}_{0.9}\text{La}_{0.1}\text{Fe}_{0.9}\text{Co}_{0.1}\text{O}_3$

La-BFCO30: $\text{Bi}_{0.9}\text{La}_{0.1}\text{Fe}_{0.7}\text{Co}_{0.3}\text{O}_3$

LAO: LaAlO_3

LCO: LaCrO_3

Ln-BFCO: $\text{Bi}_{1-y}\text{Ln}_y\text{Fe}_{1-x}\text{Co}_x\text{O}_3$

Ln = Lanthanide

LSCO: $\text{La}_{0.75}\text{Sr}_{0.25}\text{CrO}_3$
LSMO: $\text{La}_{0.7}\text{Sr}_{0.3}\text{MnO}_3$
P: Polarization
 P_{inc} : Power irradiance
 P_r : Remnant polarization
 P_{sat} : Saturation polarization
pDOS: Partial Density of Electronic States
PCE: Power Conversion Efficiency
PFM: Piezoelectric Force Microscopy
PPMS: Physical Property Measurement System
PTFE: Polytetrafluoroethylene
PV: Photovoltaics
 r_i : Ionic radius
R: Resistance
SE: Spectroscopic Ellipsometry
SEM: Scanning Electron Microscopy
STEM: Scanning Transmission Electron Microscopy
STO: SrTiO_3
TCO: Transparent Conducting Oxide
 t : Goldschmidt tolerance factor
T: Transmittance
TEM: Transmission Electron Microscopy
TGA: Thermogravimetric Analysis
ToF-SIMS: Time-of-Flight Secondary Ion Mass Spectrometry
V: Voltage
 V_{BI} : Built-in potential
VB: Valence Band
VBM: Valence Band Maxima
VBO: Valence Band Offset
 V_{oc} : Open circuit voltage
 V_{poling} : Pre-polarization voltage

UV-Vis: Ultraviolet-Visible

XAS: X-Ray Absorption Spectroscopy

XRD: X-Ray Diffraction

XPS: X-Ray Photoelectron Spectroscopy

Table of Contents

1	Introduction	2
1.1	Current perspectives and challenges in photovoltaics (PV)	2
1.2	Functional metal oxides for PV applications	5
1.2.1	Oxides as light-absorbers	8
1.3	Perovskite oxides for PV applications	9
1.3.1	Photoferroelectric perovskite oxides as light-absorbers: BiFeO ₃ -based thin films .	9
1.3.2	Perovskite oxides as transparent conducting oxides: La _{0.75} Sr _{0.25} CrO ₃ thin films .	15
1.4	Preparation of thin film heterostructures by chemical solution deposition (CSD)	16
1.5	Objectives and outline of this thesis	19
1.5.1	Objectives	19
1.5.2	Outline	20
2	Experimental	21
2.1	Thin film and heterostructure synthesis	21
2.1.1	Chemical Solution Deposition	21
2.1.2	Other deposition methodologies	33
2.2	Solution and thin film characterization	37
2.2.1	Solution characterization	38
2.2.2	Thermal decomposition characterization	38
2.2.3	Structure characterization	39
2.2.4	Surface morphology characterization	45
2.2.5	Optical characterization	49
2.2.6	Surface chemical composition characterization	52
2.2.7	Photoemission characterization	55

2.2.8	Electric characterization	56
2.3	PV heterostructure characterization	58
2.3.1	Macroscopic ferroelectric characterization	59
2.3.2	Photoresponse characterization	61
2.3.3	Band alignment determination	64
3	Cation co-substitution in BiFeO₃ photoferroelectric thin films for optimized phase stability and enhanced optoelectronic performance	66
3.1	Introduction	67
3.2	La-doped BFCO thin films	69
3.2.1	Crystallinity, structure and surface morphology	69
3.2.2	Optical properties	74
3.2.3	Electronic structure	75
3.2.4	Ferroelectric properties	78
3.2.5	First-principles studies	79
3.3	Ce-doped BFCO thin films	82
3.3.1	Crystallinity, structure and surface morphology quality	83
3.4	Conclusions	86
A3	Annex Information of Chapter 3	87
A3.1	La-doped BFCO thin films	87
A3.1.1	Valence band spectra	87
A3.1.2	Ferroelectric properties	88
A3.1.3	First-principles study based on DFT method	88
A3.2	Ce-doped BFCO thin films	89
A3.2.1	Solution chemistry and processing conditions optimization	89
A3.2.2	Optical and electrical properties	90
4	Interface engineering in all-oxide photovoltaic heterostructures based on cation-substituted BiFeO₃ photoferroelectric thin films	94
4.1	Introduction	95
4.2	Results and discussion	97
4.2.1	Crystallinity and surface morphology	97

4.2.2	Optical properties	98
4.2.3	Photoresponse and ferroelectric properties	98
4.2.4	Energy band alignment determination	102
4.2.5	Influence of cation co-substitution in BFO on the photoresponse	104
4.2.6	Compositional gradient in BFCO photoabsorber	106
4.3	Conclusions	114
A4	Annex Information of Chapter 4	116
A4.1	Crystallinity and phase purity	116
A4.2	Optical properties	117
A4.3	Photoresponse and ferroelectric properties	119
A4.4	Chemical analysis (XPS) and energy band alignment determination	122
5	Chemical solution processing of $\text{La}_{0.75}\text{Sr}_{0.25}\text{CrO}_3$ thin films for <i>p</i>-type transparent conducting electrodes	127
5.1	Introduction	127
5.2	Results and discussion	129
5.2.1	Solution preparation and characterization	129
5.2.2	Thermal decomposition and fine tuning of processing conditions	130
5.2.3	Crystallinity and surface morphology	133
5.2.4	Optical properties	135
5.2.5	Electrical properties	136
5.2.6	Detailed structural analysis	137
5.3	Conclusions	141
A5	Annex Information of Chapter 5	143
A5.1	Study on metalorganic route	143
A5.2	Solution preparation	145
A5.3	Fine tuning of processing conditions	146
A5.4	Detailed structural characterization	148
A5.5	Electrical characterization	149
A5.6	Surface chemical analysis	152

6	General conclusions and future perspectives	155
6.1	General conclusions	155
6.2	Future perspectives	159
	List of figures	161
	Bibliography	164

Chapter 1

Introduction

1.1 Current perspectives and challenges in photovoltaics (PV)

It is undeniable that the years in which this doctoral thesis has been developed have been surrounded by a crescent unstable socioeconomic framework arising from the pandemics in 2019 and, more recently, from Russia's invasion of Ukraine in 2022. This scenario has triggered dramatic record prices of natural gas, and consequently of electricity, escalating into the first truly global energy crisis. As a result, decades of investment in infrastructure and energy policies for natural gas are now being questioned and the international energy trade is being further reoriented to accelerate the development and implementation of cleaner, sustainable and more secure energy sources such as renewable wind and solar, which expansion in the next five years will be much faster than what was expected just a year ago.[1, 2] In fact, solar photovoltaics (PV), which involves the immediate conversion of sunlight into electricity, is now considered the lowest-cost option for electricity generation and it is predicted to become the largest power capacity in the world by 2027,[3, 4, 5] see Figure 1.1. Within this perspective, it is foreseen a power generation equivalent to the annual electricity consumption of China (~ 7400 TWh), the greatest energy consumer in the world.[6] Nevertheless, a faster annual expansion is needed in PVs to achieve this milestone. Besides the new opportunities opened by this dramatic scale up, also new challenges emerge that demand not only for greater policy regulations but also for an exhaustive research to design and produce solar cells with even higher efficiencies, longer lifetimes and reduced manufacturing costs.

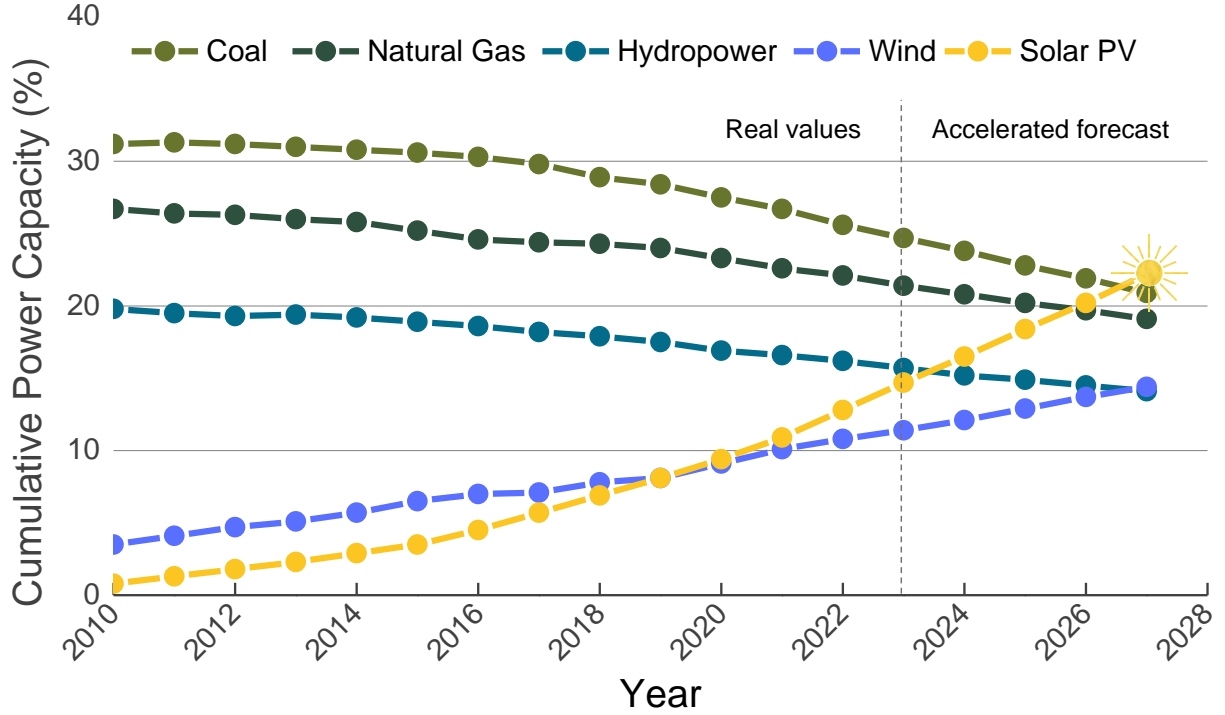


Figure 1.1: Evolution of cumulative worldwide power capacity of the most relevant technologies from 2010 to 2027. The chart includes accelerated forecast from 2022 to 2027 as a result of the current global energy crisis, stating Solar PV as the largest power capacity in the world by 2027. Adapted data from the Executive Summary of the International Energy Agency published on December 2022.[7]

To contextualize, it is important to consider that among the global PV products, first generation single-junction crystalline silicon (c-Si) solar cells have been the leader for 40 years. They constitute a well-consolidated technology that currently owns over 95 % of the market share and has held average power conversion efficiencies (PCE) of ~ 25 % for the last 20 years, see Figure 1.2.[8, 9] Throughout the history, several strategies have been (and are) vastly investigated to overcome the fundamental limitations of these cells, which according to Shockley-Queisser calculations are constrained to theoretical PCE limits of ~ 33 %.[10] The most extended strategies include the use of concentrated sunlight, restriction of the acceptance angle of the cell, control of temperature rise and the design of multi-junction cells, which enable to broaden the range of light absorption by stacking semiconducting materials with different bandgaps (E_g), such as gallium, indium or arsenic.[11, 12] From this last approach, a maximum PCE of ~ 68 % has been theoretically calculated for stacks with infinite cell numbers and even higher values up to ~ 86 % combining the use of sunlight concentrators.[13, 14] In fact, the highest certified PCE to date is 47.6 % for a four-junction solar cell based on III-V compound semiconductors under

the concentrated light condition of 665 suns, see Figure 1.2.[9, 15] Nonetheless, these stacking raw materials are sometimes toxic, their abundance is rather scarce, and the complex architectures and light concentrators are associated to high production costs, hindering the competitiveness of this technology in residential and utility-scale.

Emerging PV technologies explore the use of more affordable materials, with much interest in thin film solar cells that can be deposited onto c-Si to create highly efficient tandem cells.[16, 17, 18] In that regard, deep interest has been aroused on the organic-inorganic halide perovskite/silicon tandem,[19, 20, 21] which has reported impressive breakthroughs in less than a decade by achieving a record PCE of 33.7 % that surpasses the values reported for traditional Si-based cells, Figure 1.2.[9]

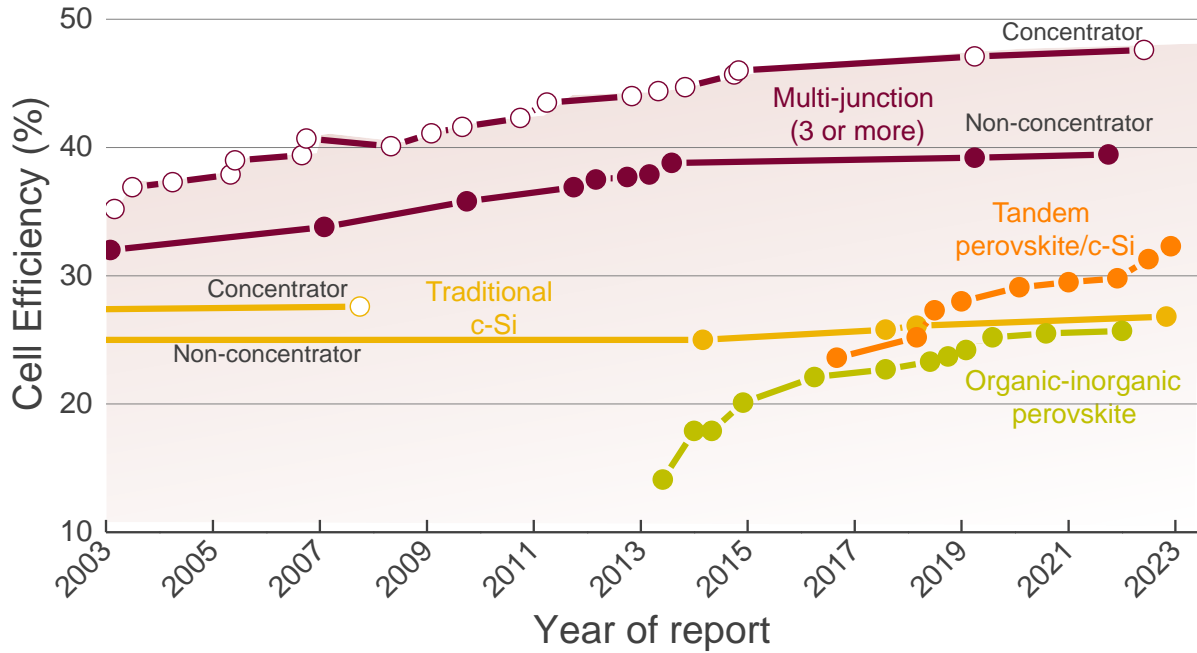


Figure 1.2: Comparative chart of best-research cell efficiencies reported over the last 20 years for different PV technologies including (yellow) traditional c-Si (c-Si and heterojunction with intrinsic thin layer (HIT)), (bordeaux) multi-junction, and emerging (gren) organic-inorganic halide perovskite and (orange) perovskite/Si tandem solar cells. Adapted from NREL best-research efficiency chart (last update June 3rd, 2023).[9]

However, these large efficiencies are also gained at the cost of highly complex engineered multi-

layered/tandem architectures and the use of sometimes heavy, rigid, unstable and/or toxic materials that require for encapsulation to ensure their durability and protection against thermal, mechanical and chemical agents present in the environment, such as water and oxygen. These factors strongly contribute to raise the manufacturing intricacy and the associated expenses, obstructing the market penetration of these solar cells that still mainly remain at laboratory level.[22] Therefore, it is of special interest to explore the development of disruptive environmentally friendly, abundant, and versatile PV materials that also exhibit long-term stability in their functionalities and could be easily prepared using accessible and potentially scalable techniques. With respect to that, oxides appear as solid candidates that could fulfill these requirements.[23, 24, 25, 26]

1.2 Functional metal oxides for PV applications

Metal oxides are particularly interesting because of their unique and versatile characteristics including excellent chemical, thermal and mechanical stability. Moreover, due to the large electronegativity of oxygen, which easily creates strong chemical bonds with almost all elements of the periodic table, oxides are ubiquitous in nature and can be regarded as naturally earth-abundant compounds with a large variety of chemical compositions, atomic structures and crystalline shapes that deliver an spectacular diversity of functionalities.[25] Indeed, these functionalities depend on the composition, structure and defects, and in the particular case of thin film oxides, factors such as thickness, strain, grain boundaries and interfacial effects with other materials are relevant.[23, 26]

Importantly, an entire range of electrical conductivity can be found in oxides depending on the filling of the d electronic shells, going from insulator (closed-shell) to semiconductor and metallic conductor (quasi-closed shell) behavior.[27, 28] In addition, semiconductors can display different optical properties with either transparency or light absorption in the visible spectral region due to the large availability of energy gaps between the O $2p$ and metal $3d$ orbitals, that span from wide to narrow bandgaps.[29] Most interestingly, in the particular case of complex metal oxides, collectively to these classical properties, more exotic magnetic and electronic properties can be provided, which often arise from their strongly correlated electrons in the d or f orbitals.[26]

In the framework of complex metal oxides, those with perovskite structure constitute an attractive family of materials. These oxides have general ABO_3 structure, where six O^{2-} anions are coordinated to B-site cations forming a BO_6 octahedra and the A-site cations are occupying the center of four BO_6 octahedra

in 12-fold coordination, see Figure 1.3. Normally, the A-site is composed by alkali, alkaline-earth or rare-earth metal cations whereas the B-site is occupied by transition metals. Importantly, perovskites can remain stable under A and B-site cation substitutions, delivering from orthorhombic and rhombohedral to cubic unit cell structures, when the Goldschmidt tolerance factor, t , is in the range of 0.8 - 1.0.[30] This tolerance factor can be calculated following the Equation 1.1,

$$t = (r_{i,A} + r_{i,O}) / \sqrt{2}(r_{i,B} + r_{i,O}) \quad (1.1)$$

where $r_{i,A}$, $r_{i,B}$ and $r_{i,O}$ are the ionic radii of A, B and O sites in the ABO_3 structure. This is a parameter that should be taken into account when designing new compositions and performing cation engineering. The high versatility of structure and composition offered by perovskites makes them an appealing family of materials: (i) it allows for "*à la carte*" properties engineering that result in fascinating functionalities such as ferromagnetism, ferroelectricity, multiferroicity, piezoelectricity, thermoelectricity or superconductivity, and (ii) ease to integrate compatible crystalline structures into multi-layered architectures. [26, 31, 32, 33, 34]

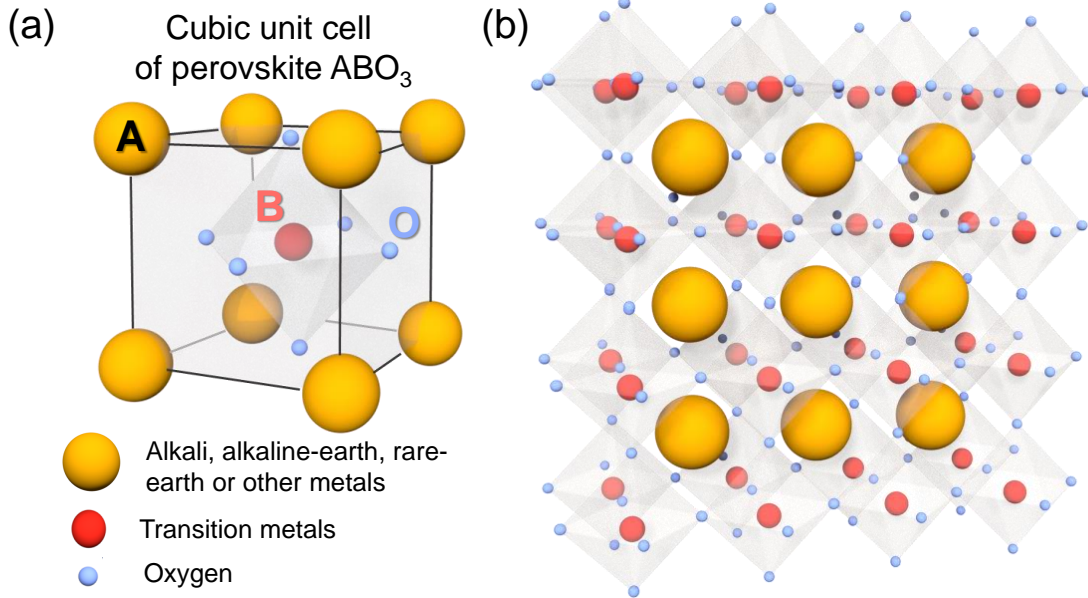


Figure 1.3: Sketch of (a) unit cell of a cubic perovskite with ABO_3 structure and (b) the extended crystal network structure connected by the corner-sharing BO_6 octahedra.

Within this context, oxides are opening the whole periodic table for present and future scientists to

discover and synthesize innovative and cost-effective materials that are increasingly being incorporated into a myriad of cutting edge technology areas such as electronics, memory, magnetics, photonics, health and energy.[23, 26, 35]

Narrowing down to the applications in photovoltaics, metal oxide thin films have been, and are, extensively applied in traditional [36, 37, 38, 39, 40, 41] and emerging PV technologies like organic,[42] kesterite [43, 44] and halide perovskite solar cells.[25, 45, 46, 47, 48] Indeed, due to their broad functional versatility, oxides can be integrated as different components of a solar cell, including charge carriers selective transport layers, passivation layers, electrodes for charge collection and even light-absorbers.[49, 50] Figure 1.4 shows a sketch of a simple thin film vertical PV heterostructure with a selection of oxides which either are, or hold the potential to be, integrated as the different components of the device. It is envisaged that the use of oxides in solar cells could even accelerate the implementation of PVs in modern applications such as wearable electronics, smart windows, building facades or automobile bodywork, which demand for stable materials with more specific requirements, including flexibility, low-weight, semi-transparency, aesthetic appearance or visual comfort.[51, 52] The recent demonstration to prepare free-standing oxides can accomplish flexibility and low-weight needs.[53, 54, 55, 56]

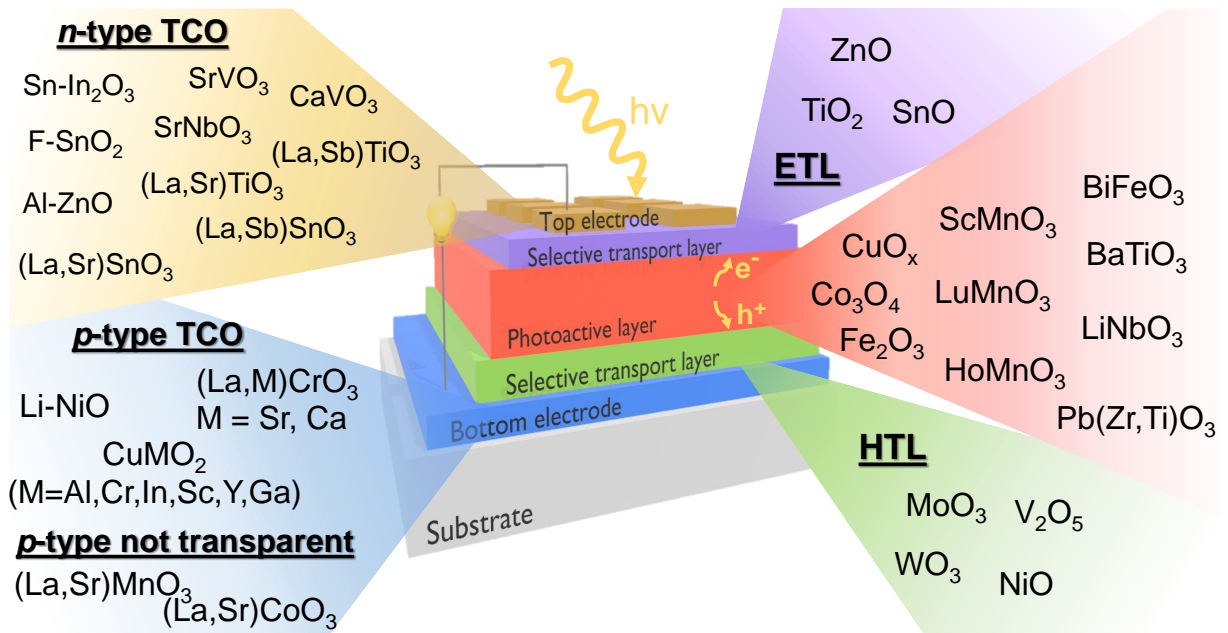


Figure 1.4: Sketch of a simple vertical thin film PV heterostructure and selection of oxides with potential to be integrated as the different components of the device. The abbreviations TCO, ETL and HTL make reference to transparent conducting oxide, electron transport layer and hole transport layer, respectively.

1.2.1 Oxides as light-absorbers

The light-absorber or photo-active film constitutes the central component of any PV device and, as its own name suggests, it is in charge of absorbing the incident sunlight (photons) and producing the charge carriers (electron-hole pairs). In conventional PV devices the electron-hole pairs are separated and extracted from the absorbing material by a built-in electric field arising from a p - n junction, and subsequently transported through the device owing to the presence of an appropriate energy band alignment between the different materials in the system (adequate valence band and conduction band offsets, VBO and CBO, respectively).[57] According to this basic description, a good photo-active material should meet specific requirements. On one hand, it must present a bandgap that ensures light absorption in the visible range of the spectra. According to the Shockley-Queisser model, maximum conversion efficiencies would be obtained for an ideal semiconductor with $E_g \sim 1.3$ eV in a single p - n junction configuration,[10, 14] limiting the choice of light-absorbers only to those with narrow bandgaps. Also, other parameters including high absorption coefficients (α), adjusted carrier density, high minority carrier diffusion length and high mobility need to be considered to promote good absorption and low charge carriers recombination.[58] Although many metal oxides could initially fulfill at least some of these characteristics, and thus potentially be used as light harvesters, only a few of them have been considered and studied for this purpose. The most popular ones are p -type CuO_x ($E_g \sim 1.4 - 2.2$ eV),[59, 60, 61] Co_3O_4 ($E_g \sim 1.5$ eV - 2.2 eV) and Fe_2O_3 ($E_g \sim 2.0$ eV - 2.2 eV), which have been integrated in p - n junction PV architectures in combination with n -type counterparts such as binary ZnO , TiO_2 , Ga_2O_3 or other ternary oxides.[50, 62] Although the reported conversion efficiencies in these systems still need to improve (PCE < 6 %),[63, 34] they constitute a trailblazer in the attempt of using oxides as light-absorbers, and set the basis to continue investigating on novel and alternative oxides.

On that matter, the exploration of complex photoferroelectric oxides has opened a great deal of interest to be used as central light-absorbers [64] due to their unconventional PV mechanism, the bulk PV effect, which is inherent of their non-centrosymmetric structure. These oxides possess three distinctive features: (i) the generation and separation of charge carriers takes place in the bulk of an homogeneous material with no need of a p - n junction. Therefore, the open circuit voltage is not limited to the bandgap of the absorber,[65] opening the possibility to achieve abnormally large photovoltages and surpass the fundamental efficiency limits of traditional semiconductors using simplified device architectures.[66, 67, 68, 69] (ii) The photocurrent and photovoltage are dependent on the polarization direction of the incoming light with respect to the crystal lattice.[70, 71, 72, 73] (iii) The ferroelectric polarization switching could offer

an extra mechanism to modulate and even reverse the charge transport properties. The internal electric fields can be modulated due to polarization-induced depoling fields and/or due to changes in the height of the Schottky barriers at the interfaces of the photoferroelectric, which take place because of surface charges associated to ferroelectric polarization.[68, 74, 75] In addition, it turns out that the magnitude and switchability of the photocurrent can be further affected by the presence of non-switchable electric fields such as imprint electric fields, which favor one direction of polarization. This phenomenon can be originated from different factors, being one of the most important the formation of distinct Schottky barriers at the interfaces when the photoferroelectric film is placed between asymmetric electrodes. This finding already anticipate that the design of the device composition will also play an important role on the resulting ferroelectric-coupled photoresponse. Other factors could be the presence of strain gradients and/or non-homogeneous defect distribution along the film.[76, 77, 78, 79, 80, 81, 82]

Within such promising scenario, the ferroelectric photovoltaic effect has been extensively studied in many non-centrosymmetric oxides as hexagonal h-RMnO₃ manganites (R = Sc, Lu and Ho), which present narrow bandgaps ranging from 1.1 to 1.6 eV but low ferroelectric polarizations,[80, 81, 83, 84, 85] and in perovskite oxides such as Pb(Zr,Ti)O₃ ($E_g \sim 3.0 - 3.5$ eV),[77, 86, 87] BaTiO₃ ($E_g \sim 3.4 - 3.6$ eV),[79, 69, 88], KNbO₃ ($E_g > 4$ eV),[89] LiNbO₃ ($E_g \sim 3.6 - 3.7$ eV),[90] and multiferroic BiFeO₃ ($E_g \sim 2.7$ eV).[91, 92, 93, 94, 95] However, most of the latter oxides exhibit low photocurrents because of their generally low charge carrier mobility and sometimes wide bandgaps that enable light absorption only in the UV region of the solar spectrum. Nonetheless, the high stability and compositional versatility of perovskite oxides offer the opportunity to investigate new compositions with optimized optical and electrical properties.

1.3 Perovskite oxides for PV applications

1.3.1 Photoferroelectric perovskite oxides as light-absorbers: BiFeO₃-based thin films

Among the wide range of ferroelectric perovskite oxides, BiFeO₃ (BFO) is a unique multiferroic material that has been extensively studied as lead-free light absorber because of its high spontaneous ferroelectric polarization at room temperature and its relatively narrow bandgap of ~ 2.7 eV. The crystal structure of BFO is characterized by two distorted perovskite unit cells connected along their body diagonal by

the pseudocubic $[111]$ direction to form a non-centrosymmetric rhombohedral unit cell with space group $R3c$. [96, 97] In relation with the general perovskite structure, A-site cations are occupied by Bi^{3+} in 12-fold coordination with $r_i \sim 1.54 \text{ \AA}$ and B-site cations by Fe^{3+} in 6-fold coordination with $r_i \sim 0.65 \text{ \AA}$ in high spin configuration. [98, 99] In this structure, the lattice constant is $a = 3.965 \text{ \AA}$ and the FeO_6 octahedra is rather distorted along the $[111]$ direction due to the lone pair mechanism, where the s^2 electrons from the Bi hybridize with the oxygen p electrons and induce ferroelectricity. Thus, very large spontaneous polarization in the diagonal $[111]$ pseudocubic direction are reported, with saturation ferroelectric polarizations of $\sim 100 \mu\text{C}/\text{cm}^2$ in epitaxial (111) -oriented thin films and slightly lower values for (110) and (100) -oriented films ($\sim 60 \mu\text{C}/\text{cm}^2$), see Figure 1.5. Note that epitaxial growth offers an opportunity to maximize ferroelectric properties compared to randomly oriented thin films or bulk BFO that present a significantly lower polarization ($6.1 \mu\text{C}/\text{cm}^2$, bulk). [100, 101, 102, 103]

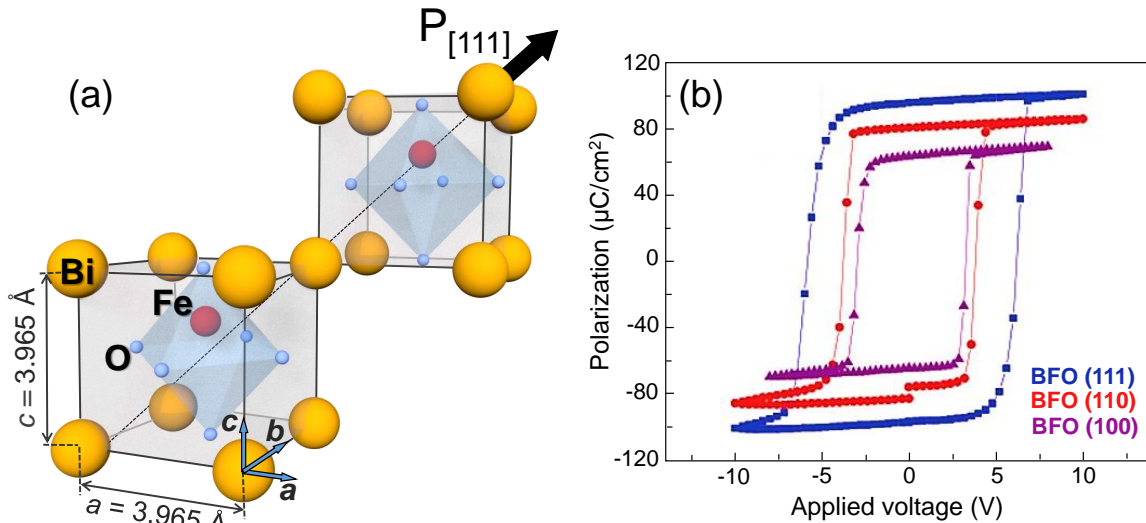


Figure 1.5: (a) Representation of two pseudocubic perovskite unit cells combined along the $[111]$ direction to form the doubled BFO unit cell and the maximum FE polarization direction across the pseudocubic $[111]$. (b) Comparative ferroelectric polarization hysteresis loops of $\sim 170 \text{ nm}$ BFO thin films epitaxially grown on SrRuO_3 -buffered DyScO_3 substrates with different crystallographic orientations, namely (001) , (110) and (111) , by means of pulsed laser deposition, extracted from Ref. [100].

On the other hand, the energy bandgap of BFO is mostly affected by the chemical bonding between Fe^{3+} and the surrounding oxygen anions. Although its value is narrower than that of most classic photo-ferroelectric perovskites, it is still far from the ideal value of $\sim 1.3 \text{ eV}$, [10] and hence it only allows to harvest $\sim 20 \%$ of the solar spectrum. As a consequence, modifying the Fe-O bond properties, while

controlling the Bi-O bond, could allow for bandgap engineering to design new visible-light absorbing BFO-based materials with effectively engineered bandgaps and unaffected ferroelectricity.

The role of compositional engineering: Bandgap tuning in BiFeO₃-based thin films

From the various approaches that have been studied for bandgap tuning, as introduction of oxygen vacancies,[104, 105] FeO₆ octahedral distortions by polarization rotation,[106] or film strain,[107] compositional tuning has demonstrated to be one of the most successful,[108, 109] reporting narrowed bandgap of 1.4 eV in the double-perovskite Bi₂FeCrO₆, which holds record PCE of 3.1 % and 8.1 % in single and multi-layer photoabsorber, respectively.[108] However, controlling site engineering in BFO it is not straightforward because of the generation of Bi-rich secondary phases such as Bi₂O₃, Bi₂Fe₄O₉ and Bi₂₅FeO₄₀,[110] and charge defects including changes in Fe oxidation state as well as bismuth and oxygen vacancies. These charge defects tend to be detrimental for the ferroelectric polarization switching and can act as trap centers for the photogenerated carriers, increasing recombinations when integrated in PV devices.[111, 112] Moreover, the electrical properties of BFO-based oxides have reported to be tightly influenced by their inherent defect chemistry, showing both *n* and *p*-type semiconductor behavior depending on bismuth and oxygen off-stoichiometries.[78, 92, 113, 114, 115, 116, 117] For that reason, there are still fundamental issues in BFO-based light-absorber that need to be investigated and addressed to further understand how cation engineering affects the structure, chemical and physical properties. Learning how to control charge defects and secondary phases formation, which in part depends on the material synthesis technique and the subsequent processing conditions, is of major interest to produce phase pure materials that could potentially deliver improved device performances.

Previous studies have predicted that cation substitution of Fe by Co ($r_i \sim 0.61$ Å,[98]) in BiFe_{1-x}Co_xO₃ (BFCO) system can affect the Fe-O characteristics and the ultimate film absorption, and give rise to high ferroelectric polarizations reaching 170 $\mu\text{C}/\text{cm}^2$ due to crystal structure transitions in fully substituted BiCoO₃. [118] Therefore, this approach could offer the possibility to put forward an attractive active material towards visible light absorption while improving ferroelectricity. Nonetheless, the stabilization of BFCO phases has been limited to low Co content $x < 0.3$ as well to a rather narrow window of growth conditions that demand for high-vacuum or high-pressure processings.[119, 120, 121] Interestingly, a previous study carried out in our group has demonstrated the feasibility to prepare BFCO thin films with Co content up to $x=0.3$. Cobalt-doping in these films showed bandgap narrowing from 2.7

eV to 2.4 eV along with improved and robust ferroelectricity, by means of an inexpensive, flexible and potentially scalable solution-based chemical route.[122] Figure 1.6 summarizes the results published for solution processed-BFCO thin films in Ref.[122]. This study has provided a robust platform to study the correlation between low loads of cation substitution and the optoelectronic properties of the attractive photo-active BFCO. Nonetheless, BFCO with Co loads of $x=0.3$ is already in the threshold of phase stability and secondary phases can occasionally form. Also, preliminary studies on the oxidation states present in this composition anticipated the presence of Fe^{3+} , $\text{Co}^{3+}/\text{Co}^{2+}$ species, expecting altered charge defect scenario (i.e. oxygen vacancies formation) that can affect the physical properties. Therefore, improving the stability of this system with Co loads $x \geq 0.3$ remains a challenge and hinders further progress towards its use as a photo-active material.

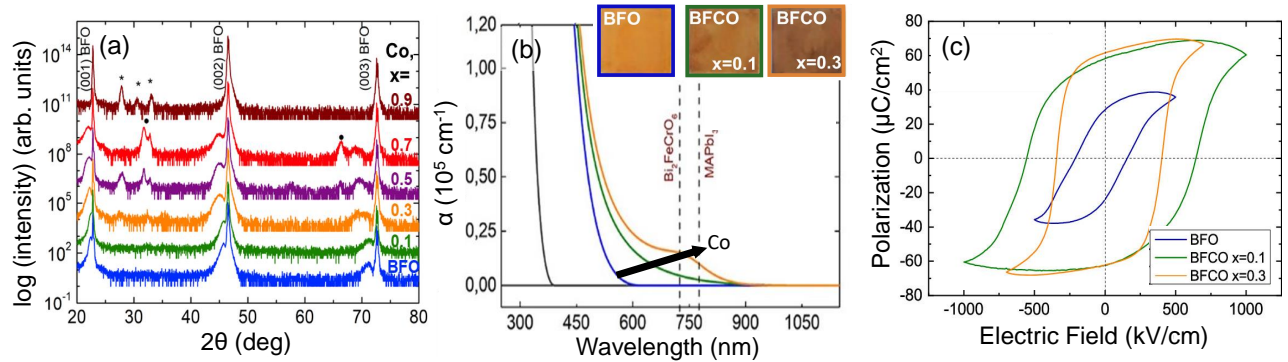


Figure 1.6: Recompilation of the published results on solution-processed BFCO thin films grown on single-crystalline SrTiO_3 from the study of Ref.[122]. (a) Crystallinity and phase purity study, θ - 2θ X-Ray Diffraction scan of BFO and BFCO thin films with cobalt loads in the range $x=0.1 - 0.9$, showing phase-pure BFCO $x < 0.3$ and presence of Bi-rich secondary phases for $\text{Co} = 0.5 - 0.7$. No traces of the BFCO phase are observed for $x = 0.9$. The inset shows a representative scheme of the studied samples. (b) Optical properties study, absorption coefficient spectra of BFO and BFCO thin films indicating monotonous shifts of α to the visible range with increasing Co content. The inset shows photographs of the BFO and BFCO samples anticipating changes in the optical properties. (c) Ferroelectric polarization hysteresis loops of BFCO thin films grown on $\text{La}_{0.7}\text{Sr}_{0.3}\text{MnO}_3$ -buffered SrTiO_3 substrate, improved FE polarization is exhibited upon Co doping.

In this spirit, several reports have underlined the benefits of Bi-site doping in pristine BFO with lanthanide (Ln) cations as La, Ce, Nd or Gd to improve phase purity, film crystallinity and morphology and to help decreasing the leakage currents.[123, 124, 125, 126] It is well known that strong evaporation of Bi occurs during the film fabrication process, in part as a consequence of the low dissociation energy of Bi-O bond ($\sim 340 \text{ kJ/mol}$) which contrast with that of Ln-O ($\sim 800 \text{ kJ/mol}$),[99, 127] and can produce the discussed cation charge defect scenario. In addition, the use of Ln cations for Bi-site substitution

is expected to have little to no influence on the electronic structure of the system.[126, 128] Nevertheless, structural transitions that influence on the ferroelectric and magnetic properties of BFO-based systems have been reported upon Ln concentrations of $> 20\%$. [126, 129] Interestingly, previous studies have effectively prepared Ln-doped BFCO films with robust FE and improved leakage currents, but Co loads remain low ($x = 0.02 - 0.05$), indicating that controlling the doping concentration is relevant although very challenging from the experimental standpoint.[130, 131, 132, 133] The frontiers in BFO co-substitution will be studied in Chapter 3.

It is worth to mention that apart from bandgap tuning with cation substitution,[108, 109, 121, 122, 134] different strategies based on engineering the photo-active BFO-based layer have been evaluated to improve the device performances through enhanced charge carriers transport. These strategies include epitaxial growth with controlled film strain [135, 136] and design of strain gradients,[137, 138, 139, 140] FE domain wall engineering,[65] artificial design of internal electric fields [141] or combination of different FE materials [142, 143, 144]. However, the associated conversion efficiencies still remain low.[94]

In the vein of tuning the photoabsorber to improve the photovoltaic properties, the design of vertical composition gradient appears to be an attractive route. In fact, it has already been adopted in thin film and in emerging PV technologies as CIGS, kesterite and organic solar cells.[145, 146, 147] In these systems, a number of approaches have been developed to control the morphology and composition throughout the photoabsorber including sequential processing, co-evaporation, appropriate solvent choice, slow drying and annealing. [148, 149, 150, 151, 152] Nonetheless, this area is barely explored in epitaxial photoferroelectric oxide perovskites, [82] where two key advantages could be offered: (i) extend the light absorption to a broader region of the solar spectrum compared to single-compositional films and (ii) generate a gradient of the electro-chemical potential, which is equivalent to the generation of an additional built-in electric field. The latter could enhance the transport of electrons and holes towards appropriate electrodes and reduce recombination.[153] However, the influence of discrete versus compositional gradient on the functional properties of photoferroelectrics is, to the best of our knowledge, still to be determined. Here, the complexity appears to be transferred to the fabrication of the gradient itself. The feasibility to prepare vertical gradients in epitaxial BFCO films is discussed in Chapter 4.

Nevertheless, other strategies beyond engineering the photoactive layer itself also need to be taken into consideration to advance towards improved performances and to further understand the behavior of these photoferroelectric-based PV devices. A very interesting approach, although barely explored in BFO photo-absorbers, is to identify the optimal components to build the PV device, i.e. to perform

interface engineering.

The role of interface engineering: Integration of BiFeO₃-based thin films in PV heterostructures

A simplified PV architecture can comprise five basic components: the photo-active layer which is sandwiched between electron and hole selective transport layers (ETL and HTL, respectively), to assess the charge transport through the device, and front and back electrodes to improve charge collection, see Figure 1.4. Indeed, this architecture has already been implemented in traditional and emergent thin film solar cells.[38, 50, 154] In such multi-layered devices, numerous interfaces between the different components are created, where important phenomena as the charge transport, collection and recombination can occur. Consequently, the chemical, physical and electrical characteristics between these layers definitively play an essential role in the ultimate performance, stability and life-time of the devices, into such as extent that, in words of the Nobel Prize in Physics Herber Kroemer, it could be considered that "*the interface is the device*".[155]

In that sense, it is not only crucial the choice of the materials in relation to their optoelectronic properties to ensure adequate light transmission, good transport properties and appropriate energy band alignment at the interfaces, but also the chemical and structural compatibility between the different components of the heterostructure and the deposition methodologies, which should be considered to obtain high quality and low defect films by environmentally friendly and versatile processes.[26]

In this scenario, oxides appear as attractive candidates. Indeed, the use of ETL such as ZnO, TiO₂ and SnO₂,[156, 157, 46, 158, 159, 160], or HTL as MoO₃, NiO and V₂O₅,[41, 161, 162] combined with transparent conducting oxides (TCO), as Sn-doped In₂O₃ (ITO) [163], F-doped SnO₂ (FTO) [164] or Al-doped ZnO (AZO) [165], has already been implemented in conventional and emerging PV technologies.[36, 38, 39, 41, 43, 48]

The exploration of compatible oxide materials for BFO-based architectures has gained interest in the last years although this field still remains at its infancy. Previous studies have reported improved performances upon the substitution of metallic top electrodes by TCOs as ITO or AZO,[78, 166] as well as with the integration of selective transport layers. On one side, TiO₂, SnO₂ and ZnO have been evaluated as ETL,[167, 168, 169, 170, 171] being the later the most popular choice either as thin film [172] or nanostructure.[115, 173] Other architectures involving transport layers such as WS₂ [174, 175]

and reduced-graphene oxide,[176] have also been tested, although the material dissimilarity can add complexity in the device integration and processing.[177] It is worth emphasizing that most of the documented studies involve polycrystalline BFO films, leaving yet little understanding of the implications of interface engineering on epitaxial BFO-based thin film devices,[178] although in other compositions the influence of crystallinity and texture have been anticipated.[179, 180] Importantly, these epitaxial layers impose the use of structurally compatible substrates such as SrTiO_3 (STO), DyScO_3 , LaAlO_3 (LAO) or $\text{La}_{0.18}\text{Sr}_{0.82}\text{Al}_{0.59}\text{Ta}_{0.41}\text{O}_3$, which indeed limit the nature of the bottom electrode and account for the scarce literature found in this area. Conductive perovskite oxides as LaNiO_3 [181, 182, 183], SrRuO_3 [75, 78, 92, 108, 184, 185] or $\text{La}_{0.7}\text{Sr}_{0.3}\text{MnO}_3$ (LSMO) [95, 186, 122, 117] have been reported as promising electrode candidates able to promote the epitaxial growth of photoferroelectric BFO-based films. Nevertheless, the availability of TCOs with perovskite structure that could confer structural compatibility is rather scarce, limiting to advance in investigations on interface engineering of the bottom electrode of the system. This demanding investigation on interface engineering to build a compatible oxide heterostructure is explored in Chapter 4.

1.3.2 Perovskite oxides as transparent conducting oxides: $\text{La}_{0.75}\text{Sr}_{0.25}\text{CrO}_3$ thin films

TCOs are a class of materials that must simultaneously exhibit two properties that according to the simplest description of band theory are contrasting,[187] namely high metallic conductivity and transparency in the visible range. These materials can be generally obtained from tuning the electrical properties of wide bandgap binary or complex transparent metal oxides ($E_g > 3.1$ eV), whose valence band and conduction band are oxygen $2p$ and metal s or d derived, respectively, by increasing the carrier concentration and maintaining mobilities using doping agents.[34, 46, 188] Depending on the nature of the majority carriers, TCOs can be either n -type if electrons are introduced in the conduction band of the oxide or p -type if holes are introduced in the valence band, allowing for an extra selective collection of electrons or holes, respectively, when integrated in PV devices.

Up to date, the majority of TCOs present in the solar cell context, and in technology industry in general, are n -type owing to their easy dopability and high mobilities.[163, 187, 189] The most extended TCO by far is ITO. However, its high and fluctuating price as a consequence of indium scarcity [190] has called for the study of alternative candidates. In addition, the fast development of novel functional materials with perovskite structure demands for structurally compatible TCOs for their epitaxial growth. Still,

this is a sparsely explored research field. On that matter, some of the most promising compositions investigated include *n*-type TCOs, such as $\text{Sr}_{1-x}\text{M}_x\text{SnO}_3$ and $\text{Ba}_{1-x}\text{M}_x\text{SnO}_3$ with $\text{M} = \text{La}, \text{Sb}$ and Nd , $\text{Sr}_{1-x}\text{M}_x\text{TiO}_3$ with $\text{M} = \text{La}$ and Sb , [34], CaVO_3 , SrVO_3 and SrNbO_3 , which have reported excellent performances compared to ITO. [33, 34, 191, 192]

In turn, the study on *p*-type TCO counterparts with perovskite structure is even much less extended, constraining not only the compatible structural growth of functional perovskite oxides but also the development of PV systems with more efficient hole collection. These oxides generally show lower electrical conductivity than their *n*-type counterparts. Also, achieving *p*-type conductivity from doping transition metal oxides is more challenging due to their intrinsic electronic structure, where the strongly localized nature of the O 2*p* orbitals at the top of the valence band hinders the introduction of shallow acceptors and large hole effective masses. [193, 194, 195, 196] Importantly, chemical modulation of the valence band, which involves introducing covalency in the metal-oxygen bond, has appeared as an effective method to overcome this limitation and increase *p*-type conductivity. [197] Closed and quasi-closed shell electronic configurations of cation species (d^{10}, d^6, d^3) are the best candidates to reduce localization of holes in oxygen ions and shift the Fermi level below the valence band maxima, as well as to minimize colorization from the metal *d-d* excitation and ensure optical transparency. For this approach, a series of complex delafossite oxides such as CuMO_2 ($\text{M} = \text{Al}, \text{Cr}, \text{In}, \text{Sc}, \text{Y}$ and Ga) have been extensively studied. [195] Also, novel *p*-type TCOs based on Cr^{3+} oxides (d^3) have been already identified, [198, 199, 200] among which A-site doped perovskite $\text{La}_{1-x}\text{M}_x\text{CrO}_3$ ($\text{M} = \text{Sr}, \text{Ca}$), have aroused as strong candidates with reasonably high transparency and *p*-type conductivity. [201, 202, 203, 204] Nevertheless, their preparation has been limited to high-vacuum techniques and no literature has been found on the use of more cost-effective or flexible chemical methodologies, stimulating the research on this untapped area. This challenge is explored in Chapter 5.

1.4 Preparation of thin film heterostructures by chemical solution deposition (CSD)

The use of deposition methodologies that enable precise atomic-scale control during the preparation of the oxide thin film components in a PV device is instrumental to promote high quality interfaces, long-term stability, and optimized cell operation. It is undeniable that high vacuum deposition techniques (molecular beam epitaxy, pulsed laser deposition, sputtering) allow accurate control of film composition and thickness, and in terms of structure and surface quality, the produced films are almost unbeatable.

However, when evaluating the suitability of an oxide material, apart from film perfection, it is also important to consider the use of cost-effective, sustainable and versatile processing methodologies.

Over the past decades, significant progress has been made to fabricate high quality metal oxide thin films using chemical solution deposition (CSD), a well-established, inexpensive and potentially scalable route. This technique offers the possibility to fabricate thin films by simple precursor salt intermixing, following four basic steps, see Figure 1.7. (i) The synthesis of the precursor solution with the desired stoichiometry using chemically and thermally compatible precursor salts and solvents. (ii) The solution deposition onto a substrate by means of different methods as classic spin-coating, dip-coating and spray-coating or more modern inkjet printing that produces films with improved conformality and reduced solution consumption/waste. Then, the as-deposited samples are subjected to (iii) a low-temperature treatment (< 450 °C) to decompose the organic components, and (iv) a high-temperature thermal process to promote the crystallization of the amorphous coating into the desired oxide phase ($\sim 500 - 1100$ °C).[205, 206, 207] In addition, significant efforts are being currently dedicated to reduce the crystallization processing temperature, targeting a lower-budget process and higher compatibility to integrate the complex oxides in Si-based electronic devices and/or low-cost plastic substrates for cutting-edge flexible electronics, where the integration barrier is at ~ 400 °C.[208, 209, 210] On that purpose, appealing approaches involve controlling the chemistry of the solution, for instance with the use of photosensitive precursors which decrease the crystallization temperatures through exposure to light,[211, 210, 212] the addition of a fuel for self-sustained combustion with highly exothermic reactions,[213] or the proper selection of substrates with compatible interface engineering.[82]

Additional details and fundamentals of CSD are described in the Experimental Section 2.1.1.

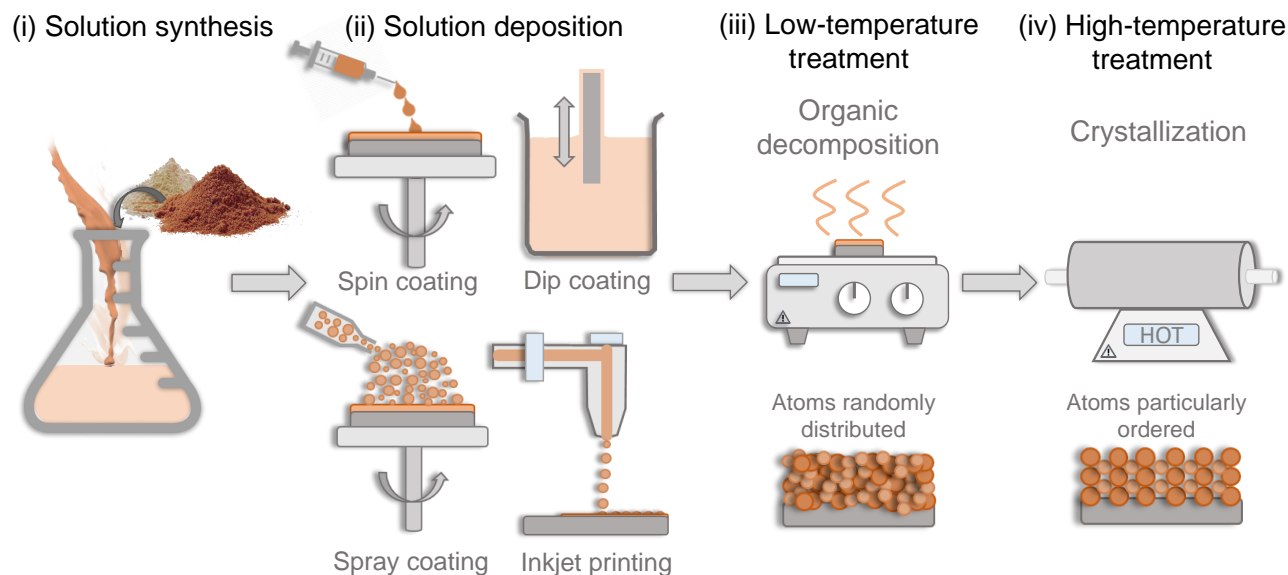


Figure 1.7: Scheme of a general CSD process including the four basic steps (i) precursor solution synthesis, (ii) solution deposition by means of different methods as spin coating, dip coating, spray coating or inkjet printing, (iii) low-temperature thermal treatment for organic decomposition and (iv) high-temperature thermal treatment for desired oxide phase crystallization.

Interestingly, the use of CSD has already been explored for the preparation of thin films of semiconductor binary oxides (ZnO , TiO_2 and MoO_x)[214] and TCOs (ITO , FTO , AZO),[215, 216, 217] with a focus on its implementation at the industry level. This methodology also offers the possibility to prepare epitaxial complex oxides and perform compositional tuning on demand due to its good control over stoichiometry. Achieving epitaxial growth is of particular interest to further control the physical properties, which will ultimately define the functionality of the solution-processed complex oxide.[212] In that regard, several studies have already underlined the effective preparation of a broad range of epitaxial perovskite-type oxides with different functionalities, including high temperature superconductors ($\text{YBa}_2\text{Cu}_3\text{O}_{7-\delta}$),[218, 219] electrically conducting materials ($\text{La}_{1-x}\text{Sr}_x\text{CoO}_3$, SrRuO_3 , LSMO)[220, 221, 222] and ferroelectrics ($\text{PbZr}_{1-x}\text{Ti}_x\text{O}_3$, BaTiO_3 or BFO).[122, 223, 224, 225]

Nonetheless, although the apparent simplicity and versatility of CSD to synthesize crystalline functional oxide thin films, when pursuing the development of novel and unexplored compositions and their integration in an heterostructure, is crucial to conduct an in-depth study to optimize each of the steps involved in the process. This includes analysis of the thermal decomposition of the solution precursors and additives and fine-tuning of the processing parameters such as temperature, time, heating and cooling

rate, and atmosphere according to the chemistry, nucleation, and growth behavior of the oxide material. Therefore, understanding the close relationship between solution chemistry, processing parameters, and the ultimate film growth is essential to fabricate high quality functional complex oxides with the desired physical properties and functionalities, and hence, to widen the repertory of solution-processed complex oxides.

1.5 Objectives and outline of this thesis

1.5.1 Objectives

BiFeO₃ has attracted high interest to be used as an homogeneous single-phase light-absorber in simple PV devices, owing to its bulk photovoltaic effect and robust ferroelectric polarization switching at room temperature. Nonetheless, numerous factors need to be explored in order to unlock its full potential. First, it is essential to improve its photo-absorbing properties by narrowing the bandgap towards the visible range of the solar spectrum, while ensuring phase stabilization, epitaxial growth, and low defect formation to retain high ferroelectricity. Second, the optimal photovoltaic components for its integration into a functional and stable device with structural, optical and electrical compatibility are yet to be revealed. In addition, the use of a cost-effective approach to assess these aspects adds a new challenge to the study.

Based on these requirements, in this PhD thesis we establish three objectives:

1. Investigate the frontiers of cation nanoengineering in epitaxial BiFeO₃-based thin films and determine how it affects on the structure, crystallinity and morphology as well as the impact on the optoelectronic and ferroelectric properties.
2. Evaluate the design of a simple device based on oxide materials that enable the integration of stable cation-substituted photoferroelectric BiFeO₃-based thin films in an heterostructure for improved PV performances. The influence of interface engineering with ZnO and ITO coatings will be examined by first developing compatible synthetic processes to ultimately investigate how they affect the photo- and ferroelectric properties and its inter-relationship.
3. Explore the development of a synthetic route by solution processing for a *p*-type TCO with composition La_{0.75}Sr_{0.25}CrO₃, which could be used as a potential bottom electrode for epitaxial BiFeO₃-based thin films.

1.5.2 Outline

This thesis contains six Chapters organized as follows:

- Chapter 1 provides an introduction to the topic of research.
- Chapter 2 describes the fundamentals and conditions of the synthesis and characterization techniques used to prepare and analyze the thin films and heterostructures of this thesis, respectively.
- Chapter 3 studies the cation engineering in BiFeO_3 photoferroelectric thin films for optimized phase stability and optoelectronic performance.
- Chapter 4 investigates the interface engineering in all-oxide photovoltaic heterostructures based on cation-substituted BiFeO_3 photoferroelectric thin films.
- Chapter 5 tackles the design of a chemical solution processing route for $\text{La}_{0.75}\text{Sr}_{0.25}\text{CrO}_3$ thin films to be used as p -type transparent conducting electrodes.
- Chapter 6 contains the general conclusions and future perspectives of this thesis.

Chapter 2

Experimental

In this PhD thesis, much effort has been dedicated to the design of chemical routes for the preparation of epitaxial complex perovskite oxide thin films and their subsequent integration into all-oxide vertical PV heterostructures. This Chapter describes the fundamentals and conditions of the deposition and characterization techniques used. For ease of reading, the Chapter is divided into three sections:

- **2.1) Thin film and heterostructure synthesis.**
- **2.2) Solution and thin film characterization.**
- **2.3) PV heterostructure characterization.**

2.1 Thin film and heterostructure synthesis

The main deposition methodology used for the synthesis of the studied oxides is chemical solution deposition (CSD). For the preparation of the PV heterostructures, CSD has been combined with atomic layer deposition and sputtering for the deposition of specific components. These other techniques have been used in collaboration with other researchers or scientific services and therefore they are not described in detail.

2.1.1 Chemical Solution Deposition

Solution-based chemical processing techniques allow an easy and versatile deposition of high quality thin films with a variety of compositions.[207, 226] In this PhD thesis, a series of complex oxides were prepared using CSD: BiFeO_3 (BFO), $\text{BiFe}_{1-x}\text{Co}_x\text{O}_3$ (BFCO), $\text{Bi}_{1-y}\text{Ln}_y\text{Fe}_{1-x}\text{Co}_x\text{O}_3$ (Ln-BFCO, with Ln

= La, Ce), $\text{La}_{0.7}\text{Sr}_{0.3}\text{MnO}_3$ (LSMO) and $\text{La}_{0.75}\text{Sr}_{0.25}\text{CrO}_3$ (LSCO). The preparation of epitaxial BFO-based and LSMO oxides was carried out from optimization of an already existing process developed in the group.[122, 227] On the other hand, the unprecedented preparation of epitaxial LSCO by CSD is presented in Chapter 5 and here it will be described the optimal conditions.

In this section, an extended description of the fundamentals of a common CSD process is first presented, followed by the specific synthesis routes of BFO-based, LSMO, and LSCO thin film oxides.

General CSD process

As anticipated in the Introduction Section 1.4, the CSD process is divided in four main steps: (i) synthesis of the precursor solution, (ii) deposition of the coating solution on a substrate, (iii) low-temperature thermal treatment to dry the as-deposited solution and convert solid organic materials into gases and liquids, and (iv) high-temperature thermal treatment to obtain the desired crystalline film, see Figure 1.7.

(i) Synthesis of precursor solution: The CSD process starts with the preparation of the solution, which can be obtained by mixing stoichiometric amounts of the individual precursors such as metal oxide powders, nitrate salts, carboxylates, or other metalorganic compounds with a suitable solvent (or solvent blend). In addition, complexing or ligand-modifying agents can be used to design the optimal solution formulation and ensure long-term stability and desired viscosity, which will ultimately influence on the substrate wettability and film thickness. The homogeneous mixing of the precursors, additives, and solvents can be obtained by magnetic stirring at ambient, moderate, or sometimes higher temperatures using a reflux condenser. Finally, the resulting precursor solution can be filtered with an adequate particle microfilter to avoid the presence of inhomogeneities, such as pinholes and comet streaks in the as-deposited film.[206, 228]

(ii) Deposition of the precursor solution: The precursor solution can be deposited using different coating techniques. In this PhD thesis, spin coating was selected because of its easy homogeneity of deposition, its low cost and potential scalability, which actually converts it into one of the most extended techniques in research.[229] In short, in the spin coating process a liquid solution is deposited onto a substrate in order to produce a thin film of solid material by means of centripetal forces and surface tension. This process can be divided into 4 main steps: solution deposition, spin up, spin off and evaporation, as depicted in Figure 2.1.

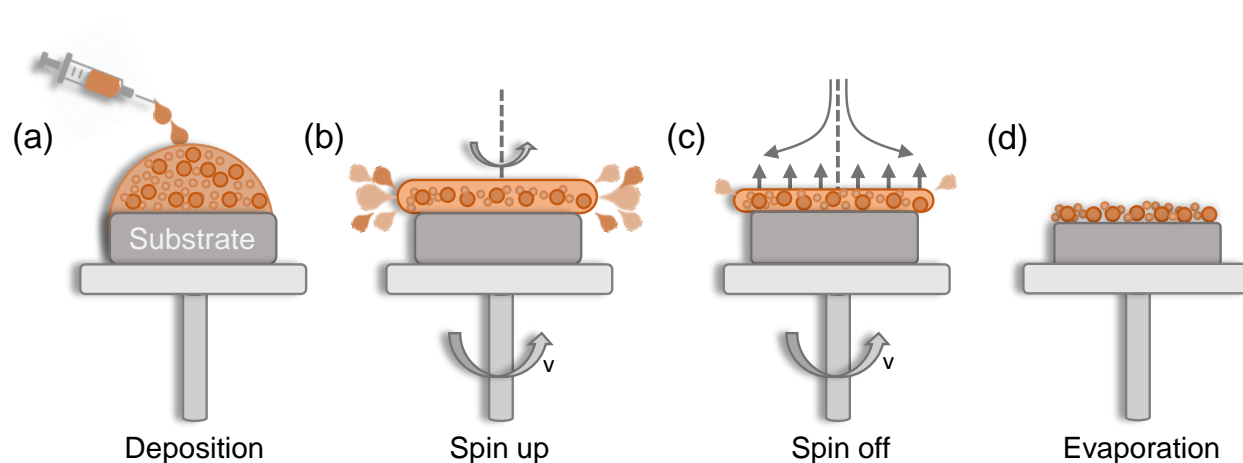


Figure 2.1: Schematic of the four steps involved in the precursor solution deposition process: (a) the precursor solution is deposited onto the substrate, (b) spin up, the substrate starts rotating at high speed, and the majority of the solution is expelled from the substrate, (c) spin off, the solvent starts drying, and the deposited film becomes thinner and (d) evaporation, the film fully dries, leaving a gelated coating. Note that v denotes the rotational speed of the process.

In the initial **deposition** step, a controlled volume of the precursor solution is cast onto the desired substrate until its complete coverage, normally using a microsyringe or micropipette, Figure 2.1 (a). This step can be performed in static or dynamic mode if the substrate is either static or already spinning during casting, respectively. In this work, the static mode is described since its the one that was used for the preparation of the studied films. The coverage of the solution across the substrate (wettability) will be determined by the surface tension of the liquid and the surface energy of the substrate, which in part will depend on the nature of the solution and its rheology. It is important to mention that in water-sensitive solutions, deposition in humidity controlled box should be pursued to avoid degraded properties of the final film.

During **spin up**, the substrate starts to spin until it reaches the desired rotation speed and most of the solution is expelled from the substrate owing to the centripetal force, Figure 2.1 (b). In this stage, the solution initially spins at a rate different than the substrate speed, but eventually the two rotation speeds match up, leading to the formation of a thin fluid layer.

As the solution continues to flung off the substrate, during the **spin off** stage, the fluid layer continues to thin until the centripetal force equals the viscosity force and the film starts drying and becomes leveled, Figure 2.1 (c). However, in most cases, an accumulation of the solution occurs at the edges of

the substrate, contributing to the formation of a thicker film in this area, which produces a border or edge effect.

Finally, when the fluid outflow ceases, the thinning process is dominated by the **evaporation** of the solvent, Figure 2.1 (d), which rate depends on several factors, including the vapor pressure, boiling point, and volatility of the solvent, as well as ambient conditions (temperature and humidity). During this stage, the gelation of the film is (sometimes) driven, entailing the appearance of interactions between the precursor species. As it will be mentioned below, the gelation process depends on the solution chemistry. It is important to consider that non-uniform evaporation rates undergo in the edges of the as-deposited film where the amount of material is higher, what also contributes to the above-mentioned border effect.

Importantly, precise control of the spin coating parameters such as speed and duration is critical for the obtention homogeneous films with the desired thickness. In one hand, the spin speed (v) affects the degree of centrifugal force applied to the liquid fluid as well as the velocity and characteristic turbulence of the air immediately above it, having an impact in the final thickness (d) of the film according to the Equation 2.1.[229, 230]

$$d \propto \frac{1}{\sqrt{v}} \quad (2.1)$$

On the other hand, the optimal duration of the process will depend on the nature of the solvents used. Normally, the objective is to keep the substrate spinning until the film is completely dry, what takes place within ~ 30 seconds for most common solvents. However, in those with low vapour pressure (high boiling point) drying may take considerably longer and substrate coating becomes difficult, compromising the uniformity of the deposited film. Therefore, these solvents are most commonly used either as additives or with additional drying steps. In fact, a good approach to optimize spin coating homogeneity is to mix two solvents with different evaporation rates, using one with fast evaporation rate as major component to allow for good coverage and uniform film and a minor amount of a solvent with slow evaporation rate, which will act as chelating agent and provide plasticity to the film, resulting in a more uniform coating, see Figure 2.2.[230]

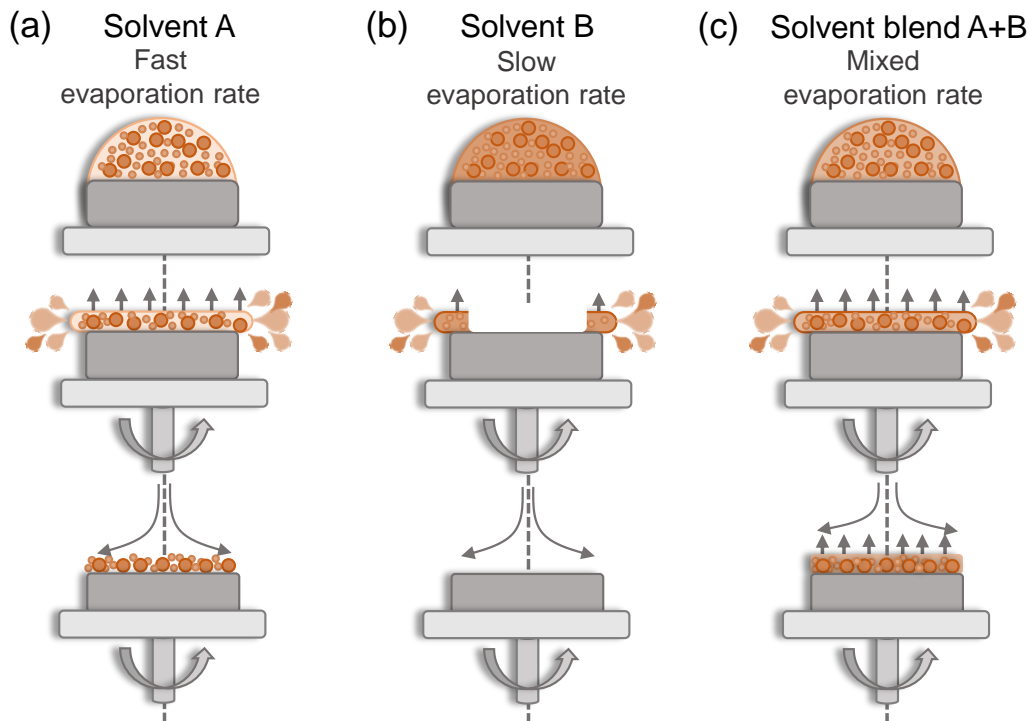


Figure 2.2: Effect of the solvent nature on the ultimate uniformity of the as-deposited film: (a) Precursor solution containing solvent A with high evaporation rate, which provides easy coating but the resulting film is less uniform, (b) precursor solution containing solvent B with slow evaporation rate, the deposition is more difficult because the solution has time to dewet and it is completely expelled off the substrate, leaving no coating. (c) Blend of solvents, using a major part of solvent A and minor part of solvent B, the fast evaporating solvent is removed quickly during rotation, providing good coverage whereas the remaining solvent leaves enough plasticity to the film that results in higher homogeneity.

Following, a thermal treatment is normally carried out. The as-deposited film typically possess a gelated amorphous network that retains a significant fraction of organic compounds, which nature is highly dependent on the characteristics of the precursor species and solvents in the solution. However, if additives or solvents with low evaporation rate are used, the gelation of the film may not be completed after evaporation and could require to be subjected to drying/gelation treatment below 200 °C, see Figure 2.3 (a,b). On the other hand, the organic fraction needs to be removed and the resulting metal-ligand inorganic network rearranged to obtain the metal oxide with desired crystallization phase, normally by means of accurate thermal treatments at low (< 450 °C) and high temperatures ($\sim 500 - 1100$ °C), respectively, see Figure 2.3 (c,d).

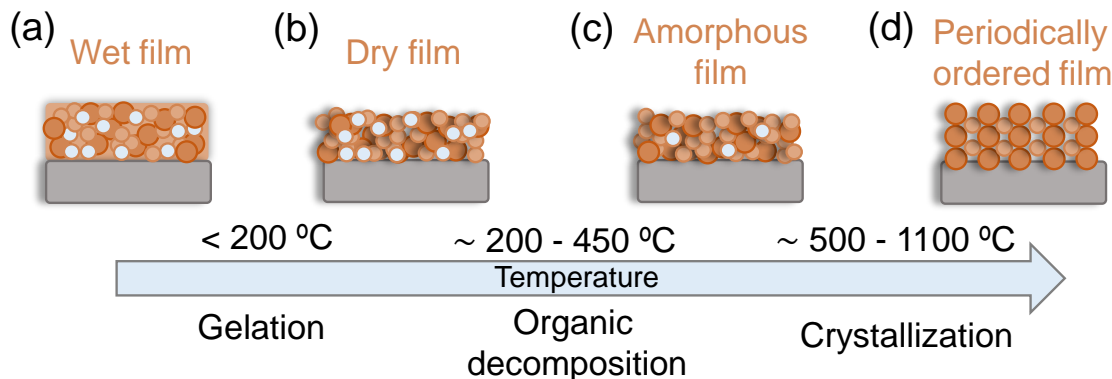


Figure 2.3: Schematic of the thermal treatments carried out in the as-deposited film to obtain a crystallized thin film: (a,b) gelation of the (sometimes) wet as-deposited film, (b,c) organic decomposition through a mild-temperature treatment and (c,d) evolution of amorphous to crystalline film through high-temperature treatment.

(iii) Low-temperature treatment: During this process, the dry coating is subjected to a low-temperature thermal treatment between 200 and 450 °C, mostly known as pyrolysis when it undergoes under oxygen or air atmosphere. This process allows for the removal of the organic constituents by combustion and condensation reactions that break the metal-ligand bonds to volatile organic molecules, entailing a variety of bond reorganizations and structural relaxation processes that lead to the formation of an amorphous metal-oxygen-metal inorganic network,[206, 207, 228] Figure 2.3 (c)

(iv) High-temperature treatment: After organic decomposition, the films are heated to higher temperatures between 550 and 1100 °C to induce the crystallization of the desired oxide phase through nucleation and growth processes, which characteristics will define the microstructure of the film and will be in part determined by factors such as the solution and material chemistry, the structural compatibility with the substrate and the thermal processing conditions.[231] In fact, the nucleation events are highly influenced by the energy difference between the amorphous and the crystalline states (ΔG), which is minimized at higher temperatures, determining whether the nucleation process is homogeneous or heterogeneous. At higher temperatures (lower ΔG), an heterogeneous nucleation process takes place at the interface with the substrate and can promote the formation of epitaxial and highly oriented (textured) films, Figure 2.3.[206, 228]

According to the solution formulation and the material composition, the thermal treatment processing parameters (temperature, dwell, heating and cooling rates, and atmosphere) will need to be specifically designed in order to avoid undesired phenomena such as dewetting, formation of film cracks

and segregation of secondary phases, as well as to ensure minimal inter-diffusion between the film interfaces.[207, 228, 214]

Therefore, the solution chemistry and the processing conditions for the preparation of the BFO, BFCO, Ln-BFCO (Ln = Ce, La), LSMO and LSCO thin films have been accurately selected.

Synthesis of BFO-based thin films by CSD

Solution preparation: A metal nitrate chemical route was used for the preparation of BFO-based thin films, owing that films produced from these metal precursors are generally denser, contain fewer impurities and require lower processing temperatures due to the high volatility of their decomposition byproducts.[232] For each BFO-based composition, that is BiFeO_3 , $\text{BiFe}_{1-x}\text{Co}_x\text{O}_3$ (BFCO) where $x=0.1$, $x=0.2$ and $x=0.3$ and $\text{Bi}_{1-y}\text{Ln}_y\text{Fe}_{1-x}\text{Co}_x\text{O}_3$ (Ln = La, Ce; La-BFCO and Ce-BFCO, respectively) where $y=0.1$ and $x=0.1$, $x=0.3$, the solutions were prepared by weighting stoichiometric amounts of the chemical precursors (powder): bismuth nitrate, $\text{Bi}(\text{NO}_3)_3 \cdot 5 \text{H}_2\text{O}$ (98.0 %), iron nitrate, $\text{Fe}(\text{NO}_3)_3 \cdot 9 \text{H}_2\text{O}$ (98.0 %), cobalt nitrate, $\text{Co}(\text{NO}_3)_2 \cdot 6 \text{H}_2\text{O}$ (98.0 - 102.0 %), lanthanum nitrate, $\text{La}(\text{NO}_3)_3 \cdot 6 \text{H}_2\text{O}$ (99.999 %) and cerium nitrate, $\text{Ce}(\text{NO}_3)_3 \cdot 6 \text{H}_2\text{O}$ (99.0 %). Also, the preparation of BFCO films with a vertical compositional gradient of Co was attempted, in that case the Fe concentration was adjusted according to the theoretical incorporation of Co. After weighting, the precursors were dissolved under magnetic stirring and a moderate heating at 55 °C for 2 hours in a solvent blend with volume proportion (3:1) of 2-methoxyethanol (MOE) and acetic acid (AcA), to obtain an homogeneous solution free of precipitates with final concentration of 0.25 M.[122] In addition, since Ln precursors are difficult to dissolve in the solvents here mentioned, the La-BFCO and Ce-BFCO solutions were left under stirring at the moderate heating using a reflux condenser for 24 hours. Note that MOE was selected as the major solvent, rather than water, because it provides good solubility for various of the starting nitrates as well suitable viscosity and surface tension for spin-coating deposition, whereas AcA was used in a minor proportion as chelating agent, since it has demonstrated to further optimize the solution viscosity through the formation of oligomeric structures and help controlling film morphology in previous reports.[233] Finally, the solutions were filtered using a (PTFE) filter of 0.22 μm pore size.

Solution deposition by spin coating: Prior to deposition, the substrates were properly cleaned with ethanol rinsing and dried with compressed N_2 gas to avoid any dust or particulate on the surface that could cause inhomogeneities such as pinholes and comet streaks in the as-deposited film. The process of

deposition itself was carried out using a spin-coater from *Ossila* located in a dry N_2 box with controlled humidity (10 - 20 %) to improve the homogeneity of deposition, see Figure 2.4 (a). 18 μ l of the 0.25 M BFO-based solution were taken with a microsyringe, deposited on the substrate and then spin coated at 6000 rpm for 36 seconds. The substrates selected for deposition were a 5 mm x 5 mm commercial monocrystalline (001)-oriented $SrTiO_3$ (STO) from *CrysTec* and *Shinkosha* and a CSD-processed LSMO//(001)-STO, which envisages the architecture bottom electrode//substrate. The recipe to prepare LSMO films by CSD is described below.

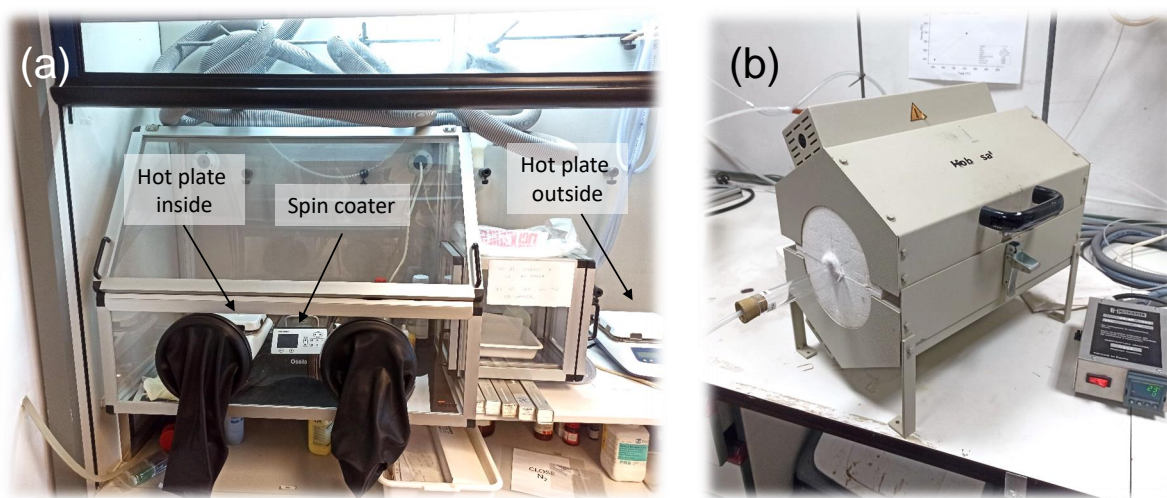


Figure 2.4: Equipment used for the preparation of thin films by means of CSD methodology. (a) Dry N_2 box with controlled humidity containing the spin coater and hot plate for deposition and thermal treatment. Note that the box contains a pre-chamber to introduce/remove material. (b) Tubular furnace used for the high-temperature treatment (i.e. crystallization). A mass flow controller can be used to modulate the gas flow through the quartz tube.

Thermal treatment: Following, the samples were exposed to a thermal treatment at 90 °C for 10 minutes to favor the gelation of the wet as-deposited film, and to 270 °C for 4 minutes to eliminate the organic compounds.[122, 233] The gelation process was carried out in a hot plate situated inside the dry N_2 box with controlled humidity, whereas the organic decomposition process was performed in a hot plate outside the box, and thus, in air atmosphere (pyrolysis), see Figure 2.4 (a). Next, the samples were subjected to a high-temperature crystallization treatment in a pre-heated tubular furnace at 600 °C (BFCO, Ln-BFCO) or 650 °C (BFO) for 30 minutes and quenched at room temperature, see Figure 2.4 (b). The heating and cooling rates were monitored placing a thermocouple in the position of the

sample inside the furnace, and were found to be 660 °C/min. The thermal treatment is sketched in Figure 2.5.

Note that with this CSD-procedure film thickness results in ~ 25 nm. To prepare thicker films up to ~ 100 nm, a multi-deposition process was optimized by repeating the solution deposition and the low temperature treatments (90 °C and 270 °C) four times and finally increasing the crystallization time up to 150 minutes, see Figure 2.5.

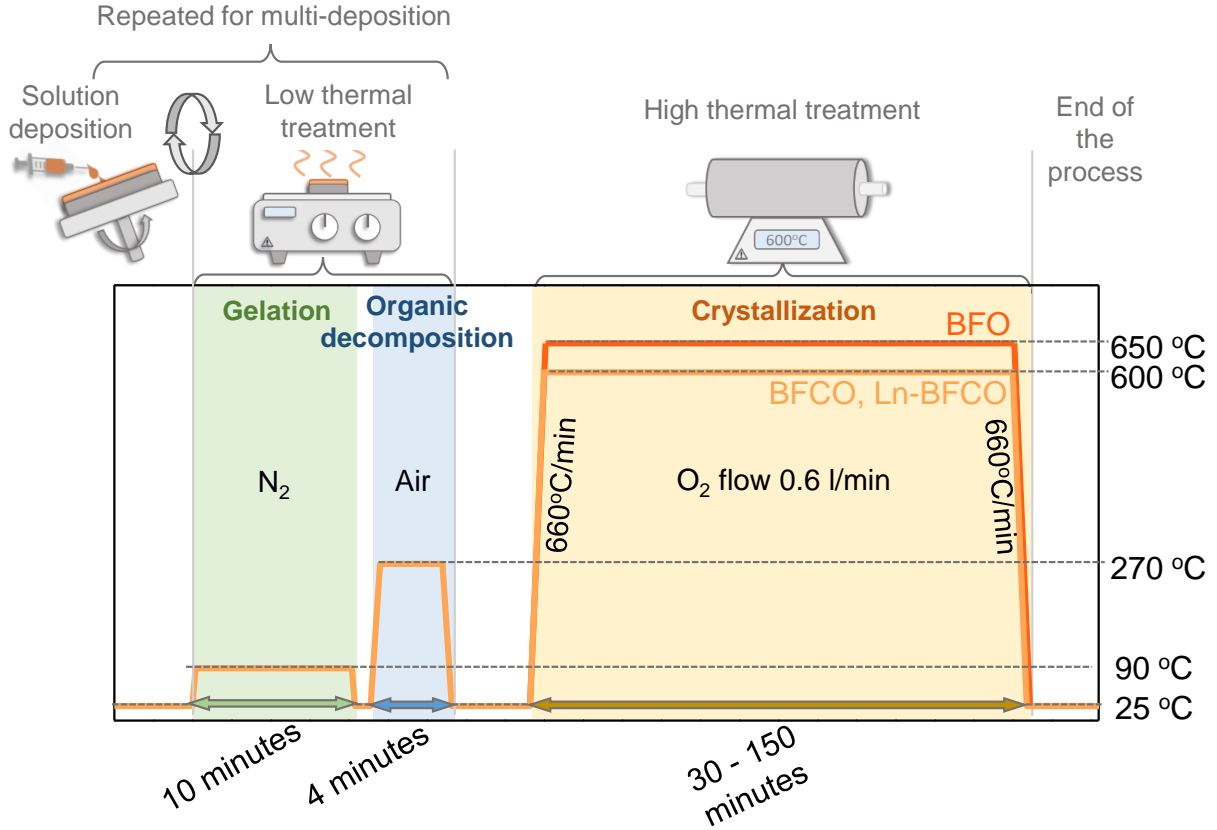


Figure 2.5: Profile of the thermal process carried out for the preparation of BFO-based thin films, indicating the gelation (green), organic decomposition (blue) and crystallization (yellow) steps, with the corresponding atmospheres, times, temperatures and equipments used. The procedure to prepare thicker films through multi-deposition is also represented. Note that the samples remain at room temperature, 25 °C, before gelation, between the different thermal treatments and after crystallization (end of the process).

Synthesis of LSMO thin films by CSD

The CSD process carried out for the preparation of the LSMO thin films was optimized taking as reference a previously reported process developed in our group.[122, 227]

Solution preparation: The precursor solutions were prepared by means of a metalorganic chemical route. Stoichiometric amounts of powder precursors of lanthanum acetate, $\text{La}(\text{CH}_3\text{CO}_2)_3 \cdot x \text{H}_2\text{O}$ (99.9 %),

manganese acetate, $\text{Mn}(\text{CH}_3\text{CO}_2)_2$ (98 %), and strontium acetate, $\text{Sr}(\text{CH}_3\text{CO}_2)_2$ (99.9 %), were dissolved in a solvent blend in volume proportion (5:1) of distilled water and AcA under magnetic stirring at a moderate temperature of 50 °C for 3 hours and at room temperature for the next 48 hours, to obtain an homogeneous solution free of precipitates with final concentration of 0.1 M. Prior to deposition, the solution was filtered using a PTFE filter of 0.22 μm pore size.

Solution deposition by spin coating: 18 μl of the LSMO precursor solution were deposited on clean 5 mm x 5 mm (001)-STO substrates at 6000 rpm for 30 seconds using a spin coater from *Ossila* located inside a dry N_2 box with controlled humidity (35 - 50 %). The process followed for the substrate cleaning is the same described above.

Thermal treatment: The as-deposited films were subsequently introduced inside a tubular furnace at room temperature and heated up to 900 °C for 15 minutes under O_2 flow of 0.6 l/min and cooled down to room temperature. Both heating and cooling rates were 3 °C/min. Note that the O_2 flow was opened when the sample was heated up to 700 °C and kept flowing for 150 minutes until it was cooled down to 700 °C, see Figure 2.6. In this process, film gelation, organic decomposition and crystallization take place inside the tubular furnace. Finally, LSMO thin films with a thickness of ~ 10 nm were obtained.

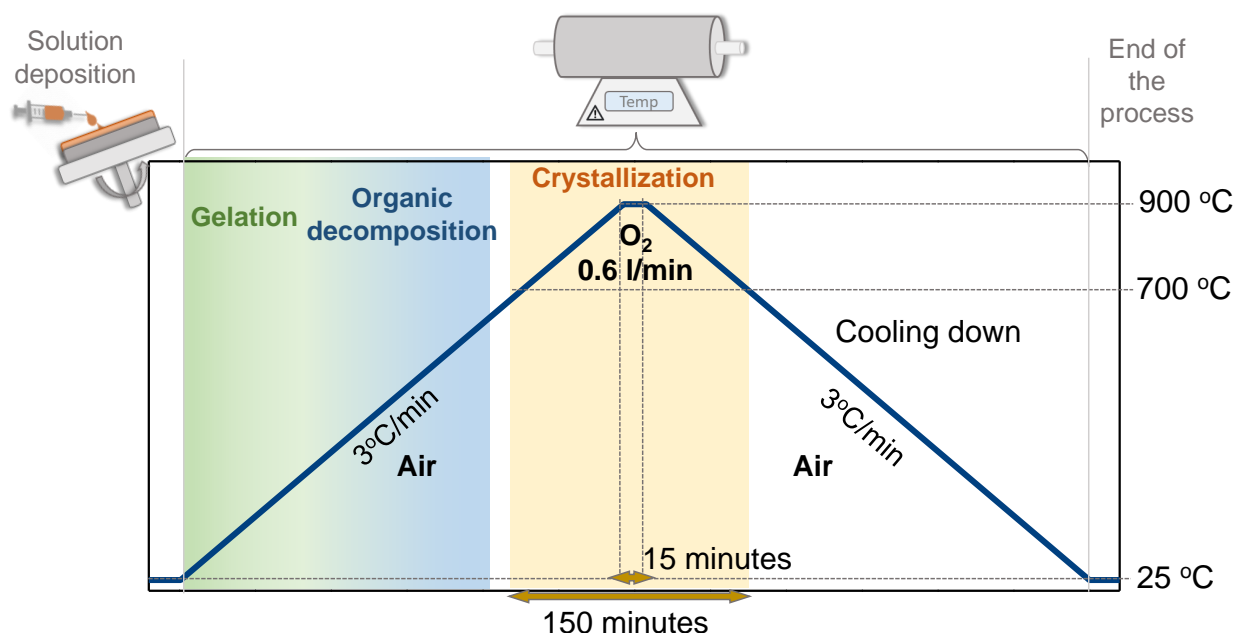


Figure 2.6: Profile of the thermal process carried out for the preparation of LSMO thin films, indicating the gelation (green), organic decomposition (blue) and crystallization (yellow) steps, with the corresponding atmospheres, times and temperatures. The complete thermal treatment was performed in a tubular furnace.

Synthesis of LSCO thin films by CSD

Motivated by the design of a non-existent chemical route to fabricate LSCO thin films, the use of CSD was thoroughly explored by a systematic study on the influence of solution chemistry on the gel thermal decomposition and the resulting surface morphology and crystallinity of the films, which directly influence on their functionalities. The complete study is presented in Chapter 5 and in this section the optimized solution formulation and processing conditions are described.

Solution preparation: Two different precursor chemistries were investigated, namely the metalorganic and metal nitrate routes. From the study presented in Chapter 5, the metal nitrates route was adopted as the most robust approach. Within this route, the use of different solvents and additives was investigated.

The 0.25 M LSCO precursor solution with optimized chemical formulation were prepared by weighting stoichiometric amounts of anhydrous strontium nitrate, $\text{Sr}(\text{NO}_3)_2$, hydrated lanthanum nitrate, $\text{La}(\text{NO}_3)_3 \cdot 6 \text{H}_2\text{O}$ (99.999 %) and chromium nitrate, $\text{Cr}(\text{NO}_3)_3 \cdot 9 \text{H}_2\text{O}$ (99.9 %), which were mixed in a solvent blend (3:1) of MOE and AcA under magnetic stirring and moderate temperature at 55 °C for 2 hours and at room temperature for the next 24 hours. After that, the solution was filtered using a

PTFE filter of 0.22 μm pore size, and diethanolamine (DEA) was added as chelating agent in a molar ratio to Cr of (1:4) and stirred for 15 minutes at room temperature.

Solution deposition by spin coating: 18 μl of the precursor solution were spin coated on previously clean commercial 5 mm x 5 mm (001)-STO and (001)-LaAlO₃ (LAO) substrates at 6000 rpm for 36 seconds in a N₂ box with controlled humidity ($\leq 10\%$).

Thermal treatment: The as-deposited samples were subjected to a mild-temperature treatment for organic decomposition at 400 °C for 30 minutes in a hot plate, and to a subsequent crystallization treatment in a pre-heated tubular furnace at 850 °C for 45 minutes and quenched to room temperature. The complete thermal treatment was performed in air atmosphere, see Figure 2.7. This procedure leads to LSCO films with thickness of ~ 45 nm.

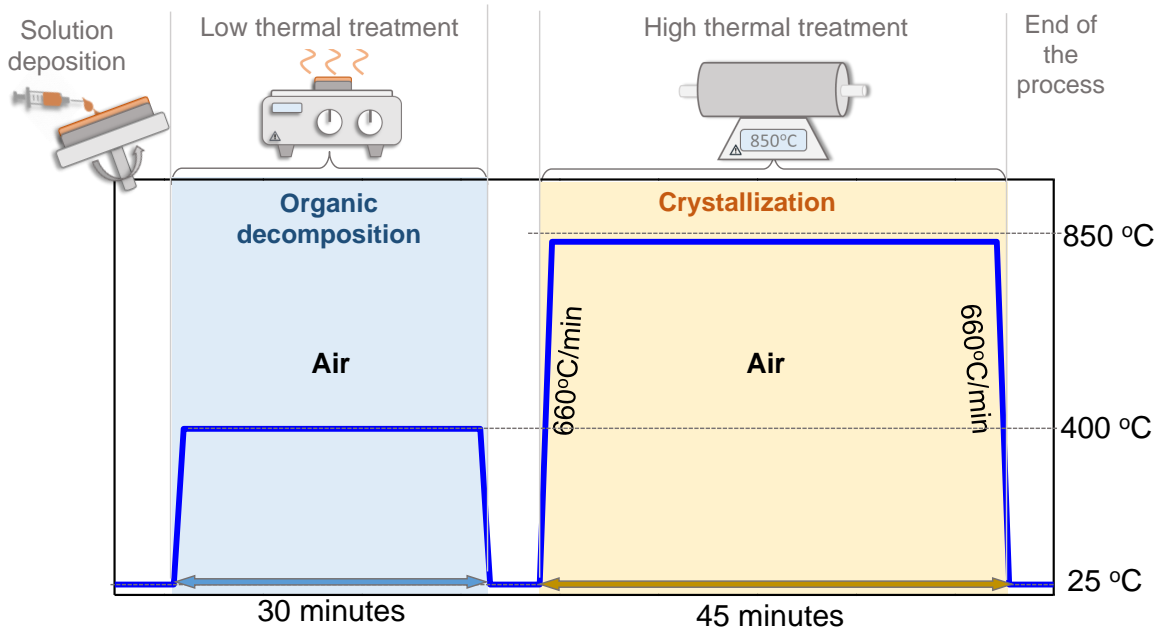


Figure 2.7: Profile of the thermal process carried out for the preparation of optimized LSCO thin films, indicating the organic decomposition (blue) and crystallization (yellow) steps, with the corresponding atmospheres, times, temperatures and equipment used. Note that the sample remains at room temperature, 25 °C, before, after and between the thermal treatments of organic decomposition and crystallization.

2.1.2 Other deposition methodologies

Atomic layer deposition

Atomic layer deposition (ALD) is a low-temperature and low-vacuum chemical vapor deposition technique that has emerged as an attractive approach for the preparation of thin films of functional materials for a variety of applications. It is already integrated into the semiconductor industry and is widely used in photovoltaics, organic electronics, catalysis, and energy storage research. Although ALD is traditionally being used to grow binary oxides, it also enables the deposition of more versatile chemistries, such as complex oxides, which exploration is an active area of research under current expansion.[234] The basic operation of ALD relies on the alternate pulsing of precursors, separated in time, that react with the surface (sometimes previously functionalized) in a self-limiting manner, since there are only a finite number of surface sites where the pulsed precursors can be deposited. After each precursor pulse, the ALD chamber is purged with an inert gas, such as N_2 or Ar, and ready for the next precursor pulse, see Figure 2.8. Interestingly, the self-limiting characteristic of ALD offers atomic-scale control over the composition and thickness, and provides access to homogeneous ultrathin coatings with unbeatable conformality. This technique also allows for the preparation of pinhole-free thin films with atomically sharp interfaces for a broad range of heterostructures, providing extraordinary opportunities to tune and engineer the oxide interfaces, as well as potential compatibility with many materials and production steps because of its mild processing conditions.[234, 235]

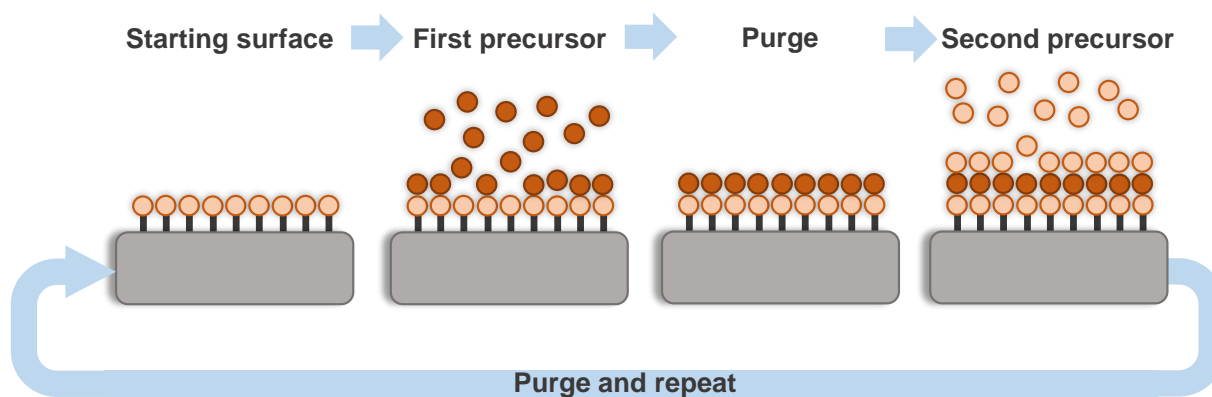


Figure 2.8: Illustration of a general ALD process. The first pulse of a precursor reacts with the sites on the substrate surface until all the available sites are occupied (self-limitation). Then, the chamber is purged and the second pulsed precursor reacts with the as-deposited surface. The purge and precursor pulses can be repeated until the desired thickness is achieved, allowing for atomic-scale control.

In this PhD thesis, ALD was used for the deposition of ZnO thin films to study its viability as selective layer. Several systems have been prepared for this purpose, ZnO/BFO-based/LSMO//STO, ZnO/LSMO//STO and ZnO/SiO₂//Si. Also, CoO_x thin films were deposited by ALD to prepare BFCO films with vertical compositional gradient of Co in combination with CSD. These studies are presented in Chapter 4. Prior to the deposition, the samples were cleaned by rinsing with ethanol and dried with compressed N₂ gas.

The deposition was carried out by Dr. Pol Sallés from our research group, using an ALD reactor from *Savannah-Cambridge Nanotech 100* located at the cleanroom Nanoquim Platform, ICMA B, Barcelona, Spain. For ZnO coatings, Diethylzinc and Milli-Q water were alternatively pulsed/purged for 0.15 s/20 s and 0.015 s/20 s, respectively, under 20 sccm N₂ carrier gas. The reactor temperature was set at 160 °C and the number of cycles was varied to obtain different ZnO thicknesses between 4 - 130 nm. The estimated growth rate per cycle was 1.1 ± 0.2 Å/cycle. For the PV-device, the film thickness was optimized to 20 nm based on the optical and electrical properties of the heterostructures. On the other hand, CoO_x films were prepared at 250 °C by alternate pulsing of cobaltocene (Co(Cp)₂) combined with ozone (O₃). The number of cycles was modified according to the desired film thickness (0.6 to 11 nm).[236]

Sputtering

Sputtering is a physical vapor deposition technique that has been broadly extended in the vacuum technology industry for the preparation of a wide range of materials, such as metals and functional binary and complex oxides.[237, 238] This technique plays an important role in the research of high-temperature superconductors, ferroelectrics, (transparent) conductors, luminescent materials, and giant magnetoresistive thin films, to name a few.

In general terms, the sputtering process itself is defined as the ejection of atoms or molecules of a material from a solid target due to the bombardment of energetic ionized particles on its surface, which will move towards the desired substrate to be deposited. To carry out the ionization of these particles (gas inserted inside the chamber, generally argon), a potential difference has to be applied between the target and the substrate. In addition, the ejected atoms from the target need to be able to move freely towards the substrate, requiring for high vacuum to prevent atom-gas collisions after their ejection from the target and help maintaining high ion energies.

Different variations of sputtering can be found depending on the characteristics of this process. For direct current (DC) sputtering, the difference potential is created by a DC power supply. In the case of radio frequency (RF) sputtering, this potential difference varies at a certain frequency. Moreover, a magnetron can be used to improve the yield of the sputtering process by creating a magnetic field close to the target, which allows for better electron confinement, see Figure 2.9. Indeed, magnetron sputtering is characterized by its ease of deposition at room and low temperatures, allowing for high deposition rates and large and uniform coating areas of high-purity films with extremely high adhesion to the substrates.

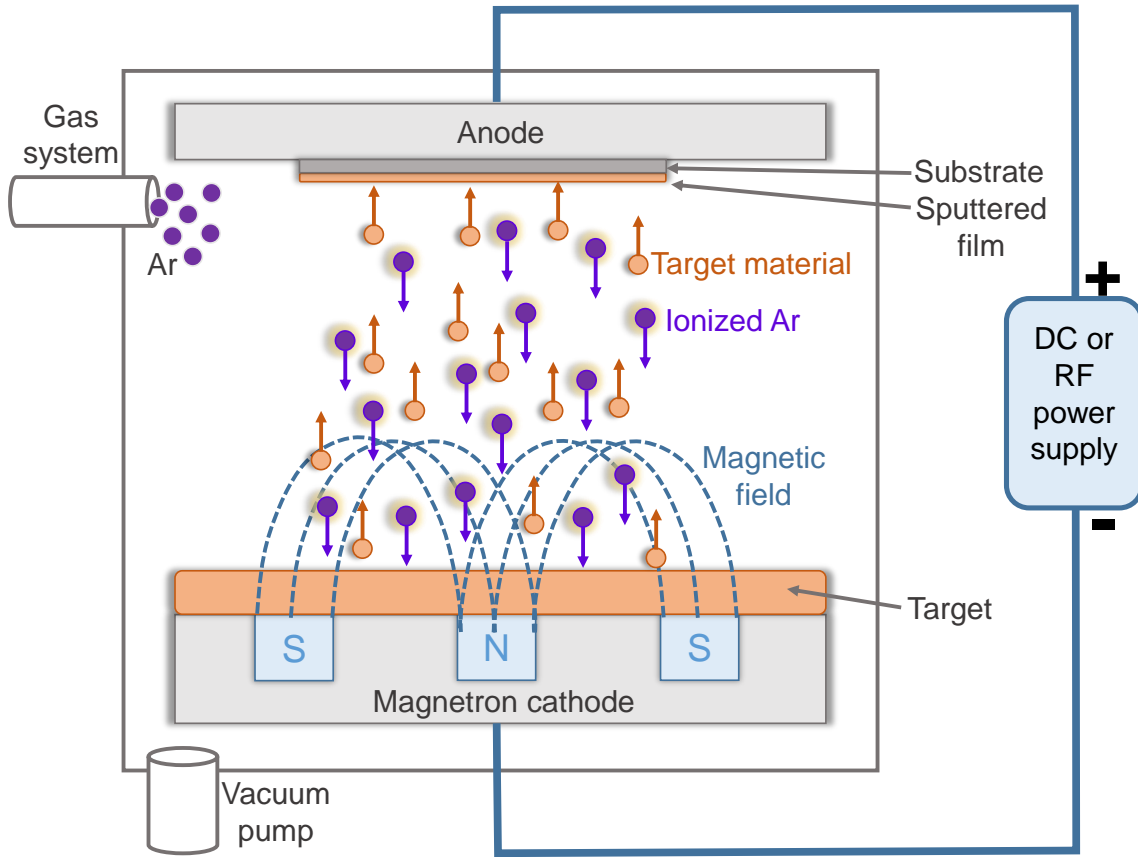


Figure 2.9: Representation of a magnetron sputtering chamber and deposition process. The argon gas is ionized because of the application of a potential difference between the target (cathode) and the substrate or substrate holder (anode). The ionized argon particles impact the target, ejecting atoms or molecules of the target material that move towards the substrate and adhere to its surface, creating a sputtered film.

Deposition of Pt electrodes by RF magnetron sputtering. 10 nm Pt top electrodes were deposited on the surface of clean BFO-based/LSMO//STO systems for ferroelectric characterization (Chapter 3). Pt was considered an appropriate electrode material owing to its noble metal nature, its difficult oxidation and its hardness that makes it difficult to be scratched. The deposition itself was carried out by the

scientific service of ICMAB, Barcelona, Spain using a *PLASSYS* magnetron sputtering system operating at room temperature and high vacuum (10^{-6} Torr) with an Ar flow of 10 sccm and power of 20 W. A grid was used as a shadow mask that is positioned on top of the samples, to obtain an array of contacts of $40\text{ }\mu\text{m} \times 40\text{ }\mu\text{m}$.

In this PhD thesis, ALD was used for the deposition of ZnO thin films to study its viability as selective layer. Several systems have been prepared for this purpose, ZnO/BFO-based/LSMO//STO, ZnO/LSMO//STO and ZnO/SiO₂//Si.

Deposition of ITO electrodes by RF magnetron sputtering. ITO thin films were deposited on top of different heterostructures, either to complete the all-oxide PV device, that is 70 nm ITO/(ZnO)/BFO-based/LSMO//STO and 70 nm ITO/ZnO/LSMO//STO, or to determine the energy band alignment, that is 50 nm ITO/300 nm SiO₂//Si, 3 nm ITO/BFCO10/LSMO//STO, 3 nm ITO/25 nm ZnO/300 nm SiO₂//Si (Chapter 4). All the depositions were carried out by means of an RF magnetron sputtering at the Institut Català de Nanociència i Nanotecnologia, Barcelona, Spain, and in collaboration with Dr. Gabriele De Luca. An In₂O₃:SnO₂ 90:10 wt% target of 1.5 inches of diameter was used in on-axis configuration and at a working distance of 15 cm. The process was carried out at room temperature with sputtering power density of $2.2\text{ W}\cdot\text{cm}^2$ and a working pressure of ~ 2 mTorr was stabilized with a constant Ar flow of 10 sccm and a butterfly valve operated in static mode. The estimated growth rate was 0.6 nm/min. A grid was used as a shadow mask to obtain an array of contacts of $40\text{ }\mu\text{m} \times 40\text{ }\mu\text{m}$ and $130\text{ }\mu\text{m} \times 130\text{ }\mu\text{m}$ for ferroelectric and photoresponse characterization, respectively (Chapter 4).

Deposition of Au electrodes by DC sputtering. 50 nm Au top electrodes of $1\text{ mm} \times 1\text{ mm}$ were placed at the vertices of clean LSCO//LAO (Chapter 5) by means of DC-sputtering system from *TSST* located at Nanoquim Platform, ICMAB, operating at high vacuum (10^{-6} Torr) and with a constant Ar flow. This deposition was carried out with the collaboration of Jordi Alcalà and Dr. Anna Palau. Previous to sputtering deposition, I defined the contacts by means of optical lithography: (i) A commercial photoresist *Shipley S1813* was spin coated on top of clean LSCO//LAO samples following a well-established process (5000 rpm / 25 seconds), (ii) the previously designed pattern (*CleWin 4.1* software) was written using a *Micro-Writer ML3* from *Durham Magneto Optics Ltd* located at Nanoquim Platform, that works with a resolution of $1\text{ }\mu\text{m}$ and a light source of 385 nm, and (iii) the photoresist was developed using a commercial developer *Microposit S1213 G2 Positive* for 20 seconds. This process was stopped

by introducing the sample in distilled water and dried with nitrogen gas.

2.2 Solution and thin film characterization

Here it is described the fundamentals of the characterization techniques used for the study of the chemical solutions and the oxide thin films, as well as the corresponding measurement conditions and the subsequent data analysis.

For the study of **chemical solutions**, rheological and thermal decomposition characterizations by means of simultaneous thermogravimetric (TGA) and differential scanning calorimetry (DSC) analyses were performed.

The structure of the **oxide thin films** was evaluated using X-ray diffraction (XRD) and advanced scanning electron transmission microscopy (STEM), and the surface morphology was studied using atomic force microscopy (AFM) and scanning electron microscopy (SEM) coupled with energy-dispersive X-ray (EDX) analysis. The optical properties were evaluated by means of spectroscopic ellipsometry (SE) and spectroscopy in the ultraviolet-visible (UV-Vis) range. The surface chemical composition was analyzed by X-ray photoelectron spectroscopy (XPS) and the electronic structure by X-ray absorption spectroscopy (XAS) and electron energy-loss spectroscopy (EELS). Elemental depth profiles were obtained with time-of-flight secondary ion mass spectrometry (ToF-SIMS). The microscopic ferroelectric characteristics of the films were evaluated using piezoelectric force microscopy (PFM), and electrical resistivity measurements were performed using a physical property measurement system (PPMS).

It is important to note that my implication on the measurements and data analysis differed depending on the technique. In some cases, I carried out both measurements and data analysis as it is for rheology, SEM-EDX, SE, and UV-Vis spectroscopy. In other cases, the data acquisition was carried out by a scientific technical service and I was in charge of the data analysis and interpretation, as it is for TGA-DSC, XRD, AFM, and XPS. In addition, STEM-EELS, XAS, ToF-SIMS, PFM, and PPMS analysis were performed in collaboration with experts in the field as detailed below.

2.2.1 Solution characterization

Rheology

Rheology makes reference to the science of deformation of a material as a response to an applied force (stress). In the case of liquids and fluids, this deformation is determined by their viscosity.[239] For the study of the viscosity of the BFO-based and LSCO precursor solutions, a stress research rheometer was used. I performed all the measurements using a *Haake RheoStress RS600* rheometer from *Thermo Electron Corporation* located at the Nanoquim Platform, ICMA B, at a controlled temperature of 22 °C and at a fixed speed of 2880 s⁻¹ for 30 s. Results presented in Chapters 3, 5.

2.2.2 Thermal decomposition characterization

Thermogravimetric and differential calorimetry scan analysis

Thermogravimetric analysis (TGA) is a powerful tool for monitoring the mass change of a substance as a function of temperature and/or time when the sample is subjected to a controlled temperature program and in a specific atmosphere. The atmosphere is created by a purge gas flowing through the precision weight balance and can be inert, such as N₂, Ar or He, oxidizing such as air or O₂ or reducing such as H₂:N₂. The resulting TGA profile allows to obtain information on the thermal stability and volatility of the studied components. When combined with differential scanning calorimetry (DSC), which measures the heat flow that occurs in a sample subjected to a temperature program, endothermic and exothermic energetic transitions and reactions that do not result in a change in the mass of the system can be detected, such as melting, sublimation, solid-solid transitions, chemical reactions, decompositions, and crystallization. The use of simultaneous TGA-DSC analysis present advantages over separate experimentation and can provide substantial information to design an optimized thermal profile for the studied composition.[240, 241]

In this work, simultaneous TGA-DSC analysis was used to evaluate the influence of LSCO solution chemistry on thermal decomposition and to design adequate thermal profiles for each formulation, as described in Chapter 5. To perform this study, I previously dried the precursor solutions to a gel using a rotary evaporator *R-210/215* from *Büchi* located at the Nanoquim Platform, ICMA B. Next, the TGA-DSC study was carried out with a thermal analyzer *TGA/STA 449 F5 Jupiter* from *NETZSCH* at the University of Alicante, Spain, with a temperature range from 30 °C to 900 °C and a heating

rate of 30 °C/min under O₂-rich atmosphere, i.e. N₂:O₂ (1:9), and air atmosphere, i.e. N₂:O₂ (4:1). The atmosphere of study was selected depending on the formulation of the solutions, as it is detailed in Chapter 5.

2.2.3 Structure characterization

X-Ray Diffraction

X-ray diffraction (XRD) is one of the most useful and versatile non-invasive techniques to characterize the structure of thin films, obtaining information on the structural composition, crystalline phase and purity, lattice parameters, degree of crystallinity and preferential orientation or texture, grain size and film thickness.

To explain the principles of XRD, the atoms in a crystal can be imagined as a periodic array of coherent scatterers in atomic planes. When an incident X-ray beams encounter this arrange, most of the interferences will be destructive and will cancel out with each other, but in some specific directions, when conditions satisfy the Baggs law, Equation 2.2, constructive interferences will occur, producing a diffracted X-ray, see Figure 2.10. The complete X-ray diffraction pattern will determine the crystal structure.

$$n\lambda = 2d_{h,k,l}\sin\theta \quad (2.2)$$

Where n is an integer (1, 2, 3, ..., n), λ is the characteristic wavelength of the incident X-ray source, $d_{h,k,l}$ is the distance between atomic planes and θ is the angle of incidence of the X-ray beams.

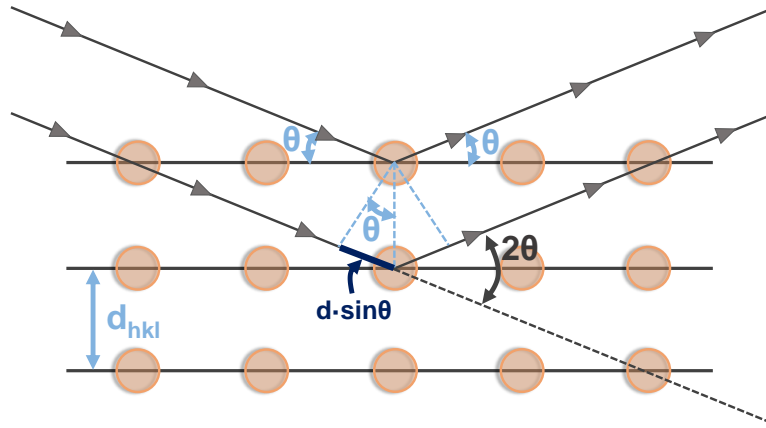


Figure 2.10: Schematic of diffraction geometry in atomic planes and Bragg law condition.

A basic X-ray diffractometer is comprised by five main components, the X-ray source, the incident beam optics, the sample holder (goniometer), the diffracted beam optics and the detector. The X-ray source is a cathode ray tube where the monochromatic X-rays are generated. Here, a filament is heated to produce electrons that are accelerated towards a target material (normally Cu, Fe, Mo or Cr) from where characteristic X-ray spectra (K_α and K_β) are produced and subsequently monochromated and collimated to be directed to the sample (incident beam optics). Note that Cu is the most common target material for single-crystal diffraction (and used in this thesis) and possess a Cu K_α radiation of 1.5418 Å. To perform the measurements, the sample and/or the detector are rotated and the intensity of the reflected X-rays is recorded when Bragg condition is satisfied. The angles between the source, the detector and the sample surface are set by the goniometer and depending on the geometry of the measurement, different XRD scan modes are found. Figure 2.11 shows an schematic of the notation used for the angles in a XRD system for thin films. [242] Specifically, ω is the angle at which the incident beam intersects the sample surface, usually changed by keeping the X-ray source fixed and moving the sample. The rotation of the sample in the other two directions is described by the angles ϕ and χ . On the other hand, the rotation of the detector is described by the 2θ angle.

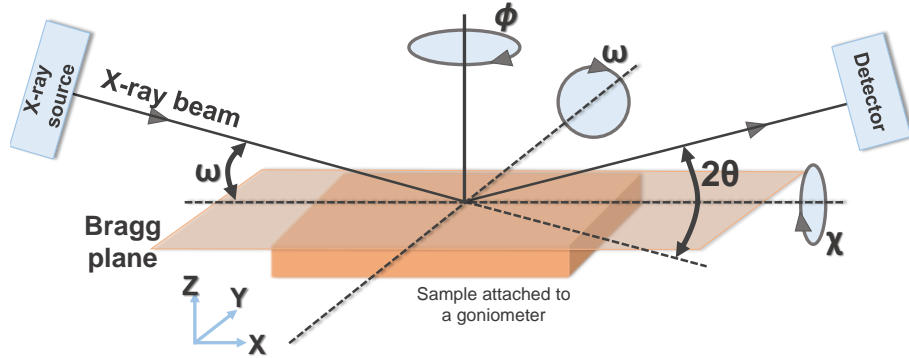


Figure 2.11: Illustration of the XRD geometry configuration, indicating the angle notation used for thin film characterization.

The XRD analysis performed in this work include: θ - 2θ scan, grazing incidence X-ray diffraction (GIXRD), ω scan (rocking curve scan), ϕ scan (azimuth scan) and reciprocal space map (RSM).

θ - 2θ scan:

θ - 2θ or ω - 2θ scan is one of the most used modes to analyze the crystallinity of thin films. For this

measurement, the geometry of the diffractometer is such that the sample and the detector rotate in the path of the X-ray beam at an angle of $\omega = \theta$ while the X-ray detector rotates at an angle of 2θ . The Bragg plane is always aligned with a crystallographic axis of the substrate and is kept parallel to the surface of the sample (fixed χ) so that only the (hkl) planes which are parallel to the sample fulfill the Bragg condition and are detected. For thin films with preferential orientation, the peaks observed will depend not only on the phases present, but also on their orientation.[242]

From this scans several information can be obtained: subtle shifts in the peak positions can indicate residual stresses, substrate induced strain or compositional changes in the film, whereas the size of the grains, the presence of strain distributions or compositional gradients determine the shape and width of the peaks (broad or sharp). Different diffraction patterns can be observed depending on the crystalline nature of the film, i.e. epitaxial, textured, randomly-oriented polycrystalline whereas no diffraction pattern is displayed for amorphous films.

For epitaxial films, that is single crystal with both in-plane and out-of-plane lattice planes in well align with the substrate (biaxial align), it can be expected a diffraction pattern with a single set of peaks according to a single orientation. However, the reflections observed in a θ - 2θ scan only depend on the out-of-plane orientation, requiring of additional measurements to ensure that a film is fully epitaxial. On the other hand, in textured films with an anisotropic distribution of crystallites (with preferred orientation), reflections from each orientation can be observed. It has to be considered that the preferential orientation can exist both in-plane and out-of-plane with respect to the substrate crystal axis. To investigate both in-plane and out-of-plane texture, additional phi scan and rocking curve analysis are required.

In polycrystalline films with no preferential orientation, the pattern is expected to show all the diffraction peaks with their corresponding relative intensities of the reference powder spectrum ("bulk" intensities). Finally, amorphous films will be essentially invisible to this scan mode since no periodic crystalline structure can be detected.

In addition, two-dimensional (2D) θ - 2θ patterns can be measured using a 2D area detector which acquires a large 2θ and χ range simultaneously (also known as 2θ - χ scan). With such configuration the measured pattern is not limited to a diffraction plane (specific χ) but within a diffraction cone. Therefore, depending on the crystallinity of the sample, 2D measurements allow to distinguish between diffraction rings for polycrystalline samples and isolated spots for single-crystal samples. Nevertheless, the resolution in 2D patterns tends to be worse than in a conventional θ - 2θ scan, but this will depend on the diffractometer.

GIXRD scan:

Grazing incidence X-ray diffraction (GIXRD) is a surface-sensitive technique particularly useful to characterize polycrystalline thin films. In conventional θ - 2θ scans with large incidence angles, the weak diffraction contribution of a thin film could be hindered by that of the substrate because of the μm -order penetration depth of X-rays. On the other hand, the diffraction contribution of the film can be maximized if the angle of incidence, ω , is kept fixed at a value shallow enough ($< 5^\circ$) and the spectrum is collected by only moving the detector along 2θ . For randomly-oriented polycrystalline films, the diffraction pattern should follow the relative "bulk" intensities. Note that this configuration is not suitable for epitaxial films.

 ω -scan:

In a ω -scan or rocking curve the position of the detector (2θ) is fixed at the Bragg angle of a particular reflection of study, and the sample is slightly tilted (or "rocked") in the ω axis, such that planes that are no longer parallel with the sample surface are brought onto the Bragg plane. As a result, a single curve which gives the distribution of planes as a function of the tilt (ω) is obtained. The width of the curve depends upon the mosaic spread of the grains, density of dislocations, and substrate curvature, which disrupt the parallel nature of the lattice planes. Therefore, the full-width half-maximum (FWHM) of the rocking curve is generally used to indicate preferential orientation or the quality of an epitaxial growth. An epitaxial film generally shows small FWHM ($< 2^\circ$) and sharp peak, whereas a more disoriented film may show a broadening of several degrees. This scan mode is particularly useful for epitaxial or textured films, but would yield little information for randomly-oriented polycrystalline films.

 ϕ -scan:

In ϕ -scan or azimuth scan, the sample is oriented to a particular interplanar angle parallel to the surface and scanned by rotating along ϕ while ω and 2θ are kept constant. In this measurements, in-plane and out-of-plane contributions can be observed. If the rotation is done while measuring the intensity of a diffracted spot with in-plane contribution, for instance (301), any in-plane twisting of the crystallites will involve a change of diffraction in ϕ , giving information on the in-plane crystalline order of the sample. When the ϕ scans is recorded in 360° it can be used to determine the in-plane orientation of the film related to the substrate.

Reciprocal space map (RSM):

A reciprocal space map, also known as q-plot scan, is a powerful method for the study of epitaxial films that allows accessing any Bragg reflection of the crystal. RSM is obtained by measuring a 2D region of the reciprocal space from collecting diverse ω - 2θ coupled scans ($\omega = \theta$) at slightly different tilts (offsets) in the ω axis. As a result, a 2D diffraction pattern along ω and 2θ is obtained, which can be converted to the reciprocal space units (Q_x and Q_z) according to the Equations 2.3 and 2.4.[243]

$$Q_x = \frac{2\pi}{\lambda} \cdot [\cos(2\theta - \omega) - \cos(\omega)] \quad (2.3)$$

$$Q_z = \frac{2\pi}{\lambda} \cdot [\sin(2\theta - \omega) + \sin(\omega)] \quad (2.4)$$

Reciprocal space mapping can be used to investigate the in-plane, a , and out-of-plane, c , lattice parameters according to Equations 2.5 and 2.6 (for pseudocubic structure), and the strain of textured films that are heteroepitaxially grown on substrates with certain lattice mismatch. Moreover, the broadening of the diffracted peaks can be related with defects in film strain or in the distribution of crystal plane orientations (mosaicity).

$$a = \frac{\sqrt{h^2}}{Q_x} \quad (2.5)$$

$$c = \frac{\sqrt{l^2}}{Q_z} \quad (2.6)$$

Note that the lattice mismatch, m , can be calculated according to the fractional difference between the in-plane lattice parameter of the substrate and that of the deposited layer, Equation 2.7, whereas the in-plane and out-of-plane film strain, ϵ_{xx} and ϵ_{zz} , respectively, can be calculated from the fractional difference between the film lattice parameter and the bulk lattice parameter, Equations 2.8 and 2.9.

$$m = \frac{a_{\text{substrate}} - a_{\text{film}}}{a_{\text{substrate}}} \quad (2.7)$$

$$\epsilon_{xx} = \frac{a_{\text{film}} - a_{\text{bulk}}}{a_{\text{bulk}}} \quad (2.8)$$

$$\epsilon_{zz} = \frac{c_{\text{film}} - c_{\text{bulk}}}{c_{\text{bulk}}} \quad (2.9)$$

Herein, three diffractometers located at the Scientific Services of ICMAB, Spain were used to perform

the different XRD measurements. For fast routine θ - 2θ scans a *Siemens D-5000* Diffractometer with a Cu anode (Cu $K\alpha$ $\lambda = 1.5418$ Å) was used. High resolution θ - 2θ scans, GIXRD scans, ω scans, ϕ scans and reciprocal space maps were obtained using a *Bruker D8 Discover A25* diffractometer (Cu $K\alpha$ $\lambda = 1.5418$ Å). Finally, a *Bruker D8 Advance* general area detector diffraction system (GADDS) equipped with a 2D Vantec 500 detector was used to obtain $\theta - \chi$ 2D scans. The specific measurements conditions for each sample are described in the Chapters 3-5. Figure 2.12 shows photographs of the diffractometers herein used. Note that the measurements were performed by the scientific service and I analyzed the collected data using different softwares as *OriginPro 2020b* and *GADDS V 4.1.51* from Bruker.

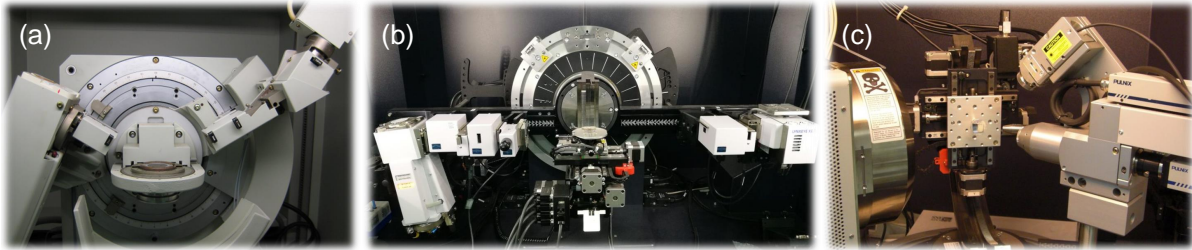


Figure 2.12: Photographs of the three diffractometers used to characterize the samples in this PhD thesis: (a) Siemens D-5000, (b) Bruker D8 Discover A25 and (c) Bruker D8 Advance GADDS. The equipments are located at the Scientific Service of ICMA.

Scanning Electron Transmission Microscopy

Transmission electron microscopy (TEM), as its own name indicates, is an imaging technique that uses a focused beam of electrons to scan through a thin sample. It is a particularly useful tool for atomic scale imaging of epitaxial metal oxide thin films that allows to investigate the atomic and electronic structure of the atom species in the material and their distribution in the epitaxial films and at their interfaces, with spatial resolution down to several tens of picometers.[244, 245] Depending on the imaging mode, the TEM techniques can be categorized in (i) conventional TEM when a confined electron beam is transmitted through a sufficiently thin sample, and as (ii) scanning TEM (STEM) when the electron beam is focused to an angstrom-size fine spot (< 2 Å) and then scanned over the sample point by point while the relevant signals are simultaneously recorded pixel by pixel using different detectors to obtain the corresponding image.[246] The annular detector is the most used one in STEM, which allows to form annular dark-field images. When the detector is coupled to intermediate lenses, the length of the used camera can be changed and the angular range of electrons falling onto the annular detector can be controlled. In high-angle annular dark-field (HAADF) STEM imaging mode, or Z-contrast imaging, only the electrons that have been scattered under large angles by the specimen are collected on the annular

detector. This mode leads to an image intensity that is approximately proportional to the square of the atomic number (Z^2) and to the thickness of the specimen, resulting in both chemically and thickness sensitive imaging. Moreover, STEM imaging can be simultaneously combined with spectroscopic imaging by energy dispersive X-ray spectroscopy (EDX) and electron energy loss spectroscopy (EELS), to provide additional information on the chemical composition and the electronic structure of the films.

In this PhD thesis, the crystalline and electronic structure of BFO-based//STO, BFO-based/LSMO//STO (Chapters 3 and 4) and LSCO//LAO thin films (Chapter 5) was explored by acquiring aberration corrected STEM images and monochromated EELS spectra using a *Nion HERMES-100* STEM operated at 60 kV, at the University of Chinese Academy of Sciences, Beijing, China. To do so, cross-sectional STEM specimens were prepared using the standard focused ion beam (FIB) lift-out process in a Thermo Fisher Scientific FIB system. The HAADF images were acquired using an annular detector with collection of semi-angles of 75 – 210 mrad. The probe-forming semi-angle was 32 mrad and the collection semi-angle for the EELS spectrometer was 75 mrad. After monochromation, the best energy resolution obtained was ~ 0.1 eV with the beam placed on the sample. To record the spectra, a dispersion of 0.05 eV per channel was used, and a set of 40 spectra with 500 ms time per acquisition were collected while scanning on the film to prevent radiation damage, and subsequently aligned and integrated. The integrated spectra were slightly smoothed using a 3 channel low pass filter to reduce noise. In addition, strain maps were obtained from STEM images using geometrical phase analysis (GPA). The collection of STEM images and data analysis were carried out by Dr. Roger Guzman at the University of Chinese Academy of Sciences (UCAS), Beijing, China.

2.2.4 Surface morphology characterization

Scanning Electron Microscopy

Scanning Electron Microscopy (SEM) is an imaging technique that uses a focused electron beam to scan over the surface of a sample with a resolution down to the nanometer scale. When the high energy electron beam reaches the sample surface, they interact with the atoms at various depths within the sample, producing different signals that provide information on the surface morphology and the composition. These signals include secondary electrons, reflected or back-scattered electrons and characteristic X-rays,[247] as it can be observed in Figure 2.13.

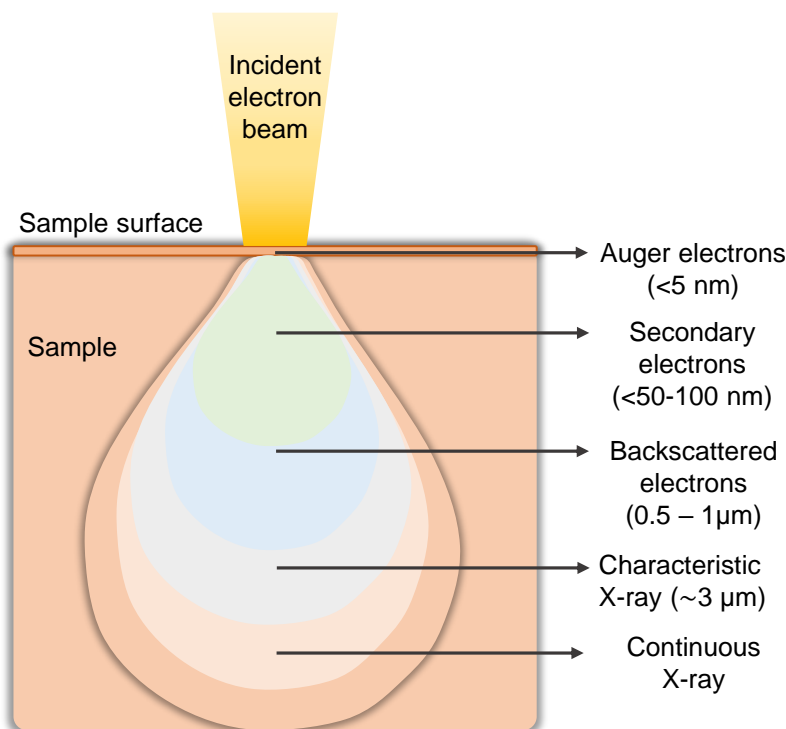


Figure 2.13: Representation of electron-matter interactions showing the different types of generated signals and the corresponding depth.

Due to their low energies of ~ 50 eV, secondary electrons present limited free path in the solid matter and are able to escape only from the first nanometers of the sample. Normally, the signal from these electrons is highly localized making possible to collect images of the sample surface with resolution in the nanometer scale. On the other hand, back-scattered electrons are beam electrons that are reflected from the sample by elastic scattering, and have much higher energy. They emerge from deeper locations of the sample, resulting in lower resolution images. The intensity of these electrons is strongly related with the atomic number, Z , and can provide distributional information of the elements present in the sample. However, the identity of these elements can not be distinguished only with imaging.

When the incident electron beam hits atoms in the specimen, causing the ejection of an inner shell electron from the sample and the subsequent electronic transitions from outer shell electrons, characteristic X-rays are emitted. These X-rays contain information on which and how much elements are present in the specimen, and can be measured by EDX spectroscopy. Therefore, the combination of SEM and EDX allow to identify the elements in the sample and measure its abundance while mapping their distribution.

Also, when the incident electron beam is retarded by the electric field of the nucleus of the atom, an energy loss is released in form continuous X-rays, which do not contain any information on the chemical identity of the element from which this radiation originates, but its intensity is related to the total mass of the analyzed volume in the specimen and can be used in quantitative analysis.[248]

In this thesis, I acquired routine surface morphology images by SEM using a *QUANTA FEI 200 FEG-ESEM* equipped with an EDX detector, located at ICMAB. SEM imaging was performed either on conductive samples or isolating samples grown on conductive substrates under high vacuum conditions and at a working voltage of 10-15 kV. The spotsize of the electron beam was 3.0. EDX analysis were performed at 10-15 kV for 70 seconds to qualitatively identify the elemental presence in the samples. Further specifications are described along with the presentation of results, in the corresponding Chapters 3-5.

Atomic Force Microscopy

Atomic Force Microscopy (AFM) is a type of scanning probe microscopy (SPM) that is commonly used for the topographical imaging of a material, obtaining information of the surface morphology, roughness, grain size, and height profiles, among other. The working principles of AFM are simple, a cantilever with an atomically sharp tip is used to scan over the surface of the sample, which lateral and vertical position is controlled with a piezoelectric scanner. [249, 250, 251, 252] As the tip moves over the surface, the force applied by the cantilever is deflected by the interaction force between the tip and the sample, which depends on the working distance. This deflection is tracked by a reflected laser beam, that is directed to a photodetector (photodiode). When deflections are detected, the feedback mechanism of the system enables the piezoelectric scanner to maintain the tip at a constant force or height above the sample surface, see Figure 2.14 (a).

Generally, AFM can operate in three different modes depending on the tip force and tip-surface separation: non-contact mode, contact mode, and dynamic or tapping mode, see Figures 2.14 (b-e). When the tip and the surface are widely separated, in non-contact mode, Van der Waals forces cause them to weakly attract and the oscillation of the cantilever is measured, Figures 2.14 (b,c). On the other hand, in contact mode, when they draw too closely together, their electron clouds overlap and electrostatic repulsive forces physically push them apart, being necessary to apply a force to keep the contact between tip and surface, Figure 2.14 (b,d). Finally, the dynamic mode occurs when the cantilever is positioned at a close distance from the surface and oscillates at its resonant frequency, so that it only taps the

surface for a very small fraction of its oscillation period. While scanning the sample, the change in the amplitude of oscillations is corrected by adjusting the tip-surface distance and the topographic image is recorded, Figure 2.14 (e). Because of its gentle nature, dynamic mode operation is preferred in most of the cases.

In addition, one of the major advantages of AFM is that materials with all kinds of nature (metallic, semiconductors and insulators) can be measured because forces are detected rather than current.

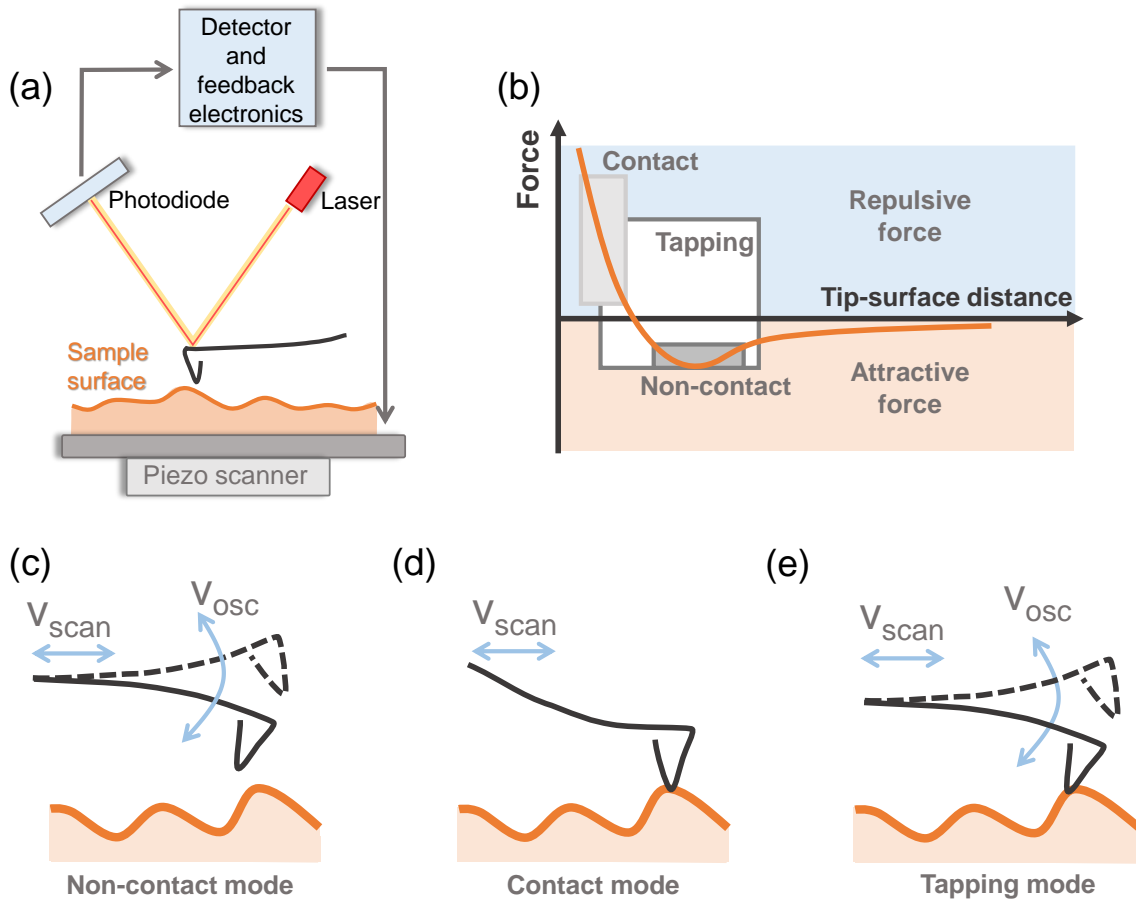


Figure 2.14: Illustration of (a) typical components in an AFM, (b) evolution of the tip-surface force upon tip-surface distance and schematic of the three AFM working modes being (c) non-contact mode, (d) contact mode and (e) tapping or dynamic mode. Note that v_{scan} and v_{osc} makes reference to scan and oscillation frequencies, respectively. Adapted from Ref.[253]

In this work, the surface morphology and root-mean-square (rms) roughness were studied from the topographic images acquired in a constant amplitude dynamic mode with an AFM *Keysight 5100* in-

strument located at Scientific Services of ICMA. I further processed the images using *MountainsMap Premium 9* software from *Digital Surf*. [254] Note that for all the topography images, a line by line correction was applied to reduce the effects produced by the change of line of the instrument during the measurements.

2.2.5 Optical characterization

Spectroscopic Ellipsometry

Spectroscopic ellipsometry (SE) is a non-destructive, non-contact, and non-invasive technique used to obtain the complex refractive index (refractive index, n , and extinction coefficient, k) and thickness of thin films and multilayers. [255, 256] In SE, a linearly polarized light beam with in phase p and s components is incident on the film surface at an specific angle of incidence. Due to the interaction with the sample, a change in polarization is produced, resulting in a reflected light with elliptical polarization state that is measured with a detector to obtain an ellipsometry spectra. This spectra consists on the amplitude ratio of the reflected p -polarized light to s -polarized light, Ψ , and the phase shift difference between both, Δ , see Figure 2.15. In order to obtain the optical properties and film thickness of the sample, the ellipsometry spectra (Ψ , Δ) data needs to be fitted using computational structure models. In addition, the spectroscopic ellipsometer can be used in photometry mode to measure the transmitted light through a transparent sample. In this case, changes in light polarization are not measured, and the transmittance spectra is directly obtained, hence not requiring for structure models and data fitting.

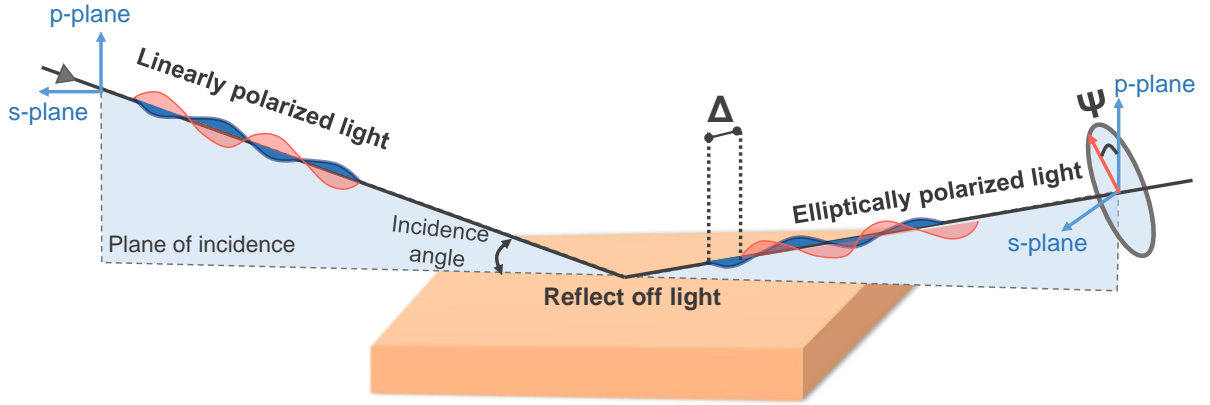


Figure 2.15: Schematic of a spectroscopic ellipsometry measurement in which linearly polarized incident light (left) changes to elliptically polarized light (right) after being obliquely reflected from the sample.

Herein, I carried out the SE measurements using a *SOPRALAB GES5E* ellipsometer with a Xe lamp as light source and charge-coupled device detector located at Nanoquim platform, ICMAB. The optical properties and thickness of BFO-based, ZnO and ITO thin films were evaluated in reflection mode using a microspot of 50 μm . The ellipsometric spectra (Ψ , Δ) were recorded within the spectral range 1.3 to 4.5 eV at a fixed analyzer angle of 20° or 45° and varying the angle of incidence ranging from 65° to 75° . After the measurements, I analyzed the data sets using *WinElli II* piece of software. The fitting ellipsometric spectra of BFO-based films was carried out following the multi-layer model void/rough layer/BFO-based film/substrate. The rough layer assumes a medium consisting of air and film (1:1) that uses the Bruggeman approximation to model the effective dielectric function. Roughness values were taken from the AFM images and the Tauc-Lorentz model was used to describe the optical properties of the BFO-based films,[122]. On the other hand, for ZnO and ITO films, the fitting was performed following the multi-layered structure void/ZnO or ITO film/substrate and the Cauchy optical model.[257, 258]

The absorption coefficient of the films, α , was obtained from the fitted complex refracted index, according to the Equation 2.10:

$$\alpha = \frac{4\pi\kappa}{\lambda} \quad (2.10)$$

where λ is the wavelength of the reflected light.

In addition, the absorption coefficient was used to extract the optical bandgaps of the films through the

Tauc relationship, Equation 2.11.[259]

$$\alpha h\nu \propto (h\nu - E_g)^n \quad (2.11)$$

Where h is the Planck's constant, ν the frequency of light, E_g the optical bandgap and n is related to the electronic nature of the bandgap, being $n=2$ for allowed direct transitions and $n=1/2$ for allowed indirect transitions.

On the other hand, I measured the optical transmittance (%T) of LSCO thin films on double-side polished STO with the same SE equipment, using a microspot with diameter of 50 μm but in photometry mode (Chapter 5). For these measurements, the light source was incident in the film side with an angle of 90° and data was collected in the wavelength range of 300 to 1000 nm with an integration time of 2 seconds to avoid saturation of the detector. The %T were obtained averaging values at wavelengths of 400 nm, 500 nm, 600 nm, 700 nm, 800 nm and 900 nm and without subtracting the contribution of the substrate.

UV-Vis spectroscopy

UV-Vis spectroscopy is an analytical technique that measures the interaction of an incident light with a sample (herein thin film). It measures the amount of discrete wavelengths of ultraviolet (UV) or visible light that are absorbed by or transmitted through a sample in comparison to a reference sample. Therefore, the absorption or transmission spectra of thin films are obtained, which provide information on the composition, thickness and bandgap. The absorbance and transmittance of the films are related with the Equation 2.12, and the estimated absorbance coefficient, α , can be obtained from Equation 2.13:

$$A = -\log(T) \quad (2.12)$$

$$\alpha \sim A/d \quad (2.13)$$

where A is the absorbance, T the transmittance and d the thickness of the film.

Herein, I used this technique to obtain the optical transmittance and absorbance spectra of BFO-based heterostructures in Chapter 4. A UV-Vis/NIR spectrophotometer from *Jasco V780* was used in the wavelength range of 200 – 800 nm, with scan speed of 400 nm/min and in continuous scan mode at

normal incidence. The measurements were performed on samples prepared on one-side polished or both-side-polished STO substrates and considering the holder and ambient as reference (blank). The contribution of the substrate was not subtracted.

2.2.6 Surface chemical composition characterization

X-Ray Photoelectron Spectroscopy

X-ray photoelectron spectroscopy (XPS) is an accurate surface-sensitive analytical technique used to investigate the chemical state, the quantitative elemental composition and the electronic structure of materials. In XPS, the sample is bombarded with X-rays with a penetration depth between 1-10 nm, causing the emission of photoelectrons from the sample surface and leaving the atom in ionized state, see Figure 2.16 (a). By measuring the kinetic energy and number of these emitted photoelectrons, it is possible to determine the binding energy (BE) of the electrons, which is element specific since it corresponds to the energy of the orbital from where the electron is ejected, and thus allows to identify and quantify the elements present in the sample. Moreover, since the BE is influenced by the chemical environment of the atom from which they originate, XPS can also provide information on the chemical state of the atoms in the sample.[260]

On the other hand, immediately after the photoemission event takes place, the relaxation of excited ions can cause the outer shell electrons to fall into the inner orbitals, promoting the emission of another outer shell electron (Auger electron) to compensate the energy, see 2.16 (b). These Auger electrons are also characteristic of the individual chemical elements and are independent on the photoelectrons, resulting also very useful for elemental analysis.[261]

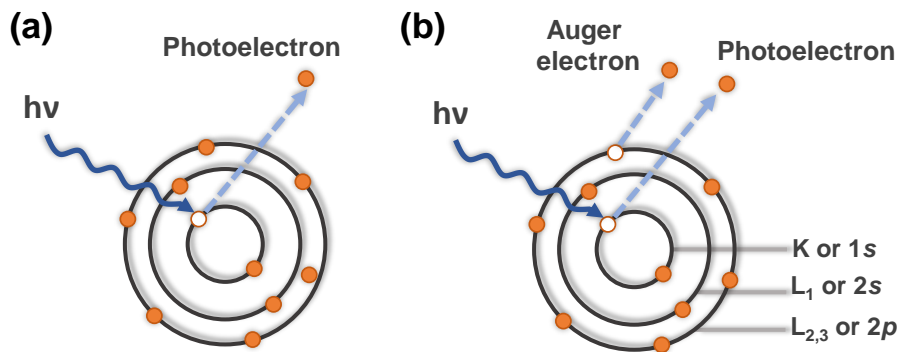


Figure 2.16: Schematic diagram showing the principles of XPS for a model atom during the (a) photoemission process and (b) the relaxation process of the ionized atom resulting in the emission of one outer shell Auger electron.

As a surface sensitive technique, the samples measured by XPS are specially susceptible to contamination from the atmosphere or from sample handling. Thus, it is very important to control their exposition before the measurements. In this thesis, the as-prepared samples were momentarily exposed to air when removed from the synthesis equipment and brought to the XPS sealed in vacuum.

XPS measurements were performed in collaboration with Dr. Guillaume Sauthier at Institut de Nanociencia i Nanotecnologia (ICN2), Spain, using a *PHOIBOS 150 NAP* hemispherical electron energy analyser (*SPECS GmbH*) operated at 300 W and a monochromatic Al K α radiation source with photon energy 1486.74 eV. The samples were analyzed with a spot size of 3.5 mm \times 0.5 mm at a base pressure ranging from 4 to 8.5×10^{-10} mbar.

In Chapter 4, XPS was used to study of core level binding energies and valence band maxima (VBM) of films surface and interface systems to ultimately extract the energy band diagrams. The energy resolution measured at the full width at half maximum (FWHM) of the Ag 3d_{5/2} peak for a sputtered silver foil was 0.62 eV. Data processing was carried out by the Master Student Alexander Frebel in our group, using the *CasaXPS* software. The BE were measured with respect to the Fermi energy of the analyzer, which was calibrated by measuring an atomically clean Au/glass sample. Details on the samples configuration specifics can be found in Section 2.3.3.

Also, XPS measurements were performed to study the surface chemical composition of LSCO thin films in Chapter 5. Pass energies of 20 and 50 eV and step sizes of 0.05 and 1 eV were used for the high-resolution and survey spectra, respectively. I processed the acquired data with *CasaXPS* software and

using Shirley background subtraction. The binding energies were calibrated using C $1s$ at 284.9 eV.

Additionally, XPS spectra were recorded using a *PHOIBOS 150 NAP* hemispherical electron energy analyser (*SPECS GmbH*) at the *NAPP* end station from *CIRCE* beamline at the ALBA Synchrotron Light Source, Spain,[262] to obtain the valence band spectra of cation engineered BFCO thin films, Chapter 3. The angle between the analyser axis and the incoming synchrotron radiation horizontal linear polarization vector was 54.7° , the magic angle, and the take-off angle were approximately 55° . The spectra were acquired with a $20\text{ }\mu\text{m}$ exit slit, and the X-ray spot was estimated to be in the order of $100\text{ }\mu\text{m} \times 50\text{ }\mu\text{m}$ (H \times V). Two different photon energies were used, 1032 eV and 525 eV, the former for the survey spectra with a pass energy of 20 eV and the latter for the high resolution scans with 10 eV pass energy. All the measurements were performed under high vacuum conditions. Both measurements and data processing were carried out by Dr. Carlos Escudero and Dr. Massimo Tallarida.

Time-of-flight secondary ion mass spectrometry

Time-of-flight secondary ion mass spectrometry (ToF-SIMS) is an analytical technique that allows to obtain qualitative elemental information from the surface or depth profile of a solid sample. This technique uses a pulsed primary ion beam and a time-of-flight mass analyzer to detect molecular ions with a certain mass-to-charge ratio (m/z ranging from 1 to 10^4).[263] The ion beam collides with the sample surface and it causes secondary ions and ionic clusters to be removed. These secondary ions are then passed into a mass spectrometer and accelerated along a flight path in vacuum conditions to prevent interferences. The respective masses of the individual ions will affect the length of time that takes them to pass through the flight chamber. Once they reach the end of the spectrometer, the ions are registered by a detector, and the information is saved.

Herein, ToF-SIMS was used to analyze the elemental depth profile of BFCO thin films with vertical gradient composition of Co (Chapter 4). The measurements were performed using a Bi^+ primary ion beam at 25 keV to generate positively charged secondary ions of the BFCO//STO systems, that is Bi^+ , Fe^+ , Co^+ , Sr^+ , Ti^+ and O^+ . The measurement area was $50\text{ }\mu\text{m} \times 50\text{ }\mu\text{m}$. [264] These measurements were performed in collaboration with Prof. Christian Hagendorf, Alexander Müller and Stefan Lange at Fraunhofer Center for Silicon Photovoltaics CSP, Germany.

2.2.7 Photoemission characterization

X-Ray Absorption Spectroscopy

X-ray absorption spectroscopy (XAS) is a surface sensitive (~ 10 nm) analytical technique that uses a monochromatic synchrotron X-ray source to provide information on the chemical and electronic structure properties of certain elements in materials. In XAS, an incident photon (with specific X-ray energy) is absorbed and interacts with a deep-core electron producing its excitation, and thus its transition to some unoccupied state (photoemission), leaving a core-hole behind. Immediately after, a lower energy electron will decay into the core-hole, generating an excess of energy that is emitted through a fluorescent X-ray or through an Auger electron, see Figure 2.17 (a). Different XAS modes can be found in function of which contribution is measured, namely the fluorescence mode when the fluorescent X-rays are measured and the total electron yield mode when the absorption edge of the emitted photoelectrons and the Auger electrons are measured. Note that in XAS, the absorption edges are determined by which electron is excited, and are named *K* (excitation in $1s$), *L* (excitation in $2s$ or $2p$) and *M* (excitation in $3s$, $3p$ and $3d$), see Figure 2.17 (b).

Since electronic transitions are measured, the samples need to be conductive (or grown in a conductive substrate).[265, 266]

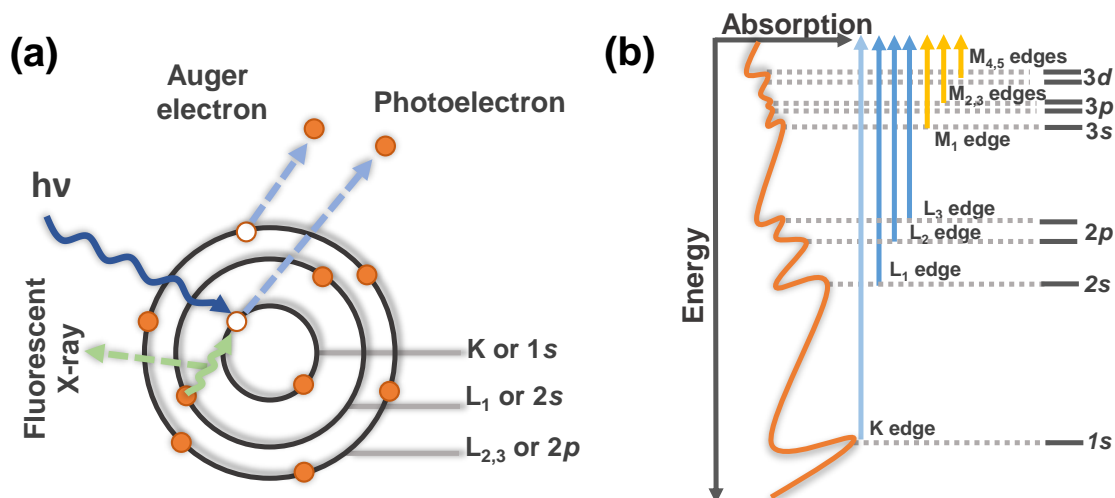


Figure 2.17: (a) Schematic diagram showing the principles of XAS for a model atom during the photoemission process and the relaxation process of fluorescent X-rays and Auger electrons, (b) absorption edges and transitions contributing to XAS spectra.

Here, a fine chemical and electronic structure study of BFO-based samples was performed by XAS measurements. To do so, the samples were grown on conductive Nb-doped STO substrates and Au top contacts were deposited by means of DC-sputtering to improve the conductivity of the sample and avoid charge effects during the measurements. The X-ray absorption spectra were obtained at the NAPP end station from the ALBA Synchrotron Light Source, Spain by Dr. Carlos Escudero and Dr. Massimo Talarida. The measurements were performed in total electron yield mode upon measuring the drain current on the samples by an electrometer (ALBA Em current amplifier)[267] and corrected by the incoming photon flux in a gold mesh just upstream the sample. The beam dimensions and sample orientation were the same as for the XPS measurements.

2.2.8 Electric characterization

Piezoelectric Force Microscopy (PFM)

Piezoelectric Force Microscopy (PFM) is an AFM-based technique applied for nanoscale and microscale characterization of ferroelectric and piezoelectric materials. The basic operation of PFM is based on the converse piezoelectric effect that implies that the material changes its dimensions when it is subjected to an external electric field. In the case of ferroelectrics, a conductive probe (top electrode) is scanned

in contact mode across the surface of the sample, which is normally connected to a bottom electrode. An alternating current (AC) voltage is applied to the probe tip in order to induce a deformation of the sample that undergoes a periodical expansion or contraction, as well as polarizing an specific location. As a result of the deformations and poling, the probe of the cantilever deflects and there is a 180° phase shift in the PFM response for the domains pointed up and down, allowing for simultaneous high resolution topographic and ferroelectric domains imaging. The effect of polarization, its magnitude, and possible dissipation can be monitored providing information of domain switching and local hysteresis.[252]

The polarized domains in BFO-based films were observed with a *MFP-3D Asylum Research* microscope from *Oxford Instrument Co.*, using the *n*-type AppNano silicon cantilevers with Pt coating (ANSCM-PT50). The scanned areas were $30\ \mu\text{m} \times 30\ \mu\text{m}$ and the electrically written regions were $10\ \mu\text{m} \times 10\ \mu\text{m}$. To achieve better sensitivity, the Dual-Frequency Resonance Tracking (DART) mode was employed.[268, 252] PFM voltage hysteresis loops were always performed at remanence, using a dwell time of 100 ms. The quantification of the piezo coefficient using DART was difficult due to the simultaneous variation of measurement frequency and the variation of the maxima of the resonance amplitude while measuring; consequently arbitrary units (arb. units) are indicated in the amplitude of the piezoresponse. These measurements were carried out by the PhD student Huan Tan and Dr. Ignasi Fina at ICMAB.

Electrical resistivity - PPMS

The physical property measurement system (PPMS) is an automated low-temperature and magnet system that allows for the measurement of the material properties like specific heat, magnetic susceptibility and electrical and thermal transport properties. The system is equipped with a vacuum chamber with helium cryostat that allows to work with good precision in the temperature range of 1.8 K to 400 K and controlling the temperature of the sample with a thermometer placed below the sample holder. The different measurement options result from the use of different measurement inserts or sample holders.[269] In this PhD thesis, the temperature dependence of the electric resistivity, $\rho(T)$, was measured over the 150 - 350 K temperature range using a PPMS from *Quantum Design* from ICMAB scientific services, Figure 2.18 (a), in 4-point configuration (i.e. Van der Pauw method) for the Au/LSCO//LAO samples. The 4-point configuration consists on two external electrodes to inject the current and 2 intermediate contacts to measure the voltage. To carry on the measurements, the 1 mm x 1 mm Au top electrodes placed at the vertices of the LSCO films (see Section 2.1.2) were contacted to a PPMS puck with Ag wires, Figure 2.18 (b). The electric resistivity was obtained from the sheet resistance (R_{sheet}) and

considering the film thickness (d), according to Equation 2.14:

$$\rho = R_{sheet} \cdot d \quad (2.14)$$

where R_{sheet} corresponds to:

$$R_{sheet} = \frac{\pi}{\ln 2} \cdot R_{PPMS} = 4.53 \cdot R_{PPMS} \quad (2.15)$$

Due to limitation of the used PPMS instrument, the resistivity was measured only in the temperature range that provided resistances (R_{PPMS}) below $\sim 10^7 \Omega$. These measurements were carried out in collaboration with the PhD student Jordi Alcalà and Dr. Anna Palau at ICMAB, Spain.

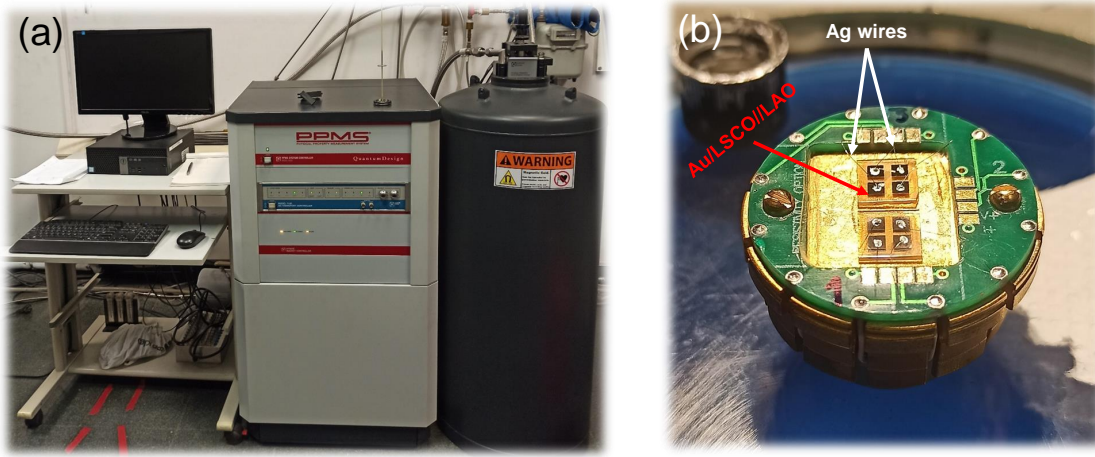


Figure 2.18: Photographs of (a) PPMS system from Quantum Design at ICMAB, CSIC and (b) Au/LSMO//LAO sample wired to a PPMS puck using Ag wires.

2.3 PV heterostructure characterization

In this section the fundamentals of the characterization techniques that were used to study the PV heterostructures as well as the corresponding measurement conditions and data analysis are described, including macroscopic ferroelectric and photoresponse characterization as well as band alignment determination.

Note that macroscopic ferroelectric and photoresponse characterization were performed in collaboration with MULFOX department who provided access to its facilities and fruitful discussions, whereas I carried out the measurements and data analysis. On the other hand, band alignment determination was

performed in collaboration with the student Alexander Frebel in the scope of his Master Thesis, where part of the work presented here is also included.

2.3.1 Macroscopic ferroelectric characterization

The macroscopic ferroelectric characterization is carried out by studying the switching behaviour of the ferroelectric layers in a capacitor-like heterostructure. To do so, a voltage with triangular waveform is swept to the films at a constant frequency while measuring the resulting current, $I(\tau)$, using the virtual ground method,[270] where τ is the time. The polarization (P) can be obtained by displacive current, integrating $I(\tau)$ through time and normalizing to the electrode area, A, following the Equation 2.16:

$$P \approx D = \frac{Q}{A} = \int I(\tau) d\tau \quad (2.16)$$

where D is the electric displacement and I typically has three contributions, being the leakage current coming from the electrons flowing through the material, the dielectric current corresponding to the charging and discharging current of the capacitor-like architecture and the ferroelectric current caused by the domain switching. In order to minimize the influence of leakage currents, the Dynamic Leakage Current Compensation (DLCC) method can be used.[271]

The obtained polarization and current density (J) hysteresis loops can be presented in function of the electric field, E, namely P-E and J-E, respectively, according to $E = V/d$ where d is the thickness of the ferroelectric within the capacitor architecture. On one hand, from the P-E loop, the switching characteristics of the films can be determined. A representative well-saturated P-E hysteresis loops is depicted in Figure 2.19, where the characteristic parameters that can be extracted, the coercive field (E_c) and the remnant and saturation polarizations (P_r , P_{sat} , respectively), and the different ferroelectric domains configuration are indicated. First, at the initial stage of the measurements, when no electric field is applied, all the domains are randomly oriented and the net polarization is zero (state A). With increased applied electric field the domains are poled in one same direction and the P_{sat} is reached (state B). When the applied electric field decreases, part of the domains switch back and part of the ferroelectric polarization remains at zero applied E, corresponding to P_r (state C). On the other hand, the J-E loops (not represented) are useful to identify non-ferroelectric contributions such as leakage currents that may not be compensated with DLCC method and could tentatively alter the polarization loop, leading to fictitious values of the ferroelectric parameters.[272]

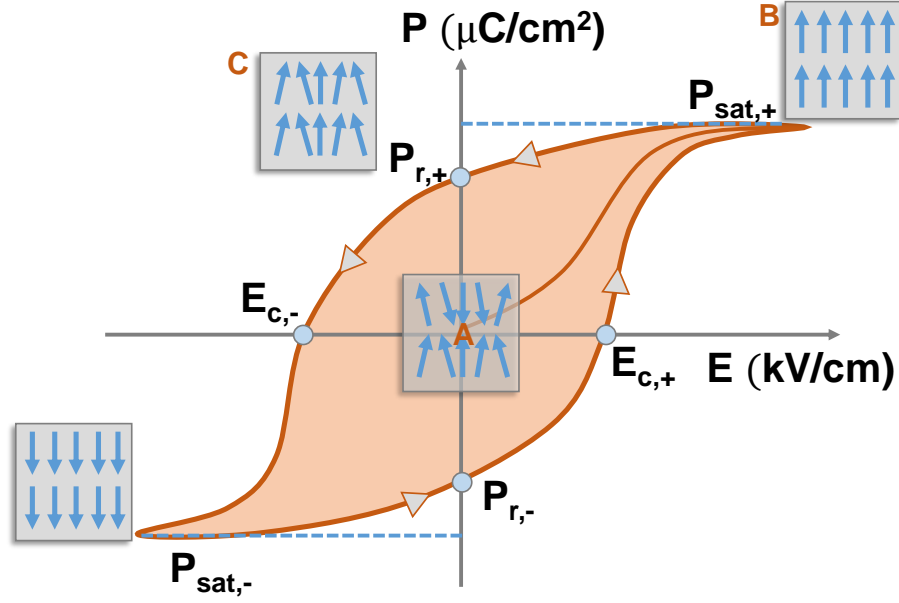


Figure 2.19: Representation of a well-saturated P-E hysteresis loop showing the characteristic parameters that can be extracted, namely P_r , P_{sat} and E_c . The ferroelectric domain configuration is represented at each stage of the P-E loop, being A the initial stage with randomly oriented domains, B the completely polarized state upon application of an electric field and C when part of the domains switch back because of application of lower electric field, but a polarization state remains.

In this thesis, the P-E and J-E loops of BFO-based films were recorded in two different architectures: (Pt or ITO)/BFO-based/LSMO//STO (Chapters 3 and 4) and ITO/ZnO/BFO-based/LSMO//STO (Chapter 4). The measurements were performed at room temperature and in dark conditions, using an *aixACCT TFA analyzer 2000* system with virtual ground method [273, 270] and DLCC to minimize leakage current effects. An electric field of up to 1100 kV/cm was applied at a constant rate with frequencies of 500 - 2000 Hz. In order to contact the samples, a probe station with micrometer tips was used. P-E and J-E hysteresis loops were collected using two different electrode configurations, bottom-top (asymmetric) and top-top (symmetric). In bottom-top configuration the E is applied to the top electrode (40 $\mu\text{m} \times 40 \mu\text{m}$ Pt or ITO) and the bottom electrode (LSMO) is grounded, whereas in top-top (symmetric) configuration E is swept in one of the top electrodes and the other one is grounded, see Figure 2.20. As explained in Section 2.9, the 10 nm Pt and the 70 nm ITO top contacts were deposited by DC sputtering and RF magnetron sputtering, respectively.

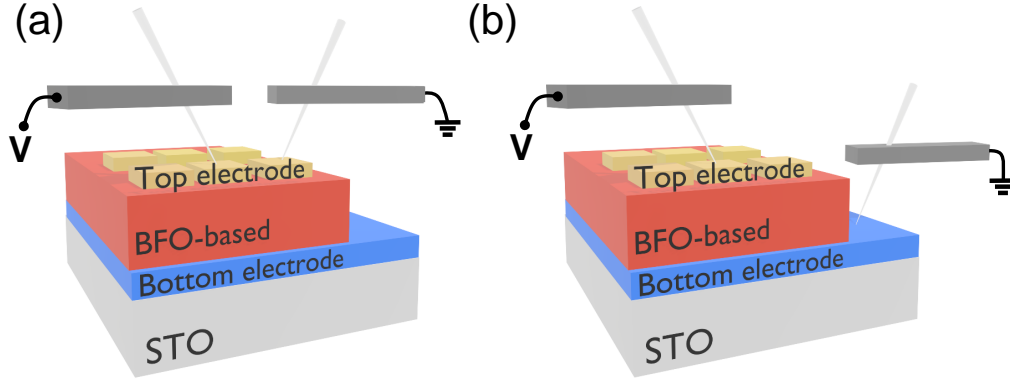


Figure 2.20: Electrode configurations for macroscopic ferroelectric characterization. (a) top-top and (b) top-bottom. Note that the thickness of the ferroelectric to calculate the electric field is " $2d$ " in top-top configuration and " d " in top-bottom configuration.

2.3.2 Photoresponse characterization

The photoresponse characterization makes reference to the measurements that allow to investigate the electric response of the samples while subjected to illumination.

In this work, the photoresponse of photoferroelectric BFO-based thin films is included in Chapter 4. To perform the measurements, the films were integrated into all-oxide devices following the architecture: ITO/(ZnO)/photoferroelectric layer/LSMO. All the measurements were carried out at room temperature, illuminating from the top of $130\text{ }\mu\text{m} \times 130\text{ }\mu\text{m}$ ITO electrodes and using a blue monochromatic laser with a wavelength of 405 nm and irradiance of 350 mW/cm^2 , see Figure 2.21. The laser irradiated the sample at an angle of 44° .

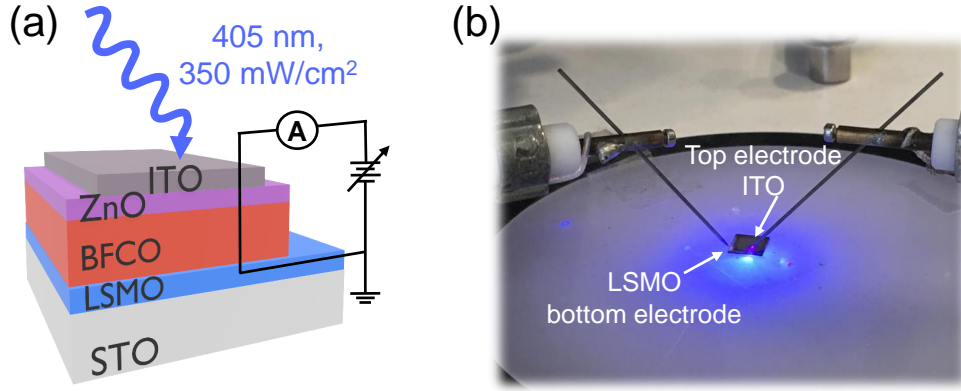


Figure 2.21: (a) Sketch of the electrical configuration used to measure the photoresponse of BFCO-based devices and (b) image of the experimental setup, showing contacted sample under illumination with a laser of 405 nm and 350 mW/cm².

The photoresponse properties were evaluated in virgin as-prepared systems, that is without pre-poling with an external voltage, and in pre-polarized systems in order to evaluate dependence of photoresponse with ferroelectric polarization.

Virgin BFCO-based systems

J-V curves:

The collection of the current density (J) vs applied voltage (V) characteristic curves was one of the measurements used in this thesis to evaluate the photoresponse of photoferroelectric BFO-based thin films. J-V curves can provide information on fundamental parameters of a PV device, such as the open circuit voltage (V_{oc}), that is the maximum potential generated by the cell when no current is flowing, and the short circuit current density (J_{sc}), which indicates the photogenerated current when the voltage across the device is zero. Together, V_{oc} and J_{sc} can help to determine the conversion efficiency of the device. In this work, the incident photon to current efficiency (IPCE) was calculated to define how efficiently the devices convert the incident light into electricity at a given wavelength,[274] following the Equation 2.17:

$$IPCE(\%) = \frac{1240 \cdot J_{sc}}{\lambda \cdot P_{inc}} \cdot 100 \quad (2.17)$$

where λ and P_{inc} correspond to the wavelength and power irradiance of the incident monochromatic light, respectively.

The J-V characteristics of the devices were measured using a *Keithley 2517B* electrometer by applying a sweeping voltage of up to ± 0.6 V at the top of ITO electrode and grounding the LSMO bottom contact. This sweeping voltage is lower than the coercive electric field of BFCO-based, ensuring no switching of J-V curve. In addition, J-V curves were collected in a time interval of 2 months to test the operational stability of the systems.

 J_{sc} -time dependence:

The time-dependence of J_{sc} under light pulses was used to study the response speed, stability and repeatability of the photogenerated current density in BFCO-based PV devices. These measurements were performed using an *aixACCT TFAalyzer2000* system and applying light pulses of ~ 10 s from the top of ITO electrode. Since J_{sc} was measured, no external voltage was applied.

Pre-polarized BFO-based systems. Study of the role of ferroelectricity on photoresponse.**J-V curves:**

To investigate the possible role of ferroelectric polarization switching on the photoresponse, J-V curves were collected in pre-polarized systems. To do so, prior to J-V collection, a unipolar triangular voltage larger than the coercive voltage of the film was applied to the top of ITO to induce the polarization state. This voltage was denoted as V_{poling} . Upward and downward pre-polarization states were induced when either a negative or a positive V_{poling} voltage of ± 6 V was applied to the top of ITO for 0.2 s using a *Keithley 2517B* electrometer. J-V curves were subsequently recorded with a time delay of ~ 10 s, by applying a sweeping voltage of ± 0.4 V at the top of ITO electrode and grounding the LSMO bottom contact. Figure 2.22 (a) shows the protocol measurement.

 J_{sc} - V_{poling} dependence:

The evolution of J_{sc} under the application of different V_{poling} was measured in a continuous manner using a *Keithley 2517B* electrometer and shortening the delay time of the measurements. A train of V_{poling} of up to ± 6.5 V were applied for 1 s to the top of ITO and the generated current density under illumination at zero voltage was collected with a time delay of ~ 0.1 s for each V_{poling} , see Figure 2.22 (b). [80]

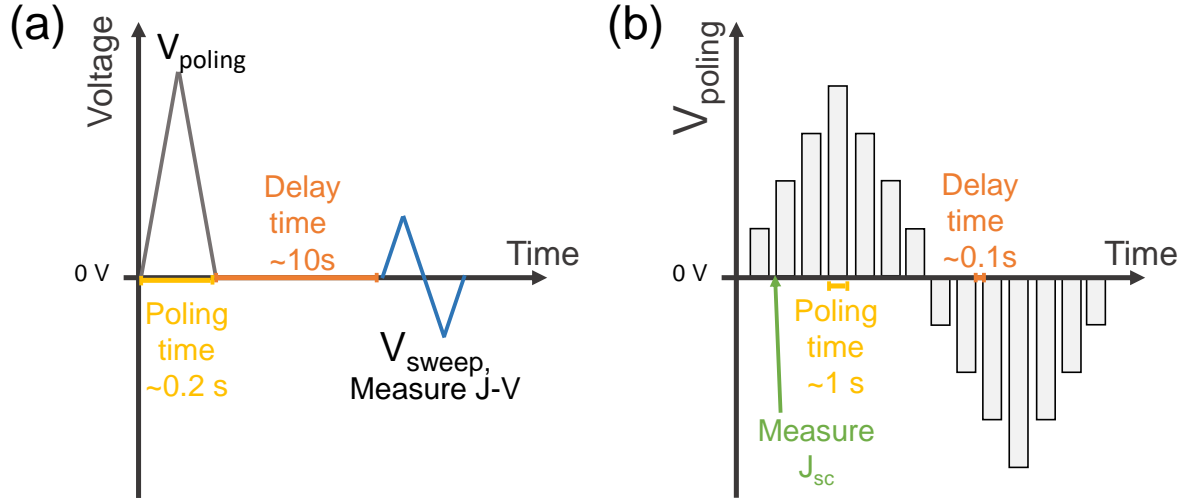


Figure 2.22: (a) Protocol to measure a J-V curve of a pre-polarized system. A unipolar triangular V_{poling} is applied for 0.2 s to induce the pre-polarization state in BFCO. After ~ 10 s (time delay), a sweeping voltage (V_{sweep}) is applied and the J-V curve is collected. (b) Protocol to measure the J_{sc} - V_{poling} dependence, where a train of V_{poling} is applied and J_{sc} is recorded at 0 V with a time delay of ~ 0.1 s. Note that the graphs are not scaled and values of applied voltages are not indicated.

2.3.3 Band alignment determination

Understanding and controlling the alignment of the energy bands is essential to ensure optimized device operation, since the electrons and holes flow rate strongly depends on the valence-band and conduction-band offsets (VBO-CBO) across the device interfaces.[275, 276, 277] Moreover, these offsets imply the presence of built in potentials (V_{BI}), which strongly affect the modulation of the Schottky barriers height and the charge carriers recombination at the interfaces.[276]

In this PhD thesis, the band alignment at the interfaces was determined in Chapter 4. Note that the composition of BFCO selected for this study was $\text{BiFe}_{0.9}\text{Co}_{0.1}\text{O}_3$ (BFCO10), within the systems ITO/BFCO10/LSMO//STO and ITO/ZnO/BFCO/LSMO//STO.

First it was studied the surface of sputtered-ITO, ALD-ZnO, CSD-BFCO10 and CSD-LSMO single-layers in the following configurations: 50 nm ITO/300 nm SiO_2 //Si; 25 nm ZnO/300 nm SiO_2 //Si; 100 nm BFCO10/10 nm LSMO//STO and 10 nm LSMO//STO. To do so, the core level binding energies of In 3d, Sn 3d, Zn 2p, Bi 4f, Sr 3d and the respective valence band maxima (VBM) were extracted from XPS analysis. The Co 2p and Mn 2p core level spectra were also recorded to identify possible

oxidation/reduction in BFCO and LSMO, respectively.

The interface experiments were carried out by depositing 3 nm of ITO on 25 nm ZnO/300 nm SiO₂//Si; 3 nm of ITO on 100 nm BFCO10/LSMO//STO; 6 nm of ZnO on 25 nm BFCO10/LSMO//STO and 5 nm BFCO10 on 10 nm LSMO//STO.

The valence band offset (ΔE_{VBM}) at ITO/BFCO, ITO/ZnO, ZnO/BFCO and BFCO/LSMO interfaces were obtained by measuring the energy differences associated to the relative position to the VBM and core levels of the different materials. The study was completed by extracting the conduction band minima (CBM) and conduction band offset (ΔE_{CBM}) using the bandgaps. BFCO and ZnO optical bandgaps were determined experimentally by SE whereas the value for ITO was extracted from the literature.[278, 279] These results are presented in Chapter 4.

In order to extract the values of ΔE_{VBM} , ΔE_{CBM} and the built-in potential from XPS data, $V_{BI,XPS}$, the Equations 2.18, 2.19 and 2.21 were used, respectively:

$$\Delta E_{VBM} = (E_{CL,single-layer1} - E_{VBM1}) - (E_{CL,single-layer2} - E_{VBM2}) - (E_{CL,layer1,interface} - E_{CL,layer2,interface}) \quad (2.18)$$

where E_{CL} is the core level binding energy and 1 and 2 refer to the upper and inferior layers (or interfaces), respectively.

$$\Delta E_{CBM} = (E_{CL,single-layer1} - E_{CBM1}) - (E_{CL,single-layer2} - E_{CBM2}) - (E_{CL,layer1,interface} - E_{CL,layer2,interface}) \quad (2.19)$$

where E_{CBM} is obtained from:

$$E_{CBM} = E_{VBM} - E_g \quad (2.20)$$

and E_g correspond to the bandgap energy extracted from SE or literature.

Finally, the $V_{BI,XPS}$ is obtained from:

$$V_{BI,XPS} = E_{CL,interface1} - E_{CL,interface2} \quad (2.21)$$

were the E_{CL} values of the photoferroelectric BFCO10 with the upper (1) and inferior (2) interfaces are considered.

Chapter 3

Cation co-substitution in BiFeO_3 photoferroelectric thin films for optimized phase stability and enhanced optoelectronic performance

Compositional engineering by means of controlled cation substitution in photoferroelectric perovskite oxide thin films with general formula ABO_3 , has positioned as an appealing strategy to tune their structure and the optoelectronic properties. B-site substitution in BiFeO_3 films has shown to affect the physical properties, in particular the optical bandgap. The system $\text{BiFe}_{1-x}\text{Co}_x\text{O}_3$ (BFCO) is of special interest because large cobalt loads leads to narrow bandgaps, being of great interest to improve sun light harvesting.[122] Nonetheless, the larger the cobalt substitution, the more difficult to incorporate it in the crystalline structure.

Previous reports have underlined the benefits of Bi-site doping using lanthanide (Ln) cations to improve phase stabilization and film quality. Nevertheless, the integration of two cations in the perovskite structure is rather complex and its study has been limited to low Co loads ($x = 0.02 - 0.05$). In this chapter it is investigated the challenging task to perform cation co-substitution in $\text{Bi}_{0.9}\text{Ln}_{0.1}\text{Fe}_{0.7}\text{Co}_{0.3}\text{O}_3$ with $\text{Ln} = \text{La}$ and Ce . We explore how the site nanoengineering impacts the defect chemistry, structure, optical and photoferroelectric properties of the films. X-ray diffraction, spectroscopic ellipsometry and X-ray absorption spectroscopy measurements are presented to gain insight on the influence of the defect

chemistry on the structure, optical and electronic properties of the films, respectively. Additionally, first-principles calculations based on density functional theory are performed and compared to the experimental observations.

Part of the work presented in this Chapter has been published in *J. Mater. Chem. C*, 2021, 9, 330-339, DOI: 10.1039/D0TC04304D

3.1 Introduction

The use of photoferroelectric oxide perovskites as a stable photo-active layer has opened up a groundbreaking new arena of research in the field of energy owing to their alternative mechanism for solar energy conversion.[66, 108, 88, 280] Of the various oxide perovskite materials with general ABO₃ structure, BiFeO₃ (BFO) has generated much interest being ferroelectric at room temperature with a relatively narrow bandgap at 2.7 eV.[91, 281, 71] Interestingly, B-site cation compositional substitution in BFO has turned out to be effective to tune their structure and physical properties.[108, 122] However, controlling site nanoengineering is often complicated because of the generation of secondary phases (such as Bi₂Fe₄O₉ and Bi₂₅FeO₄₀)[110] and charge defects including Fe²⁺, Fe⁴⁺, bismuth, and oxygen vacancies, which at the same time depend on the processing conditions.[111, 112] Indeed, vacancies are the dominant point defects in perovskite oxides and can dramatically interfere on their physical properties, ultimately determining their functionality. Therefore, the study of defect chemistry combined with the use of an adequate synthesis methodology is essential to comprehend the origin of the material's properties and learn how to effectively tune them.

In that regard, solution-processing has demonstrated to be an effective, low-cost and versatile approach to prepare chemically engineered BFO films. [282, 233, 283] It allows good control to alter the cation composition by incorporating different stoichiometric amounts of the corresponding metal precursors. Previous studies carried out in our group have demonstrated that Fe-site cation substitution in solution-processed BiFe_{1-x}Co_xO₃ (BFCO) system can put forward an attractive active material towards visible light absorption while preserving robust ferroelectricity.[122] The valence configuration of these cobalt-doped systems has been found to be Fe³⁺ for iron and Co³⁺/Co²⁺ for cobalt.[284] Importantly, the charge defect scenario, such as the ubiquity of oxygen vacancies, is expected to be altered due to the presence of Co²⁺. [285] This phenomenon can interfere in the leakage current of the system and potentially affect the performances of PV devices when BFCO is integrated as the photo-active layer. Hence, identifying an

approach to suppress or compensate the formation of oxygen vacancies would be desirable. In addition, phase stabilization in BFCO still remains a challenge for cobalt loads $\geq 30\%$, at which segregation of secondary phases start to take place, limiting the possibility to further narrow the bandgap and optimize the absorption properties.[286, 119, 122, 287]

Within this context, partial Bi-site doping with lanthanides (Ln) could be suitable to address the above mentioned issues. Owing to the notably larger bond dissociation of energy of Ln-O ($D^\circ_{298K} = 700\text{-}800$ kJ/mol) compared to that of Bi-O ($D^\circ_{298K} = 343$ kJ/mol),[127] lanthanides help stabilizing oxygen octahedron and decrease Bi volatilization and improve phase stability. In fact, partial Bi-site doping ($< 20\%$) in BFO by La, Ce, Nd, Sm or Gd has already been presented to be beneficial to improve the properties of BFO, in particular the crystallinity, purity and leakage currents.[125, 288, 124, 130, 131, 133] On the other hand, the use Ln cations with different oxidation states, such as Ce, could also impact the charge defect scenario. Nonetheless, controlling the cation substitution, in particular two-site substitution, is delicate when targeting two different properties such as optical absorption and ferroelectricity.

In this Chapter, it has been investigated the effect of Bi-site substitution in solution processed BFCO thin films to gain insights on its influence on the structure, optical, ferroelectric and electronic properties while securing the formation of single phase BFCO films. It is expected that obtaining a stable, pure-single crystalline phase with improved surface morphology, could positively affect the good traits of BFO-based for PV applications, as it will be evaluated in Chapter 4.

Herein, two cations have been evaluated for Bi-site substitution, namely La and Ce. First, the use of La³⁺ cation in Bi_{1-y}La_yFe_{1-x}Co_xO₃ (La-BFCO) system has been explored owing to its trivalent oxidation state and the relatively close ionic radii with Bi³⁺, see Table 3.1. Also, it is expected that the fact that La has one unique stable oxidation state (3+) could bring more robustness to the phase stabilization by avoiding the formation of additional charge defects.

In addition, it has been investigated the influence of Ce cation, which has two valence states being Ce³⁺ and Ce⁴⁺. On one hand, Ce³⁺ has a similar ionic radii as Bi³⁺, Table 3.1, whereas Ce⁴⁺ could act as donor impurity in oxygen octahedron and compensate oxygen vacancies, leading to a decrease in the leakage current of the films.[289, 288] Therefore, Ce is also a potentially attractive candidate to stimulate the formation of stable Bi_{1-y}Ce_yFe_{1-x}Co_xO₃ (Ce-BFCO) perovskite structure. In this study, Ce and La-doping have been kept at low concentration, 10%, to stay far from the values in which structural phase transition occur.[290, 126, 291]

Table 3.1: Ionic radii of A-site and B-site cations in BFO. Note that the ionic radii of Bi³⁺ in CN = 12 is not tabulated in Shannon et al. [98] For consistency, an estimated value for CN = 12 is included although it might be overestimated.[99]

Cation	r_i (Å) A-site NC=12	r_i (Å) B-site NC=6
Bi ³⁺	1.54	
La ³⁺	1.36	
Ce ³⁺	1.34	
Ce ⁴⁺	1.14	
Fe ³⁺		0.55 LS/0.65 HS
Co ³⁺		0.55 LS/0.61 HS
Co ²⁺		0.65 LS/0.75 HS

*LS= low spin HS= high spin

3.2 La-doped BFCO thin films

The viability of La-substitution has been explored in BFCO thin films with Co loads of 30%, Bi_{0.9}La_{0.1}Fe_{0.7}Co_{0.3}O₃ (La-BFCO30), and compared to pristine BFO and BFCO with different cobalt loads, BiFe_{0.8}Co_{0.2}O₃ (BFCO20) and BiFe_{0.7}Co_{0.3}O₃ (BFCO30). The main goals of this study are twofold: (i) investigate the viability to integrate La in BFCO30 films and (ii) study how cation co-substitution affects the physical properties and the electronic structure.

The structure, surface morphology, optic, electronic and local ferroelectric properties have been studied on 25 nm thin films. Also, 75 nm and 100 nm films have been prepared to perform STEM analysis and macroscopic ferroelectric measurements, respectively.

3.2.1 Crystallinity, structure and surface morphology

The preparation of La-BFCO30 film has been attempted and its crystallinity and phase purity has been compared to that of BFO, BFCO20 and BFCO30. Figure 3.1 (a) shows the comparative XRD θ -2 θ patterns, where the (00l) Bragg reflections of the BFO-based phases can be observed next to the intense (00l) reflections of the STO substrate. These diffraction patterns suggest *c*-axis oriented growth of the perovskite films indexed assuming a pseudocubic cell (indicated with an asterisk (*)). It is observed that when Co loads reach 30% the (00l) reflections from the BFCO30 broaden in comparison to pristine

BFO, evidencing a worsened crystalline quality. Moreover, additional diffraction peaks appear between 2θ angles of 25° and 38° (highlighted with a grey square), which are characteristic of Bi and Fe oxide rich phases.[122] With the incorporation of La in BFCO30, the segregation of these secondary phases is suppressed and the (001) reflections from La-BFCO30 are sharpened, being an indicative of the formation of pure phase films with improved crystallinity. In order to rule out that randomly oriented secondary phases are formed on the film surface, which would be a clear indication that either Co or/and La were not integrated in the BFO structure, GIXRD analysis have been carried out for La-BFCO30 and compared to BFCO30, Figure 3.11 (b). The intensity of the La-BFCO30 reflections is significantly higher than that of BFCO30, suggesting an improved crystalline quality upon La incorporation also at the film surface.

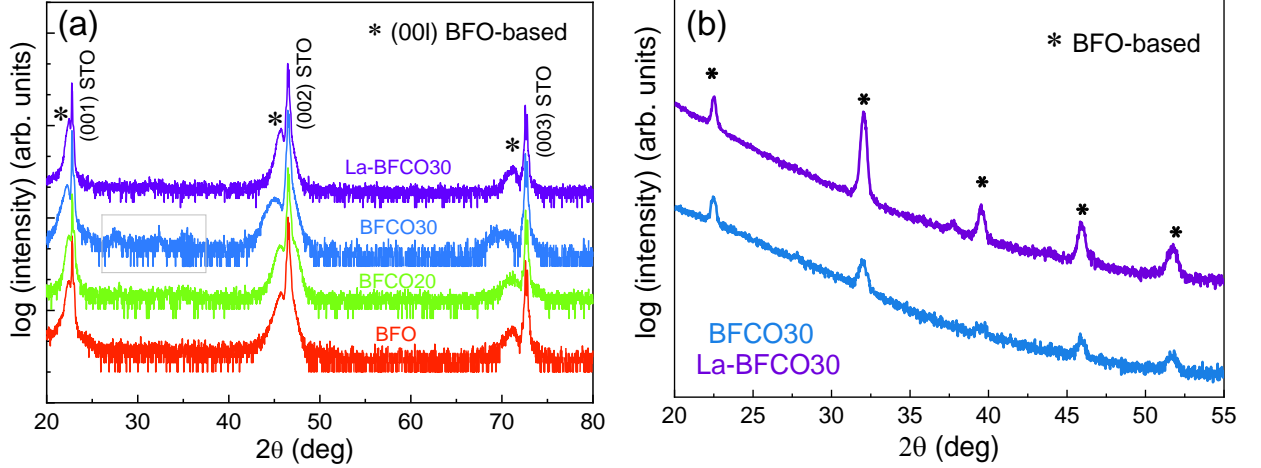


Figure 3.1: Crystallinity and phase purity study. (a) Comparative XRD θ - 2θ scan of 25 nm BFO, BFCO20, BFCO30 and La-BFCO30 thin films grown on (001) STO and (b) GIXRD θ - 2θ scan of BFCO30 and La-BFCO30 thin films.

With a view to get further insights into the structure quality and phase purity of La-doped films, cross-sectional HAADF STEM images have been obtained for 75 nm La-BFCO30 on non-optimized LSMO//STO, Figure 3.2 (a). A rather homogeneous film with minor presence of few secondary phases is observed. Overall, the film presents improved homogeneity compared to previously reported CSD-processed BFCO30, see supporting information of Ref.[122]. It is emphasized the absence of secondary phases at the top of the film surface (white square) in well agreement with GIXRD analysis. However it has to be noted that in this sample the interface of La-BFCO30 with the bottom electrode is not

perfectly sharp, and LSMO presents terraces. LSMO surface quality has been optimized afterwards to perform high quality devices as will be shown in Chapter 4 (Figure 4.13).

A higher magnification image has been taken from the surface area highlighted in white, in order to further evaluate the crystalline quality of La-BFCO30 at the film surface, see 3.2 (b), where a clear epitaxial growth can be observed. These results are in line with the sharpened and high peak intensity seen in θ -2 θ and GIXRD scans (Figure 3.1). Moreover, the EELS mapping of Fe and La atomic species at the region marked with a purple square indicate an homogeneous distribution of Fe and clear integration of La within the perovskite structure. The EEL spectra of Fe and Co L-edges and La M-edge, extracted from the corresponding area scan, are represented in Figure 3.2 (c), confirming the presence of Fe, Co and La within the BFO-based film structure. Background-subtracted EEL spectra, see inset of Figure 3.2 (c), allows to better identify the Co L-edge and La M-Edge.

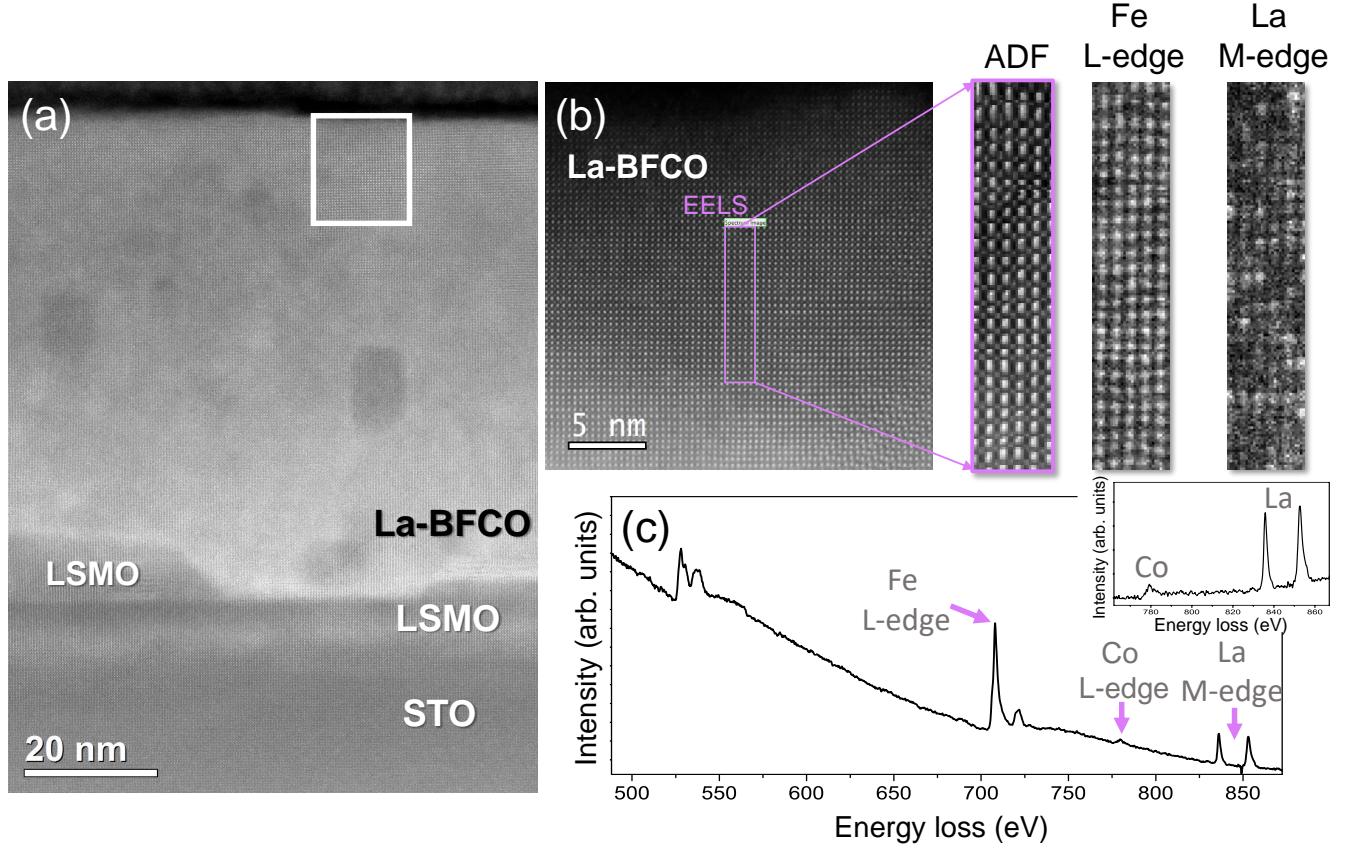


Figure 3.2: (a) Z-contrast cross-section HAADF STEM image of ~ 75 nm La-BFCO₃₀/LSMO//STO. The white square indicates the area studied in (b). (b) Atomic-resolution STEM image of the surface of La-BFCO₃₀ and EELS mapping of Fe and La atomic species from the area marked with a purple square. (c) Corresponding EEL spectra acquired from (b) showing the Fe and Co L-edges and La M-edge. The inset shows the background-subtracted spectra of Co and La region for clarity in the detection of spectral feature of Co.

Since improvements in film purity and crystalline quality have been obtained upon La-doping, we proceed on performing advanced XRD characterization by means of high-resolution RSM around the (103) reflection for 25 nm BFO, BFCO₂₀, BFCO₃₀ and La-BFCO₃₀, see Figure 3.3. The in-plane and out-of-plane lattice parameters (a and c , respectively) and unit cell volume have been determined and are summarized in Table 3.2. Note that a and c have been extracted from averaging the 3 most intense (q_x, q_z) coordinates and calculating dispersion from 12 (q_x, q_z) points. All our films show similar in-plane lattice parameter as STO substrate ($a_{\text{STO}} = 3.905$ Å), indicating in-plane strain. On the other hand, upon Co-doping the out-of-plane lattice parameter and the volume monotonously increases from $c = 3.97 \pm 0.01$ Å for pristine BFO to $c = 4.06 \pm 0.02$ Å for BFCO₃₀, suggesting minimal unit cell distortion, as expected from the subtle differences between Fe and Co ionic radii, see Table 3.1. In La-BFCO₃₀, the out-of-plane lattice parameter and the unit cell volume slightly decrease compared to BFCO₃₀, because

of the smaller ionic radii of La³⁺ than Bi³⁺, see Table 3.1.

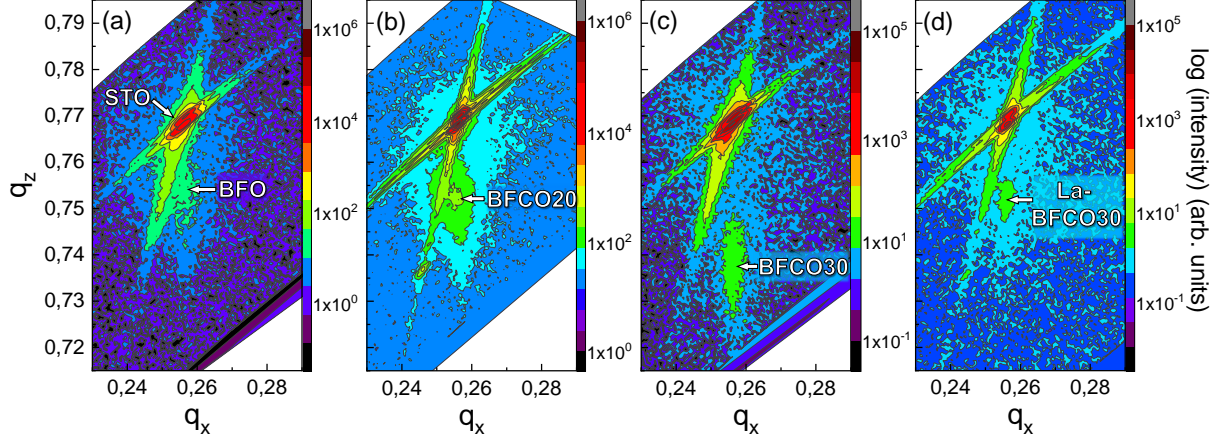


Figure 3.3: Comparative of XRD analysis reciprocal space map of 25 nm (a) BFO, (b) BFCO20, (c) BFCO30 and (d) La-BFCO30 thin films on STO around the (103) reflection.

Table 3.2: Cell parameter a and c and unit cell volume (V) for 25 nm BFO, BFCO20, BFCO30 and La-BFCO30 films on STO substrate calculated from the reciprocal space map of Figure 3.3.

Composition	a (Å)	c (Å)	V (Å ³)
BFO	3.908 ± 0.004	3.97 ± 0.01	60.63
BFCO20	3.909 ± 0.003	3.99 ± 0.01	60.97
BFCO30	3.902 ± 0.003	4.06 ± 0.02	61.82
La-BFCO30	3.909 ± 0.003	3.99 ± 0.01	60.97

The influence of La substitution on the surface morphology has been evaluated by means of AFM, Figure 3.4. The topographic images of BFCO20 and BFCO30 reveal that the films are homogeneous and dense identifying granular surface resulting in a rms roughness of 2 nm. For La-BFCO30 the surface is smooth and dense with much smaller grain size although few precipitates are identified. Overall the surface roughness is decreased (1 nm) compared to the two previous samples. In all cases, the films show crystallites-like morphology. Thus, it is confirmed an overall improvement in surface film quality upon La-doping, although few surface particles can be identified.

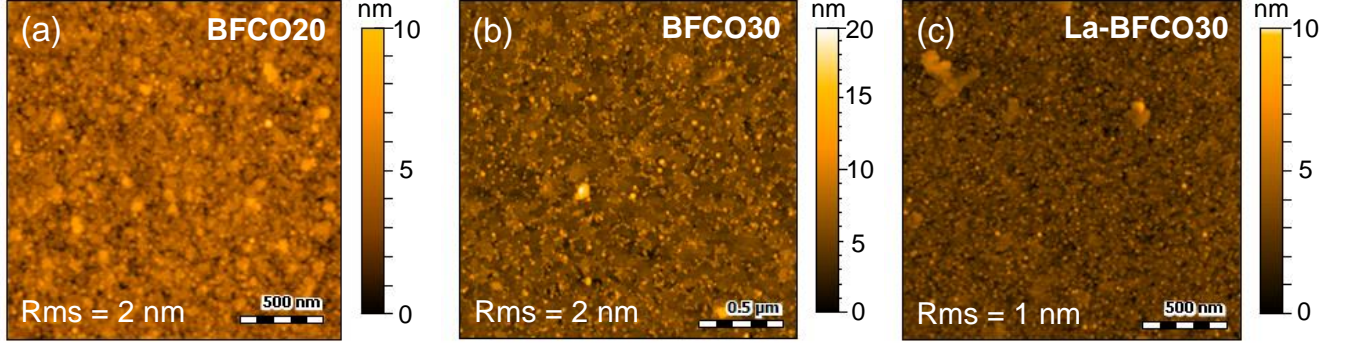


Figure 3.4: Surface morphology study. 5 μm x 5 μm AFM topography images of (a) BFCO20, (b) BFCO30 and (c) La-BFCO30 films on STO.

3.2.2 Optical properties

The effect of Co and La chemical doping on the optical properties of BFO-based systems has been studied by means of spectroscopic ellipsometry. The experimental data was fitted using the Tauc-Lorentz model and considering the structure void/rough layer/BFO-based film/substrate, as it is detailed in Experimental Section 2.2.5. This analysis enabled to extract the complex refractive index (n , κ) of the films, see Figure 3.5 (a). Starting from the index of refraction of BFO film, two spectral features can be identified at ~ 320 eV and ~ 440 eV, which have been previously assigned to metal $3d$ - metal $3d$ or metal $3d$ - oxygen $2p$ charge-transfer transitions.[107, 292] As already reported in similar systems,[122] the intensity of these two features is gradually modified with cobalt integration. On the other hand, in La-BFCO30, the intensity of these peaks resembles that of BFCO20 whereas the position is slightly modified. The optical absorption coefficient, α , has been obtained from the extinction coefficient, κ , following the Equation 2.10, see Figure 3.5 (b). It is found that cobalt-substitution gradually introduces a red shift on the absorption edge, as it was already reported in BFCO films,[122] whereas La-BFCO30 shows similar optical properties than BFCO30. This same trend can be observed in the Tauc plots for direct $(\alpha h\nu)^2$ transitions (inset). For pristine BFO films it is shown a nearly linear dependence with photon energy in line with previous observations of CSD-processed BFO.[293, 122] The extrapolation of the linear region of the plot to the x-axis intercept ($\alpha=0$) allows to obtain the Tauc gap, being 2.7 eV for BFO, whereas a bandgap decrease results from cobalt doping.[122] La-substitution barely modifies the shape of the direct transition with respect to its parent compound (BFCO30), and therefore no changes in the bandgap, reinforcing the formation of a stable co-substituted perovskite phase with preserved optical properties.

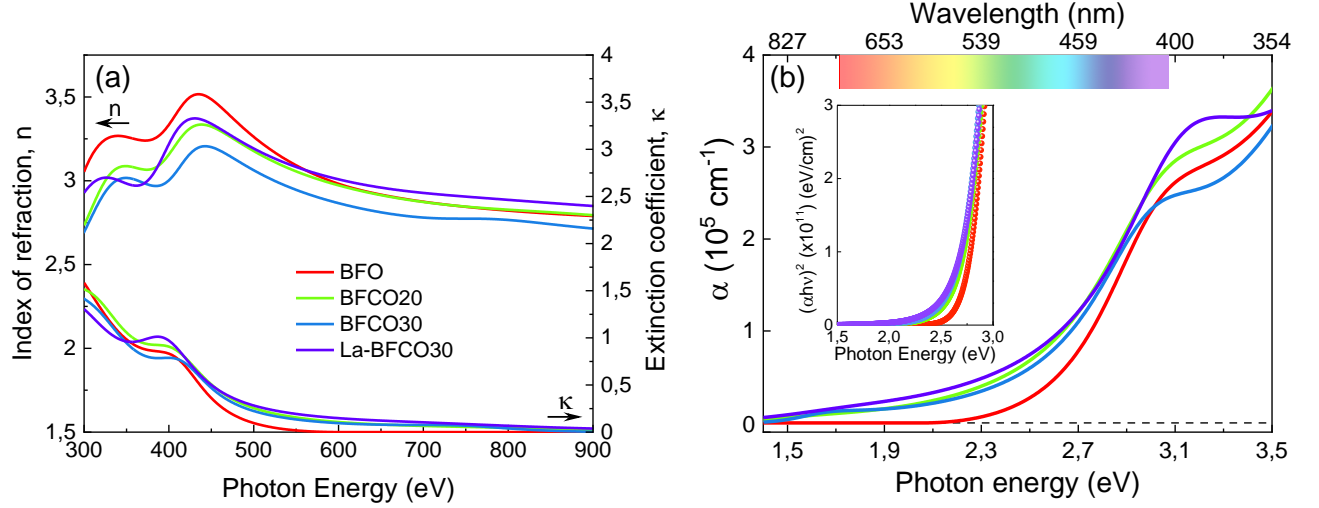


Figure 3.5: Optical properties of BFO, BFCO20, BFCO30 and La-BFCO30 thin films grown on STO substrate extracted from spectroscopic ellipsometry (SE). (a) n and κ optical constants, (b) absorption coefficient, α , and $(\alpha h\nu)^2$ Tauc plots for direct transition energies (inset).

3.2.3 Electronic structure

In order to better understand the effect of gradual change in the chemical substitution on the electronic structure of BFO, X-ray Absorption Spectroscopy (XAS) of the Fe L_{2,3}, Co L_{2,3} and O K-edges have been carried out. As specified in the Experimental Section 2.2.7, in order to perform this study, the samples were grown on conductive Nb-doped STO, and Au top contacts were sputtered to minimize charge effects during the measurements. Note that the absorption at the Fe L_{2,3}-edge (or Co L_{2,3}) corresponds to electron transitions from Fe 2*p* (Co 2*p*) to Fe 3*d* (Co 3*d*) orbitals and it is very sensitive to crystal-field interactions. Figure 3.6 (a) shows the Fe L_{2,3} spectra of all the samples studied in this Chapter. It is observed that regardless of the A-site and B-site substitution there are negligible differences in the peak positions and the line shape of all spectra. A comparison of our results with the well known Fe L_{2,3} spectrum of both BiFeO₃ and LaFeO₃, which exhibit a high spin Fe³⁺ ground state,[294, 295] shows a good agreement. Therefore, Fe³⁺ is the dominant oxidation state for both undoped and doped samples and the 3*d* occupancy of Fe barely changes with neither the Co nor La doping, being consistent with previous XAS studies on cation engineered La_{1-x}Sr_xFeO₃ and La_{0.8}Bi_{0.2}Fe_{1-x}Mn_xO₃ systems.[296, 297]

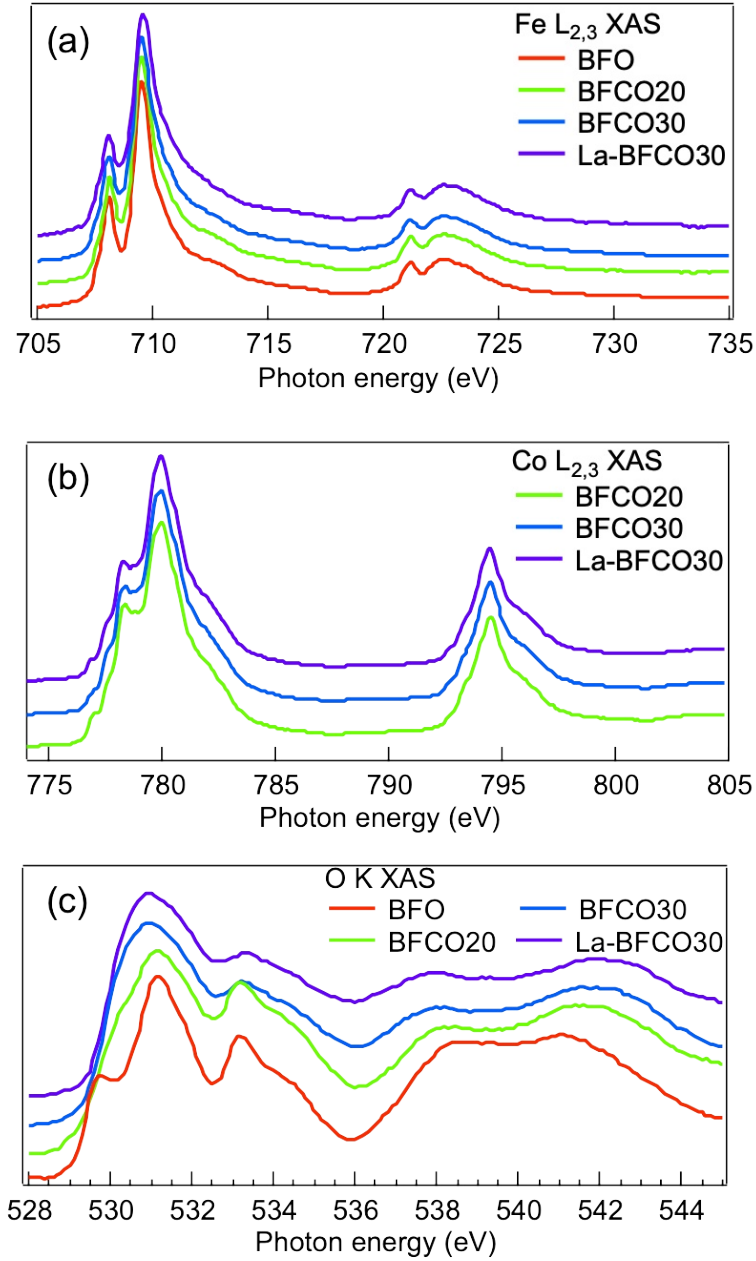


Figure 3.6: XAS spectra of the 25 nm BFO, BFCO20, BFCO30 and La-BFCO30 thin films on Nb-STO (a) at the Fe L_{2,3}-edge, (b) Co L_{2,3}-edge, (c) O K-edge. Note that spectra have been vertically shifted for clarity in the presentation of the results.

On the other hand, Figure 3.6 (b) shows the absorption spectra at the Co L_{2,3}-edge, which shape reveals the presence of a combination of Co²⁺ and Co³⁺ species, [298, 299] with small variation of the Co²⁺/Co³⁺ ratio for the different cobalt concentrations, being ~ 0.7 in BFCO20 and ~ 0.5 in BFCO30 and La-BFCO30. Hence, the substitution of Bi by La, does not change this ratio significantly. Besides the XAS of the transition metal elements, it is also interesting to follow the behaviour of the oxygen

K-edge for all the samples, Figure 3.6 (c). In this case, the variations are more complex as they involve the density of oxygen-related unoccupied states which originate from the hybridization between the O 2*p* and Fe/Co 3*d* states (region 528 - 532 eV), as well as with the unoccupied Bi 6*p* states (region 532 - 536 eV), and the Fe/Co 4*s*4*p* states (region 536 - 544 eV).[294] It is observed that the feature near the onset (528 - 532 eV) undergoes a continuous transformation by the substitution of Fe by Co, i.e. the O 2*p* - Fe 3*d* hybridized states are substituted by O 2*p* - Co 3*d* hybridized states, while the La substitution does not bring any further change in comparison with BFCO30. Moreover, the integrated intensity of this first region of the spectra increases for higher amount of Co doping. This trend can be related to the increase in *d*-electron number when Fe is substituted by Co and therefore the O 2*p* - Fe/Co 3*d* hybridized states increases concordantly. Similar behavior has been previously observed in LaBO₃ samples (B= Cr, Mn, Fe, Co, Ni) under the claim that at fixed transition metal valence, going from left to right in the first row of the periodic table, the electronegativity of the transition metal increases (more covalent) and, as a consequence, the 3*d* orbitals may get closer to the O 2*p* leading to stronger hybridization.[300, 301] Indeed, this change in the number of *d* electrons has already been reported to modify the optical bandgap.[302, 300] Nonetheless, it is important to note that our samples contain a mixture of Co³⁺ and Co²⁺ species, with a decreasing Co²⁺/Co³⁺ ratio with Co substitution, Figure 3.6 (b). Based on that, the first feature of the O K-edge spectra indicates that the hybridization increases for those samples with moderately higher content of Co³⁺. This behavior agrees with the study of Suntivich *et al.*[301] carried out in a series of La-Ni-O compositions in which the hybridization between Ni 3*d* orbitals and O 2*p* orbitals increased by varying the oxidation state of Ni from Ni²⁺, Ni^{2.7+} to Ni³⁺. Upon this change, the level of the transition metal 3*d* lowered, leading to smaller charge-transfer energy (Δ) that explained the increase in orbital hybridization.[300] Note that the effect of Co doping is also observed in the shape of the valence band showing an increase of the feature at valence band maximum (VBM) attributed to the O 2*p* - Co 3*d* occupied states, see Figure A3.1. Therefore, it is very likely that the optical bandgap reduction identified from spectroscopic ellipsometry upon cobalt substitution (Figure 3.5) is due to an increase in the hybridization between the transition metal 3*d* and O 2*p* orbital states, which is enabled by the presence of Co³⁺. Nevertheless, it can be anticipated that the first-principles calculations described below suggest that this hybridization is mediated by the presence of both, Co³⁺ and Co²⁺ ions. Finally, we recall that low level of A-site substitution barely modified the O K-edge spectra and thus the hybridization, being consistent with the reported less significant role of A-cation on the electronic structure.[296, 301]

3.2.4 Ferroelectric properties

The macroscopic and microscopic ferroelectric properties of La-BFCO30/LSMO//STO systems have been evaluated in Figure 3.7. Regarding the macroscopic ferroelectric measurements, the polarization-electric field (P-E) hysteresis loop of La-BFCO30 have been compared to that of pristine BFO and cobalt-doped BFCO30 films, see Figure 3.7 (a). These measurements have been carried out at room temperature, in dark conditions and with a frequency of 2 kHz after completing the systems with a 10 nm Pt top electrode to obtain a device architecture: Pt/100 nm BFO-based/LSMO//STO. The well-saturated P-E hysteresis loops determine robust ferroelectric polarization for the three systems, with increased remnant polarization (P_r) upon Co integration, being $\sim 26 \mu\text{C}/\text{cm}^2$ for BFO, $\sim 60 \mu\text{C}/\text{cm}^2$ for BFCO30 and $\sim 53 \mu\text{C}/\text{cm}^2$ for La-BFCO30. Previous reports demonstrate that the magnitude of ferroelectric polarization can be modified because of lattice deformations,[303, 304] that in our case take place due to Bi and Fe-site cation substitution, as it has been discussed earlier in this Chapter from RSM-XRD analysis and as already reported in analogous BFCO systems.[122] Note that the P_r of La-BFCO30 is within the range of that of BFCO30, and minimal magnitude variations could be tentatively attributed to the differences in the lattice volume of the two compositions (see Table 3.2). Note that a similar behavior has also been identified in thicker (> 300 nm) La and Co-doped BFO polycrystalline films but with lower Co contents.[305, 132, 133] On the other hand, the enlarged coercive electric field (E_c) between pristine BFO (~ 160 kV/cm) and cation-engineered systems (BFCO30 ~ 370 kV/cm and La-BFCO30 ~ 250 kV/cm) could suggest the presence of defects within the film, which are lower in La-BFCO30 than in BFCO30. Owing to the robust and stable ferroelectric properties displayed in our La-BFCO30 films, the electric properties will be further evaluated in a device architecture in Chapter 4. Additionally, piezoelectric characterization has been carried out in 25 nm La-BFCO30/LSMO//STO systems to evaluate the local microscopic ferroelectric properties of the film. Figure 3.7 (b,c), shows the amplitude and phase signal images that have been collected after applying -8 V and +8 V in the regions indicated in panel (c). No voltage has been applied to the outer region, therefore it corresponds to the as-grown state. It can be observed that 180° phase contrast is obtained and that the amplitude signal at domain walls between domains written with opposite voltage is near zero. These results are indicative of the genuine ferroelectric nature of the observed contrast.[306, 307] The corresponding amplitude and phase signal loops depicted in Figure 3.7 (d,e) show butterfly and 180° hysteresis, respectively, also revealing the ferroelectric nature of the material.

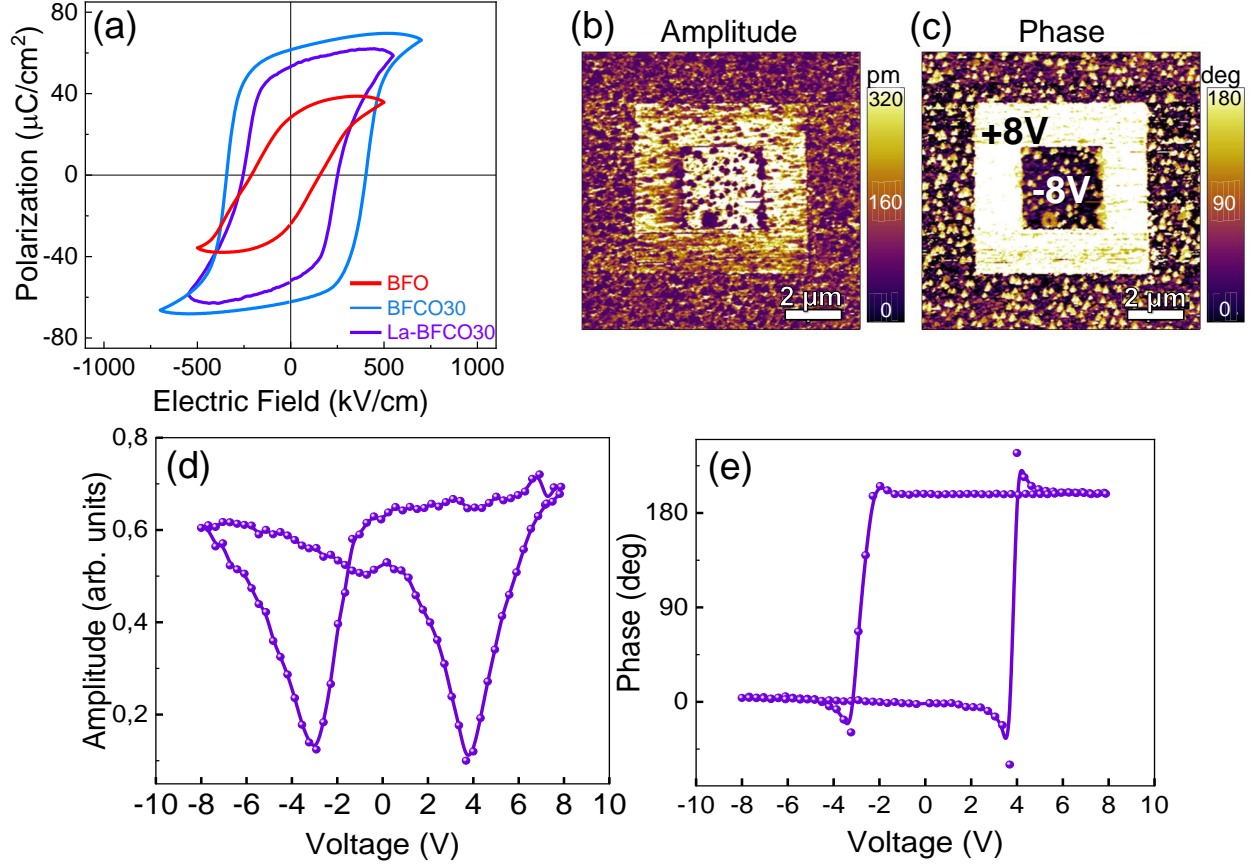


Figure 3.7: Macroscopic and local microscopic ferroelectric characterization. (a) Comparative P-E hysteresis loop obtained in 100 nm BFO, BFCO30 and La-BFCO30 films grown on LSMO//STO systems. (b,c) Amplitude and phase PFM images of 25 nm La-BFCO30/LSMO//STO films after electric lithography using -8 V and +8 V in the regions indicated in (c). The outer region corresponds to the as-grown state. (d,e) Corresponding amplitude and phase PFM loops.

3.2.5 First-principles studies

In order to characterize the synthesized materials also theoretically, a first-principles study based on density functional theory (DFT) has been performed on BFCO and La-BFCO solid solutions with 12.5 % and 25 % Co and 12.5 % La contents. Although such concentrations of substitutional atoms are not identical to the experimental ones (due to the constraints imposed by the size of the adopted simulation cell), and the limitations of DFT methods to predict exact energy bandgaps are well known,[308] it is expected that these theoretical results will be qualitatively meaningful and comparable to the experimental findings. For technical details refer to Section A3.1.3. To perform the DFT calculations and analysis, it has been adopted a low-symmetry rhombohedral-like phase presenting large anti-phase O₆

rotations along the three pseudo-Cartesian axes (i.e. similar to the BFO ground-state phase described by the space group $R3c$ [309] but with lower symmetry), following previous experimental and theoretical works.[310, 311] From all the possible Fe/Co B-site arrangements compatible with the adopted simulation cell, our sampling indicates that Co atoms tend to disperse homogeneously in the solution, meaning that the nearest neighbours of Co are Fe ions, as it is depicted in Figure 3.8 (a).

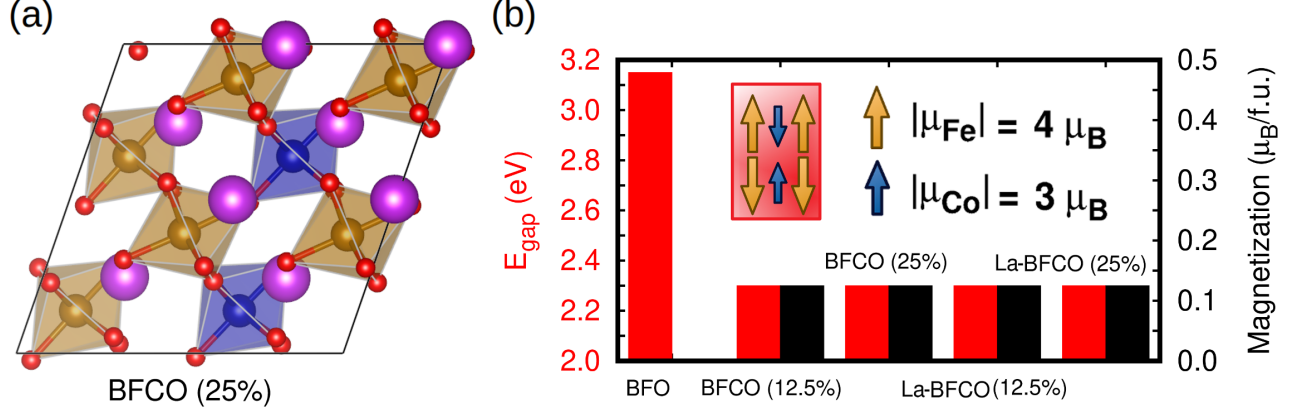


Figure 3.8: First-principles estimation of the structural, bandgap and magnetic properties of BFCO and La-BFCO systems. (a) Sketch of the employed solid-solution supercell with 25% Co content. Bi, Fe, Co and O atoms are represented with violet, yellow, blue and red spheres, respectively. (b) DFT estimation of the energy bandgap and total magnetization per formula unit (f.u.) of several BFCO and La-BFCO systems considering the presence of Co³⁺ ions only. The percentages within parentheses indicate the content of Co atoms.

The energy bandgap, E_{gap} and magnetic properties of several BFCO and La-BFCO solid solutions have been estimated and compared to those obtained for bulk BFO using analogous computational methods, Figure 3.8 (b). Overall, the DFT results are consistent with the experimental results explained above. In particular, the bandgap of the system is significantly reduced by $\sim 30\%$ with respect to that of pristine BFO as a consequence of Co substitution. As it was expected, the introduction of La atoms does not have any noticeable impact on E_{gap} because the corresponding $6s$ orbitals lie well below the Fermi energy level, as it will be explained below from partial density of electronic states in Figures 3.9 (a,b). From Figure 3.8 (b), it has been found that the analyzed solid solutions present a net magnetization of $\sim 0.1 \mu_B$ per formula unit at low temperatures, which is consistent with recent magnetic hysteresis loop measurements reported by Gao *et al.*[312] The origin of the estimated net magnetization is a magnetic spin imbalance between the Fe and Co sublattices. That is, the magnetic spins arrange antiferromagnetically but the individual Co magnetic moments are smaller than the Fe ones, a mechanism that is similar to what has been predicted recently for off-stoichiometric BiCoO₃ thin films.[313]

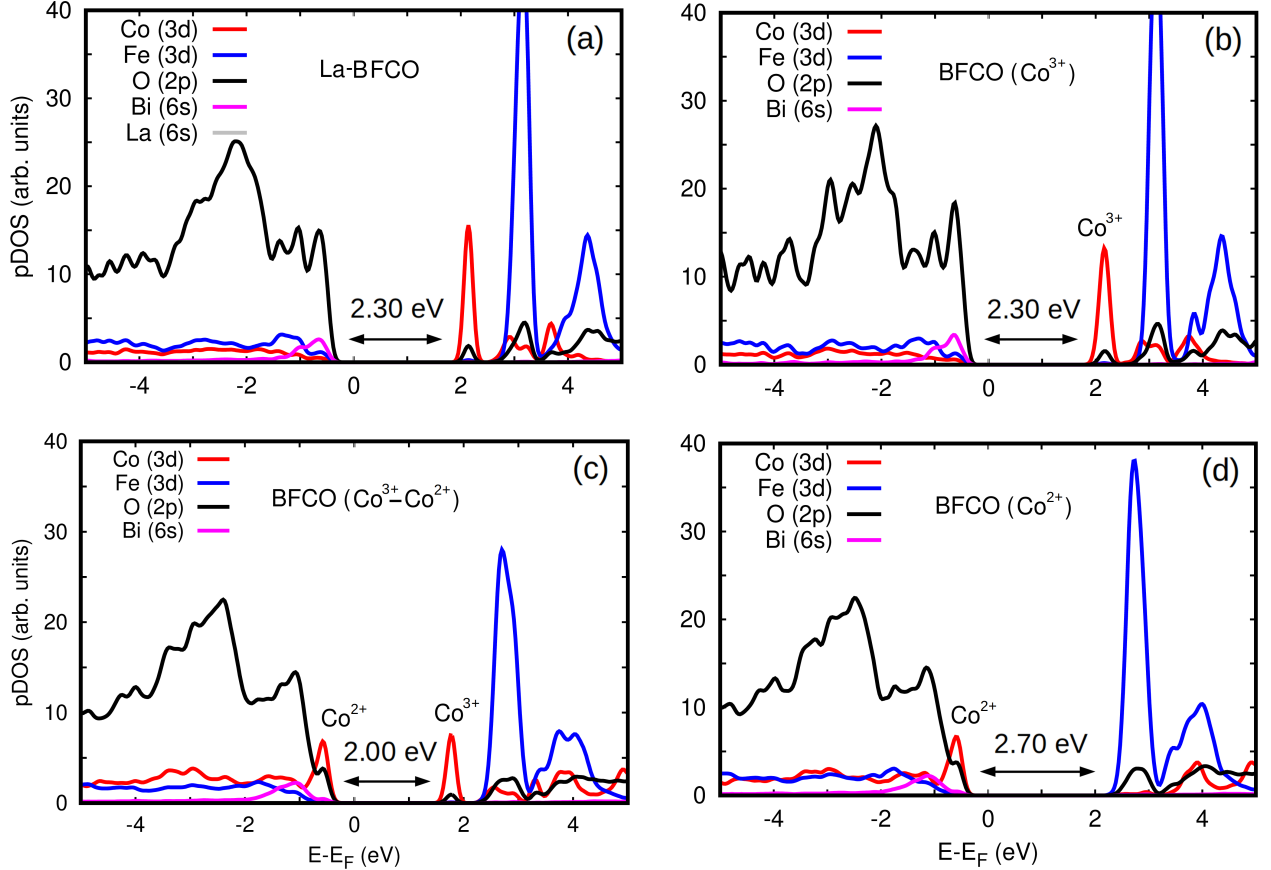


Figure 3.9: Partial density of electronic states for BFCO and La-BFCO systems with 25% of Co content estimated with DFT methods for different Co²⁺/Co³⁺ concentrations. (a) La-BFCO with Co³⁺ ions only. (b) BFCO with Co³⁺ ions only. (c) BFCO with both Co²⁺ and Co³⁺ ions. (d) BFCO with Co²⁺ ions only.

To gain further insight into the bandgap reduction observed in BFCO and La-BFCO solid solutions compared to pristine BFO, it has been analyzed the partial density of electronic states (pDOS) around the Fermi energy level, simulating three different charge scenarios for Co in BFCO, see Figure 3.9. In the DFT simulations of pristine BFCO systems, the oxidation state of Co ions has been identified as 3+. Nevertheless, upon the introduction of oxygen vacancies it is considered that the Co ions surrounding the point defects are reduced and consequently adopt the oxidation state 2+, as shown by an increase in the amount of charge occupying *d*-orbitals and by a decrease of $\sim 10\%$ in the corresponding magnetic moments. The electronic properties of Fe ions are hardly affected by the introduction of oxygen vacancies, which agrees with our XAS observations. In the simulated pristine BFCO system, Figure 3.9 (b), in which only Co³⁺ ions are present, it is observed a strong Fe/Co *d* and O *p* orbitals hybridization at the VBM and the appearance of a large pDOS peak corresponding to unoccupied Co *d* states at the minimum of the conduction band (CBM). When enough oxygen vacancies are introduced in the system

so that all the cobalt ions are Co²⁺, Figure 3.9 (d), the energy bandgap increases appreciably with respect to the pristine case due to an increase in the occupation of Co *d* electronic states at the VBM and the disappearance of the Co *d* pDOS peak at the CBM. Meanwhile, when both Co³⁺ and Co²⁺ ionic species coexist in the material, Figure 3.9 (c) a significant energy bandgap reduction follows from the simultaneous presence of Co *d* peaks at the VBM and CBM.

The qualitative discrepancy between XAS and DFT on whether the generation of Co²⁺ at the VBM or the existence of unoccupied Co³⁺ states are the origin of the bandgap change could be due to having considered an oversimplified scenario on the local symmetry of the BFCO system due to the large spin variability of the cobalt ions. In particular, high-spin was systematically identified as the energetically most favorable state for Co in the DFT simulations, but it could be possible that other intermediate and/or low spin configurations existed also in the solid solution.[314, 315] In future works, it will be interesting to clarify these important aspects on the magnetic properties of BFCO system.

Nonetheless, our first-principles results reproduce the experimentally observed influence of the relative population of Co²⁺/Co³⁺ ions on the optoelectronic properties of BFCO and La-BFCO solid solutions and could explain the superior functionality of Co-doped films as compared to pristine BFO that has already been reported from previous studies carried out in our group,[122] and that will be further explored in Chapter 4 in a device architecture.

3.3 Ce-doped BFCO thin films

Aiming to investigate the potential benefits that the double valence state of Ce cation could confer to the stability of BFCO30 system, the viability of Ce-substitution has been explored in 25 nm Bi_{0.9}Ce_{0.1}Fe_{0.7}Co_{0.3}O₃ (Ce-BFCO30) and compared to those of 25 nm BFCO30. Macroscopic ferroelectric measurements have been performed on 100 nm Ce-BFCO30 films.

Note that preliminary first-principles studies based on DFT, performed in collaboration with Dr. C. Cazorla (UPC), suggested that Ce-substitution in BFCO with Co loads of 25% could result in a strong decrease in the bandgap compared to pristine BFO,[122] see Figure 3.10. Technical details of the simulation can be found in Section A3.1.3. These predictions further encourage us to tackle the preparation of Ce- and Co-substituted BFO films.

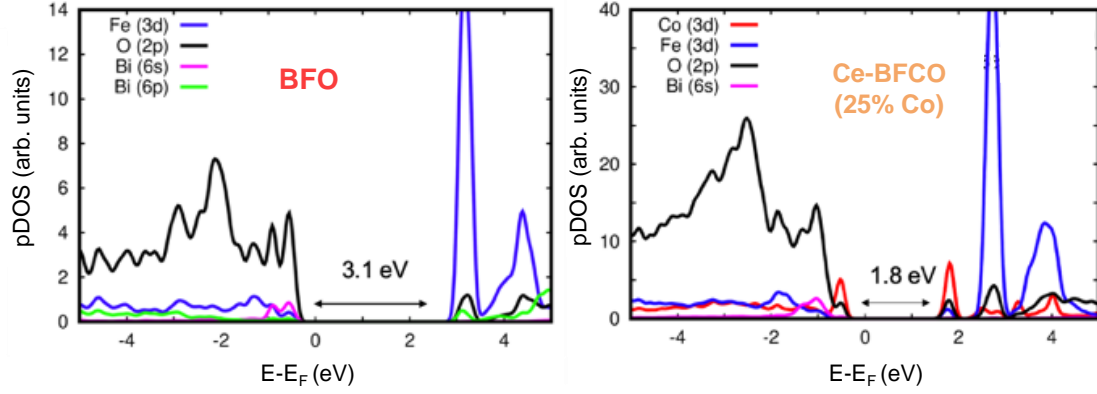


Figure 3.10: Partial density of electronic states for BFO and Ce-BFCO with 25% of Co content estimated with DFT methods.

3.3.1 Crystallinity, structure and surface morphology quality

The film crystallinity and phase purity of the BFO-based systems grown on (001)-STO have been evaluated by means of routine XRD θ - 2θ scan, Figure 3.1 (a). The presence of the (00l) Bragg reflections corresponding to BFO-based phases (asterisk) and STO substrate suggest a *c*-axis oriented growth for all the films. With the incorporation of Ce in BFCO30, the presence of Bi and Fe oxide rich secondary phases (grey square)[122] are suppressed. However, GIXRD analysis, disclosed the appearance of Ce and Co oxide rich phase upon Ce-doping, Figure 3.11 (b). This phase can be tentatively attributed to cubic Ce_{0.94}Co_{0.06}O₂, although subtle differences between theoretical and experimental 2θ position could occur due to minimal stoichiometric variations. Also, in this sample the intensity of the peaks corresponding to BFO-based reflections is less intense than in BFCO30. These results contrast with La-BFCO films in which more intense reflections were observed. It can be speculated that having a double oxidation state in Ce could lead to difficulties in the preparation of phase pure film, since Ce⁴⁺ can form thermodynamically stable cerium oxide phases.[316, 317]

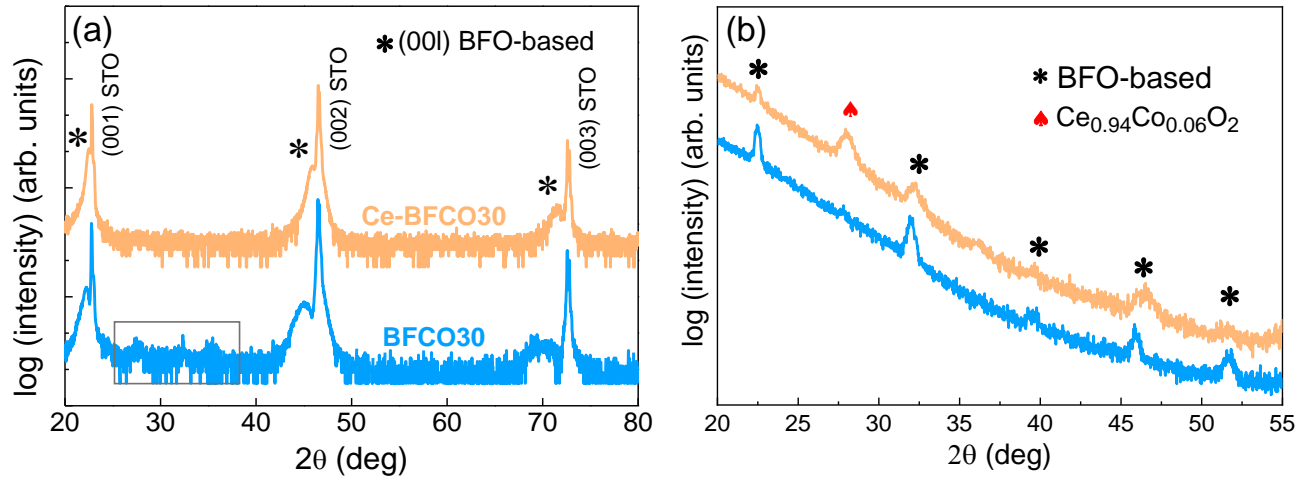


Figure 3.11: Crystallinity and phase purity of BFCO30 and Ce-BFCO30 grown on (001)-STO. (a) XRD θ - 2θ scan and (b) GIXRD θ - 2θ scan of the films.

In order to further investigate the film quality and the distribution of these secondary phases, a cross-sectional Z-contrast HAADF-STEM image of ~ 25 nm Ce-BFCO30//STO is presented in Figure 3.12 (a), depicting an heterogeneous film. While oriented crystalline growth of BFO takes place near the sharp interface with STO, a clear segregation of nanoparticles with diameter of 8 ± 2 nm is detected at the film surface. This scenario contrasts with that observed for La-BFCO30, where a clean surface without segregation of secondary phases was observed (Figure 3.2). The distribution of the O, Fe, Co and Ce atomic species has been evaluated by means of EELS mapping, Figure 3.12 (b). An homogeneous distribution of O is observed throughout the film. Conversely, the concentration of Fe primarily resides in the lower region of the film, resembling the distribution pattern of Bi atoms (not shown here), and confirming the presence of BFO phase near the interface with STO. On the other hand, a notable accumulation of Co and Ce atomic species appears at the upper region of the film, indicating their diffusion towards the surface. These observations align with the presence of the Ce and Co rich secondary phase identified in the GIXRD analysis. Moreover, based on the EELS mapping of Fe and Co atomic species, it can be suggested the formation of a Fe-Co rich oxide phase near the surface, which has not been detected by XRD, either because of the fluorescence effect of Fe when a Cu target is used in XRD analysis or because it may be amorphous and hence do not produce a diffraction pattern. Similar nanoparticle distribution has been previously observed in the preparation of YBa₂Cu₃O₇ nanocomposites with embedded CeO₂ colloidal nanoparticles.[318] It is suggested that the accumulation of nanoparticles at the film surface results from the pushing behavior of foreign particles.[319, 320]

The AFM topographic images of BFCO30 and Ce-BFCO30 are presented in Figures 3.12 (c,d), respectively. Clear differences are shown in the surface morphology of the films although they display similar rms roughness (~ 2 nm). The homogeneous surface of Ce-BFCO30 does not show crystallites-like morphology, what could be attributed to the presence of segregated nanoparticles at the film surface, in agreement with the cross-section presented in Figure 3.12 (a).

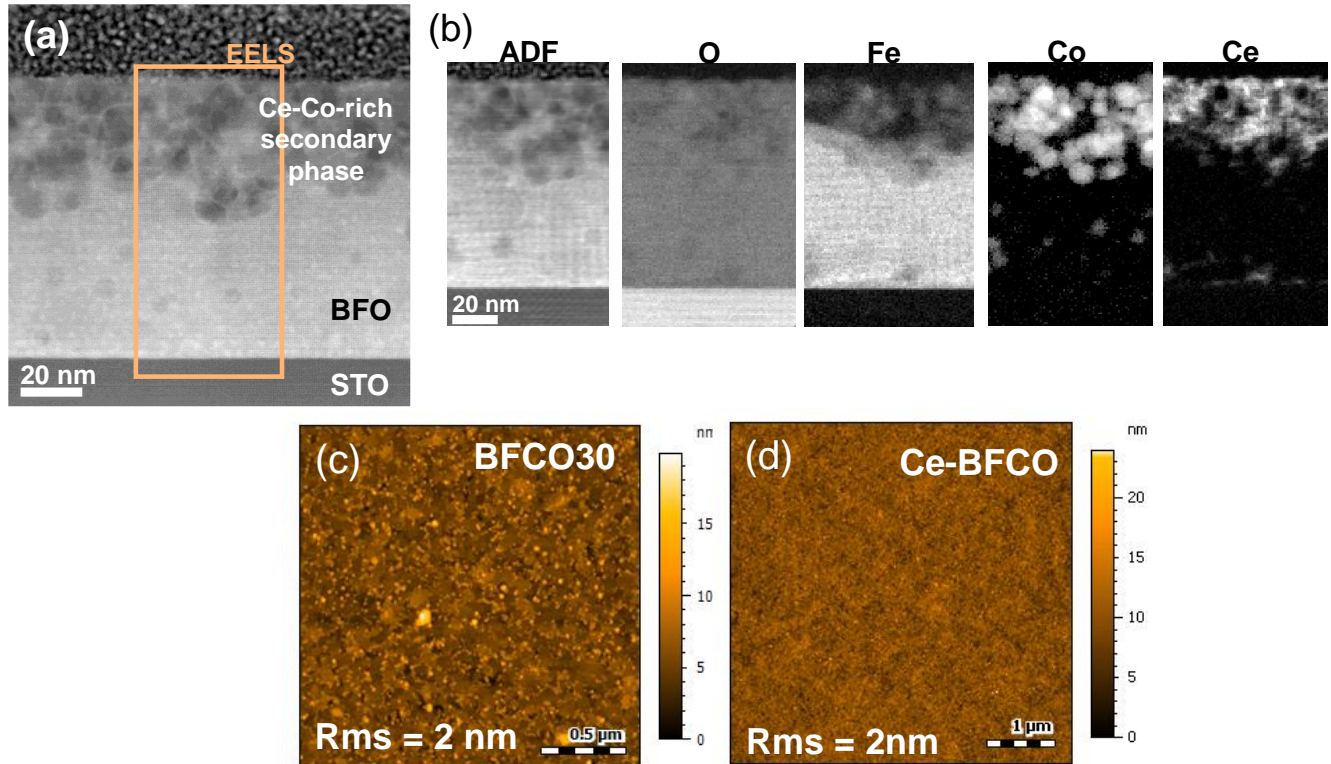


Figure 3.12: (a) Cross-sectional Z-contrast HAADF-STEM image of Ce-BFCO30//STO and (b) corresponding EELS mapping indicating the distribution of O, Fe, Co and Ce atomic species within the film. Note that ADF makes reference to Annular Dark Field image. Comparative $5 \mu\text{m} \times 5 \mu\text{m}$ AFM topographic images of (c) BFCO30 and (d) Ce-BFCO30.

On the basis of these results, an exhaustive study has been conducted to optimize the growth conditions of Ce-BFCO30 and avoid the segregation of secondary phases. With this purpose, several strategies have been explored, including the modification of the solution chemistry formulation and the thermal process, i.e. heating and cooling ramps and atmosphere, see Section A3.2.1. However, despite these efforts, the presence of secondary phases at the film surface persisted, as evidenced by the GIXRD analysis in Figure A3.3.

From these observations, it can be concluded that from the chemical solution formulations investigated

in this work, Ce is not incorporated in the BFCO30 structure and results instead on the segregation of more thermodynamically stable Ce-Co oxide nanoparticles to the film surface. Therefore Ce-doped BFCO30 films have been discarded for its integration on a PV device. The optical and ferroelectric properties of this inhomogeneous system can be found in Section A3.2.2.

3.4 Conclusions

In this Chapter it is presented a thorough study on the double cation substitution in the photoferroelectric perovskite BFO prepared by means of CSD through intermixing precursor salts. A series of cobalt-doped BFO (BFCO) compositions have been prepared. We have identified that the bandgap shift upon Co doping is mostly attributed to the Co 3*d* hybridization with O 2*p* and the coexistence of Co²⁺ and Co³⁺ species, while Fe 3*d* remains unchanged upon substitution, as supported by first-principles calculations. Importantly, the benefit of substituting Bi by La in BFCO30 has demonstrated to be twofold. (i) It helps improving stabilization of metastable BFCO30: epitaxial La-BFCO30 films are successfully obtained in which La is homogeneously distributed throughout the film thickness. (ii) The reduced optical bandgap values and electric polarization obtained in Co-doped BFCO are preserved in this co-substitution. On the other hand, inhomogeneous films with strong segregation of secondary phases result from Ce-doping in BFCO30 system. Therefore the size and oxidation state of the substituting cation are key to promote the stability of the film.

Overall, this work offers a solid strategy to improve BFO compositions with large cobalt loads, which are compatible to be integrated in PV systems.

Additionally, the multiferroicity of this new La-BFCO composition could be explored to go beyond simple photovoltaic devices envisaging new computing memories, optomechanical devices and detectors.

Chapter A3

Annex Information of Chapter 3

A3.1 La-doped BFCO thin films

A3.1.1 Valence band spectra

The peaks in the binding energy range of 3 eV to 10 eV are due to O $2p$, Fe $3d$ and Bi $6s$ occupied states, while the peak near the valence band maximum, in the range from 1 eV to 3 eV is due to the Co^{2+} occupied states, Figure A3.1. The shape of the valence band spectra clearly shows the effect of the Co doping, with the increase of the feature at the valence band maximum (VBM), i.e. near to 2 eV binding energy (attributed to the O $2p$ - Co $3d$ occupied states).

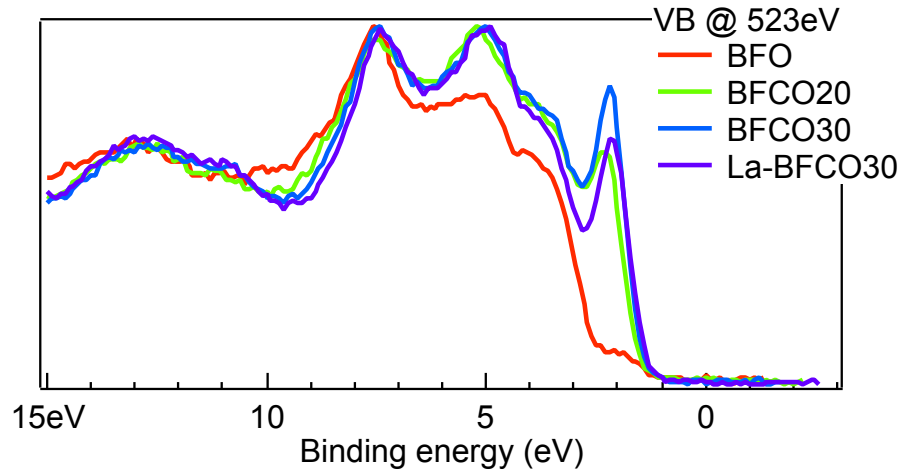


Figure A3.1: Valence Band spectra of the BFO-based films with varying doping measured with a photon energy of 523 eV.

A3.1.2 Ferroelectric properties

Piezoelectric characterization has been performed in 25 nm BFCO30/LSMO//STO films, see Figure A3.2. Similar results to those shown for the La-BFCO30 sample are obtained, indicating no jeopardization of ferroelectricity upon La-doping.

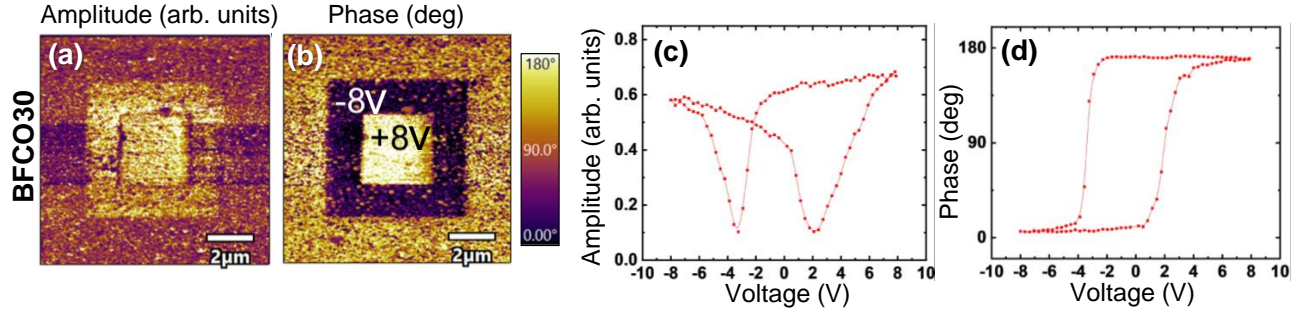


Figure A3.2: PFM characterization of 25 nm BFCO30/LSMO//STO. (a) Amplitude and (b) phase PFM images after electric lithography using -8 V and +8 V. Note that the lithographed regions are marked in phase figures and the outer region corresponds to the as-grown state. Corresponding (c) amplitude and (d) phase PFM loops.

A3.1.3 First-principles study based on DFT method

Spin-polarized density functional theory (DFT) calculations were performed by Dr. Cesar Menéndez and Dr. Claudio Cazorla using the generalized gradient approximation proposed by Perdew, Burke and Ernzerhof (PBE) as implemented in the VASP package.[321, 322] The “Hubbard- U ” scheme derived by Dudarev *et al.* was employed for the description of Co and Fe 3d electrons by adopting a U value of 6 and 4 eV, respectively. [323, 309] The “projected augmented wave” method[324] was used to represent the ionic cores by considering the following electronic states as valence: Co $4s^1 3d^8$, Fe $3p^6 4s^1 3d^7$, Bi $6s^2 5d^{10} 6p^3$, La $6s^2 5d^1 5p^6 5s^2$ and O $2s^2 2p^4$. An energy cut-off of 800 eV and a Γ -centered \mathbf{k} -point grid of $6 \times 6 \times 6$ were employed for a $2 \times 2 \times 2$ simulation cell containing 40 atoms, thus obtaining zero-temperature energies converged to within 0.5 meV per formula unit. Geometry relaxations were performed for an atomic force threshold of $0.005 \text{ eV} \cdot \text{\AA}^{-1}$.

The effects of chemical disorder were addressed by generating all possible atomic Co - Fe and Bi - La arrangements in the adopted 40-atoms supercell. The energetically most favorable magnetic ordering was determined for each configuration by considering the four possible magnetic spin arrangements compatible with our simulation cell (that is, ferromagnetic and antiferromagnetic of type A, C, and G).[323, 309] Off-stoichiometric systems were generated by removing one oxygen atom from all possible

apical and equatorial positions in the 40-atoms simulation cell,[325] thus rendering the general chemical composition $\text{Bi}_{1-y}\text{La}_y\text{Fe}_{1-x}\text{Co}_x\text{O}_{2.875}$. In order to obtain accurate electronic band structure and band gap results, a range-separated hybrid DFT calculations were performed with the *HSE06* exchange-correlation functional on the equilibrium geometries determined previously with the PBE potential.[326] The electric polarization of stoichiometric $\text{Bi}_{1-y}\text{La}_y\text{Fe}_{1-x}\text{Co}_x\text{O}_3$ systems were estimated with the Born effective charges method.[327, 328] In this approach, the electric polarization is calculated with the Equation A3.1.3.

$$P_\alpha = \frac{1}{\Omega} \sum_{i=\kappa\beta} Z_{\kappa\beta\alpha}^* u_{\kappa\beta}$$

where Ω is the volume of the cell, κ runs over all the atoms, $\alpha, \beta = \text{x,y,z}$ represent the Cartesian directions, u_x is the displacement vector of the κ -th atom as referred to a non-polar reference phase, and Z_κ^x the Born effective charge tensor calculated for a non-polar reference state. It is worth noting that recently it has been shown that the estimation of electric polarization of $\text{BiFe}_{1-x}\text{Co}_x\text{O}_3$ solid solutions with such a perturbative and computationally feasible method turns out to be very accurate.[327]

A3.2 Ce-doped BFCO thin films

A3.2.1 Solution chemistry and processing conditions optimization

On the basis of the results observed in Figures 3.11-3.12, an exhaustive study has been conducted to optimize the growth conditions of Ce-BFCO30 and improve the film quality, i.e. reduce the segregation of parasitic secondary phases at the surface. With this purpose, several strategies have been explored, including the modification of: (i) the solution chemistry by the use of acetylacetone and N-N-dimethylformamide to stabilize the solution [289] (among others,described below), (ii) heating and cooling ramps (3 °C/min - 1200 °C/min) and (iii) atmosphere (O_2 vs N_2) during the crystallization process. However, despite these efforts, the presence of secondary phases at the film surface persisted, as evidenced by the GIXRD analysis in Figure A3.3.

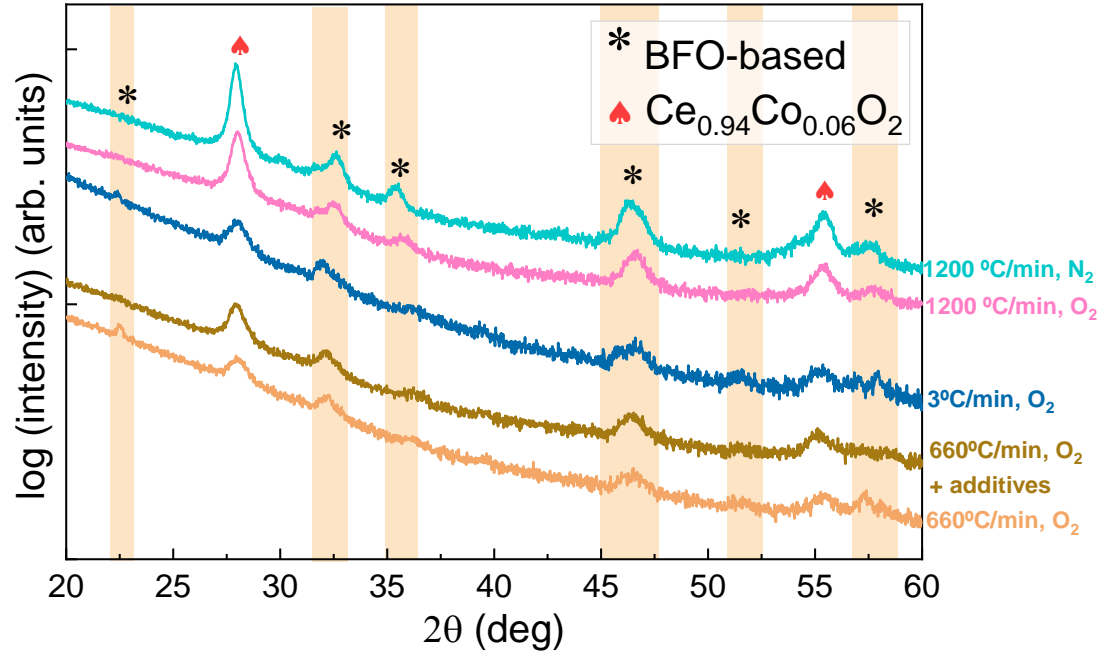


Figure A3.3: GIXRD analysis of Ce-BFCO30 thin films grown on STO. The corresponding optimization strategies are indicated at the left of the Figure.

It is worth noting that when evaluating the influence of the solution chemistry on film purity, other strategies were initially explored. On one hand, in the metal nitrates route it was also considered the use of water as solvent and citric acid as chelating agent to minimize condensation reactions.[329] Moreover, a mixed metal nitrate-metalorganic route was evaluated by using Ce acetate and Ce acetylacetonate as metal precursors instead of Ce nitrate. Additionally, a metalorganic route was also explored by using only Bi, Ce, Fe and Co acetates and/or acetylacetonates metal precursors and acetic acid and water as solvents. Nevertheless, in all cases, highly unstable solutions that precipitated immediately after their preparation were obtained, which could not be used for film deposition.

A3.2.2 Optical and electrical properties

In order to learn from this inhomogeneous Ce-BFCO30 system, the optical and electrical properties have been investigated and compared to BFO and BFCO30 films.

The optical properties have been also evaluated from spectroscopic ellipsometry. Regarding the index of refraction spectra, the intensity of the two spectral features characteristic of metal and oxygen charge-

transfer transitions at ~ 320 eV and ~ 440 eV of Ce-BFCO30 resemble that of BFCO30. However the position of these transitions is modified with Ce-doping, similarly to the scenario observed for La-doping. On the other hand, the optical absorption coefficient spectra of Ce-BFCO30 is similar to that of pristine BFO, Figure A3.4 (b), as it could be expected from the STEM analysis of Figure 3.12, where it has been revealed that neither Ce nor Co integration occurs in the perovskite film.

In addition, the Tauc plots for direct $(\alpha h\nu)^2$ transitions (inset)[259] are presented, where a bandgap decrease in Ce-BFCO30 with respect to BFO is displayed. It can be tentatively considered that the subtle variations observed between pristine BFO and Ce-BFCO30 could be attributed to the presence of nanoparticles at the film surface, which could absorb near the red or infrared region of the solar spectra and contribute to alter the optical properties of the whole system.[330, 331]

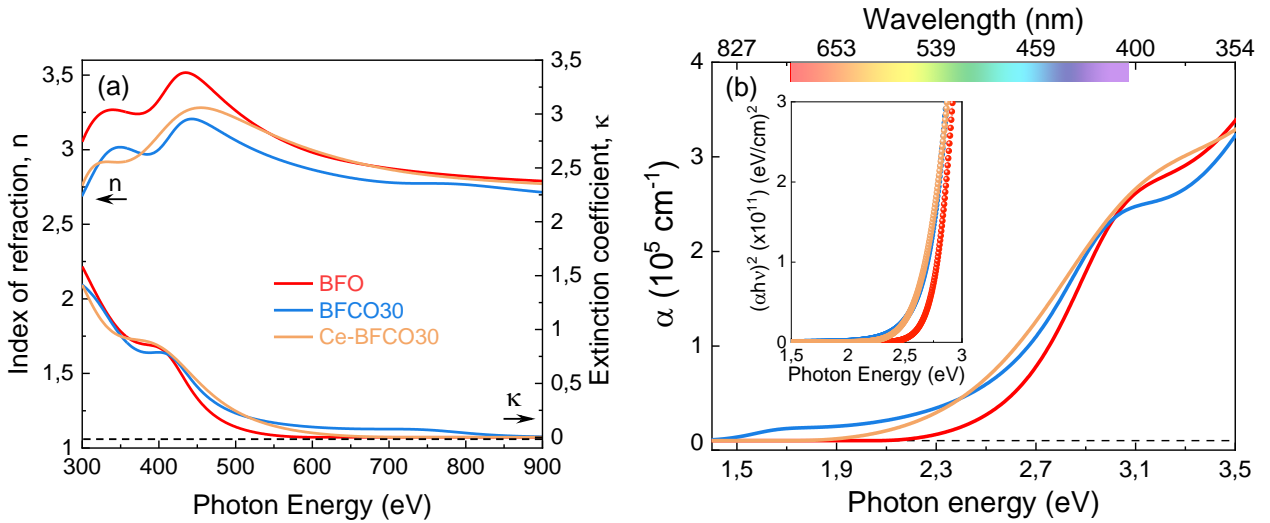


Figure A3.4: Optical properties of BFO, BFCO30 and Ce-BFCO30 thin films grown on STO substrate extracted from spectroscopic ellipsometry. (a) n and κ optical constants, (b) absorption coefficient, α , and $(\alpha h\nu)^2$ Tauc plots for direct transition energies (inset).

The macroscopic ferroelectric properties at room temperature and in dark conditions of Pt/100 nm Ce-BFCO30/LSMO//STO systems have been evaluated and compared to that of BFO, BFCO30 systems, in Figure A3.5. The corresponding P-E hysteresis loops show robust ferroelectric polarization, however for Ce-BFCO30 they are not well-saturated at high electric fields. This shape suggests that the ferroelectric response is merged with other phenomena such as leakage currents that can lead to an overestimated value of P_r . [332, 272] Indeed, current density, J , vs electric field measurements carried

out in dark conditions (inset) reveal higher leakage currents in both BFCO30 and Ce-BFCO30 systems compared to pristine BFO, which are probably related to the presence of secondary phases as well as structural and/or charge defects (Fe^{2+} , Ce^{4+} and oxygen vacancies).[122] Consistently, the significantly enlarged E_c in Ce-BFCO30 (~ 830 kV/cm) compared to BFO (~ 160 kV/cm), BFCO30 (~ 370 kV/cm) and La-BFCO30 ($E_c \sim 250$ kV/cm), confirms the presence of these defects. In this leaky system, the P_r value of Ce-BFCO30 is extracted from the ferroelectric switching peaks in the current density-electric field (J-E) hysteresis loops,[333] see Figure A3.6. From this method, the positive and negative P_r are $70 \mu\text{C}/\text{cm}^2$ and $-74 \mu\text{C}/\text{cm}^2$, respectively, which are within the range of that of BFCO30 ($61 \mu\text{C}/\text{cm}^2$ and $-63 \mu\text{C}/\text{cm}^2$).[122]

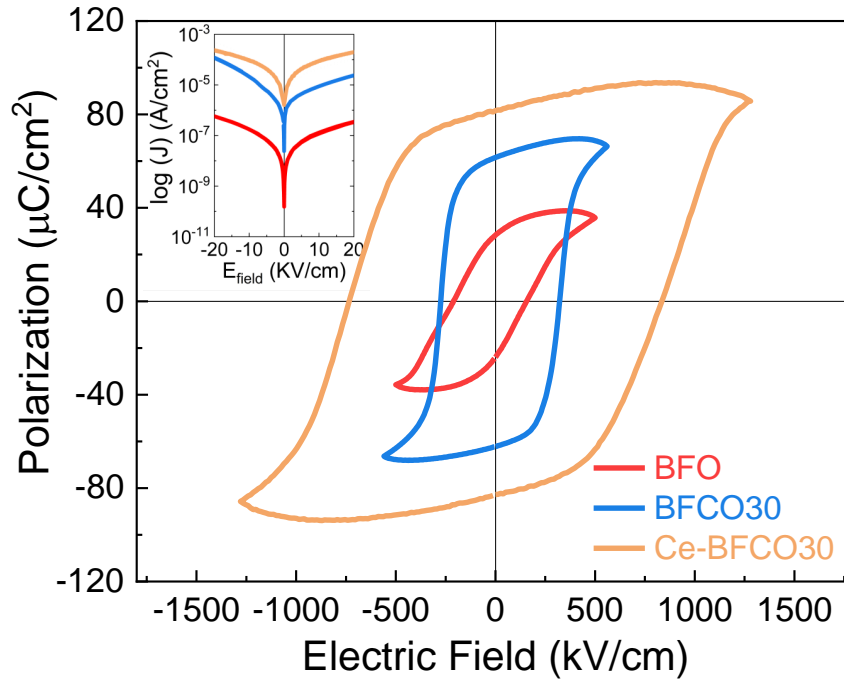


Figure A3.5: P-E hysteresis loops for BFO, BFCO30 and Ce-BFCO30 thin films grown on LSMO//STO. Inset shows comparative leakage current density measured in dark conditions.

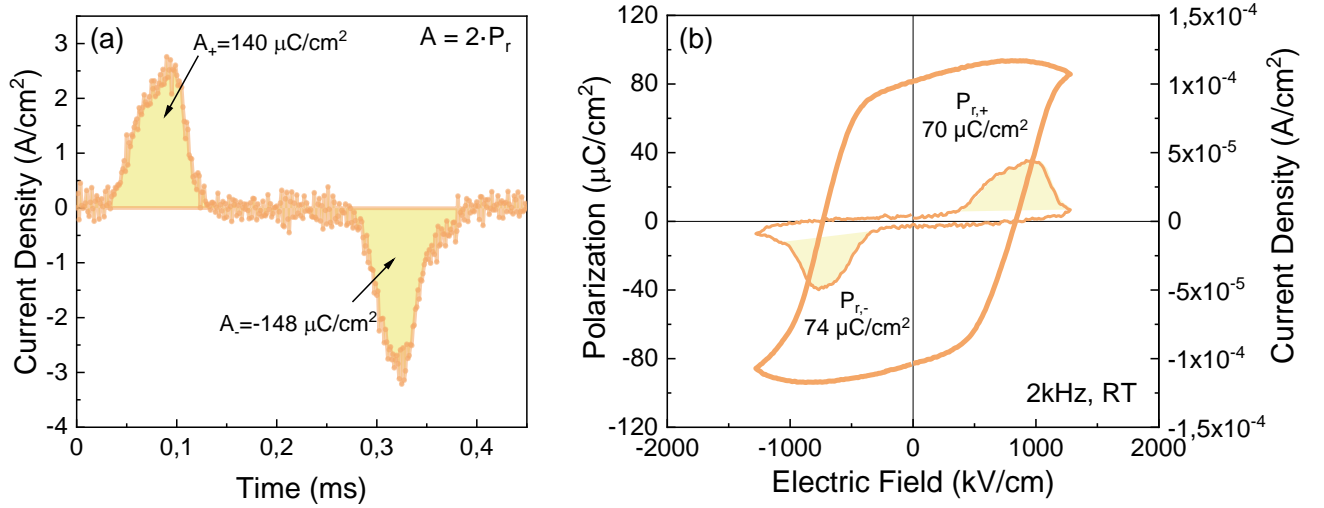


Figure A3.6: Macroscopic ferroelectric characterization: P_r calculation in Ce-BFCO30. J-time and (b) J-E loop measured at room temperature, in dark and at 2 kHz. Polarization values for positive and negative switching, evaluated from the area (A) underneath the switching peak integrated with time ($A \sim 2 \cdot P_r$, where P_r is the remnant polarization) are $70 \mu C/cm^2$ and $-74 \mu C/cm^2$, respectively.

Chapter 4

Interface engineering in all-oxide photovoltaic heterostructures based on cation-substituted BiFeO_3 photoferroelectric thin films

In the previous Chapter, cation engineering strategies have been explored to tune the functional properties of BFO. However, the optimal device configuration is yet to be reported. The hunt for materials that promote efficient charge transport along the device while retaining chemical, structural, optical and electrical compatibility, i.e. interface engineering, is an essential but highly challenging task to explore in photoferroelectric perovskite oxide films. In this Chapter, we explore the implementation of an all-oxide and stable thin film device based on epitaxial $\text{BiFe}_{0.9}\text{Co}_{0.1}\text{O}_3$ (BFCO10) thin films, prioritizing the use of chemical deposition techniques. The device architecture consists of sandwiching the epitaxial BFCO10 photoabsorber between two oxide electrodes: Sn-doped In_2O_3 (ITO) and $\text{La}_{0.7}\text{Sr}_{0.3}\text{MnO}_3$ (LSMO). The main focus is placed on the role to include ZnO electron transport layer on the device performance. Therefore, the envisaged device configuration is: $\text{ITO}/(\text{ZnO})/\text{BFCO10}/\text{LSMO}/\text{STO}$.

As a proof of concept, a device based on two-site substituted BFO (La-BFCO10) has also been fabricated and tested.

The film crystallinity, surface morphology, optical and (ferro)electrical properties of the devices are thoroughly examined by X-ray diffraction, atomic force microscopy, UV-Vis spectroscopy, FE polarization

loops and current density-voltage characteristics, respectively. Also, X-ray photoelectron spectroscopy analysis is used to sketch the energy band diagram of the heterostructures and further comprehend the role of ZnO in the device and its impact in the ultimate photoresponse properties.

Finally, pioneering investigations towards the preparation of compositional gradient BFCO thin films have been carried out envisaging potentially improved light absorption and charge carriers transport through the device. The structure, morphology, elemental distribution, optical, photo- and ferroelectric properties are studied.

4.1 Introduction

All-oxide photovoltaics (PV), envisaging a solar cell entirely based on thin film oxides, emerges as an attractive approach to complement the current PV technologies. In addition to high stability, low toxicity and the possibility of facile and cost-effective processing, it also offers versatility in structure and composition allowing the engineering of the physical properties.[26, 50] In this regard, ferroelectric (FE) perovskite oxide-based solar cells have sparked a great deal of interest due to their unconventional PV mechanism which could open the possibility to surpass the fundamental efficiency limits of traditional semiconductors using simplified device architectures.[66, 67] Additionally, the FE polarization switching of these materials could offer an extra mechanism to modulate, and potentially reverse, the charge transport properties via changes in the height of the Schottky barriers and in the internal electric field, due to polarization induced depoling field.[64, 68, 74, 75, 78, 82, 276] BiFeO₃ (BFO) has been largely investigated as lead-free light absorber with relatively narrow bandgap (~ 2.7 eV) and high FE polarization at room temperature [91, 92, 93, 94, 95] but it only allows to harvest 8-20% of the solar spectrum. Different strategies based on engineering the BFO layer have been evaluated to boost the device performance,[65, 108, 135, 137, 138, 139, 140, 141, 144], however PV efficiencies still remain low.[94] Beyond the exploration to improve the properties of the BFO layer itself, interface engineering is required to promote the travelling and collection of charge carriers to the electrodes, as previously demonstrated in emergent PV technologies.[334, 335] For this purpose, some candidates have been tested to optimize the interfaces of BFO. The most popular choice is ZnO, either as thin film [166, 172, 168] or nanostructure,[115, 173] delivering moderate improvement in short circuit current density (J_{sc}) and open circuit voltage (V_{oc}). Other architectures involving transport layers such as WS₂ [174, 175] and reduced-graphene oxide, [176] have also been investigated, although the material dissimilarity can add

complexity in the device integration and processing.[177] This is of particular relevance when epitaxial BFO films are investigated[135, 139] because the layers underneath should promote epitaxial growth and stand high temperature treatments. Consequently, the number of studies on interface engineering in epitaxial BFO systems are rather scarce and are poorly understood.[178]

Another strategy to improve the light absorption and extract the photogenerated carriers is the design of photoabsorbers with vertical composition profile, as demonstrated in organic, kesterite and CIGS emergent solar cells.[145, 146, 147] This approach aims to study the possibility to achieve a gradual modulation of the bandgap along the photo-active film, which could potentially offer two key advantages: (i) extend the light absorption to a broader region of the solar spectrum compared to single-compositional films [146] and (ii) generate a gradient of the electro-chemical potential, which is equivalent to the generation of an additional built-in electric field.[82] The latter could enhance the transport of electrons and holes towards appropriate electrodes and reduce recombination.[153] The influence of discrete versus compositional gradient on the functional properties of photoferroelectrics is still to be determined, and the complexity is transferred to the fabrication of the gradient itself.

Herein, we aim to bring better understanding on the role of interface engineering in epitaxial BFO-based heterostructures designing an all-oxide device to facilitate component integration and long-term device stability, prioritizing the use of cost-efficient deposition techniques. In particular, it is investigated the solution processed BiFe_{0.9}Co_{0.1}O₃ (BFCO10) photoferroelectric active layer, which shows suitable optical bandgap and high remnant FE polarization at room temperature.[122] The envisaged configuration is: top electrode/20 nm ZnO/100 nm BFCO10/bottom electrode, where 70 nm Sn-doped In₂O₃ (ITO) and 10 nm La_{0.7}Sr_{0.3}MnO₃ (LSMO) are the top and bottom electrodes, respectively, see Figure 4.1. The stack is grown on SrTiO₃ (STO) single crystal substrates to promote the epitaxial growth of the LSMO bottom contact and BFCO10. Details on the synthesis procedure is described in Experimental Section 2.1.1 and 2.1.2. Note that film thickness for ITO and ZnO was optimized to 70 and 20 nm, respectively, based on the optical and electrical properties, see Figures A4.2 and A4.3 of Annex Information. The analogous system with no ZnO is also fabricated for comparison. Ultimately, as a proof of concept, devices with La-BFCO and compositional gradient BFCO have also been investigated. The film crystallinity, surface morphology, optical properties as well as the ferroelectricity, photoresponse and energy band alignment are thoroughly studied for these disruptive systems.

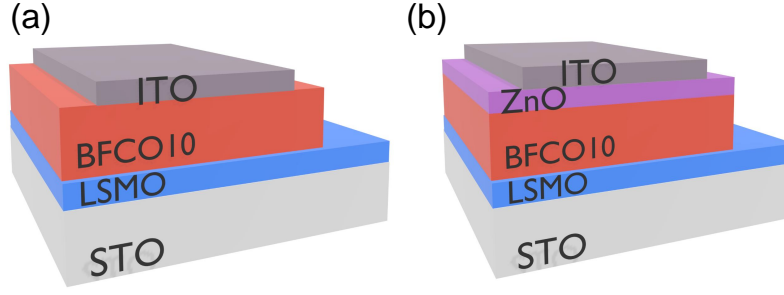


Figure 4.1: Sketch of the studied all-oxide architectures (a) ITO/BFCO10/LSMO//STO and (b) ITO/ZnO/BFCO10/LSMO//STO.

4.2 Results and discussion

4.2.1 Crystallinity and surface morphology

Starting the study with BFCO10 photoabsorber, the film crystallinity and surface morphology have been investigated for the two systems here studied and depicted in Figure 4.1: ITO/BFCO10/LSMO//STO and ITO/ZnO/BFCO10/LSMO//STO, Figure 4.2. The XRD θ - 2θ studies on the complete devices show three Bragg reflections corresponding to (002) STO substrate ($2\theta = 46.5^\circ$), (002) LSMO bottom contact ($2\theta = 47.2^\circ$) and (002) BFCO10 ($2\theta = 45.9^\circ$), suggesting c -axis oriented growth for BFCO10 and LSMO, Figure 4.2 (a). Note that the experimental out-of-plane lattice parameter, c , for 100 nm BFCO10 is ~ 3.95 Å, indicating a fully relaxed film.[122] Additional 2D XRD $\theta - \chi$ scans confirmed the textured growth of BFCO10 on LSMO. The absence of Bragg reflections for ZnO and ITO layers is expected according to the film thickness and deposition conditions,[336, 337] see Figure A4.1. On the other hand, from the AFM topography images it is observed that the optimized sequential growth results in smooth and homogeneous surfaces. From the deposition of ZnO it can be identified the formation of discrete, small and rounded-like grains. Nonetheless, the average rms roughness is ~ 2.3 nm for all the films, Figure 4.2 (b-e).

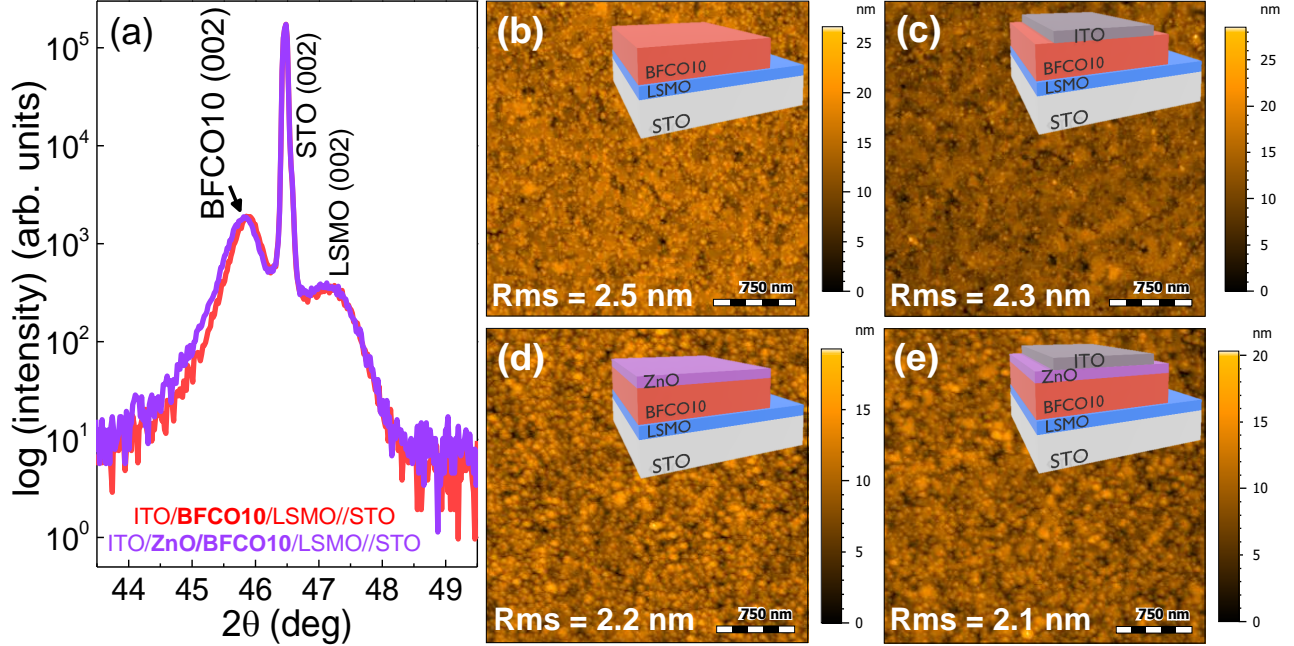


Figure 4.2: (a) XRD θ - 2θ scan of ITO/BFCO10/LSMO//STO and ITO/ZnO/BFCO10/LSMO//STO. AFM topography images of (b) BFCO10 on LSMO//STO, (c) ITO on BFCO10/LSMO//STO, (d) ZnO on BFCO10/LSMO//STO and (e) ITO on ZnO/BFCO10/LSMO//STO.

4.2.2 Optical properties

The optical properties of the oxide architectures have been studied by UV-Vis spectroscopy transmittance (%T) curves, and transmittance map simulations have been prepared using the transfer matrix method to identify the optimal film thickness of ITO and ZnO for maximum transparency,[338] see Figure A4.2. From these studies, it is observed that the light transmission in the visible is maximized with the incorporation of 70 nm ITO and 20 nm ZnO. This phenomenon is characteristic of these top coatings and suggests an anti-reflective effect that could potentially improve the device efficiency.[339, 340, 341, 342]

4.2.3 Photoresponse and ferroelectric properties

To evaluate the influence of ZnO on the performance of the all-oxide heterostructures, photoresponse measurements in virgin state (i.e. measured as prepared) are carried out. A monochromatic laser of 405 nm and irradiance of 350 mW/cm² is used to illuminate from the top of ITO electrode, see the device configuration sketched in Figure 4.3 (a). The time-dependent J_{sc} is measured in dark and under laser illumination for ~ 10 s, exhibiting stable and fast photoresponse under light that significantly increases

upon the integration of ZnO, Figure 4.3 (b).

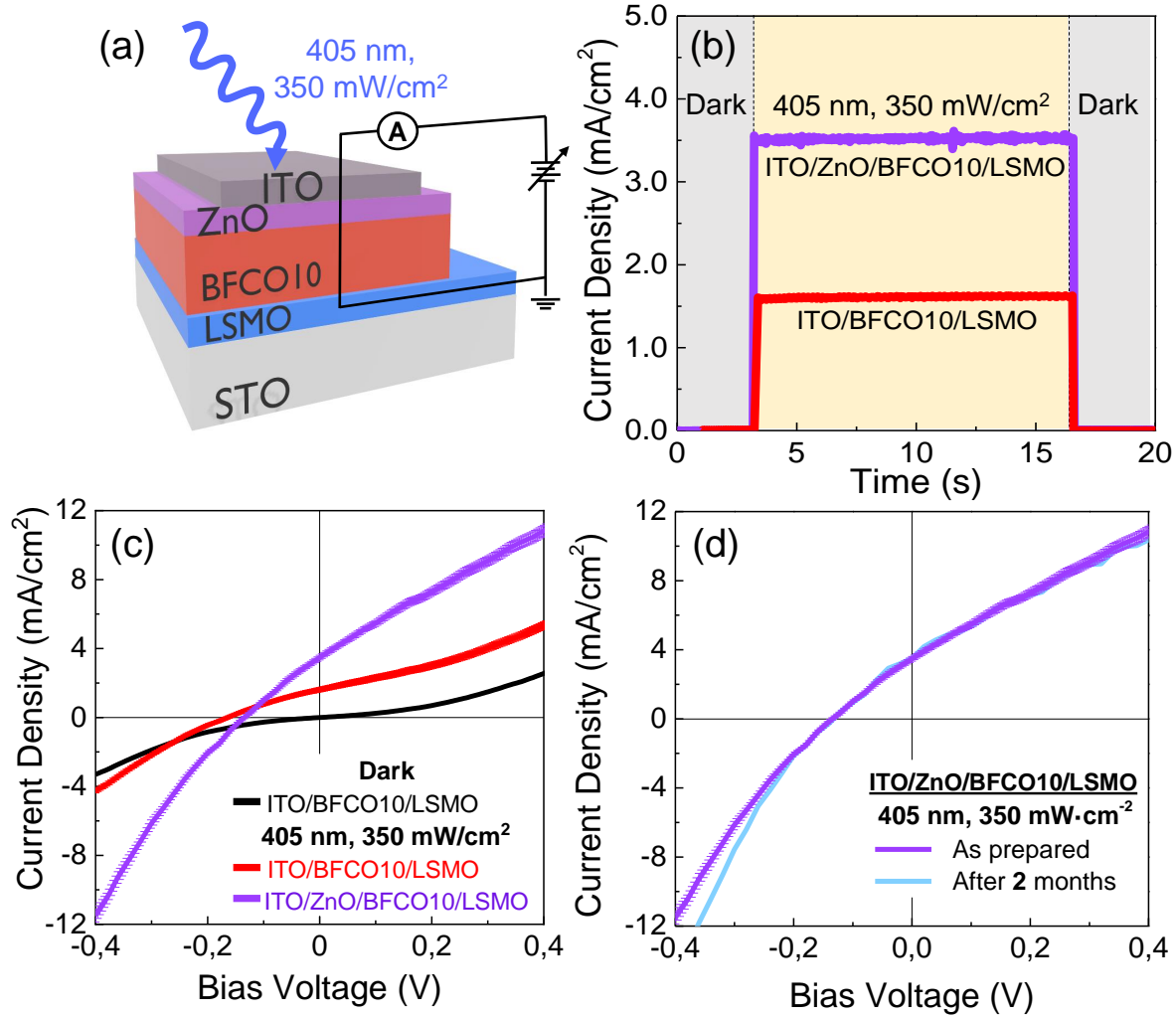


Figure 4.3: (a) Sketch of the electrical configuration used to measure the photoresponse of BFCO10-based systems. (b) Time-dependent J_{sc} and (c) J-V characteristic curves of ITO/BFCO10/LSMO//STO (red) and ITO/ZnO/BFCO10/LSMO//STO (purple). (d) Comparative J-V curves of ITO/ZnO/BFCO10/LSMO//STO measured in a time interval of two months to test the operational stability of the sample.

Figure 4.3 (c) shows the current density-voltage (J-V) characteristics in dark and under illumination, revealing a diode-like shape as well as a clear photovoltaic response upon illumination, consistent with the design of an asymmetric and rectifying junction. Similar behaviour has been reported in analogous epitaxial BFO and doped-BFO heterostructures.[92, 108] The resulting J_{sc} , V_{oc} and incident photon to current efficiencies (IPCE) are presented in Table 4.1. Note that IPCE has been calculated from Equation 2.17. There are clear differences in the magnitude of J_{sc} being 1.6 mA/cm² for bare-BFCO10 and 3.5 mA/cm² for ZnO/BFCO10 system. Notoriously, the ~ 2.2 times increased J_{sc} observed for

the ITO/ZnO/BFCO10 system leads to IPCE of up to 4.4%. In order to rule out the possibility that J_{sc} improvements arose from the photogeneration in ZnO instead of in BFCO10,[343, 172] J-V curves have been collected in the ITO/ZnO/LSMO//STO system under the same measuring conditions, Figure A4.4. The observed linear dependence that passes through J-V axes origin (and the same slope) both in dark and under illumination, clearly indicates that no photogeneration occurs in ZnO. In addition, the operational stability of the BFCO10 devices with no encapsulation at ambient conditions has been monitored for 2 months displaying reproducible performances, Figure 4.3 (d). This confirms the high stability and robustness of the all-oxide BFCO10 devices and contrasts with that of the non encapsulated hybrid perovskites.[344] On the other hand, the integration of the ZnO interface to BFCO10 does not improve the V_{oc} of the device whose value modestly shifts from -0.19 V in the ITO/BFCO10 system to -0.14 V in ITO/ZnO/BFCO10. These results are at odds with previous reports of polycrystalline BFO-based systems in which the incorporation of ZnO enhanced both J_{sc} and V_{oc} .[168, 169, 172, 173] This behavior will be studied in more detail below by sketching the energy band diagram of our system.

Table 4.1: Comparison of J_{sc} , V_{oc} and IPCE parameters from J-V characteristics of ITO/BFCO10/LSMO//STO and ITO/ZnO/BFCO10/LSMO//STO all-oxide systems measured in virgin state.

System	J_{sc} (mA/cm ²)	V_{oc} (V)	IPCE (%)
ITO/BFCO10/LSMO//STO	1.6 ± 0.1	- 0.19	2.0
ITO/ZnO/BFCO10/LSMO//STO	3.5 ± 0.1	- 0.14	4.4

The macroscopic FE properties of the heterostructure with and without ZnO have been evaluated. Figure 4.4 (a) shows the FE polarization-electric field (P-E) and the current density-electric field (J-E) hysteresis loops recorded at 2 kHz in dark and room temperature conditions. The presence of current switching peaks in J-E confirms the FE character and the nearly rectangular shape of the P-E loops indicates low leakage through the heterostructure.[75, 116, 117] Large remnant polarizations (P_r) along the (001) pseudocubic direction of $\sim 68 \mu\text{C}/\text{cm}^2$ are displayed for virgin BFCO10 films with no interface engineering and with ZnO interface. Remarkably, the exhibited P_r values are higher than those found in the analogous solution-processed system with top metallic contacts, Pt/BFCO/LSMO//STO, [122] disclosing that the interface engineering with ITO/ZnO does not degrade the ferroelectric performance.

In the two heterostructures here studied, the negative and positive coercive electric field (E_c) are ~ -370 kV/cm and ~ 530 kV/cm, respectively, indicating that the P-E loops are strongly shifted towards the positive voltage direction, and revealing the presence of an imprint electric field (E_{imp}) of 160 kV/cm pointing towards the top electrode. The observed asymmetry in the P-E loop could be attributed to the asymmetric top-bottom contact configuration of our systems.[79] In fact, P-E and J-E hysteresis loops measurements have been performed at a lower frequency using a symmetric top-top configuration, that is contacting only ITO electrodes, revealing no signatures of imprint electric field, see Figure A4.5, as it has been previously reported for ferroelectric BaTiO₃ films.[79] Additionally, to rule out the existence of heating effects upon light exposure, J-E and P-E loops have been recorded under illumination at 405 nm (not shown here), exhibiting little to no changes in the FE properties of the system.

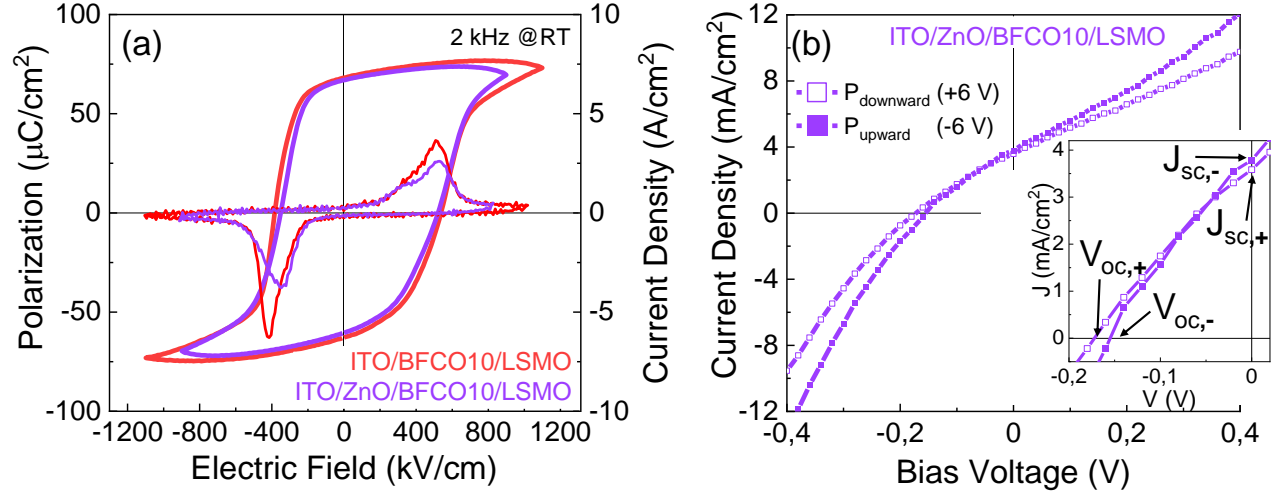


Figure 4.4: (a) J-E and P-E hysteresis loops recorded at 2 kHz and room temperature for the two studied systems and (b) J-V curve of ITO/ZnO/BFCO10/LSMO//STO heterostructure collected under illumination after downward (+6 V) and upward (-6 V) pre-polarization with a time delay of ~ 10 s.

In an attempt to investigate the role of FE polarization on J-V curves, further measurements have been carried out on the best performing ZnO/BFCO10-based device by inducing different polarization states to BFCO10. According to the E_c found in the P-E loops, triangular pre-poling voltages (V_{poling}) of ± 6 V were applied to ITO top electrode for 200 ms to induce the upward (-6 V) and downward (+6 V) polarization states. The polarization state is defined upward if polarization direction points to the top electrode and downward if it points to bottom electrode. After that, the J-V curves were

measured under illumination with a long delay time of ~ 10 s, see Figure 4.4 (b). For further details refer to Experimental Section 2.3.2. It is first noted that J-V curves remain in the same quadrant after pre-polarizations, identifying that the current flow is not reversed due to polarization switching. Similar behavior was reported in other studies using a FE semiconductor as the central light-absorber of heterostructures that presented strong imprint electric fields.[76, 92, 171]

From Figure 4.4 (b) it is extracted that the polarization switching only changes J_{sc} and V_{oc} by 5.3% and 9.7% respectively, see summary in Table 4.2. This mild modulation is attributed to the use of long time-scale measurement after applying the V_{poling} which favors the back-switching of the FE domains because of the presence of imprint fields.[80, 81]

Table 4.2: Comparison of J_{sc} , V_{oc} and IPCE from J-V characteristic of ITO/ZnO/BFCO10/LSMO//STO system measured in upward and downward polarization states ($V_{poling} \pm 6$ V) with a time delay of ~ 10 s.

Polarization state	J_{sc} (mA/cm ²)	V_{oc} (V)	IPCE (%)
Upward (-6 V)	3.8	- 0.15	4.8
Downward (+6 V)	3.6	- 0.17	4.5

Therefore, to minimize the back-switching effects, determination of J_{sc} at different V_{poling} up to ± 6.5 V has been carried out using a shorter delay time, 0.1 s, see Figure A4.6. These measurement conditions reveal that J_{sc} can be largely modulated (~ 68 %) if the photocurrent dependence with ferroelectric switching is traced at the appropriate delay time, as anticipated by Sheng et al.[80, 276]

4.2.4 Energy band alignment determination

Now, with the aim to unravel the differences observed in photoresponse between the two systems (Figure 4.3), the energy band diagrams have been extracted for both systems by means of XPS measurements. First, the transition metal oxide "bulk-like" layers, ITO, ZnO, BFCO10 and LSMO, have been investigated by measuring the valence band maxima (VBM) and the binding energy of the characteristic core levels (In 3*d*, Sn 3*d*, Zn 2*p*, Bi 4*f* and Sr 3*d*) relative to the VBM,[276] Figure A4.7. See Experimental 2.3.3 for the details of the samples measured for the bulk-like properties. Note that the extracted VBM values and binding energies are in agreement with those reported in the literature for the films with the

same composition and prepared using the same deposition techniques.[284, 278, 345, 346, 347, 348, 349, 350]

Then, the four different interfaces have been prepared and investigated (BFCO10/LSMO, ITO/BFCO10, ZnO/BFCO10 and ITO/ZnO), see Experimental Section 2.3.3. Following a similar methodology, XPS spectra of the selected core levels together with the valence band were probed and compared to the core level binding energies of the single layer, Figure A4.7. It was observed that the intensities of the core levels for the buried layers dropped compared to the single layers but it still allowed to identify the binding energy positions. In order to construct the band diagram, the measured optical bandgaps of BFCO10 (2.6 eV) and ZnO (3.4 eV) have been used whereas the fundamental bandgap has been chosen for ITO (2.8 eV).[278, 351] A schematic representation of the energy band structure focusing at the ITO/BFCO10 and ZnO/BFCO10 interfaces is depicted in Figure 4.5. First, it turns out that the ZnO/BFCO10 interface shows a larger valence band offset (VBO) (-2.6 eV) than ITO/BFCO10 (-2.04 eV). On the other hand, the VBO extracted for LSMO/BFCO10 interface is -0.54 eV, see Figure 4.5. According to that, a built-in potential calculated from XPS measurements ($V_{BI,XPS}$) of + 0.16 eV emerges across the ZnO/BFCO10/LSMO whereas a $V_{BI,XPS}$ of +0.26 eV is calculated for ITO/BFCO10/LSMO, both with the same sign ($V_{BI,XPS} > 0$), see details in Annex Section A4.4. Based on these values, it would be expected that the current will flow from the top to the bottom electrode and should be $J_{sc} > 0$. In this line, the voltage required to cancel this photogenerated current, i.e., V_{oc} , should be < 0 . This data agrees well with the experimental results obtained from the J-V curves in Figure 4.3 in which $J_{sc} > 0$ and $V_{oc} < 0$.

From this study it is likely that the large VBO generated at the engineered ZnO/BFCO10 system could favor the observed increase in J_{sc} by blocking back recombination of holes.[352] Then, regarding the comparison of the calculated values for $V_{BI,XPS}$ with the experimental V_{oc} , the $V_{BI,XPS}$ (ITO/BFCO10/LSMO) is faintly larger than $V_{BI,XPS}$ (ZnO/BFCO10/LSMO) and is consistent with the small variation identified in V_{oc} from J-V, see Table 4.1. Nonetheless, this difference is significantly smaller than that reported for ZnO/polycrystalline BFO heterostructures.[172] This variation could be tentatively attributed to differences in ZnO film thickness and the use of different thin film deposition technique which both have been reported to affect the device performance. [172, 353, 354, 355]

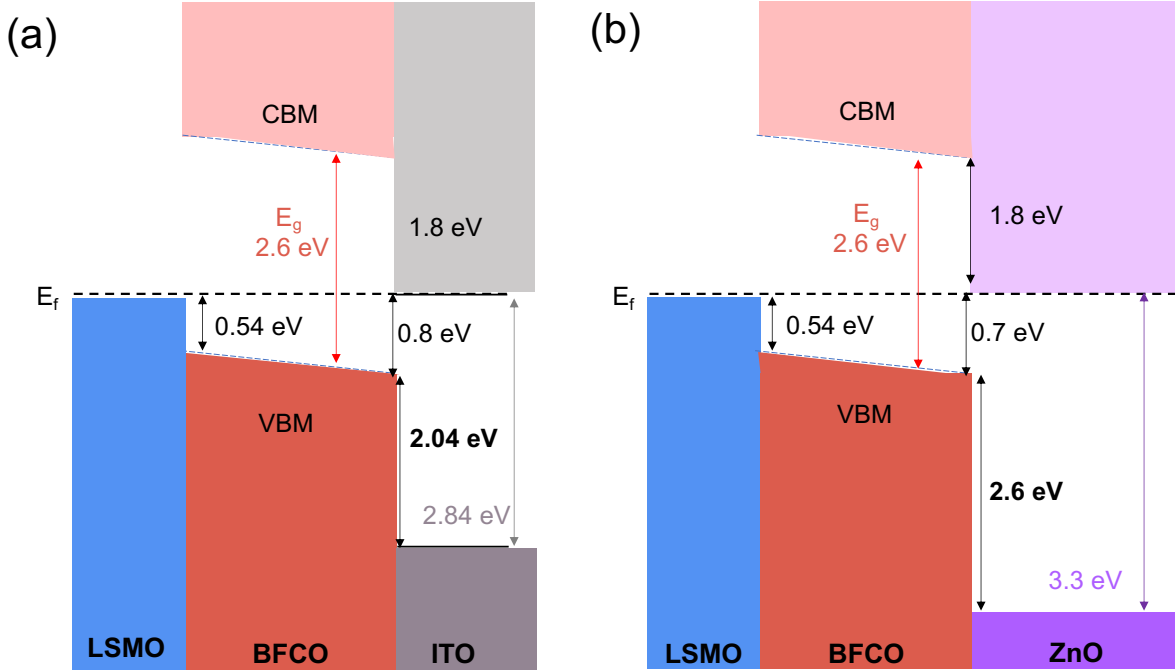


Figure 4.5: Schematic representation of the resulting energy band structure of the XPS referred to the Fermi level. The VBM positions at the interfaces were determined by the binding energy of selected core levels. The relative CBM position was determined from the bandgap. Heterojunction of (a) ITO/BFCO10/LSMO and (b) ZnO/BFCO10/LSMO.

4.2.5 Influence of cation co-substitution in BFO on the photoresponse

According to the knowledge generated from cation co-substitution in BFO films (Chapter 3) and the influence of interface engineering investigated in this Chapter, here it is explored the behavior of La-BFCO when integrated in the above optimized all-oxide photovoltaic device. For a better comparison with the results presented in this Chapter, the composition of the photoabsorber has been fixed at Co = 10%, La_{0.1}Bi_{0.9}Fe_{0.9}Co_{0.1}O₃ (La-BFCO10).

Figure 4.6 shows the comparative J-V characteristics of BFCO10 and La-BFCO10 films integrated into the heterostructure: ITO/ZnO/photoferroelectric/LSMO//STO and collected under illumination at 405 nm and 350 mW/cm² and in virgin state. Whereas little to no change is exhibited in J_{sc} (~ 3.5 mA/cm²), a significant increase of V_{oc} is displayed upon La-doping, reaching absolute values of up to 0.37 V. Performance improvement has also been previously reported in vacuum-deposited 5% La-substituted BFO.[168] This behavior has been attributed to the partial inhibition of Bi³⁺ cation volatilization that

reduces the number of Bi vacancies in the film, and hence, the amount of defects that can potentially act as charge recombination centers. Consistently, J-V characteristics acquired in dark (see inset in Figure 4.6) reveal lower leakage currents for La-BFCO10 than BFCO10 system, hence suggesting lower presence of defects upon La-substitution, in line with previous reports on solution-processed 5% La-doped BFO [356, 357] and on Sm-doped BFCO system (Sm 2.5% and Co 5%).[130] Therefore, here it is speculated that the observed increase in V_{oc} for 10% La-doped BFCO10 could be triggered by the better quality of the photoabsorber which can then provide better interface quality and both contribute to reduce the charge recombination centers.[177] On that regard, note that it has already been demonstrated by AFM topography images that the roughness of the films is improved upon La-doping (Figures 3.4 and 4.2).

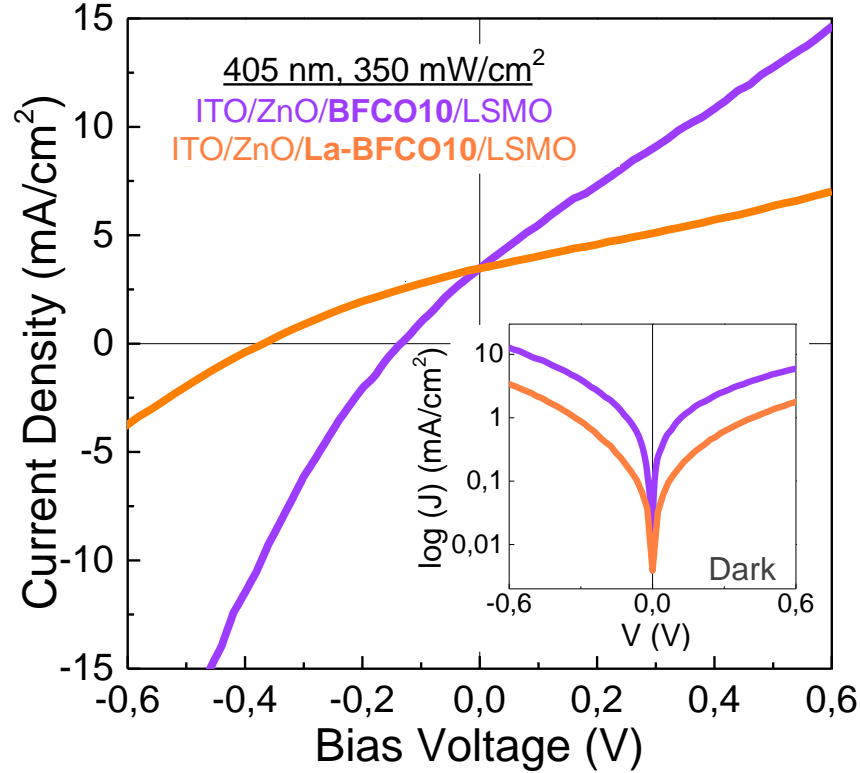


Figure 4.6: Comparative J-V curves collected in virgin state to study the photoresponse of photoferroelectric BFCO10 and La-BFCO10 films in ITO/ZnO/photoferroelectric/LSMO//STO heterostructures. The inset shows the J in dark conditions (i.e. leakage current).

Overall, La-BFCO10 is a stable and attractive composition with improved photovoltages and re-

duced leakage currents compared to BFCO10 and could open the avenue for broad applications in PV and optoelectronic devices.

4.2.6 Compositional gradient in BFCO photoabsorber

Building on the ability to tune the bandgap in BFO through cobalt doping, Chapter 3 and Ref.[122], additional efforts have been dedicated to explore new designs of BFCO photoabsorber based on the preparation of vertical gradient distribution of cobalt within BFO. The aimed gradient would be to achieve a gradual increase of Co concentration from the substrate surface to the top of the BFO surface (from wider to narrower bandgap) in order to maximize the light absorption. For the preparation of these films, two chemical deposition methodologies have been combined, namely CSD and ALD. Benefiting from the control of Co composition in BFO achieved by CSD, multideposition of BFO and BFCO with different cobalt loads has been assessed, see Figure 4.7 (a,b). In parallel, the uniqueness of the layer-by-layer growth of ALD has been combined with CSD. The aimed systems are: CSD-BFO layers alternated with ALD-CoO_x nanolaminates with different thickness, see Figure 4.7 (c,d). Since the mobility of the species within the film during the thermal treatment is not known, four different scenarios have been designed and listed below:

- (a) **CSD1**: BFCO20/BFCO20/BFO/BFO//STO
- (b) **CSD2**: BFO/BFCO10/BFCO20//STO
- (c) **CSD-ALD1**: BFO/11 nm CoO_x/BFO/1.5 nm CoO_x/BFO/0.5 nm CoO_x/BFO//STO
- (d) **CSD-ALD2**: BFO/1 nm CoO_x/BFO/1 nm CoO_x/BFO/1 nm CoO_x/BFO//STO

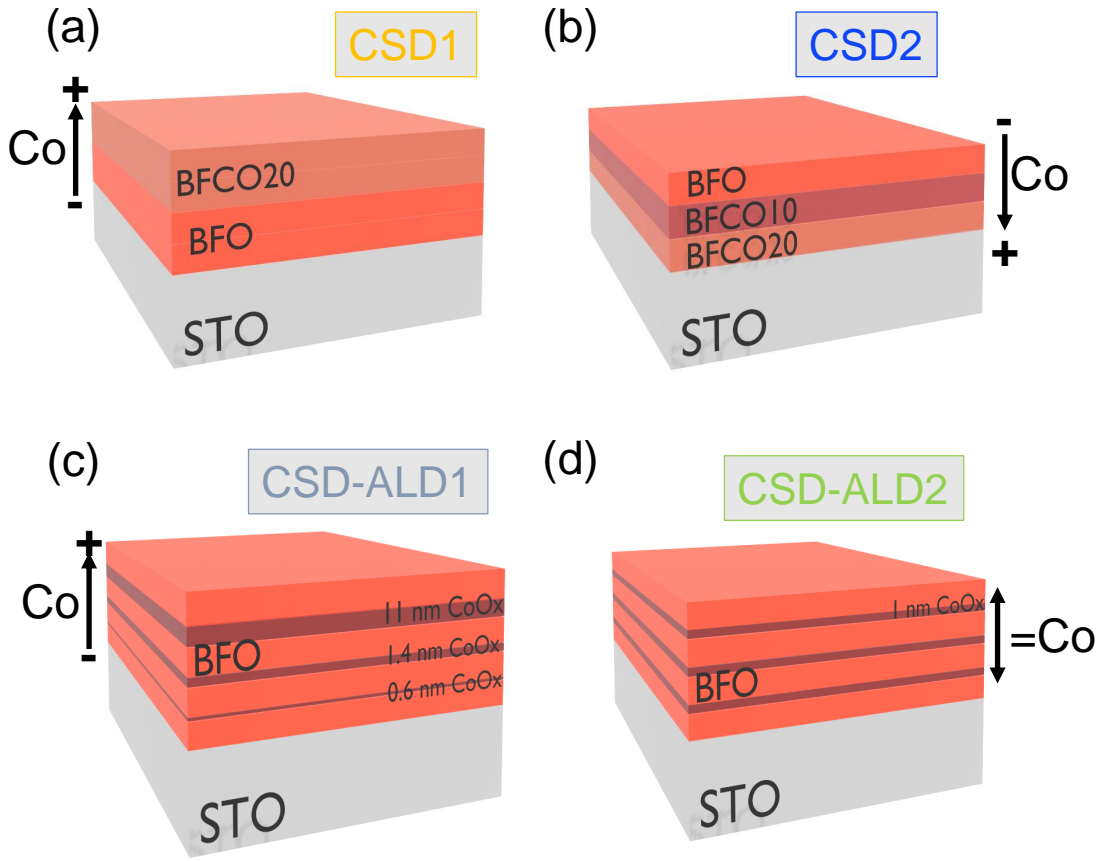


Figure 4.7: Sketches of the prepared architectures from (a,b) CSD and (c,d) CSD-ALD methodology. Note that for CSD-processed BFCO thin films, the Co loads specified for each layer refer to the solution stoichiometry. The photoactive films have been grown on (001)-STO substrate.

The crystallinity and phase purity of the different multi-composition systems grown on bare (001)-STO has been studied by means of XRD and compared to that of single-composition BFCO10 with the same thickness. The corresponding θ - 2θ scans indicate c -axis orientation in all the perovskite films, Figure 4.8 (a). Bismuth and iron rich oxide secondary phases (Bi_2O_3 and $\text{Bi}_{25}(\text{Fe},\text{Co})\text{O}_{40}$)[122] can be observed between 28° - 33° for CSD2, CSD-ALD1 and CSD-ALD2 samples. According to the knowledge generated from the La-BFCO doping study, here it could be proposed to use the same strategy to minimize the formation of these secondary phases (Chapter 3), however due to lack of time, this could not be investigated in this thesis. Returning to θ - 2θ scans, closer look at the (002) BFCO Bragg reflection, Figure 4.8 (b), reveals differences in intensity and 2θ position. The films identified with secondary phases also show lower (002) BFCO intensities. Notoriously, CSD2 is the sample with the least intense reflections which was initially designed with higher cobalt concentration at the bottom part of

the film. This is not surprising considering the experienced difficulty to stabilize high quality BFCO films with high cobalt loads.[122] Focusing on the subtle variations in 2θ positions, they could be attributed to BFCO films with different degree of Co incorporation. It is important to note that BFCO10 and CSD1 show almost the same 2θ position and intensity of (002) reflection, what indicates similar average degree of Co substitution and similar film crystallinity. Nevertheless, the cobalt distribution within the film can not be inferred from this characterization. Note that from Figure 4.8 (b) it is identified an obvious difference from the width of the (002) STO reflection for CSD2. This is attributed to the use of a different diffractometer (*Bruker D8 Discover A25*) to measure this sample. Unfortunately, this sample was could not be remeasured with the equipment used for the rest of the series (*Siemens D-5000*).

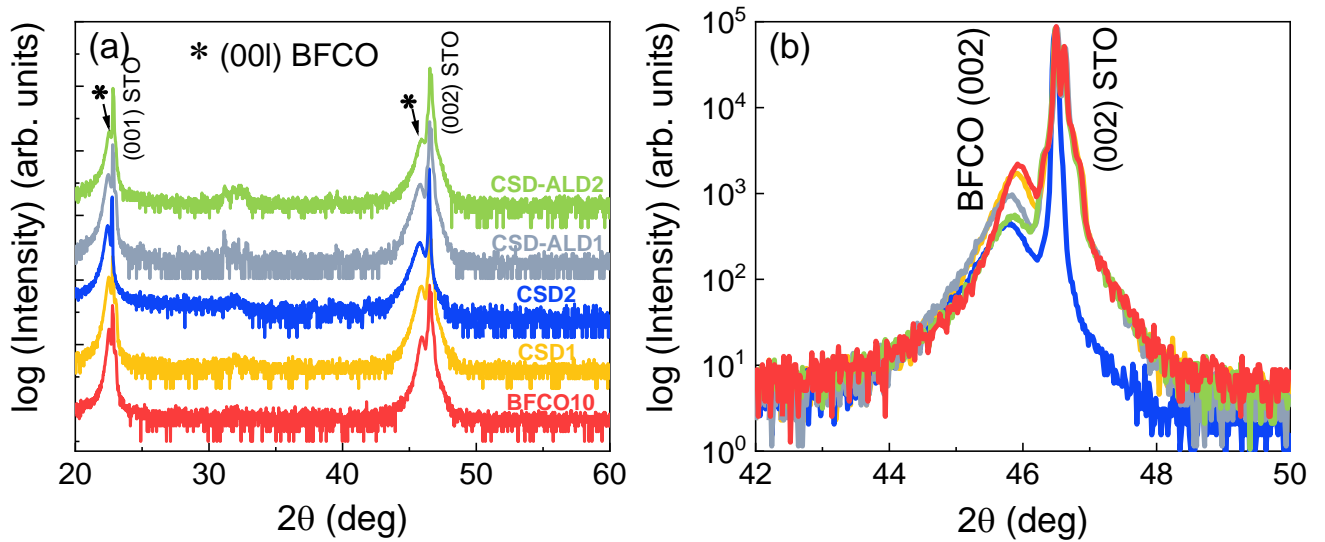


Figure 4.8: (a) XRD θ - 2θ scan of CSD-BFCO10 and compositional gradient BFCO-based thin films from CSD and CSD-ALD methodologies grown on (001)-STO. (b) Zoom of the θ - 2θ scan scan around the (002) BFCO and (002) STO Bragg reflections to observe differences in the intensity and 2θ position of the peaks. The code color is the same as in (a). The shape disparity of (002) STO peak in CSD2 is attributed to the use of a different XRD diffractometer for the measurement of this sample.

The surface morphology has been evaluated from samples grown on LSMO-buffered STO substrates by means of SEM, Figure 4.9. The gradient BFCO film derived from CSD1 exhibits a rather homogeneous and precipitate-free surface morphology with localized pores, similar to what was observed for BFCO10.[122] On the other hand, from CSD2 it can be identified different areas showing different contrast, what suggests an inhomogeneous film morphology. For CSD-ALD1 it is presented a surface morphology with Bi and Fe rich precipitates, identified by EDX, and a porous surface morphology (see

inset of Figure 4.9 (c)). The SEM image of CSD-ALD2 film, which was designed with CoO_x nanolaminates of constant thickness, shows a surface free of precipitates with few pores, which would be close to ideal film morphology. These observations also demonstrate the critical role of the preparation procedure on the film morphology. Based on these analysis, CSD-ALD1 is discarded for further characterization because of the presence of large precipitates and the formation of pores (inset).

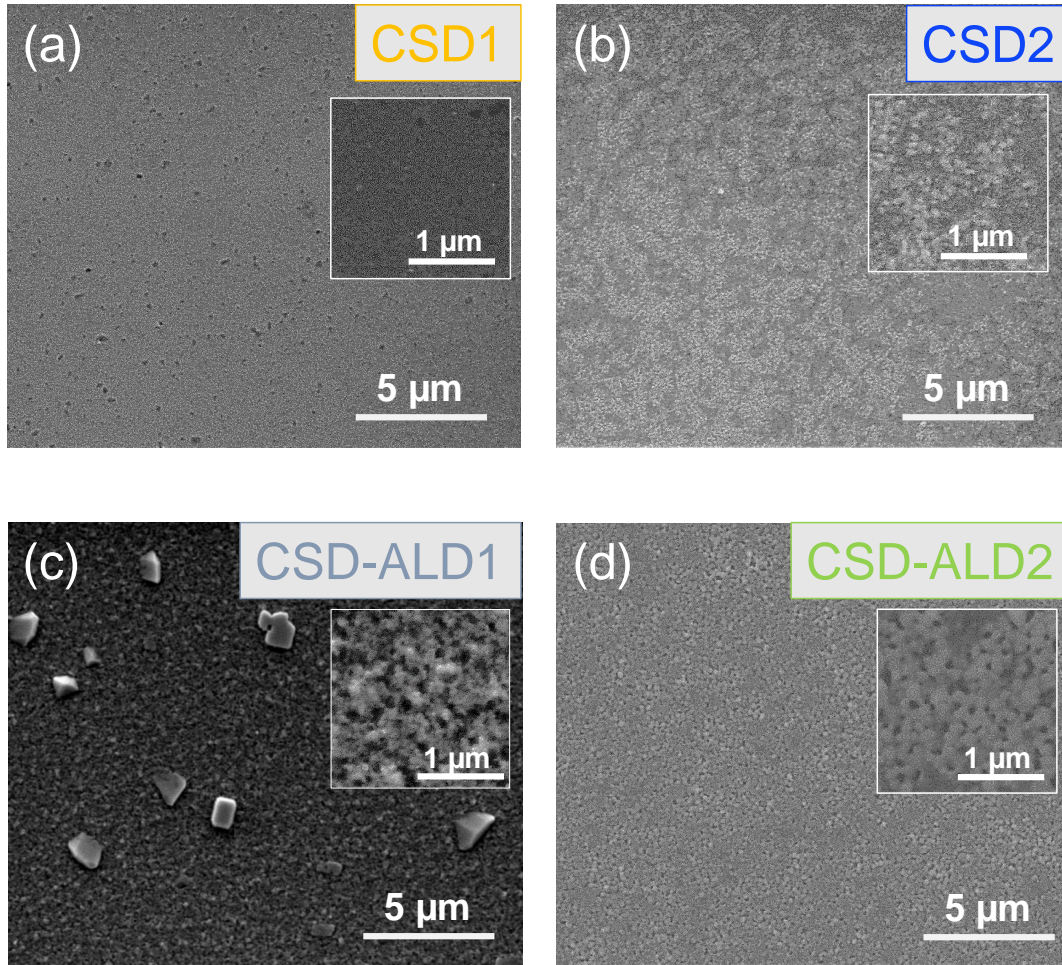


Figure 4.9: SEM surface morphology images of BFCO-based thin films from (a,b) CSD and (c,d) CSD-ALD methodologies grown on LSMO//STO.

For the three remaining samples, CSD1, CSD2 and CSD-ALD2, elemental distribution throughout the film thickness has been examined by means of time-of-flight secondary ion mass spectrometry (ToF-SIMS) depth profiling, Figure 4.10. For this study, samples were grown on STO substrates. All samples show an homogeneous vertical distribution of Bi and Fe across the film thickness. The main differences

arise from the distribution of Co ions. In the case of CSD1 and CSD2, Figure 4.10 (a,b), a significant concentration of Co is observed at the top of the samples, indicating its diffusion towards the film surface. On the other hand, in CSD-ALD2 films, a more gradual distribution of Co is observed, increasing from the STO surface to the top of the BFCO layer. In addition, CSD-ALD2 shows a wide substrate-film transition region, which could indicate the presence of pinholes in agreement with the SEM image shown in Figure 4.9 (d). At this stage we have learnt that regardless the designed distribution of cobalt in the deposition stage, the thermal treatment modifies it, being dramatic for CSD1 and CSD2.

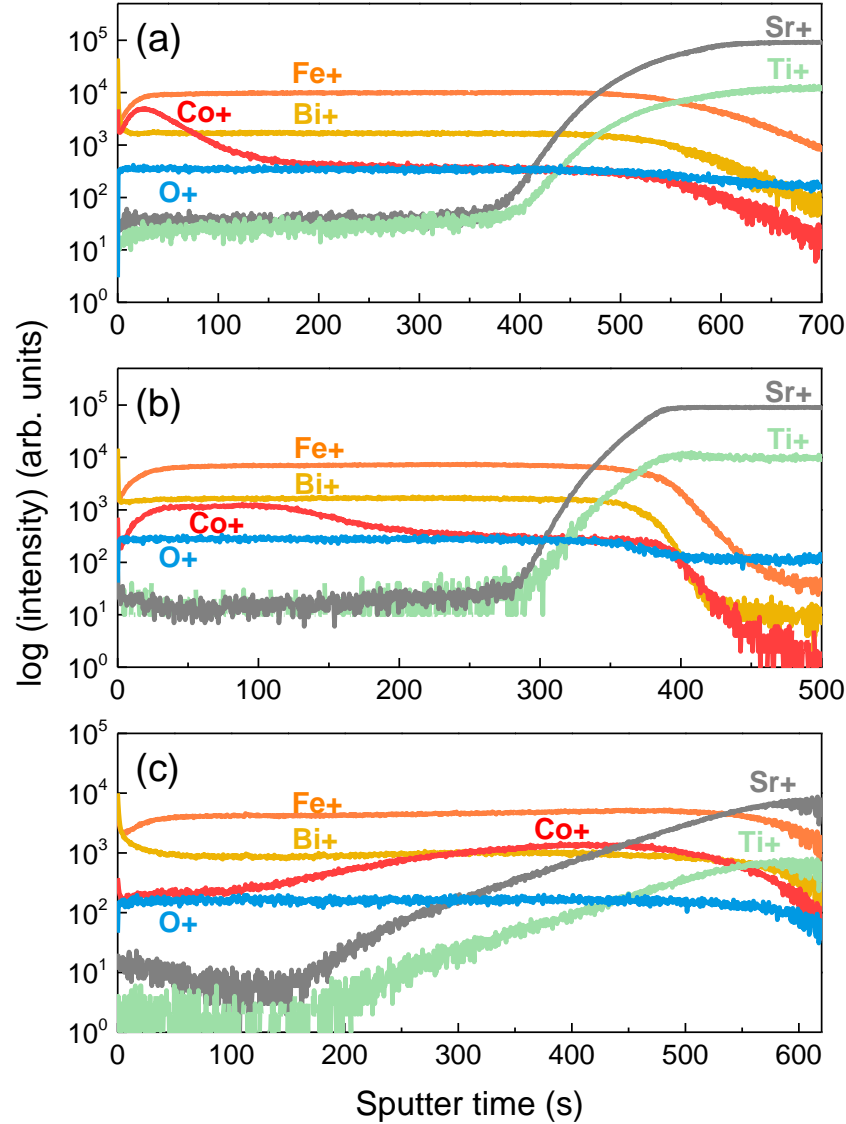


Figure 4.10: Time-of-flight secondary ion mass spectrometry depth profiling of (a) CSD1; (b) CSD2, (c) CSD-ALD2 prepared on (001)-STO.

In order to evaluate how the composition of these samples influence on the light-absorption properties, UV-Vis absorption spectra has been collected and compared to that of pristine BFCO10 in Figure 4.11. It is observed that the three "gradient" samples present a similar absorbance spectra with higher absorption near the violet region with respect to BFCO10. In addition, the inset shows the Tauc plot for direct transitions, where the extrapolation of the linear region to the x-axis intercept allows to obtain the Tauc gap.[259] Subtle variations with respect to BFCO10 are exhibited. CSD-ALD2 and CSD1 show higher absorption between 400 - 550 nm which is translated with a narrower bandgap. On the other hand, the CSD2 film shows lower absorption and higher bandgap energy. Note that this design also showed less intense XRD Bragg reflections and heterogeneous surface morphology with precipitates. Therefore, just looking at the optical characterization, the most promising compositions would be CSD-ADL2 and CSD1 over CSD2.

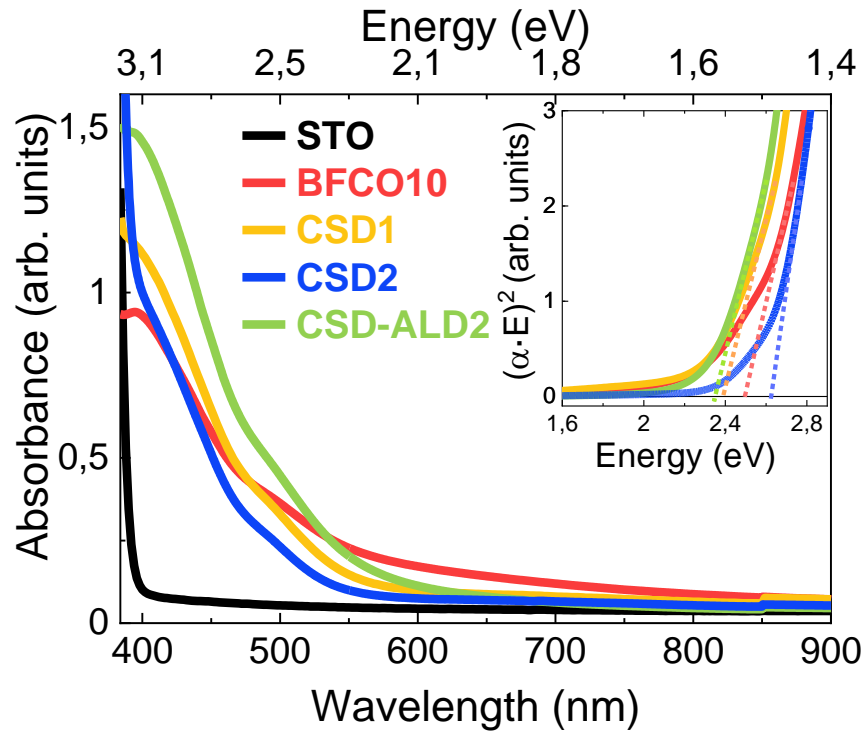


Figure 4.11: Optical absorbance spectra of STO substrate and CSD1, CSD2 and CSD-ALD2 compared to pristine BFCO10. Inset shows Tauc plot for direct bandgap extrapolation.

In order to test the photoresponse and ferroelectric properties, the gradient films were grown on LSMO-buffered STO substrates and the devices were completed with ITO top electrodes. The performance was compared to a device with BFCO10 composition. The corresponding J-V characteristic curves and P-E loops are presented in Figure 4.12. For an easy comparison, these measurements have been

performed under the same conditions previously described in this Chapter. On one hand, CSD1 displays a photoresponse behavior that is almost identical to that of BFCO10. In fact, these two samples showed almost the same film crystallinity and surface morphology and quite similar optical absorption. On the other hand, a slightly deteriorated photoresponse is exhibited by CSD2, which could be attributed to its low crystallinity and the presence of secondary phases at the film surface. Intriguingly, CSD-ALD2 shows poor photoresponse in comparison with the all-CSD processed films.

Regarding the ferroelectric response, CSD1 and CSD2 reveal robust and stable P-E hysteresis loops, which in spite of a subtly higher coercive electric field, is similar to that of pristine BFCO10. In contrast, notably inferior ferroelectric performance is displayed by CSD-ALD2, indicating that the combination of CSD and ALD techniques adversely affects the physical properties of the system.

Therefore, it becomes evident that the strategies presented in this work to prepare compositional gradient systems did not result in an overall improvement of the physical properties, specially for CSD-ALD2 which according to the XRD, SEM and optical properties was very promising. Therefore, for the sake of better understanding these unexpected poor photo- and ferroelectric properties of CSD-ALD2 films, high resolution STEM characterization has been carried out.

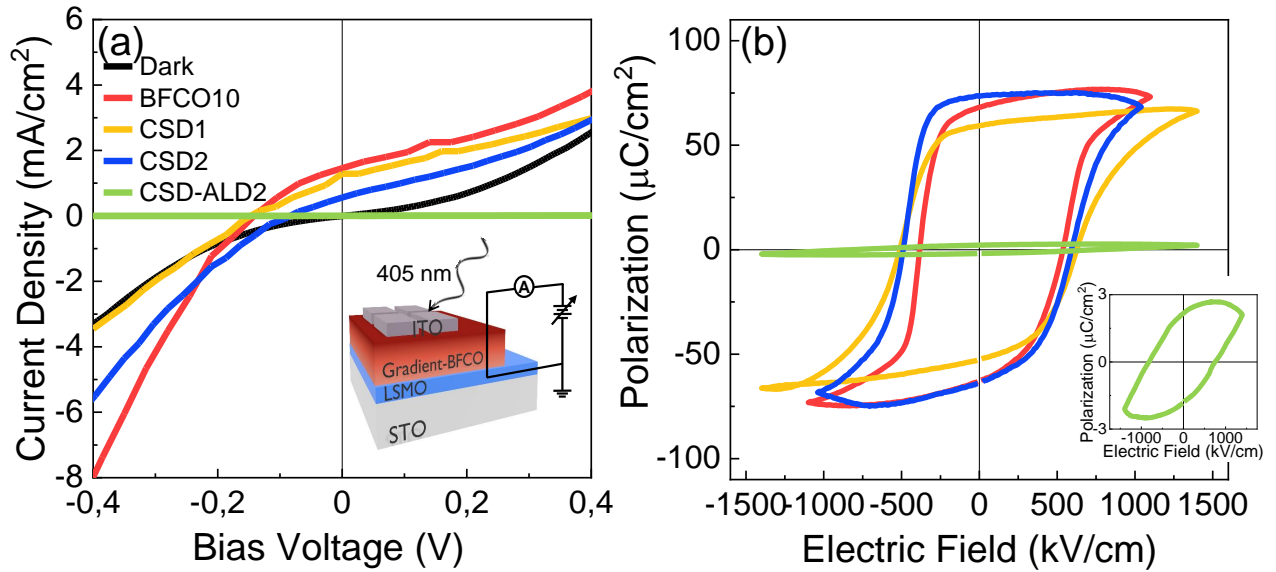


Figure 4.12: Electric characterization of compositional "gradient" systems compared to pristine BFCO10. (a) J-V characteristic curves, the inset shows the sketch of the electrical configuration used for the measurements. (b) Ferroelectric hysteresis P-E loops recorded at 2 kHz and room temperature.

Figure 4.13 shows Z-contrast HAADF-STEM cross-sectional images of CSD-ALD2//STO and

BFCO10/LSMO//STO systems. A film with a strong heterogeneous structure is observed for ALD-CSD2, with large inter-layer pores and the presence of Co-rich particles lying specially adjacent to the pores. This image contrasts with that of pristine BFCO10, which shows continuous film with clean interface with LSMO and homogeneous distribution of Bi, Fe and Co atomic species. Note that the BFCO10 layer used for comparison contains an Al-ZnO coating in which Zn content can be identified from Figure 4.13 (b). From this STEM study it turns out that the combination of ALD and CSD followed here is not appropriate to obtain dense films with a gradient composition. It is speculated that the decomposition of the ALD cobalt precursor (cobaltocene) during the growth of the whole stack at high temperature (600 °C) could obstruct the conversion process of the CSD-BFO generating the dramatic microstructure depicted in Figure 4.13 (a). However, TEM studies on quenched samples at different stages of the growth process should be performed to better elucidate the origin of this microstructure. Clearly, the poor film quality of CSD-ALD2 can explain the inferior photoresponse and ferroelectric properties observed in Figure 4.12.

Overall, the results presented in this Section showcase that designing a chemical route to obtain compositional gradient films is extremely challenging and the use of high temperature processing to induce the epitaxial growth jeopardizes the cobalt distribution generated in the deposition stage. Nonetheless, very recently it has been demonstrated the viability to prepare epitaxial PbTiO₃ films at 200 °C with polarization gradients by means of the hydrothermal method and proper choose of the growth substrate, pointing out the potential of low-temperature solution route to prepare gradient films.[82] Another potential strategy to obtain gradients could be the use of low-temperature ALD. Proper design of Co-O and Fe-O cycles with extended deposition times could probably favor retaining the original Co distribution while achieving epitaxial growth.[236] A similar procedure has been successfully demonstrated in the fabrication of Al-ZnO films with a vertical compositional gradient of Al.[358]

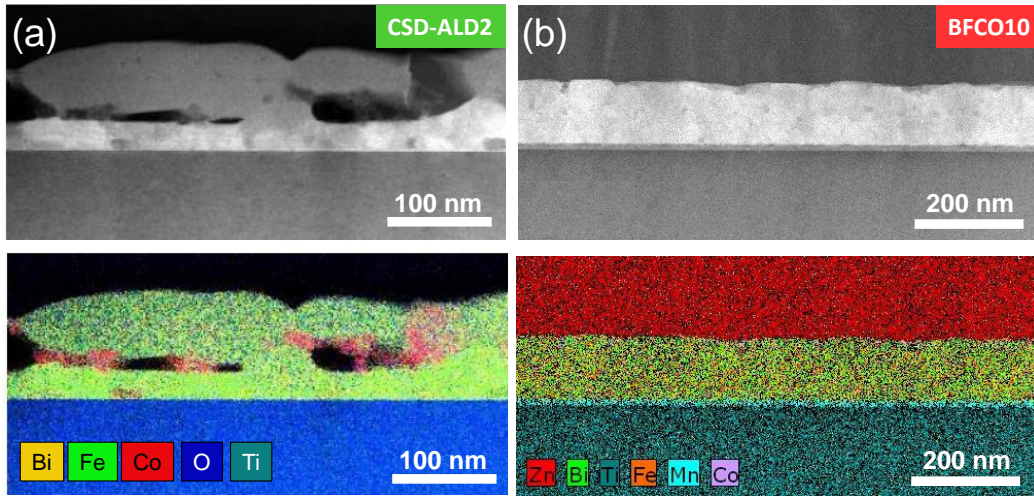


Figure 4.13: Z-contrast HAADF STEM cross-sectional imaging (up) and corresponding EDX mapping of integrated intensities of the characteristic elements in the system (down) for (a) ALD-CSD2 and (b) BFCO10 single-compositional film.

4.3 Conclusions

In this work it is assessed the critical point of interface engineering of lead-free photoferroelectric and epitaxial BFCO10 thin film by integrating a ZnO interface to ultimately built a vertical and stable all-oxide PV device completed with ITO and LSMO electrodes. It is demonstrated that upon optimized growth, the oxide heterostructure consisting in up to four different interfaces show smooth and homogeneous surface morphology while preserving *c*-axis BFCO10 oriented growth. The electrical characterization of the all-oxide devices evidenced the strong influence of interface engineering of BFCO10 on the photoresponse reporting ~ 2.2 times improved IPCE. Importantly, the robustness of the device is demonstrated by monitoring a reliable performance up to 2 months. In addition, the measurements on the coupled ferroelectricity-photoresponse with appropriate time-scales (~ 0.1 s) demonstrate that the J_{sc} can be modulated by ferroelectric polarization in ZnO-BFCO10 systems in up to ~ 68 %, displaying IPCE as high as 6.3 %. The extracted energy band diagrams from XPS are in line with the obtained photoresponse J-V measurements. The increase in J_{sc} is tentatively attributed to the formation of a large VBO at the BFCO/ZnO interface and the small variation in V_{oc} is consistent with the obtained $V_{BI,XPS}$. Interestingly, enhanced V_{oc} has been displayed in La-doped BFCO10 systems, which is likely due to an improved film quality that can also provide higher quality interfaces.

Also, the preparation of gradient composition BFCO photoabsorber has been investigated by means of CSD and ALD, yielding inhomogeneous distribution of Co throughout the film thickness.

Overall, this study is expected to encourage further investigations on epitaxial photoferroelectric oxides for optoelectronic devices, in particular to continue the search for appropriate oxide layers to improve the device interfaces while favoring an easy integration and cost-effective preparation. In this scenario, identifying compatible oxide compositions that could be used as hole transport materials will provide further understanding and guidance towards the development of the photoferroelectric systems for niche applications.

Chapter A4

Annex Information of Chapter 4

A4.1 Crystallinity and phase purity

The crystallinity and phase purity of BFCO10 thin film on different oxide architectures has been additionally studied by means of 2D XRD $\theta - \chi$ scans. Figure A4.1 (a) shows the 2D diffraction pattern for ITO/BFCO10/LSMO//STO system; the two bright spots at 22.5° and 46.5° correspond to (001) Bragg reflections of STO substrate. No Bragg reflections are observed for 10 nm LSMO thin film owing to its low thickness. The two peaks at 22.5° and 45° observed in the integrated 2θ scan correspond to (001) and (002) reflections of BFCO10, confirming its epitaxial growth on (001)-LSMO//STO. An additional weak spot is observed at 32° , which corresponds to typical bismuth and iron oxide rich phases as Bi_2O_3 or Bi_2FeO_9 . [122] ITO is not observed because of its amorphous nature arising from the room temperate and low power density deposition conditions. [337] The influence of the incorporation of 20 nm ZnO selective transport layer in BFCO10 crystallinity and phase purity is studied in Figure A4.1 (b). The same Bragg reflections for BFCO10 thin film are observed, confirming that its crystalline quality is not compromised with the integration of ZnO coating. The typical Bragg reflections of ZnO are not identified because of the low film thickness. Indeed, the preparation of analogous systems with 130 nm ZnO allows identifying diffraction rings at 31.5° and 36.5° , typical of polycrystalline ZnO films, Figure A4.1 (c). [336]

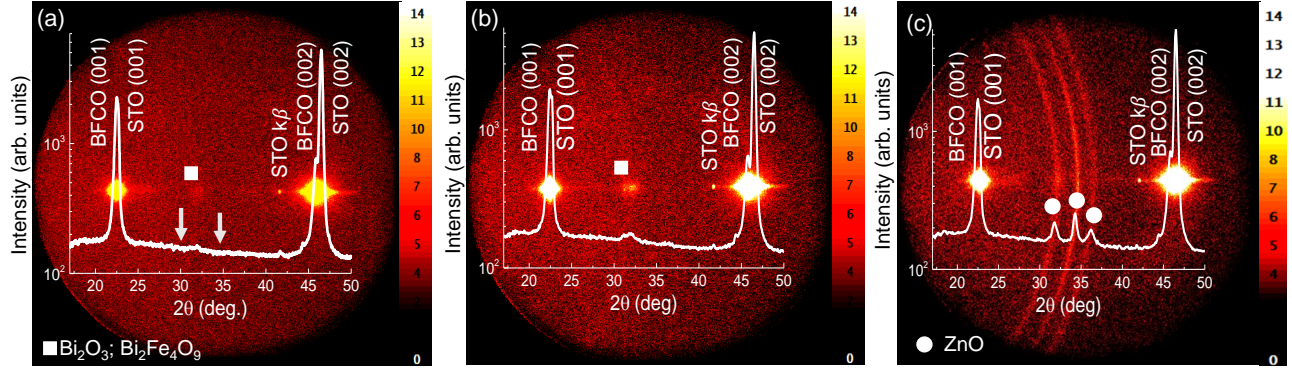


Figure A4.1: 2D-XRD analysis and integrated 2θ scan of (a) ITO/BFCO10/LSMO//STO, (b) ITO/20 nm ZnO/BFCO10/LSMO//STO oxide architectures and (c) ITO/130 nm ZnO/BFCO10/LSMO//STO oxide architectures.

A4.2 Optical properties

The optical properties of the oxide architectures have been investigated by UV-Vis spectroscopy transmittance (%T) curves measured in the wavelength range of 200 to 800 nm, Figure A4.2 (a). From the transmittance spectra of bare STO substrate (grey curve) it can be observed a strong absorption for photon energies above 3.2 eV, consistent with its band gap (see inset).[359, 107] The %T drops in LSMO//STO (blue curve) in congruence with LSMO thickness and oxygen processing conditions previously reported.[360] The addition of BFCO10 film (brown curve) exhibits no changes in the maximum transmittance, however a red-shift is revealed in the absorption edge, as it can be observed in the absorbance spectra (inset), being in reasonable agreement with the band gap reported for high quality epitaxial BFCO10 films.[107, 122] With the incorporation of ITO (red curve) and the selective layer ITO/ZnO (purple), the absorption edge slightly shifts to the violet and blue regions (inset) and higher transmittance is shown, features that are characteristic of these coatings.[339, 340, 341, 342] The inset shows the absorbance spectra measured in the same conditions. Note that the use of one-side polished STO substrates attenuate the signal in a factor of ~ 2.7 between 400 and 800 nm resulting in low %T value, see Figure A4.2 (b). In addition, the thickness of the ITO and ZnO layers have been previously optimized to obtain maximum transmittance according to average transmittance map simulation using the transfer matrix method,[338] Figure A4.2 (c). From this simulation it can be observed that the maximum of transmittance should be obtained for systems with 70 - 100 nm ITO and ~ 20 nm ZnO coatings. Importantly, the increase in T% of $\sim 15\%$ with the integration of these ITO and ZnO coatings

is in well agreement with that observed in Figure A4.2 (a).

Note that the simulation was performed by Eloi Ros (UPC). It was considered Air Mass 1.5 standard irradiance conditions and the refractive index and extinction coefficient of ITO, ZnO and BFCO10 films.

I highly acknowledge his contribution.

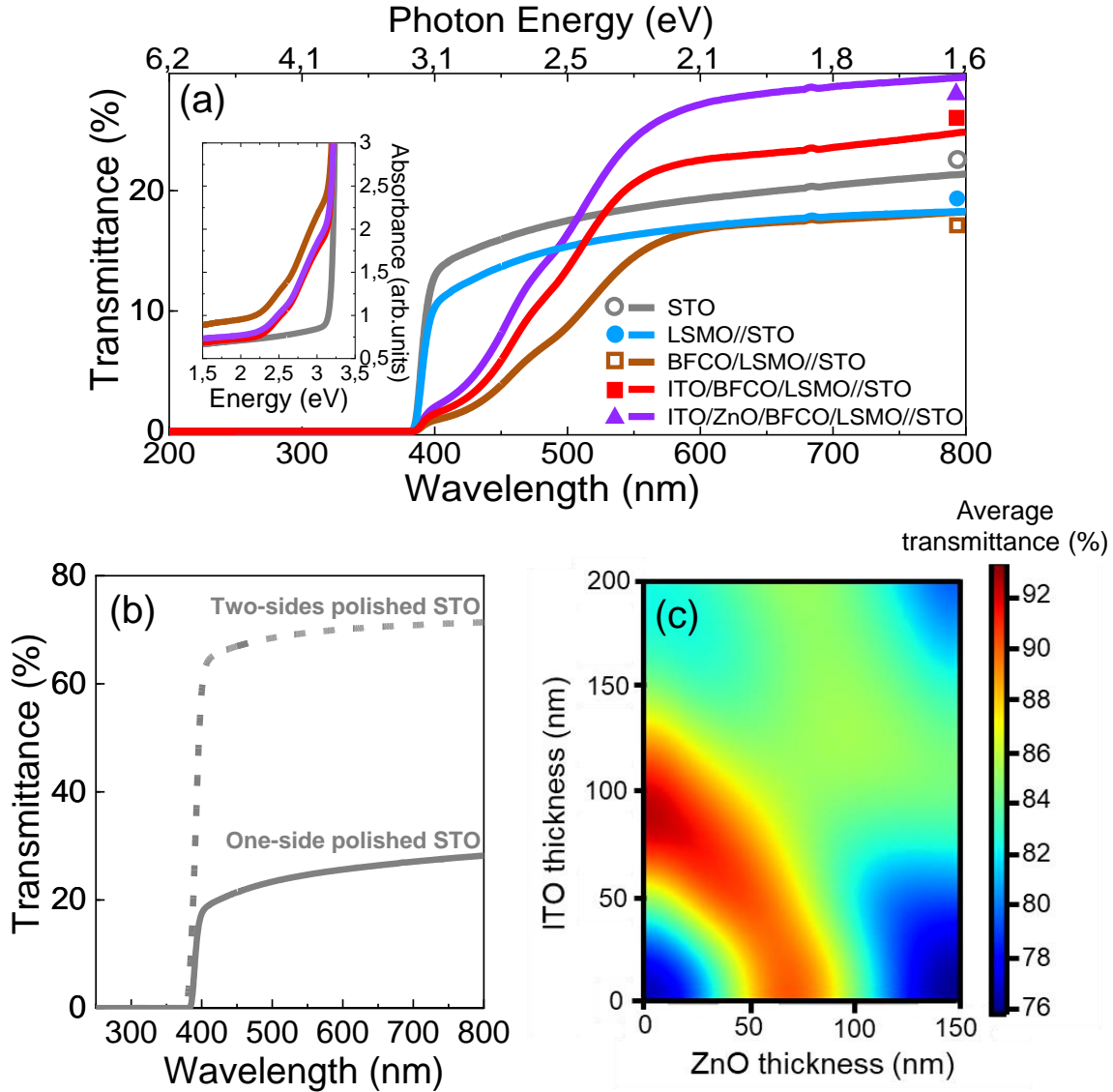


Figure A4.2: Optical characterization of BFCO10-based systems. (a) Optical transmittance spectra of the oxide heterostructures BFCO10/LSMO//STO (brown), ITO/BFCO10/LSMO//STO (red), ITO/ZnO/BFCO10/LSMO//STO (purple) and the bottom electrode LSMO//STO (blue) and STO substrate (grey). The inset shows the absorbance spectra of the systems. (b) Comparative optical transmittance spectra of one-side polished (001)-STO (solid line) and two-sides polished (001)-STO substrate (dashed line). (c) Transmittance map simulation of ITO/ZnO/BFCO system in function of ITO and ZnO thickness at AM 1.5 irradiance and obtained from transfer matrix model.

A4.3 Photoresponse and ferroelectric properties

The J-V characteristics of the ITO/ZnO/BFCO10/LSMO//STO system with different ZnO thicknesses between 4 - 130 nm have been measured under illumination with a monochromatic laser of 405 nm and irradiance of 350 mW/cm^2 , revealing optimized photoresponse with improved J_{sc} and V_{oc} values for 20 nm ZnO, see Figure A4.3.

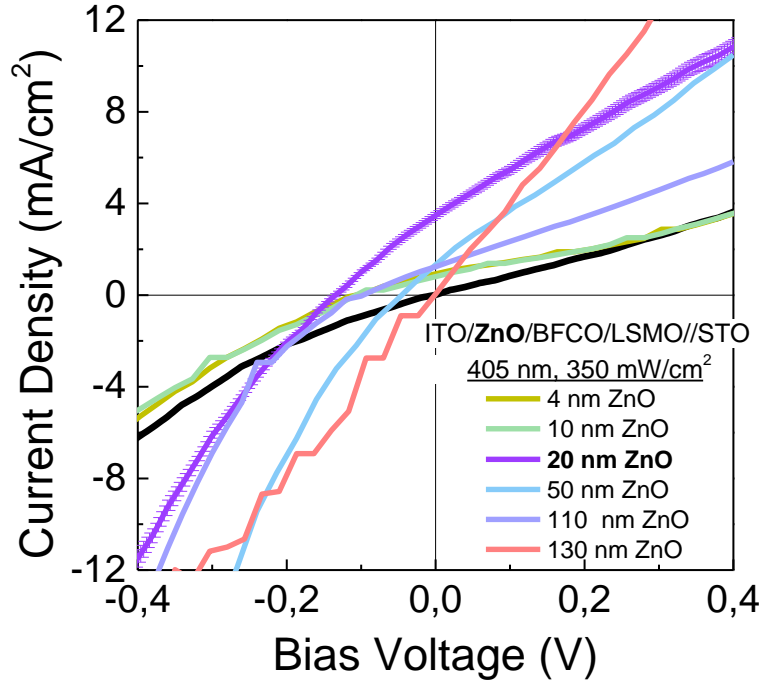


Figure A4.3: Comparative J-V characteristics of ITO/ZnO/BFCO10/LSMO//STO system with ZnO thickness of 4 nm, 10 nm, 20 nm, 50 nm, 110 nm and 130 nm, recorded under illumination with a monochromatic laser of 405 nm and irradiance of 350 mW/cm^2 .

Photoresponse measurements for the ITO/ZnO/LSMO//STO system have been carried. Figure A4.4 presents the J-V characteristic curves with linear dependence that passes through J-V axes origin in both dark and under illumination conditions, indicating that no photogeneration occurs in ZnO.

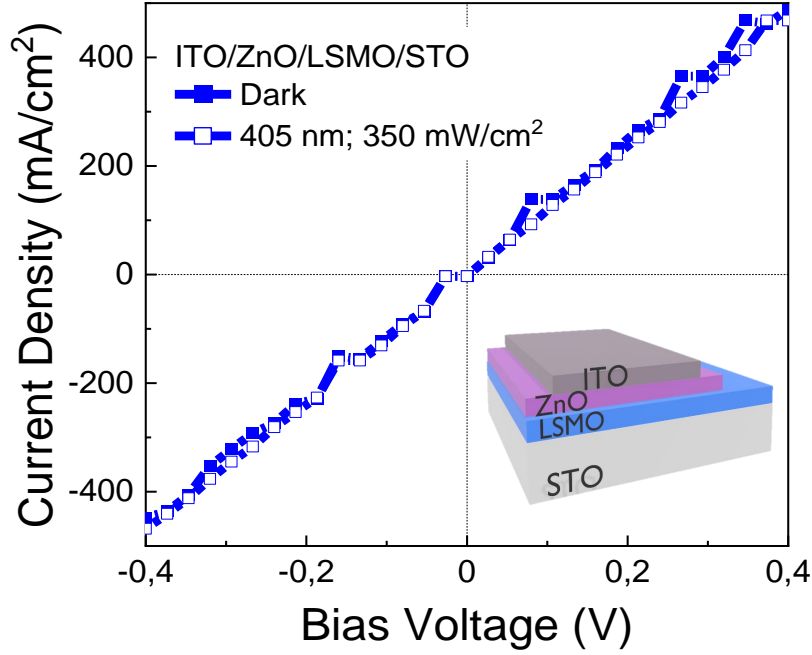


Figure A4.4: J-V characteristic curves of ITO/ZnO/LSMO//STO recorded in dark and under illumination with a monochromatic laser of 405 nm and irradiance of 350 mW/cm^2 from the top of ITO electrode.

Figure A4.5 shows P-E and J-E hysteresis loops of ITO/ZnO/BFCO10/LSMO//STO in top-top configuration, that is contacting only ITO electrodes. These loops have been recorded at lower frequency of 500 Hz, room temperature and in dark conditions. A symmetric P-E loop with $E_c \sim 385 \text{ mV/cm}$ in both positive and negative directions is observed, demonstrating no signatures of imprint electric field, probably attained to the symmetric configuration of ITO-ITO electrodes that could allow for the formation of identical Schottky barriers at the ITO/ZnO/BFCO10 interfaces, as it has been previously reported for BaTiO_3 ferroelectric oxide.[79]

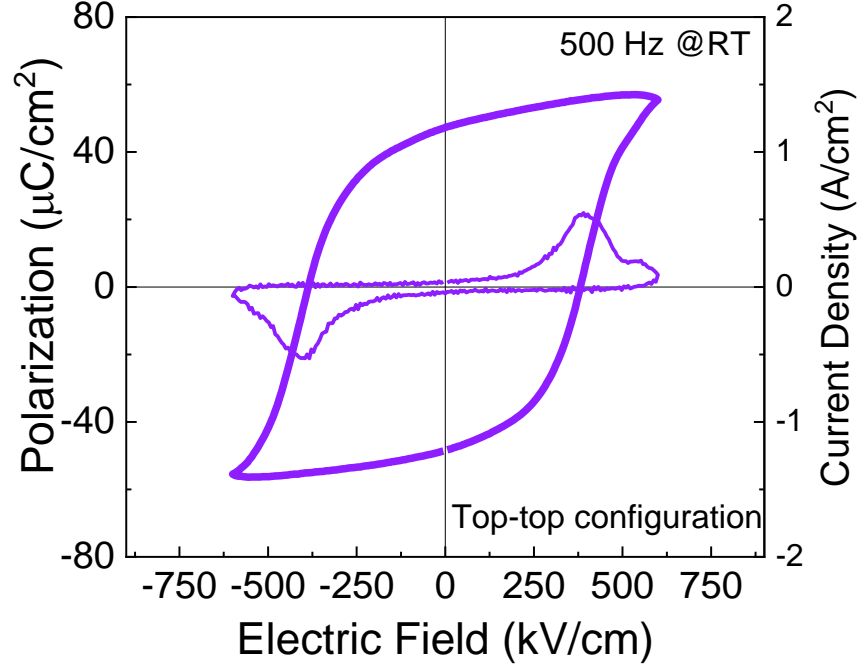


Figure A4.5: J-E and P-E hysteresis loops recorded at 500 Hz, room temperature and dark conditions for ITO/ZnO/BFCO10/LSMO//STO system in top-top configuration.

Figure A4.6 shows the study of J_{sc} in function of V_{poling} up to ± 6.5 V, where the photogenerated current was recorded at zero bias with a time delay of 0.1 s. See Figure 2.22 of Experimental Section 2.3.2 for the measurement protocol. It can be observed that the obtained J_{sc} - V_{poling} mimics the hysteresis of a FE loop showing an anticlockwise cyclic direction that is characteristic of devices with imprint electric field pointing to the top electrode.[76, 81] Importantly, the J_{sc} change upon polarization switching is now found to be larger than in the measurements with larger time delay of ~ 10 s presented in the main manuscript. A large modulation of $\sim 68\%$ in J_{sc} is now displayed upon ferroelectric switching, reaching values as high as ~ 5.0 mA/cm² and IPCE of 6.3%.

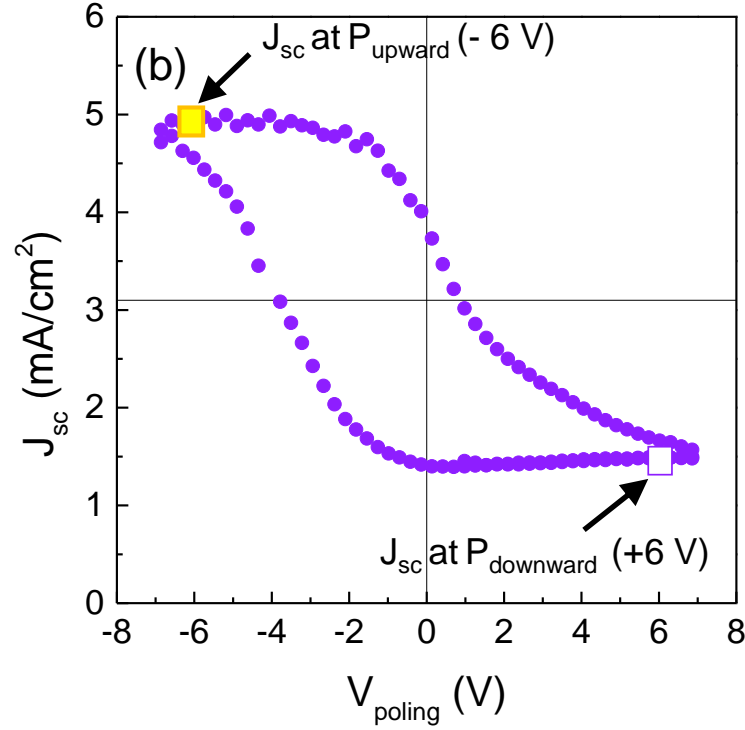


Figure A4.6: J_{sc} dependence with V_{poling} of ITO/ZnO/BFCO10/LSMO//STO heterostructure collected with a time delay of 0.1 s.

A4.4 Chemical analysis (XPS) and energy band alignment determination

Figure A4.7 shows the XPS core level emission lines and valence band of the investigated surfaces and interfaces. For additional details, refer to Experimental Section 2.3.3. Starting from the analysis of the single layers, the core level binding energy for Bi $4f_{7/2}$ is at 158.61 eV which matches Bi³⁺ in BFO.[284] The core level of Sr $3d_{5/2}$ is at 132.37 eV, typical for Sr²⁺ in LSMO.[348] Next, both In $3d$ and Sn $3d$ have been recorded for ITO as an overlapping between Bi $4d$ and In $3d$, and Sn $3d$ with Zn LMM Auger was anticipated for the interface systems and would hinder the direct comparison of the core level binding energies. Sn $3d_{3/2}$ appeared at 486.73 eV and In $3d_{3/2}$ at 444.83 eV, in agreement with Sn⁴⁺ and In³⁺ in ITO, respectively.[349] Finally, Zn $2p_{3/2}$ is centered at 1022.33 eV matching Zn²⁺ in ZnO.[350] The values of the binding energies for the core levels and valence band maxima (VBM) referred to the Fermi energy (E_F), see Figure A4.8, are listed in Table A4.1.

Then, the interfaces of the system ITO/BFCO10/LSMO are evaluated, Figure A4.7 (a,b). Upon the

formation of the interface, the intensity of the emission lines of the buried layers is reduced but allows to identify the binding energies which are listed in Table A4.1. The difference in binding energy positions between the single layer and interface system ($\Delta E_{CL} = E_{CL,interface} - E_{CL,singlelayer}$) is then used to determine the shift of the VBM and CBM which are also included in Table A4.1. The energy band diagrams for the ITO/BFCO10/LSMO and ITO/ZnO/BFCO10/LSMO systems have been proposed in Figure 4.5, where Fermi Level, bandgap (E_g) and barrier heights are indicated. Details on the calculation of the ΔE_{VBM} , conduction band minima and offset (CBM, ΔE_{CBM}) and built in potential ($V_{BI,XPS}$) [361, 276] can be found in Equations 2.18, 2.19, 2.21, respectively, described in the Experimental Section. Note that the $V_{BI,XPS}$ has been calculated for the systems ITO/BFCO10/LSMO//STO and ITO/ZnO/BFCO10/LSMO//STO, being:

$$V_{BI,XPS}(\text{LSMO/BFCO10/ITO}) = E_{Bi4f(\text{BFCO10/ITO})} - E_{Bi4f(\text{BFCO10/LSMO})} = + 0.26 \text{ eV}$$

$$V_{BI,XPS}(\text{LSMO/BFCO10/ZnO}) = E_{Bi4f(\text{BFCO/ZnO})} - E_{Bi4f(\text{BFCO10/LSMO})} = + 0.16 \text{ eV}$$

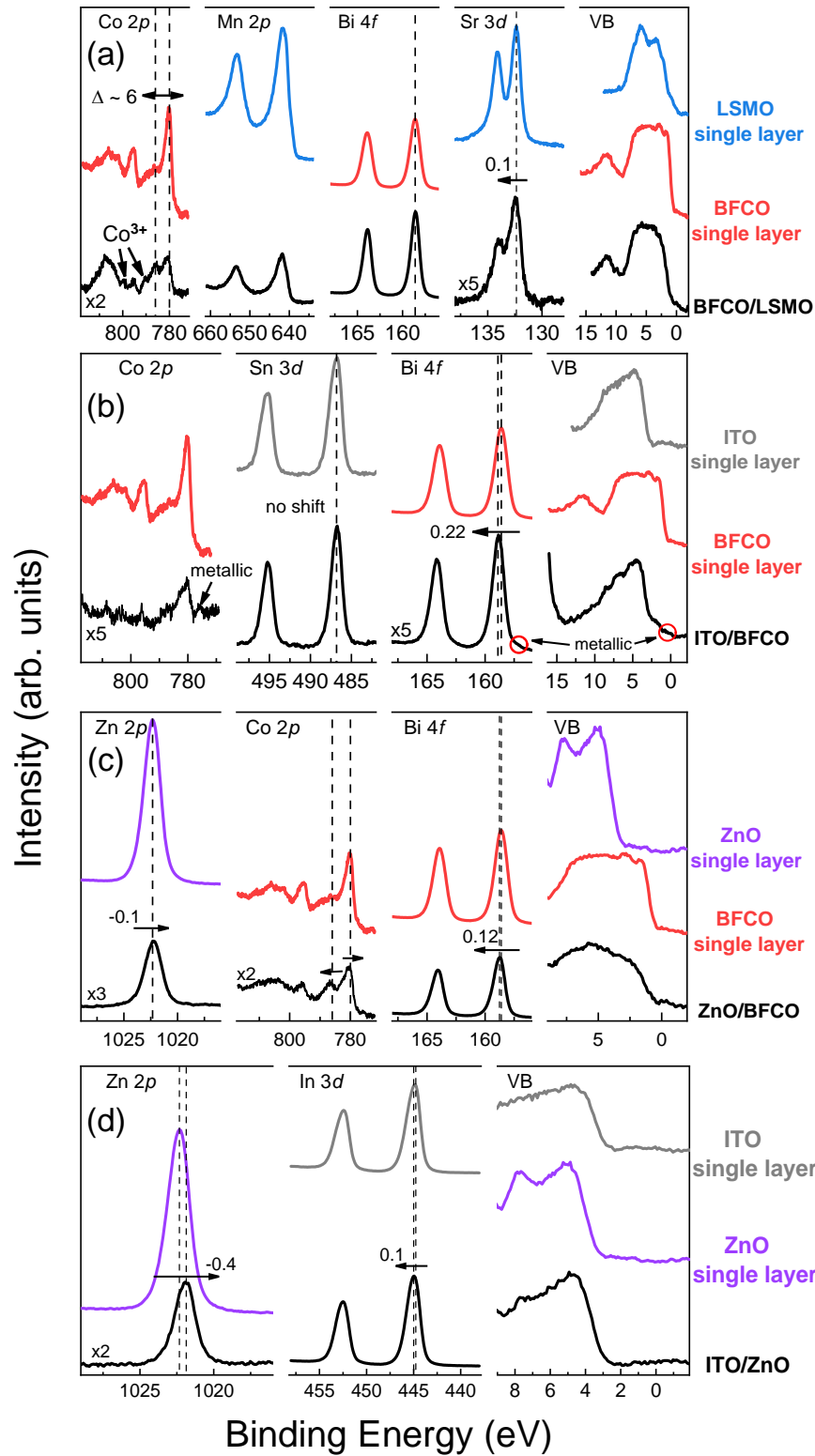


Figure A4.7: The XPS core level emission lines and valence band (VB) of the investigated surfaces and interfaces. (a) LSMO, BFCO10 single layers and BFCO10/LSMO interface. (b) ITO, BFCO10 single layers, and ITO/BFCO10 interface. (c) ZnO, BFCO single layers, and ZnO/BFCO10 interface. (d) ITO, ZnO single layers, and ITO/ZnO interface.

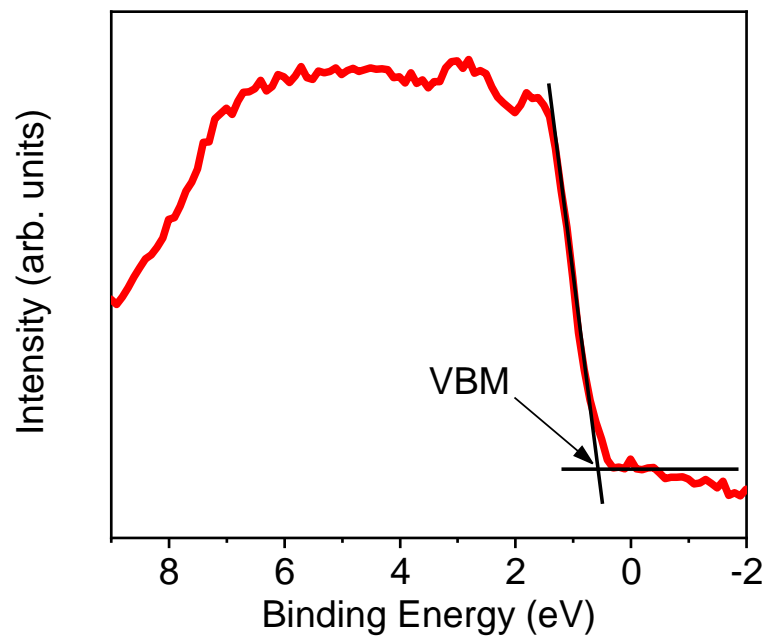


Figure A4.8: Representative methodology to determine the VBM for the 100 nm BFCO10/10 nm LSMO//STO system.

Table A4.1: Values extracted for the binding energies for specific core levels, VBM and CBM.

(a) BFCO, LSMO single layer and BFCO/LSMO interface

(eV)	Co $2p_{3/2}$ /Sat.	Mn $2p_{3/2}$	Bi $4f_{7/2}$	Sr $3d_{5/2}$	VBM	CBM
BFCO	779.9 / 786		158.61		0.58	2.0
LSMO		641.42		132.37	E_f	
BFCO/LSMO	~780/ ~786	641.72	158.57	132.47	0.54/ E_f	2.1/

(b) BFCO, ZnO single layer and ZnO/BFCO interface

(eV)	Zn $2p_{3/2}$	Co $2p_{3/2}$ /Sat.	Bi $4f_{7/2}$	VBM	CBM
BFCO		779.9/ 786	158.61	0.58	2.0
ZnO	1022.33			3.40	0
ZnO/BFCO	1022.23	780.12 / 787.77	158.73	3.3/0.70	0.1/1.9

(c) BFCO, ITO single layer and ITO/BFCO interface

(eV)	Co $2p_{3/2}$ /Sat.	Sn $3d_{5/2}$	Bi $4f_{7/2}$	VBM	CBM
BFCO	779.9 / 786		158.61	0.58	2.0
ITO		486.73		2.84	0
ITO/BFCO	~780/ ~786	486.73	158.83	2.84/0.80	0/1.8

(d) ZnO, ITO single layer and ITO/ZnO interface

(eV)	Zn $2p_{3/2}$	In $3d_{5/2}$	VBM	CBM
ZnO	1022.33		3.40	0
ITO		444.83	2.84	0
ITO/ZnO	1021.93	444.93	2.94/3.00	-0.1/0.4

Chapter 5

Chemical solution processing of $\text{La}_{0.75}\text{Sr}_{0.25}\text{CrO}_3$ thin films for *p*-type transparent conducting electrodes

The imperative need for highly performant and stable *p*-type transparent electrodes based on abundant metals is stimulating the research on perovskite oxide thin films. Apart from electrical compatibility to be used as counterpart of *n*-type electrodes, these oxides could offer structural compatibility for the epitaxial growth of functional complex oxides such as the photoferroelectric BFO-based films studied in this thesis. However, obtaining *p*-type conductivity is intrinsically challenging and the use of cost-efficient and scalable solution-based techniques adds a new difficulty to the study because of the scarce literature availability.

In this Chapter, we tackle the design of an unexisting chemical route to fabricate *p*-type $\text{La}_{0.75}\text{Sr}_{0.25}\text{CrO}_3$ (LSCO) thin films. 25-100 nm LSCO films are grown on STO and LAO substrate to be thoroughly characterized from the structure, morphology, optical, electrical and electronic standpoint. The work presented in this Section has been published in *Chem. Mater.* 2023, 35, 9, 3513-3521, DOI: 10.1021/acs.chemmater.2c03831

5.1 Introduction

Transparent conducting oxides (TCO) constitute an especial class of materials that combine properties of high electrical conductivity ($\sigma > 10^4 \text{ S}\cdot\text{cm}^{-1}$) and high optical transparency in the visible spectrum ($T > 80$

%).[362, 363, 364, 365, 163, 278, 188] Among the enormous variety of oxides, the interest on the family of perovskite oxides for TCOs arises from the wide range of available compositions and to their structural compatibility with many functional complex oxides, making them useful to prepare innovative and stable heteroepitaxial devices for electronic and energy applications.[366, 367, 368, 369, 26] Indeed, CaVO_3 , SrVO_3 and SrNbO_3 are promising n -type TCOs that have demonstrated to show excellent performances when compared with ITO.[191, 192, 33] To broaden the applications of TCOs and continue advancing in functional perovskite-based heterostructures, there is a strong need to find high performance p -type TCO counterparts although its development is intrinsically challenging. The localized nature of O $2p$ orbitals at the top of the valence band of most metal oxides hinders the introduction of shallow acceptors and large hole effective masses.[193, 194, 195] Chemical modulation of the valence band, which consists of introducing covalency in the metal-oxygen bond, can overcome this issue.[197] Consequently, closed and quasi-closed shell electronic configurations of cation species (d^{10} , d^6 , d^3) are the best candidates to reduce localization of holes in oxygen ions and minimize colorization from the metal $d-d$ excitation. In this line, some new p -type TCOs based on Cr^{3+} oxides (d^3 in octahedral configuration) have been already identified [198, 199, 200] among which Sr-doped LaCrO_3 appears as a strong candidate with reasonably high transparency and p -type conductivity.[201, 202, 203, 204] Importantly, the ability to grow these materials as epitaxial films can be used as a lever to tune the physical properties.[370, 371, 372] In fact, it has been recently demonstrated that electric conductivity of Sr-doped LaCrO_3 films grown by molecular beam epitaxy (MBE) can be finely tuned through epitaxial strain.[204] Nevertheless, when evaluating the suitability of an oxide material to be used as TCO, along with high electrical conductivity and optical transmittance, it is important to consider cost-effective and sustainable processing techniques, as it is the case of CSD.[205, 206, 373] In fact, successful previous studies have already underlined the potential of solution-processing to successfully prepare n -type TCO perovskite films, as it is the case of M-doped BaSnO_3 (M= La, Pr, Nd, Sb) [374, 375, 376, 377] and La-doped SrTiO_3 [378, 379]. However, the study of p -type TCO perovskite films prepared by means of CSD is at its infancy. As a consequence, despite the promising perspectives of this approach, yet the synthesis of many new and attractive complex oxides films, including Sr-doped LaCrO_3 , remain unexplored.

In this Chapter, an unprecedented study to fabricate p -type epitaxial Sr-doped LaCrO_3 films is explored. The influence of solution chemistry and processing conditions on gel thermal decomposition and film crystallinity and morphology is thoroughly evaluated by means of thermogravimetric analysis, viscosity and scanning electron microscopy. Film optical transparency and electrical resistivity have

been evaluated on the optimized 45 nm films of $\text{La}_{0.75}\text{Sr}_{0.25}\text{CrO}_3$ (LSCO) by spectroscopic ellipsometry and temperature dependent resistivity measurements, respectively. Detailed structural analysis has been performed by X-ray diffraction and scanning transmission electron microscopy. Monochromated electron energy loss spectroscopy allowed to unravel the electronic properties of these solution processed oxides.

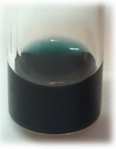
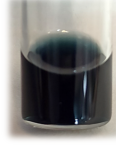

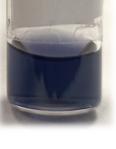
5.2 Results and discussion

5.2.1 Solution preparation and characterization

Among the plethora of salt precursors suitable for the synthesis of metal oxides, we have examined the use of two synthetic routes for the fabrication of LSCO thin films: the metalorganic route and the metal nitrate route. The use of metalorganic precursors led to non-homogeneous and unstable precursor solutions resulting in dramatically porous and non-epitaxial films, as it is described in Section A5.1. Upon thorough investigation of the processing parameters to obtain high quality LSCO films using the metalorganic formulation, it was not possible to obtain the films with the desired quality. Therefore, we decided to focus this study on the use of metal nitrate precursors which indeed have already proved superior than metalorganics in terms of requiring lower processing temperatures and they generally produce denser films with fewer impurities.[232] Herein, we focus on the use of La, Sr and Cr nitrates combined with different solvents (2-methoxyethanol *MOE*, acetic acid *AcA*, water) and additives (NN-dimethylformamide *DMF*, acetylacetone *AA*, diethanolamine *DEA* and citric acid *CA*). According to their chemical formulations, the four solutions investigated are named MOE, DMF-AA, DEA and CA, see Table 5.1. The detailed conditions for the preparation of these solutions are described in Section A5.2.

The obtained solutions are homogeneous and free of precipitates and the oxidation state of chromium gives rise to blueish/greenish coloration. The solution viscosity measured at room temperature increases from 0.0017 Pa·s for CA, 0.0043 Pa·s for MOE, 0.0045 Pa·s for DMF-AA to 0.0085 Pa·s for DEA, in accordance with the corresponding molecular weight of the solvents and additives. Importantly, these values of viscosity ensure good wettability of the working single crystal perovskite substrates.[329]

Table 5.1: Description of the four LSCO precursor solutions composition (solvent and additive) and viscosity.

Solution	Solvents	Additives	Viscosity (Pa·s)
MOE 	2-methoxyethanol and acetic acid	-	0.0043
DMF-AA 	2-methoxyethanol and acetic acid	N,N-dimethylformamide and acetylacetone	0.0045
DEA 	2-methoxyethanol and acetic acid	Diethanolamine	0.0085
CA 	Water	Citric Acid	0.0017

5.2.2 Thermal decomposition and fine tuning of processing conditions

To guarantee a controlled transformation process from the precursor solution to the formation of pure phase LSCO, simultaneous TGA-DSC analysis have been carried out from the dried gel of the four solutions described above. Note that O_2 -rich atmosphere has been used to study the decomposition of all the solutions. Additionally, the decomposition of DEA solution has been also studied in air atmosphere because of the well-known violent and exothermic decomposition of diethanolamine in O_2 . [380]

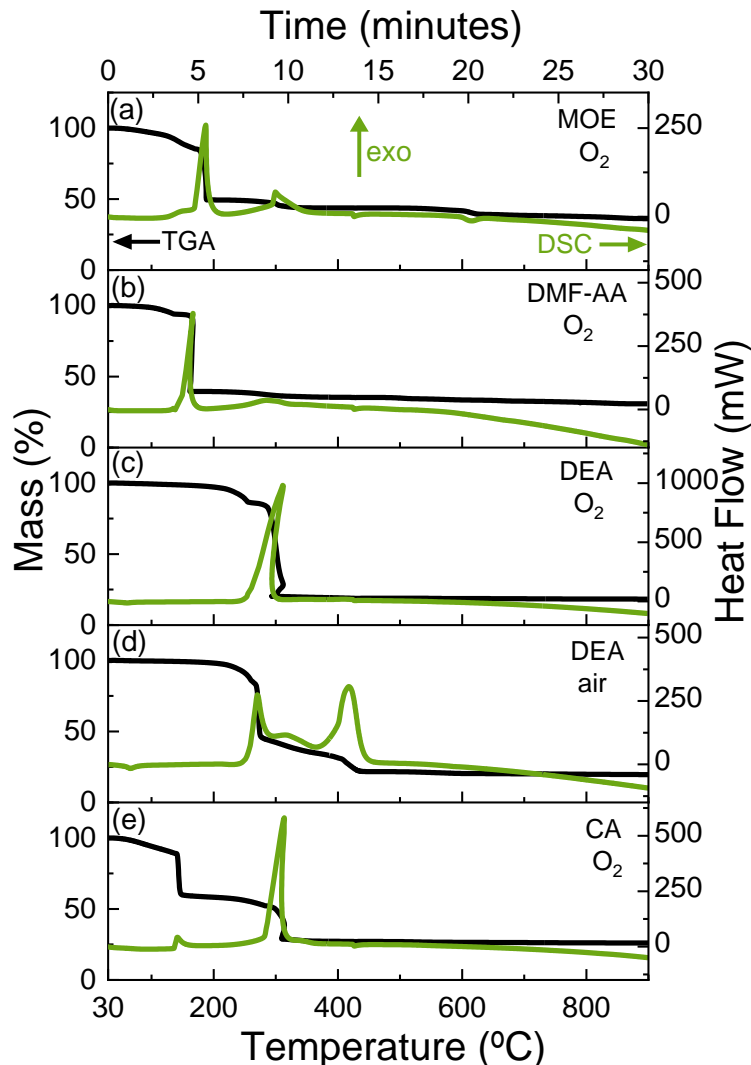


Figure 5.1: TGA-DSC curves obtained at $30\text{ }^{\circ}\text{C}\cdot\text{min}^{-1}$ from $30\text{ }^{\circ}\text{C}$ to $900\text{ }^{\circ}\text{C}$ in O_2 atmosphere for (a) MOE, (b) DMF-AA, (c) CA and (d) DEEA and (e) in air atmosphere for DEEA. The positive and negative values of heat flow in DSC curves are set to represent exothermic and endothermic phenomena, respectively.

The TGA curves of the dried gel of MOE, DMF-AA, CA and DEEA solutions in O_2 -rich atmosphere, Figure 5.1 (a-d), show the main mass losses at temperatures below $320\text{ }^{\circ}\text{C}$ ($>50\%$), which are related with two exothermic DSC peaks in MOE, DMF-AA, CA and one exothermic peak in DEEA. At these temperatures, according to the reported thermal decomposition of the individual metal nitrates,[232] simultaneous phenomena occur including dehydration of metal nitrates to form concentrated salt solutions, the condensation of $\text{Cr}(\text{NO}_3)_3$ and the elimination of NO_x and CO_2 as reaction product gases.[232, 381] The decomposition of the solvent 2-methoxyethanol into CO_2 and CO [382] is expected to occur in the same temperature range. Note that the use of additives in DMF-AA, DEEA and CA entails the formation

of intermediates such as aconitic acid in CA [329, 383] and modify the covalency of the metal-ligand bonds, changing the decomposition temperatures of the different thermal events when compared to pure nitrate decomposition.[384, 205, 385, 382, 232] In addition, in the case of DEA, the strong exothermic DSC peak at 310 °C is related to the violent oxidative decomposition of diethanolamine to NH_3 and acetic and formic acid.[380, 386] At temperatures above 320 °C it takes place the decomposition of acetic acid into CH_4 and CO_2 ,[387] and the condensation of $\text{La}(\text{NO}_3)_3$ and $\text{Sr}(\text{NO}_3)_2$ which release gases such as H_2O , NO_x and CO_2 . [232] These events are related to the presence of endothermic peaks at temperatures of ~ 400 °C and ~ 600 °C, respectively. Moreover, the downward trend of DSC curve observed at high temperatures could indicate the presence of an endothermic peak above 900 °C (not shown here) that could be related with the crystallization of LSCO.[388, 389]

The effect of the atmosphere on the thermal decomposition of the derived gel of DEA has been also evaluated. In air atmosphere, Figure 5.1 (e), the mass loss is more gradual than in oxygen, Figure 5.1 (d), and it has three exothermic peaks of less intensity compared to the one observed in oxygen, suggesting a milder decomposition.

Based on this study, fine tuning of the thermal profile parameters (temperature, interim steps, annealing time and heating ramps) has been performed to achieve a complete conversion of the precursor gel to pure-phase, epitaxial and dense LSCO films, Figure 5.2. For the purpose of film processing optimization and transmittance measurements, precursor solutions have been deposited on (001)-STO single crystal substrates. The best conditions for crystallization of LSCO thin films on (001)-STO substrate have been determined through fine tuning of the temperature (700 - 900 °C) and dwell time (15 - 45 min) according of the TGA-DSC analysis. For more details, refer to Section A5.3. It is anticipated that in order to be able to perform the electrical characterization of such films, LSCO has been also prepared on (001)-LAO single crystal substrates, as it will be described below.

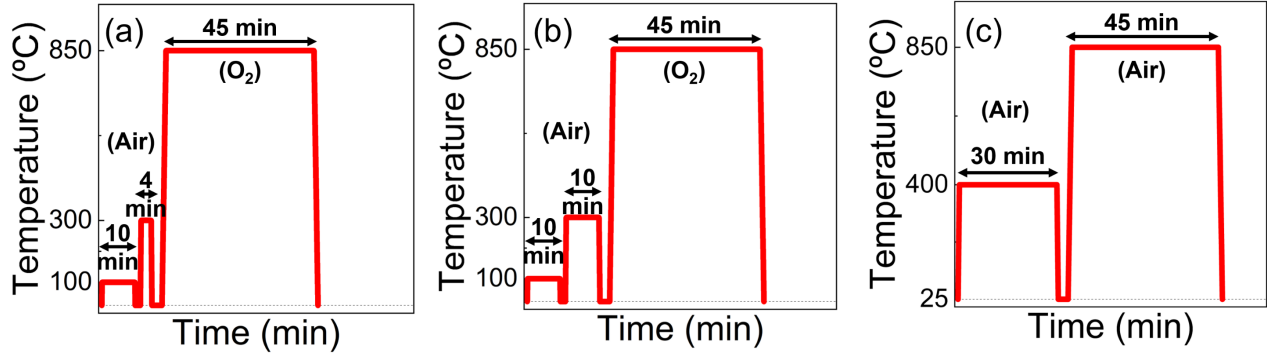


Figure 5.2: Thermal profiles defined for the preparation of LSCO films from (a) MOE, DMF-AA and CA, (b) DEA in O₂ and (c) DEA in air.

5.2.3 Crystallinity and surface morphology

The effect of the solution chemistry on the surface morphology of LSCO thin films has been evaluated by SEM, see Figure 5.3. LSCO films obtained from MOE, DMF-AA and CA solutions processed in O₂ atmosphere exhibit similar homogeneous and precipitate-free surface morphology, Figures 5.3 (a-c). However, they present rather unconnected LSCO grains that could impair the transport properties of the film, as it has been already reported for analogous (La,Sr)MnO₃ films.[390] LSCO films from DEA solution processed in O₂ atmosphere present an enhanced grain connectivity that is probably attained to the chelating effect of diethanolamine, Figure 5.3 (d), but this solution chemistry favors the formation of large Cr-rich, star-shaped precipitates (inset) as confirmed by SEM-EDX in Figure A5.3.

In contrast, when LSCO films from DEA solution are processed in air, Figure 5.3 (e), the formation of such precipitates is successfully avoided obtaining highly homogeneous films with dense surface morphology, suggesting that the Cr-rich precipitates present in Figure 5.3 (d) could be formed during the strong exothermic decomposition reaction identified in oxidizing atmosphere in the TGA-DSC analysis of Figure 5.1 (d).

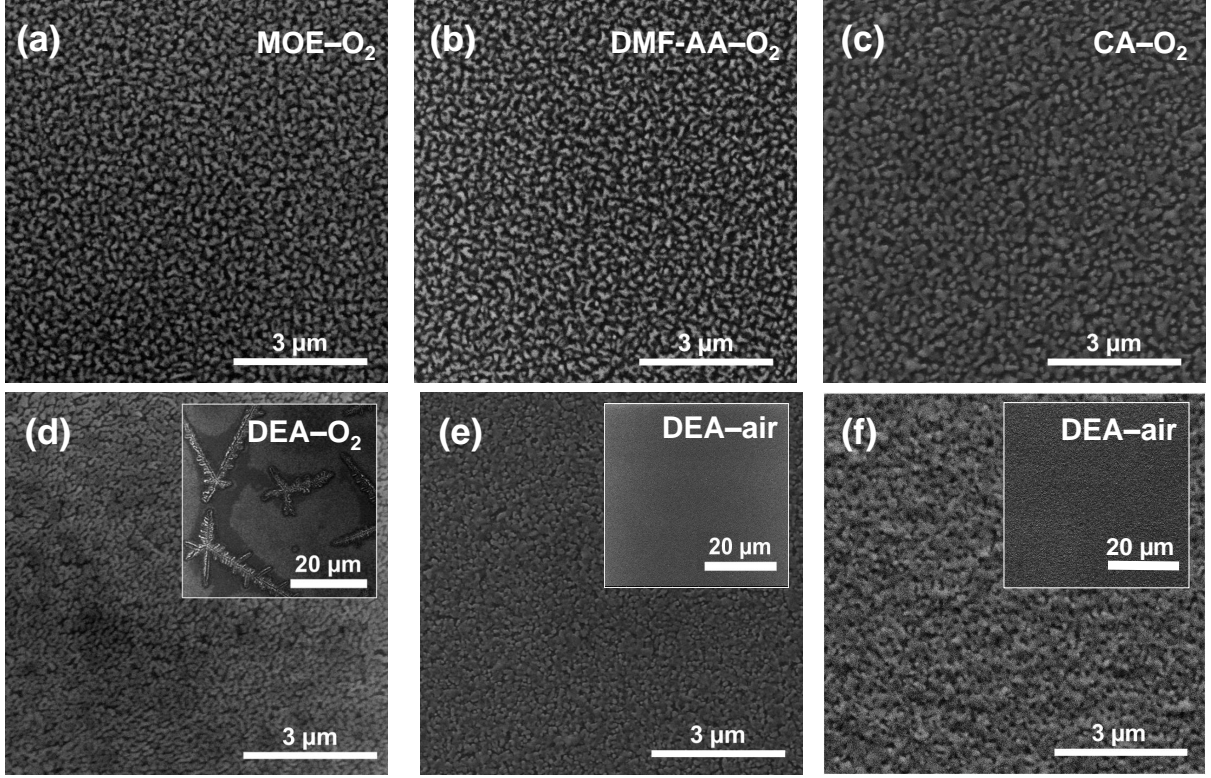


Figure 5.3: Scanning electron microscopy images of LSCO thin films on STO substrate prepared from (a) MOE- O_2 atmosphere, (b) DMF-AA- O_2 atmosphere, (c) CA- O_2 atmosphere, (d) DEA- O_2 atmosphere, (e) DEA-air atmosphere and (f) LSCO on LAO substrate from DEA-air.

In addition, the influence of the precursor chemistry on film crystallinity has been evaluated. Figure 5.4 shows the XRD θ - 2θ scan of LSCO thin films prepared on (001)-STO substrates from the different solution chemistries here studied. The main Bragg reflection at 72.55° corresponds to (003) STO substrate whereas the reflection at $\sim 73.15^\circ$ can be assigned to (003) LSCO, evidencing a *c*-axis oriented growth for all solution chemistries. Note that subtle variations observed in (003) LSCO Bragg reflection intensity could be mostly attributed to the slight difference in film thickness (40 nm for MOE films vs 70 nm for CA films). On the other hand, wider θ - 2θ scan confirmed phase pure and (001) oriented growth of the films, Figure A5.4.

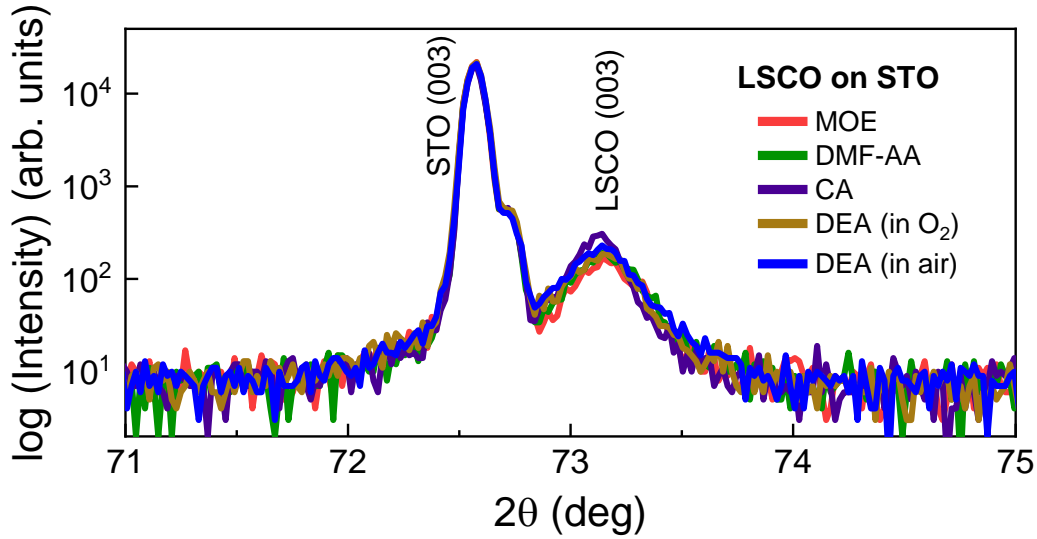


Figure 5.4: XRD θ - 2θ scan of LSCO thin films from different solution chemistries grown on (001)-STO substrate.

On the basis of these results, we have been able to establish an optimized process to prepare dense and epitaxial LSCO thin films on STO from DEA solution processed in air atmosphere, demonstrating the strong influence of solution chemistry and processing conditions on thin film surface morphology quality.

5.2.4 Optical properties

The optical transmittance of ~ 45 nm - LSCO films has been obtained with an spectroscopic ellipsometer in photometry mode from 300 nm to 1000 nm and compared to the transparent, although insulating, LCO parent compound film, Figure 5.5. As expected, the transmittance of LCO almost identical to that of the STO substrate, whereas LSCO film presents absorption near 450 nm because of the slight brown coloration, as it can be observed in the pictures below the transmittance curve. LSCO film presents an average optical transmittance of $\sim 67\%$, which is comparable to that of 67 nm - $\text{La}_{0.88}\text{Sr}_{0.12}\text{CrO}_3$ on STO (%T = 63.4%) and to the *n*-type TCO counterparts 50 nm - SrVO_3 and 40 nm - CaVO_3 , that reported %T of $\sim 60\%$. [191, 192]

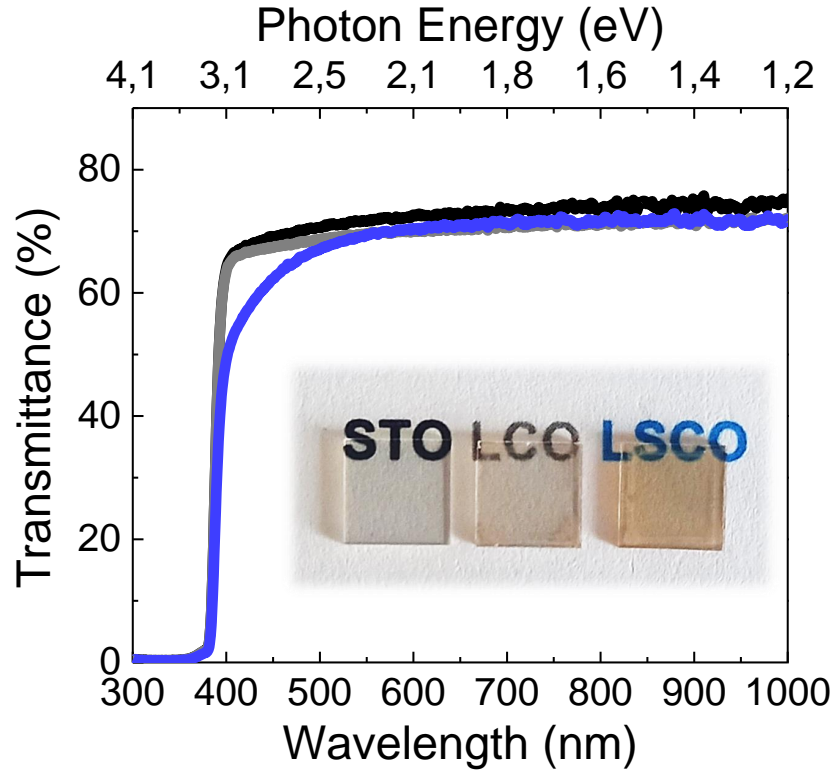


Figure 5.5: Optical transmittance spectra of STO substrate, 45 nm - LCO and 45 nm - LSCO thin films on STO from 300 to 1000 nm. Inset shows photographs of the substrate and the samples.

5.2.5 Electrical properties

The electrical resistivity of vacuum deposited epitaxial LSCO films is reported to be higher on STO substrates than on LAO due to strain effects.[204, 202, 203] Indeed, no measurable electrical conductivity was found for our CSD-LSCO films on STO. Therefore, for the purpose of this study, the electrical properties of ~ 45 nm - LSCO films have been measured on LAO substrates. Note that these films present homogeneous, dense and slightly rougher surface morphology than LSCO on STO, see Figures 5.3 (f) and A5.6 (b), probably due to the larger lattice mismatch imposed by the substrate. Figure 5.6 shows the temperature dependence of LSCO, $\rho(T)$, measured in the range of 150 - 350 K. The resistivity at room temperature, 300 K, is $1.4 \Omega\cdot\text{cm}$, one order of magnitude higher than that expected from vacuum-deposited LSCO films with the same Sr doping concentration on LAO substrates.[202] This is also reflected on the residual resistivity ratio (RRR) calculated from $\rho(300 \text{ K})/\rho(150 \text{ K})$ resulting in smaller values (0.024) than MBE films.[202] The same trend has been reported for other CSD-processed *n*-type TCO perovskite thin films when compared to their vacuum-processed counterparts.[374, 376, 377, 391, 379, 392]

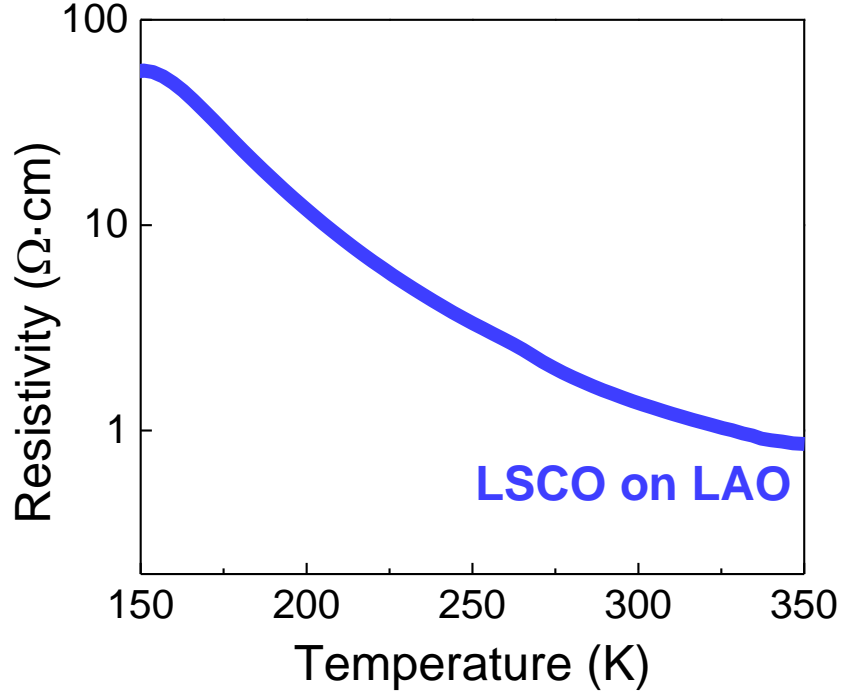


Figure 5.6: Temperature dependence of the electrical resistivity of 45 nm - LSCO on LAO from 150 to 350 K.

5.2.6 Detailed structural analysis

In order to better understand the origin of this behavior, a detailed structural and strain analysis have been performed on LSCO films grown on LAO. In-plane texture of LSCO on LAO has been investigated from phi-scan, $\Delta\phi_{(103),LSCO} = 1.4^\circ$ and $\Delta\phi_{(103),LAO} = 0.2^\circ$, and the out-of-plane texture from the rocking curve, $\Delta\omega_{(003),LSCO} = 0.4^\circ$, which confirm that films are biaxially textured, see Figures 5.7 (a,b). From XRD-RSM carried out around the asymmetrical (103) reflection, Figure 5.7 (c), the in-plane, a , and out-of-plane, c , lattice parameters of LSCO have been extracted considering a pseudocubic symmetry, resulting $a = 3.867 \pm 0.023 \text{ \AA}$ and $c = 3.896 \pm 0.005 \text{ \AA}$ ($a_{LSCObulk} = 3.876 \text{ \AA}$). [202, 203, 204] The films show subtle in-plane compressive strain of -0.232 %, and an out-of-plane tensile strain of 0.516 %. These results were further confirmed from strain maps by STEM images using geometrical phase analysis (GPA), included in Figure A5.5. This behavior differs from the results reported from MBE-LSCO films on LAO, which displayed -2.1% compressive strain. [204, 202] This difference in strain could be attained to the the different nucleation and growth thermodynamics of CSD films [393] which tend to produce relaxed and epitaxial oxide films with the formation of structural defects. [394, 395, 396, 397] Notoriously, detrimental effect of structural defects such as antiphase boundaries on the electrical resistivity has

already been reported in Fe_2O_3 films.[398]

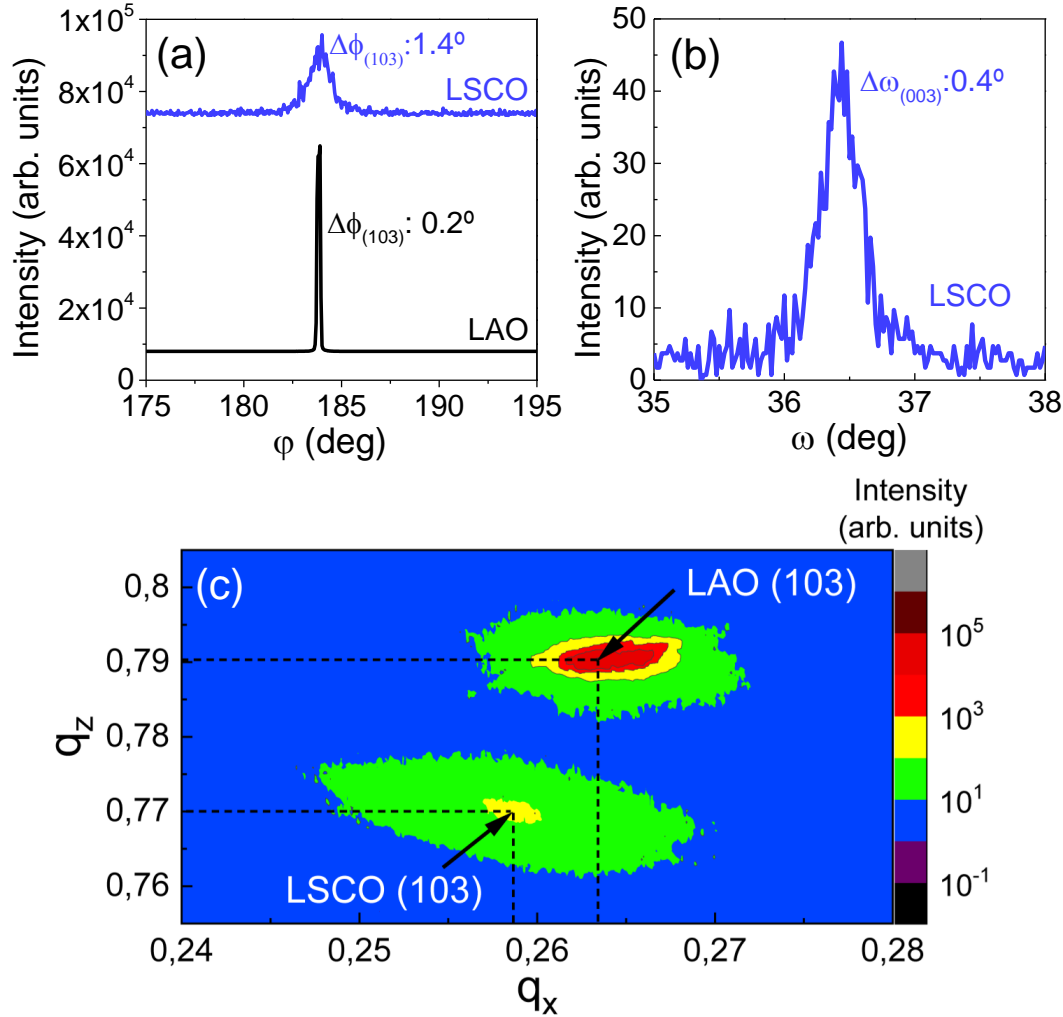


Figure 5.7: Structural study of LSCO thin film grown on LAO substrate. (a) ϕ scan of LSCO compared to LAO, (b) rocking curve of LSCO and (c) RSM around the (103) LSCO reflection.

Deeper exploration of the crystalline structure of LSCO through high-resolution STEM HAADF images indeed reveals the formation of significant amount of two types of structural defects in the film, namely antiphase boundaries and misfit dislocations. Figures 5.8 (a,b) show two types of antiphase boundaries running along the (010) and (011) perovskite crystallographic planes, respectively. In these defects, one BO_2 plane (from ABO_3 structure) is suppressed, and the two crystals are relatively shifted along a glide plane with a $\frac{1}{2}\{111\}$ shift vector, forming a rock-salt structure at the fault. The glide plane will overlap the A and B site of the perovskite structure when viewed perpendicular to the fault plane, as in the right area in Figure 5.8 (a), thus the relative Z-contrast of the A and B site equates. Figure 5.8

(b) shows an edge-on image of the antiphase boundaries with a relative shift of $\frac{1}{2}\{101\}$ of the crystal structure at both sides of the antiphase boundaries plane. Additionally, the formation of misfit dislocations is also observed near the substrate interface, Figure 5.8 (c). The misfit dislocations may form an array along the interface as observed in the GPA analysis in Figure A5.5. These extended defects are spontaneously formed to relax the misfit strain imposed by the substrate. Therefore, it is suggested that structural defects influence the resistivity behavior in our LSCO films on LAO substrate. Additionally, preliminary studies of the influence of LSCO film roughness and thickness on the $\rho(T)$ behavior indicate that film resistivity increases in films with rougher surface morphology and poorly connected grains, Figure A5.6. Indeed, it has been widely studied that surface imperfections in transition metal complex oxides can produce significant changes on the electrical properties, as previously reported for other perovskite oxides (i.e. $\text{La}_{1-x}\text{Sr}_x\text{MnO}_3$). [399, 400] Further analysis of the $\rho(T)$ indicates that the data can be fitted to both band conduction and polaron hopping transport models, suggesting a competition between these two mechanisms, [202] details on the fitting and activation energies can be found in Figure A5.7.

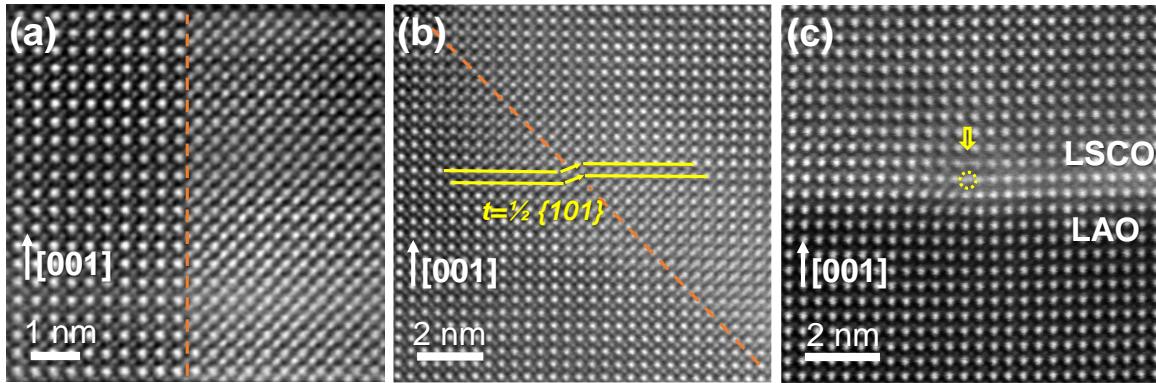


Figure 5.8: Structural defects found in LSCO thin films. (a,b) High-resolution HAADF images of antiphase boundaries where the boundary plane runs along the (010) and (011) crystallographic planes, respectively. (c) shows a dislocation core nucleated in the LSCO film near the substrate interface.

To gain further understanding on the role of Sr doping on the crystallinity and Cr $3d$ - O $2p$ orbital hybridization in the CSD-LSCO films on LAO, cross-sectional STEM-EELS have been acquired and compared to LCO. Figures 5.9 (a,c) show continuous ~ 45 nm - LCO and LSCO films, with clearly improved homogeneity and smoothness upon Sr-doping. Moreover, higher magnification STEM images, Figures 5.9 (b,d), confirm the epitaxial growth of LCO and LSCO films on LAO substrate with atomi-

cally sharp interfaces. The higher resolution inset images show atomic resolution images of both LCO and LSCO structures viewed along the (100) direction.

Due to the low concentration of Sr-doping in the LSCO films, no obvious Z-contrast difference or structural changes are observed when compared to the undoped LCO. In order to investigate possible electronic structure changes as a consequence of Sr-doping, the O K-edge and Cr $L_{2,3}$ -edge spectra of CSD-LCO and LSCO have been acquired by means of monochromated-beam EELS, see Figure 5.9 (e). The spectral Cr $L_{2,3}$ -edge of LCO shows three main peaks between 573 eV and 583 eV, which correspond to the L_3 line, and two peaks between 583 eV and 591 eV from L_2 line. The energies and line shape of these peaks are characteristic of Cr^{3+} , as it has been reported for Cr_2O_3 and LCO.[401, 202] On substituting La by Sr, it is observed that the Cr $L_{3,2}$ line shape pattern changes, the Cr L_3 line-width broadens, and the peaks indicated by blue arrows increase in intensity, turning towards spectral signatures representative of Cr^{4+} . These features would be consistent with the localization of holes doped in a lattice of Cr ions.[402, 202]

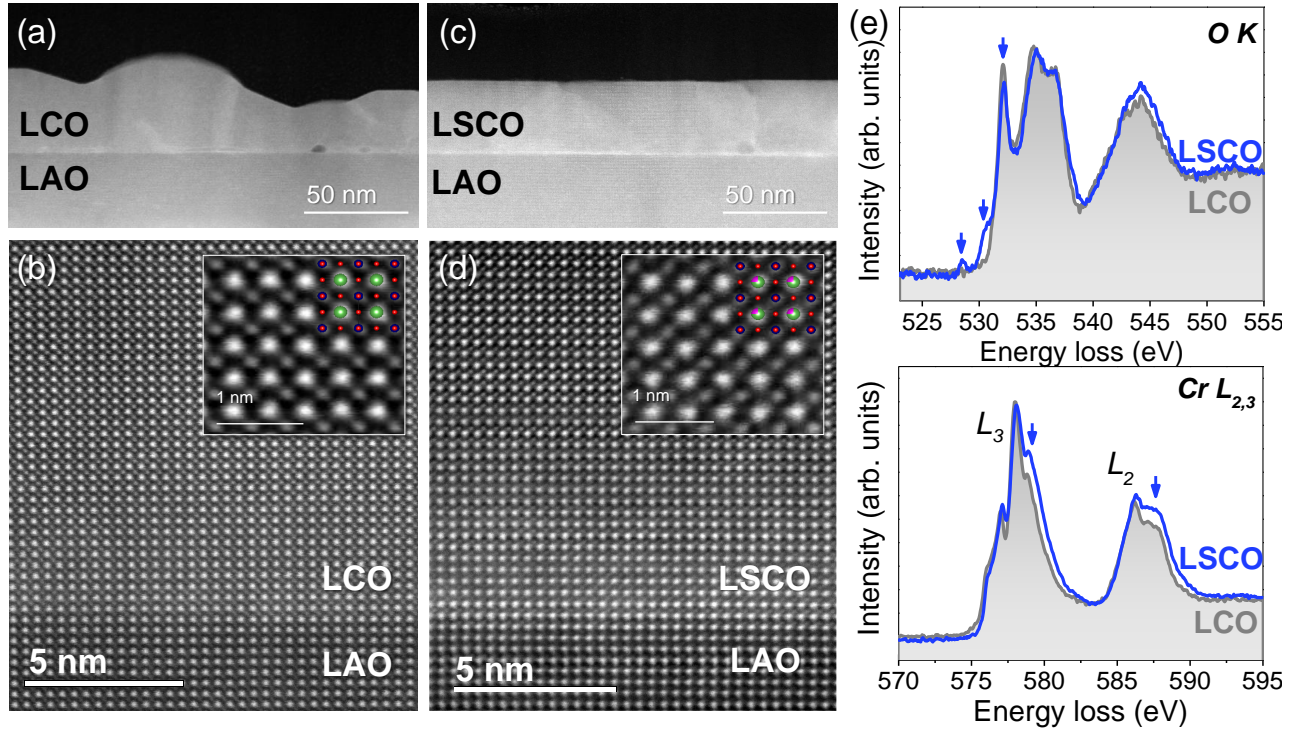


Figure 5.9: Z-contrast cross-section STEM images of (a,b) LCO on LAO and (c,d) LSCO on LAO. The insets in (b,d) are atomic-resolution STEM images of the LCO and LSCO structures with the atomic models overlaid, where green atoms correspond to La, red to Cr and pink to Sr. (e) O K-edge and Cr $L_{2,3}$ -edge monochromated-EELS spectrum of LCO and LSCO on LAO. The blue arrows point to the characteristic spectral changes induced by the Sr doping.

Moreover, the spectral O K-edge provides further details related with the unoccupied density of states of transition metal character. For LCO, a set of three peaks is observed between 525 eV and 539 eV, in well agreement with earlier reports of LCO films.[202] Upon Sr-doping, it is observed two new features at 528.5 eV and 531 eV and the decrease in intensity of the peak at 532.5 eV, indicated by the blue arrows at Figure 5.9 (e), characteristic of Sr-doped LCO and related with the appearance of new unoccupied states and partial hybridization between O $2p$ and Cr $3d$ orbitals from the bottom of the conduction band.[201, 202] These features are in line with the observed shift to lower binding energies of the XPS core-level spectra of Cr $2p$, La $3d$ and O $1s$ of LSCO films compared to LCO, which can be associated with the modification of the chemical potential towards the valence band. See XPS analysis included in Figures A5.8 and A5.9. This behavior appears to be a common phenomenon of hole-doped perovskite oxides [203, 403, 404] and could explain the introduction of holes in our Sr-substituted LCO films and therefore, the enhanced electrical conductivity compared to the highly resistive LCO.

5.3 Conclusions

In this Chapter a cost-efficient chemical route to prepare LSCO thin films has been developed. It has been demonstrated that the solution chemistry strongly influences the film morphology in which the combination of nitrate precursors, 2-methoxyethanol, acetic acid and diethanolamine processed in air results in dense, epitaxial and slightly strained films. These LSCO films display $\sim 67\%$ optical transparency in the visible spectrum being as good as those reported for some of the most promising state of the art TCOs. The values of the electrical resistivity are roughly higher than those expected based on the film chemical doping and strain state and it is attributed to the presence of structural defects. It is also revealed that Sr doping in LaCrO_3 changes the electronic structure, unoccupied states are formed in O $2p$ together with the formation of Cr^{4+} which determine its physical properties. On the basis of these results, several approaches are envisaged to continue improving the CSD-LSCO film performance including the growth on lattice matched substrates to modulate the strain, to reduce the presence of antiphase boundaries, and refine the La/Sr ratio to further boost the conductivity without diminishing the optical transmittance. It is expected that this work will stimulate further investigations on the use and improvement of LSCO as p -type transparent conducting perovskite oxide, for instance as an additional interface engineering strategy to improve the efficiency of hole collection in PV systems based on photoferroelectric perovskite oxides. Moreover, experimental efforts could be dedicated on solution processing as a cost-effective and feasible route to develop functional complex oxides that can

be of use in many energy and electronic applications.

Chapter A5

Annex Information of Chapter 5

A5.1 Study on metalorganic route

Studies have been conducted to evaluate metalorganic versus metal nitrate precursors for the preparation of LSCO thin films. For metalorganic precursors route: La, Sr, Cr acetates and a solvent blend of acetic acid and water (5:1) were initially selected but it led to non-homogeneous solutions with Cr-rich precipitates (not shown here). As an alternative, Cr acetylacetonate was tested in combination with La and Sr acetates and using the same solvent blend (acetates-acetylacetonate route), that resulted in an homogeneous solution. TGA/DSC analysis allowed to identify the starting conditions for the thermal treatment to stabilize the LSCO phase, see Figure A5.1 (a). The TGA curve shows the main mass loss at temperatures below 290 °C (~50%). At these temperatures, simultaneous phenomena occur, including dehydration of metal precursors and decomposition of Cr acetylacetonate into acetone and CO₂, which is related the endothermic peak at ~210 °C.[405, 406] At temperatures above 300 °C decomposition of acetic acid into CH₄ and CO₂,[387] and La and Sr metal precursors takes place. La acetate decomposes into carbonates (300 - 350 °C) and oxycarbonates (~450 °C) [407] and Sr acetate into carbonates (~450 °C).[408] In addition, the reaction product gases and acetone decompose at temperatures above 500 °C.[409] These events are related to the presence of exothermic peaks at temperatures of ~430 °C and ~570 °C. The downward trend of DSC curve observed at high temperatures could indicate the presence of an endothermic peak above 900 °C that could be related with the crystallization of LSCO (not shown here).[388, 389]

Before deposition, rheometry study of the solution revealed a viscosity of 0.0042 Pa·s, which has been reported to ensure effective wettability of single crystal perovskite substrates.[329] However, the spin

coated films resulted with inhomogeneities unraveling solution instability, Figure A5.1 (b). The thermal treatment was designed based on TGA-DSC analysis; a low-temperature thermal treatment at 90 °C for 10 minutes was carried out for dehydration and film gelation, followed by a mild thermal treatment at 300 °C for organic decomposition and a high temperature thermal treatment at 850 °C for 45 minutes under O₂ flow for phase crystallization. However, only reflections corresponding to the substrate, (003) STO, have been observed in the XRD θ - 2θ scan, indicating that no preferred (00l) oriented growth of LSCO is achieved, Figure A5.1 (c). Note that the inset in the latter figure shows the corresponding thermal treatment profile. In addition, SEM surface morphology images revealed a dramatically porous film, Figure A5.1 (d). Envisaging a very challenging process to improve the quality of the film, it has been decided to switch to the use of nitrate precursors.

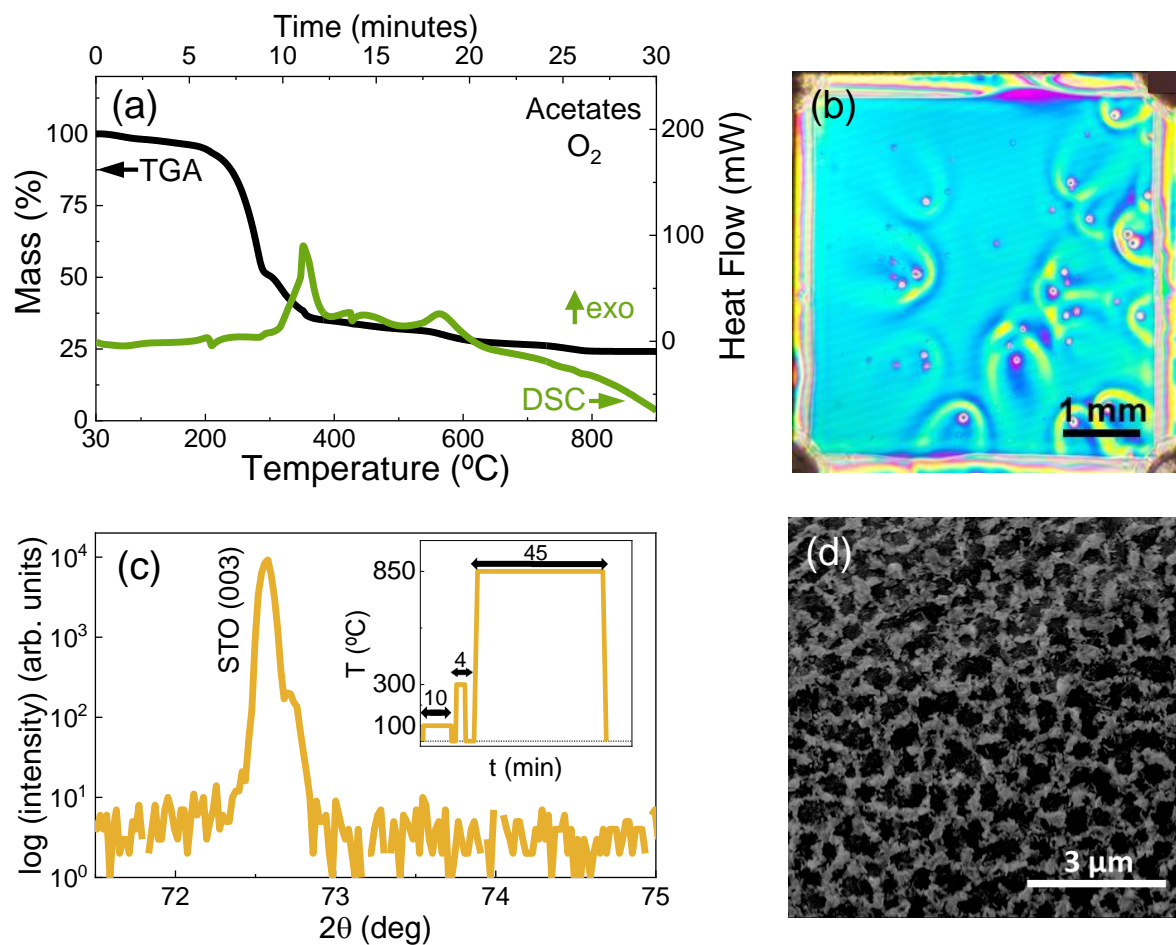


Figure A5.1: Evaluation of the preparation of LSCO thin films from acetates-acetylacetonate route. (a) TGA-DSC curves obtained at $30\text{ }^{\circ}\text{C}\cdot\text{min}^{-1}$ from $30\text{ }^{\circ}\text{C}$ to $900\text{ }^{\circ}\text{C}$ in O_2 atmosphere. (b) Optical microscope image of the as-deposited film at 6000 rpm for 30 seconds, (c) XRD θ - 2θ scan showing no reflection for the LSCO thin film on (001)-STO after thermal treatment at $850\text{ }^{\circ}\text{C}$ for 45 minutes under O_2 flow (inset shows the thermal treatment profile) and (d) corresponding SEM image.

A5.2 Solution preparation

For the preparation of the solutions denoted as MOE, DMF-AA and DEA, the metal nitrate precursors were mixed in an organic solvent blend of 2-methoxyethanol and acetic acid (3:1). DMF-AA solution was obtained from the addition of NN-dimethylformamide and acetylacetone as stabilizers in a molar ratio to total metal cations of (1:2), whereas DEA solution was prepared from the addition of the chelating agent diethanolamine in molar ratio to Cr of (1:4). On the other hand, CA solution was obtained from

mixing the nitrate precursors in water and using citric acid in molar ratio to total metal cations of (2:1) to minimize the hydrolysis and condensation reactions. For additional information refer to Experimental Section 2.2.

A5.3 Fine tuning of processing conditions

The best conditions for crystallization of LSCO thin films on (001)-STO substrate have been determined through fine tuning of the temperature (700 - 900 °C) and dwell time (15 - 45 min) according of the TGA-DSC analysis. As a case example, the influence of the processing conditions on the surface morphology and crystallinity has been evaluated for the MOE solution by XRD θ -2 θ scan and SEM, Figure A5.2. Based on this study, the optimized crystallization processing involves heating the samples up to 850 °C for 45 minutes with heating and cooling ramps of 660 °C/minute.

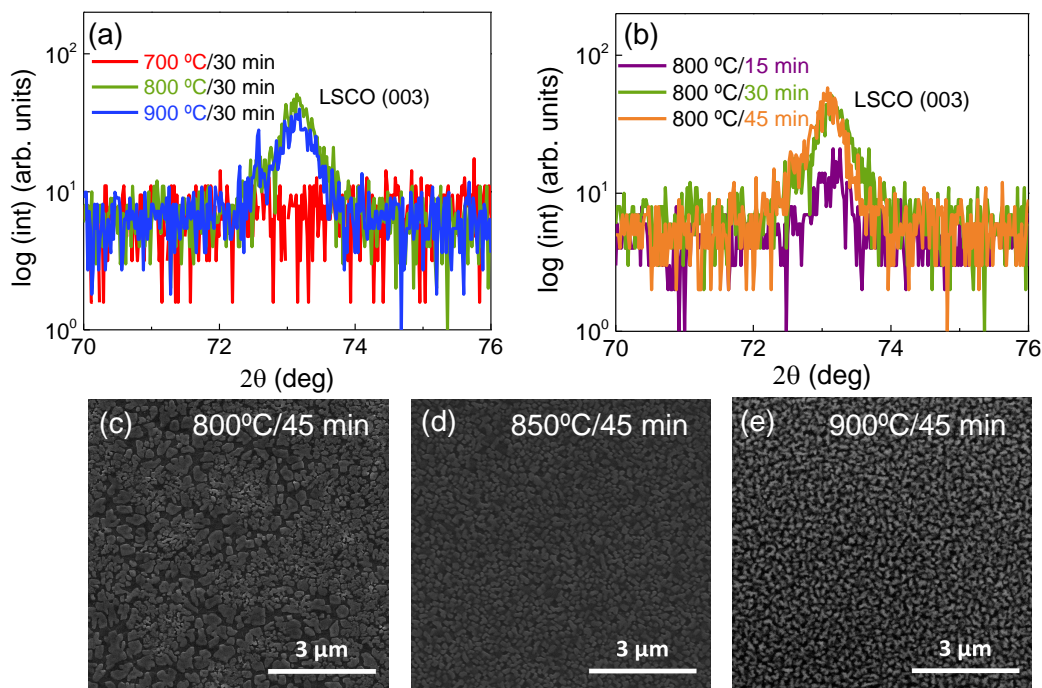


Figure A5.2: XRD θ -2 θ scans of LSCO thin films grown on (001)-STO from MOE solution under different (a) annealing temperatures and (b) annealing times. SEM images for films grown at (c) 800 °C, (d) 850 °C and (e) 900 °C for 45 minutes.

Figure A5.3 (a) shows the SEM image of the studied zone of the sample, indicating the two areas that are analyzed by EDX. Area 1 corresponds to the homogeneous matrix of the film and area 2 to the

precipitate. From the EDX analysis, Figure A5.3 (b), C, O, Sr, La, Ti and Cr have been identified. The area corresponding to the precipitate presents higher content of Cr than that of the homogeneous zone of the film, indicating the Cr-rich nature of the star-shaped precipitate.

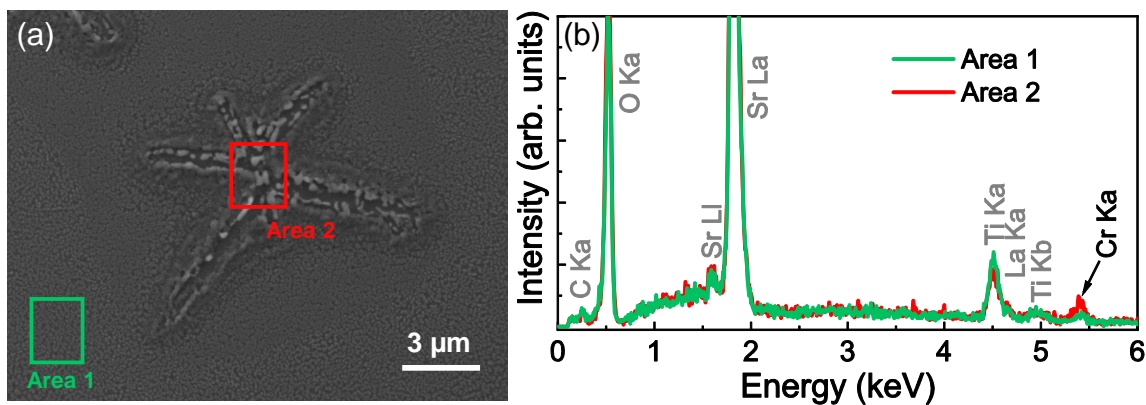


Figure A5.3: SEM-EDX analysis of LSCO thin film from DEA solution grown on (001)-STO under O₂ atmosphere. Note that SEM image shows the analyzed areas for EDX spectra.

Additional θ - 2θ XRD scans have been performed on LSCO from DEA processed in air atmosphere. Figure A5.4 (a,b) reveal the presence of (001) reflections corresponding to LSCO and STO or LAO substrates, respectively, confirming phase pure and (001) oriented growth of the films.

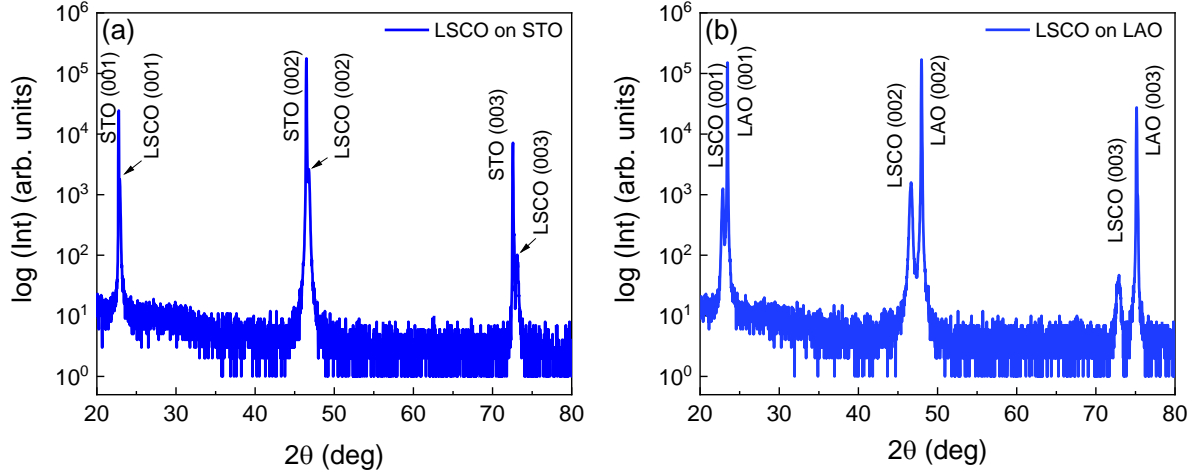


Figure A5.4: XRD θ - 2θ scan of LSCO from DEA-air on (a) (001)-STO and (b) (001)-LAO.

A5.4 Detailed structural characterization

To gain more insights in the local strain state of the LSCO films, we analyzed high-resolution STEM images with the geometrical phase analysis (GPA) tool. Figure A5.5 (a) is the HAADF images of LSCO films on LAO, seen along the $[010]$ direction. The inset corresponds to the Fast Fourier Transform (FFT), where it is shown the splitting of the LSCO reflections from the ones of LAO, suggesting that the films are in a relaxed strain state. Masking out the $g(100)$ and the $g(001)$ reflections of the FFT, we computed the in-plane ϵ_{xx} and out-of-plane ϵ_{yy} mismatch strain component maps with compared to LAO substrate, being $\sim +2.4\%$, Figure A5.5 (b,c). The color scale in the maps refers to the lattice spacing variation from a reference LAO substrate ($a_{bulk} = 3.796 \text{ \AA}$). From the maps, we also obtain a -LSCO $\sim 3.877 \text{ \AA}$ and c -LSCO $\sim 3.884 \text{ \AA}$. These results reinforce the relaxed state of the film and they are in well agreement with the XRD measurements.

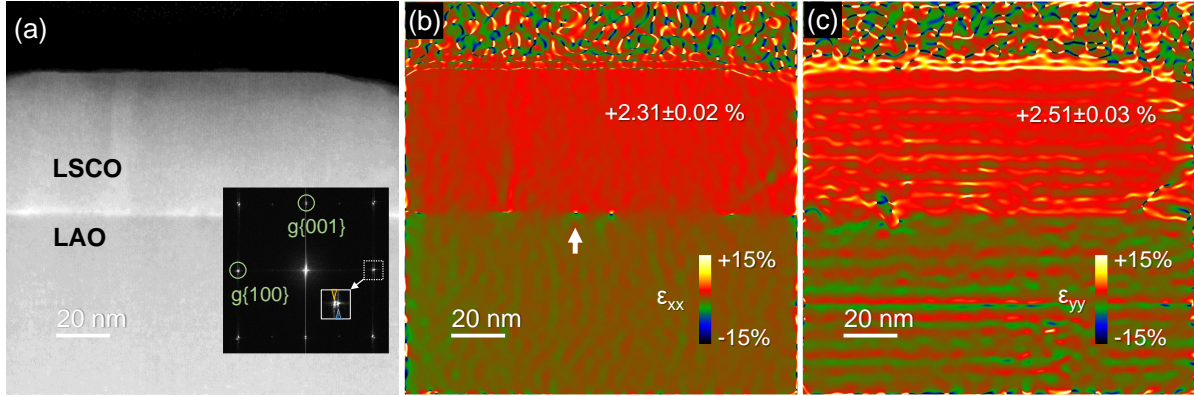


Figure A5.5: Geometrical phase analysis of the LSCO films. (a) HAADF cross sectional image of LSCO films grown on LAO substrate. The inset corresponds to FFT, where the yellow and blue arrows point to the splitting of the (100)-LSCO and (100)-LAO reflections, respectively. (b) In-plane ϵ_{xx} and (c) out-of-plane ϵ_{yy} strain component maps of the image in (a). The white arrow in the ϵ_{xx} map points to the formation of misfit dislocations at the interface.

A5.5 Electrical characterization

Influence of LSCO film thickness:

The influence of LSCO film surface roughness and thickness on the electrical resistivity, ρ , has been systematically evaluated in Figure A5.6. For this study, a series of LSCO films with different thickness have been prepared on (001)-LAO substrate by modifying the concentration of the DEA precursor solution which is well known to be proportional to the thickness.[410] The thickness of 0.25 M precursor solution is accurately determined from the TEM analysis, 45 nm (Figure 5.9 of Chapter 5). Taking this thickness as a reference, precursor solutions of 0.12, 0.25 and 0.50 M have been prepared to fabricate LSCO films with theoretical thickness of 20 nm, 45 nm and 90 nm, respectively. The surface morphology of the corresponding films has been studied by AFM topography images, Figures A5.6 (a-c). The thinnest film shows an inhomogeneous surface dictated by large pores and few outcrops. By increasing the film thickness the surface becomes more homogeneous with well defined grain size, typical of the CSD island-growth. The root mean square (rms) surface roughness calculated from these topographic images increases from 11 nm to 37 nm by increasing the film thickness, thus revealing a high surface roughness. The fact that the surface roughness increases with thickness could be attained to the high concentration of solute in the precursor solution which has a direct impact on the growth kinetics, as previously reported in CSD-processed ZnO films.[411] On the other hand, XRD θ - 2θ scans are depicted in Figure

A5.6 (d) and indicate c -axis orientation in all LSCO films. It can also be identified a gradual shift in the 2θ towards higher angles which could indicate film relaxation from epitaxial strain, Figure A5.6 (d). Clear changes are observed in the intensity of (003) LSCO reflection that increases with solution concentration and can be related with film thickness and crystallinity.[412] By correlating the studied thickness of 45 nm for 0.25 M solution concentration with the integrated (003) LSCO reflection intensity from XRD, it has been estimated that 0.12 M and 0.5 M solution produce films of ~ 18 nm and ~ 94 nm thickness, respectively. The $\rho(T)$ has been measured and compared for the three films showing that the resistivity for the 18 nm and 94 nm films is notably higher at room temperature. The poor conductivity of these 18 and 94 nm films is further disclosed for the impossibility to acquire the $\rho(T)$ for the whole range of temperatures (150 K - 350 K), Figure A5.6 (e). These results evidence that the films that show a surface morphology with poorly connected grains lead to high resistivity and it is very likely that this parameter dominates over the possible existence of epitaxial strain. Indeed, it is widely studied that surface imperfections in transition metal oxide films can widely produce changes on the electrical properties, as previously reported for other perovskite oxides (i.e. $\text{La}_{1-x}\text{Sr}_x\text{MnO}_3$).[399, 400]

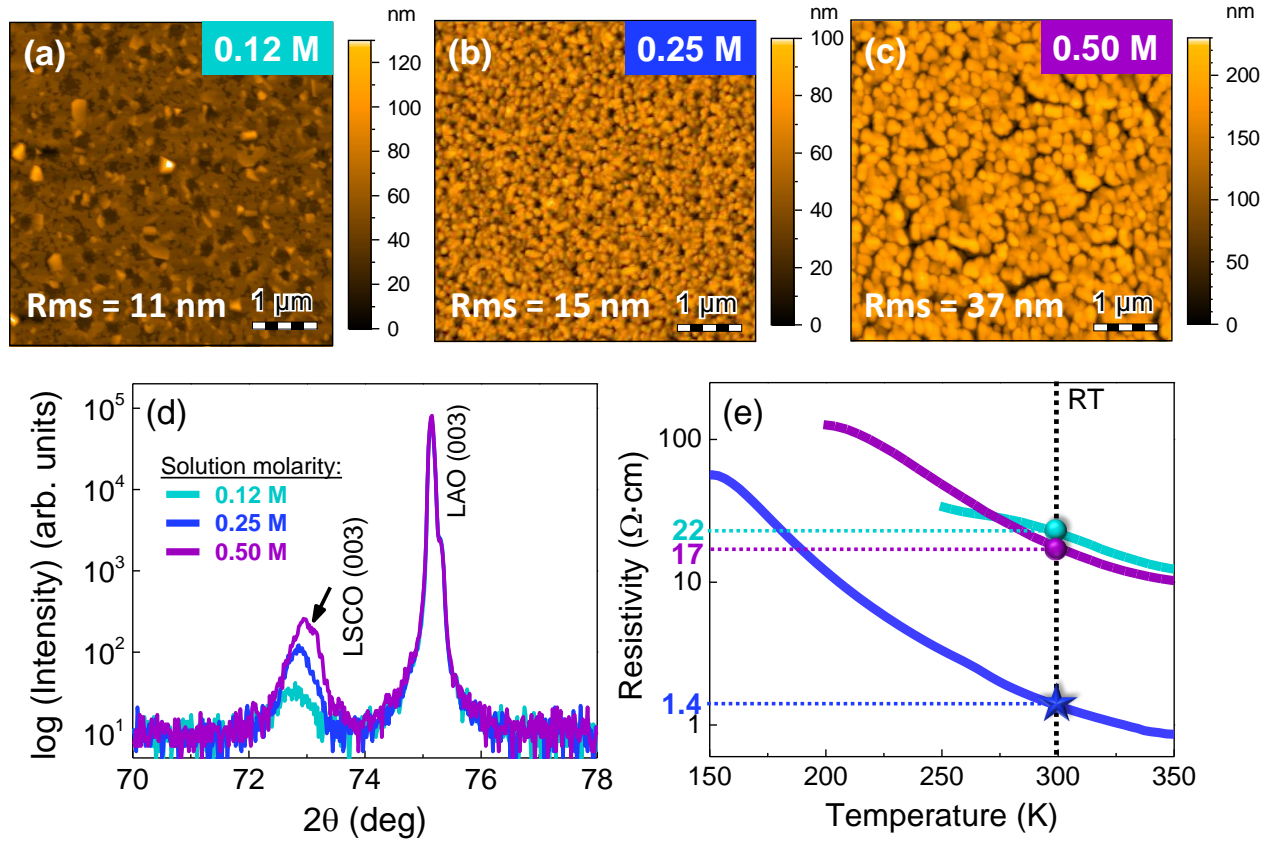


Figure A5.6: Systematic study on thickness-roughness influence on electrical resistivity of LSCO on (001)-LAO from DEA formulation of 0.12 M (~ 18 nm), 0.25 M (45 nm) and 0.5 M (~ 94 nm). (a-c) AFM topography images (d) XRD θ - 2θ scan and (e) temperature dependence of the electrical resistivity of the corresponding films.

Fits of electrical resistivity to transport models:

Fits of resistivity measurements from 150 to 300 K to band conduction ($\rho \propto \exp(E_a/kT)$) and small polaron hopping ($\rho \propto T \cdot \exp(E_a/kT)$) transport models. The estimated activation energies (E_a) have been deduced from these fits and are 0.032 eV for band conduction model and 0.038 eV for polaron hopping model, lower than those reported for epitaxial MBE-LSCO thin films on (001)-LAO.[202]

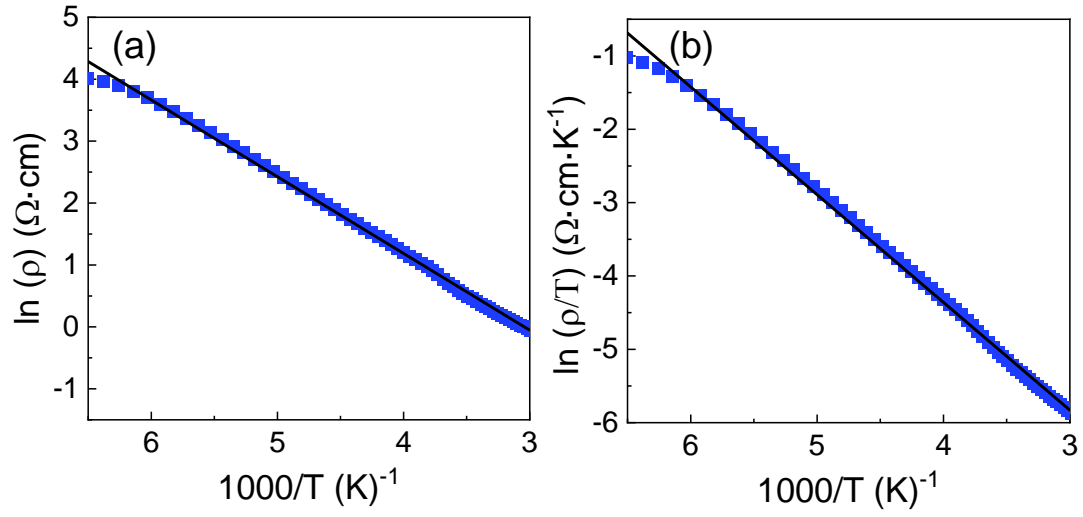


Figure A5.7: Fits of resistivity data to (a) band conduction and (b) polaron hopping transport models for LSCO film on LAO.

A5.6 Surface chemical analysis

In order to obtain further information on the surface chemical composition of undoped LCO and LSCO films, XPS analysis has been performed. Figure A5.8 shows the core-level spectra of Cr $2p$, O $1s$, La $3d$ and Sr $3d$ calibrated in energy using the C $1s$ centered at 284.9 eV, Figure A5.9.

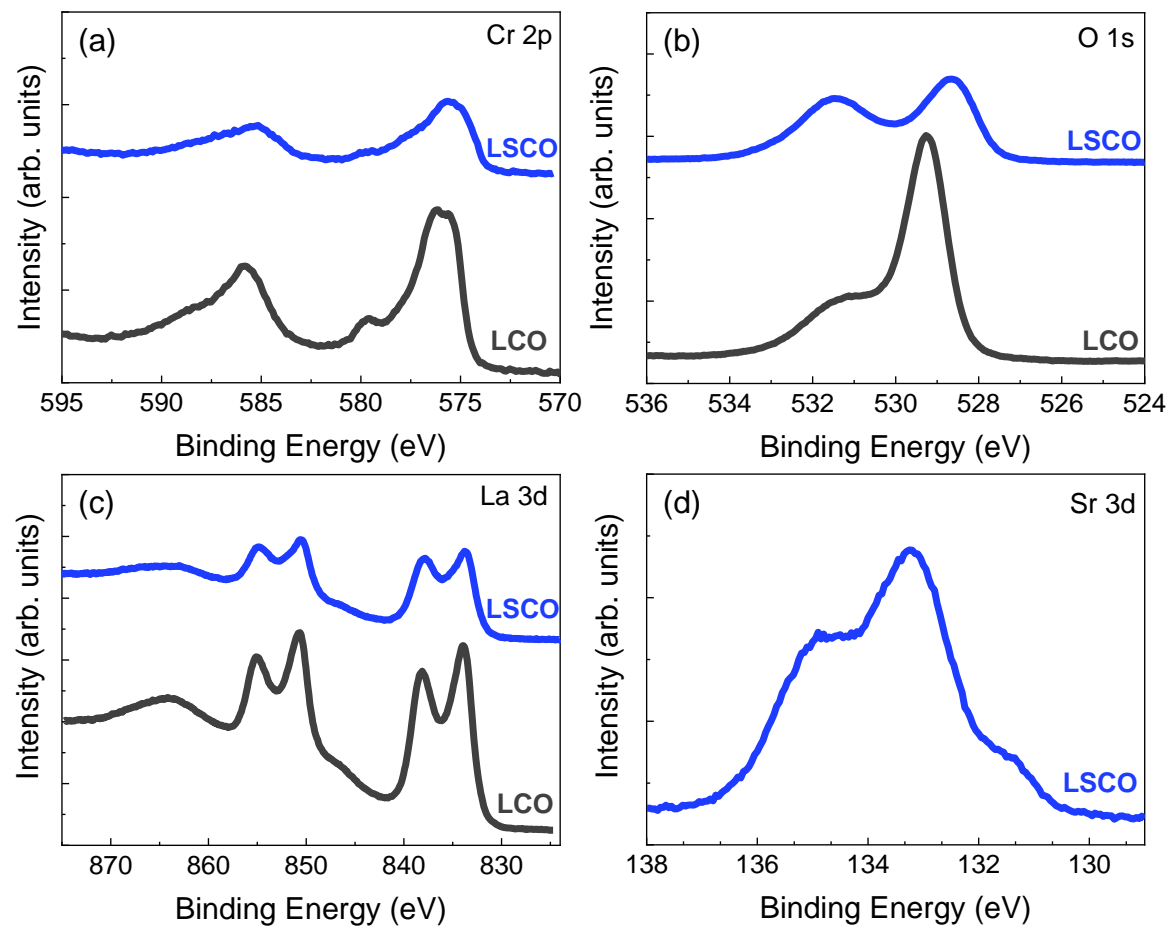


Figure A5.8: High resolution core level XPS spectra of (a) Cr $2p$, (b) O $1s$, (c) La $3d$ and (d) Sr $3d$ for LCO (grey) and LSCO (blue).

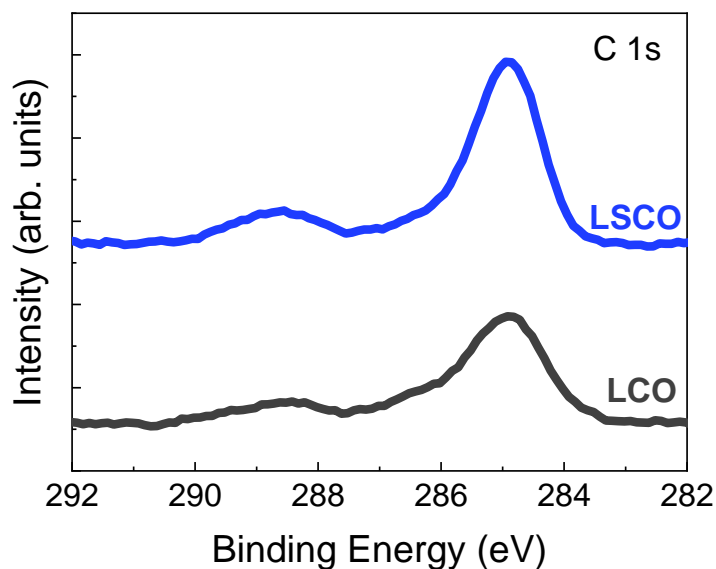


Figure A5.9: *C 1s* core level XPS spectra for LSCO and LCO films calibrated at 284.9 eV

The Cr *2p* spectra mainly show the fingerprint of Cr³⁺ species with Cr *2p*_{3/2} peak centered at 576 eV for LCO and 575.5 eV for LSCO.[413, 414, 415, 202] Both spectra also show a small contribution of Cr⁶⁺, weak peak centered at ~ 579 eV, attributed to sample surface oxidation due to air exposure prior to XPS analysis.[202] Note that the presence of the Cr⁶⁺ hinders the unambiguous detection of the possible formation of Cr⁴⁺ species upon Sr-doping. The O *1s* core level spectra, Figure A5.8 (b), show two contributions, the low-binding energy peak centered at 529.2 eV for LCO and 528.7 eV for LSCO, which corresponds to O-lattice in oxides, and the high-binding energy peak associated to adsorbed H₂O, OH and organic contamination.[260, 202] The La *3d* spectra, Figure A5.8 (c), show the typical La *3d*_{3/2} and La *3d*_{5/2} doublet peaks with a spin-orbital splitting energy of ~ 16.8 eV, characteristic of La³⁺. [260] In this case, peak binding energies are downward shifted 0.3 eV for LSCO samples. Finally, the Sr *3d* core level spectrum, Figure A5.8 (d), presents two peaks, at 134.9 and 133.2 eV, which are attributed to Sr *3d*_{3/2} and Sr *3d*_{5/2} and corresponds to Sr-O bonds. The shoulder at 132 eV could be attributed to Sr atoms with different chemical environment, already identified in other Sr-perovskite oxides.[416, 417, 418] Notoriously, the line shapes of Cr *2p*, O *1s* and La *3d* are not affected by Sr-doping but the core level spectra show a nearly constant (0.2 - 0.3 eV) down shift in binding energy compared to LCO. This shift could be assigned to a change in chemical potential and appears to be a common phenomenon in other hole-doped perovskite oxides including (La,Sr)TiO₃ and (La,Sr)MnO₃. [404, 403, 284, 202]

Chapter 6

General conclusions and future perspectives

6.1 General conclusions

In this PhD thesis we have investigated the opportunities of cation engineering in BiFeO_3 to obtain epitaxial, pure phase and stable films and have better understanding on how it impacts the optical and electronic properties. We have identified that substitution of Fe by Co modulates the bandgap due to a change in the hybridization of Co $3d$ and O $2p$ orbitals. The coexistence of Co^{3+} and Co^{2+} provides the narrowest bandgap, supported by density functional theory studies. Then, for high loads of Cobalt, i.e. 30%, whose phase is challenging to stabilize but interesting for narrowest bandgap, the substitution of Bi by 10% La provides a robust alternative to obtain phase pure and epitaxial films without affecting the optoelectronic and ferroelectric properties. Nonetheless, the substitution of Bi by 10% Ce results in an inhomogeneous distribution of Ce where Ce-Co-O phases segregate on the film surface. Therefore, the choice of a cation with trivalent and stable oxidation state is preferred to perform Bi substitution.

Next, we have been able to fabricate a multi-layered system based on the photoferroelectric $\text{BiFe}_{0.9}\text{Co}_{0.1}\text{O}_3$ to design an all-oxide thin film PV device with the configuration: $\text{ITO}/(\text{ZnO})/\text{BiFe}_{0.9}\text{Co}_{0.1}\text{O}_3/\text{LSMO}/\text{STO}$. In this process, special attention has been paid to ensure the structural, optical and electrical compatibility of the different oxide layers. The use of a single-crystalline oriented STO substrate enables the epitaxial growth of the bottom electrode and the photoferroelectric film. The integration of ZnO and ITO top coatings, widely used in conventional PV, demonstrates to preserve the crystalline quality as

well as the smooth and homogeneous surfaces of the underlying films. Interestingly, a maximized optical transmittance throughout the device is promoted owing to the anti-reflective effect of these top coatings.

The resulting $\text{BiFe}_{0.9}\text{Co}_{0.1}\text{O}_3$ -based all-oxide devices exhibit a stable photo- and ferroelectric response for at least 2 months without encapsulation. We have first investigated the complex role of ferroelectricity on the photocurrent. We found out that the photogenerated currents of the $\text{ZnO}/\text{BiFe}_{0.9}\text{Co}_{0.1}\text{O}_3$ -based system are largely modulated ($\sim 68\%$) upon positive and negative ferroelectric polarization states. On the other hand, the incorporation of ZnO in the architecture increases the J_{sc} probably due to the formation of a large valence band offset which prevents holes back-recombination. It is also observed a slight loss in V_{oc} consistent with the formation of small built in potential extracted from the energy band diagram.

Building on the knowledge generated on cation substitution and interface engineering, the photoreponse and ferroelectric properties of co-substituted BFO (La-BFCO) has been assessed in a all-oxide architecture. Upon La-doping a three fold increase in V_{oc} and maintained J_{sc} are displayed. This behavior is mostly attributed to the improved quality of the co-substituted photoabsorber which can also provide better interface quality.

With the aim to explore an alternative approach to improve light absorption and photocurrent extraction in $\text{BiFe}_{1-x}\text{Co}_x\text{O}_3$, we have tackled the challenging preparation of compositional gradient relying on ALD and CSD. The attempt to prepare compositional gradients results in an inhomogenous distribution of cobalt throughout the film thickness. It is speculated that the use of high temperature treatment to obtain epitaxial films favors cation mobility and hinders the preparation of gradients with controlled cobalt distribution.

Finally, in order to provide alternatives to p -type TCO in epitaxial BiFeO_3 -based devices, we have developed an unprecedented chemical route to synthesize p -type $\text{La}_{0.75}\text{Sr}_{0.25}\text{CrO}_3$ thin films based on metal nitrate precursors. We demonstrate epitaxial and homogeneous growth using a solution-processing methodology. The resulting $\text{La}_{0.75}\text{Sr}_{0.25}\text{CrO}_3$ films show high optical transparency similar to that of the most promising state-of-the-art n -type TCOs with perovskite structure, and moderate electrical resistivity. It turns out that the higher resistivity values displayed in our solution-processed films, in

comparison to the vacuum-processed counterparts, could be attained to the presence of structural defects such as antiphase boundaries and misfit dislocations. It is concluded that electrical resistivity strongly depends on film crystallinity, structure perfection and surface morphology. Additionally, from the study of the electronic structure of $\text{La}_{0.75}\text{Sr}_{0.25}\text{CrO}_3$ it is observed the formation of new unoccupied states in O $2p$ as well as the presence of Cr^{4+} , which determine the physical properties of the system upon Sr-doping.

Figure 6.1 shows a summary of the conclusions obtained for this PhD thesis.

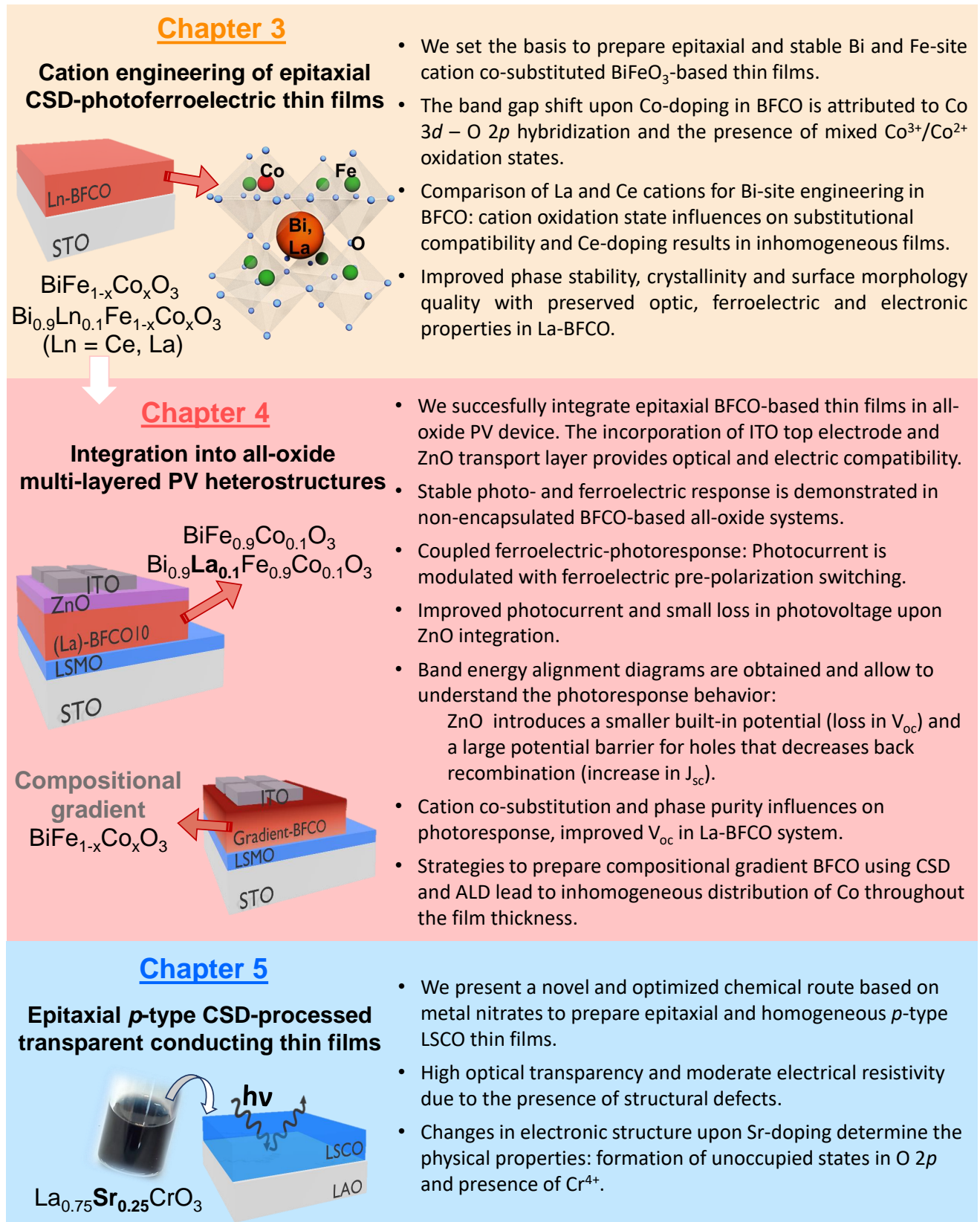


Figure 6.1: Summary of the main results obtained in each Chapter.

6.2 Future perspectives

In this PhD thesis, we have demonstrated the great versatility of the CSD as a simple and low-cost approach to design stable crystalline perovskite oxides with engineered cationic compositions. It is foreseen that the knowledge generated here could stimulate the development of solution-based synthetic routes for other unexplored perovskite oxides with refined cationic stoichiometry by simple cation intermixing. These novel compositions could yield structure and physical properties tailored on demand in materials for today's energy and electronic applications. Based on that, CSD emerges as a robust methodology to target optimal compositions that then could be easily adopted in other physical and chemical deposition techniques.

Judicious cation substitution in BiFeO_3 shows improvement in film stability and optical and ferroelectric properties. Obtaining larger V_{oc} and larger J_{sc} is still an issue. The study of the family of ferroelectric perovskite oxysulfide, i.e. performing anion substitution, could offer new venues in this field. Narrower bandgaps and strong ferroelectricity have been predicted for these materials.[419, 420]

The preparation of vertical composition gradient in epitaxial BFO by CSD is unsolved. The use of a low-temperature approach and compatible precursors (ALD) could be interesting to explore.

On the other hand, the stable BFO-based films developed in this thesis could find applications beyond PV for example in electronic devices for smart sensors. In such application, the high thermal and chemical stability as well as the robust ferroelectricity at room temperature could be leveraged to generate electrical outputs and signals from optical inputs such as UV illumination.[421]

The optimal PV device composition for epitaxial photoferroelectrics is still lacking. The structure compatibility in these photo-absorbers limits the choice of suitable transport layers and substrates. New perspectives could be envisaged when using epitaxial freestanding photoabsorbers because unlimited combination of components could come into play.[56]

The viability of LSCO as potential *p*-type TCO in perovskite oxide heterostructures needs to be studied. Testing it in BFCO systems could be the first approach.

List of contributions

ORCID: 0000-0002-4235-0370

Publications derived from this PhD thesis topic:

- **P. Machado**, M. Scigaj, J. Gazquez, E. Rueda, A. Sanchez-Diaz, I. Fina, M. Gibert-Roca, T. Puig, X. Obradors, M-Campoy-Quiles, M. Coll. Band Gap Tuning of Solution-Processed Ferroelectric Perovskite $\text{BiFe}_{1-x}\text{Co}_x\text{O}_3$ Thin Films. *Chemistry of Materials*, 2019, 31, 947-955. DOI: 10.1021/acs.chemmater.8b04380.
- N. Bein, **P. Machado**, M. Coll, F. Chen, M. Makarovic, T. Rojac, A. Klein. Electrochemical Reduction of Undoped and Cobalt-Doped BiFeO_3 Induced by Water Exposure: Quantitative Determination of Reduction Potentials and Defect Energy Levels Using Photoelectron Spectroscopy. *The Journal of Physical Chemistry Letters*, 2019, 10, 7071-7076. DOI: 10.1021/acs.jpcclett.9b02706.
- **P. Machado**, I. Caño, C. Menéndez, C. Cazorla, M. Campoy-Quiles, C. Escudero, M. Tallarida, M. Coll. Enhancement of Phase Stability and Optoelectronic Performance of BiFeO_3 Thin Films via Cation Co-substitution. *Journal of Materials Chemistry C.*, 2021, 9, 330-339. DOI: 10.1039/d0tc04304d.
- **P. Machado**, R. Guzman, R. J. Morera, J. Alcalà, A. Palau, w. Zhou, M. Coll. Chemical Synthesis of $\text{La}_{0.75}\text{Sr}_{0.25}\text{CrO}_3$ Thin Films for *p*-type Transparent Conducting Electrodes. *Chemistry of Materials*, 2023, 35, 9, 3513-3521.
- P. Salles^α, **P. Machado**^α, P. Yu, M. Coll. Chemical Synthesis of Complex Oxide Thin Films and Free-Standing Membranes. *Chemical Communications, Perspective Paper*, Submitted June 2023. ^αEqual contribution.
- **P. Machado**, P. Salles, A. Frebel, G. De Luca, E. Ros, I. Fina, J. Puigdollers, M. Coll. Interface Engineering in All-Oxide Photovoltaic Devices Based on Photoferroelectric $\text{BiFe}_{0.9}\text{Co}_{0.1}\text{O}_3$ Thin Films. To be submitted, June 2023.

List of Figures

1.1	Evolution of cumulative worldwide power capacity of the most relevant technologies.	3
1.2	Comparative chart of best-research cell efficiencies reported over the last 20 years for different PV technologies.	4
1.3	Sketch of cubic perovskite with ABO_3 structure.	6
1.4	Sketch of a simple vertical thin film PV heterostructure and selection of oxides.	7
1.5	Representation of BFO unit cell and comparative ferroelectric polarization hysteresis loops.	10
1.6	Recompilation of the published results on solution-processed BFCO thin films from Ref.[122].	12
1.7	Scheme of a general CSD process.	18
2.1	Steps involved in the precursor solution deposition process by spin-coating.	23
2.2	Effect of the solvent on the uniformity of an as-deposited film by spin-coating.	25
2.3	Thermal treatments carried out in CSD.	26
2.4	CSD equipment for spin coating and thermal treatment.	28
2.5	Thermal process for the preparation of CSD-BFO-based thin films.	29
2.6	Thermal process for the preparation of CSD-LSMO thin films.	31
2.7	Thermal process for the preparation of CSD-LSCO thin films.	32
2.8	Illustration of a general ALD process.	33
2.9	Representation of a magnetron sputtering chamber and deposition process.	35
2.10	Schematic of diffraction geometry in atomic planes and Bragg law condition.	39
2.11	Illustration of XRD geometry configuration.	40
2.12	Photographs of XRD diffractometers.	44
2.13	Representation of electron-matter interactions in SEM imaging.	46
2.14	Components and working modes of AFM.	48
2.15	Schematic of a spectroscopic ellipsometry measurement.	50
2.16	Principles of XPS for a model atom.	53
2.17	Principles of XAS for a model atom.	56
2.18	PPMS system and sample configuration.	58

2.19	Representative P-E hysteresis loops and ferroelectric domain configurations.	60
2.20	Electric configurations for macroscopic ferroelectric characterization.	61
2.21	Electric configuration for photoresponse characterization	62
2.22	Photoresponse measurement protocol in pre-polarized systems.	64
3.1	Crystallinity and phase purity of BFO, BFCO20, BFCO30 and La-BFCO30.	70
3.2	STEM-EELS analysis of La-BFCO30.	72
3.3	XRD-RSM of BFO, BFCO20, BFCO30 and La-BFCO30.	73
3.4	AFM topography images of BFCO20, BFCO30 and La-BFCO30	74
3.5	Optical properties of BFO, BFCO20, BFCO30 and La-BFCO30 by SE.	75
3.6	XAS spectra of BFO, BFCO20, BFCO30 and La-BFCO30.	76
3.7	Macroscopic ferroelectric properties of BFO, BFCO30 and La-BFCO30 and PFM of La-BFCO30.	79
3.8	First-principles studies of BFCO and La-BFCO: sketch, energy bandgap and magnetization.	80
3.9	First principles studies: pDOS for BFCO and La-BFCO.	81
3.10	First principles studies: pDOS for BFO and Ce-BFCO.	83
3.11	Crystallinity and phase purity of BFCO30 and Ce-BFCO30.	84
3.12	STEM-EELS analysis of Ce-BFCO30.	85
A3.1	Valence Band spectra of BFO, BFCO20, BFCO30 and La-BFCO30	87
A3.2	PFM characterization of BFCO30.	88
A3.3	Phase purity (GIXRD) of Ce-BFCO30.	90
A3.4	Optical properties of BFO, BFCO30 and Ce-BFCO30 by SE.	91
A3.5	Macroscopic ferroelectric properties of BFO, BFCO30 and Ce-BFCO30.	92
A3.6	Macroscopic ferroelectric properties of Ce-BFCO30: P_r calculation.	93
4.1	Sketch of the studied all-oxide BFCO10-based heterostructures.	97
4.2	Crystallinity, phase purity and surface morphology (AFM) of all-oxide BFCO10-based heterostructures.	98
4.3	Photoresponse of virgin BFCO10-based PV heterostructures.	99
4.4	Photoresponse and ferroelectric properties of all-oxide BFCO10-based PV heterostructures.	101
4.5	Energy band diagram of all-oxide BFCO10-based PV heterostructures.	104
4.6	Photoresponse of virgin all-oxide La-BFCO10-based PV heterostructures.	105
4.7	Sketches of compositional gradient all-oxide BFCO thin films.	107
4.8	Crystallinity and phase purity of compositional gradient BFCO films.	108
4.9	Surface morphology (SEM) of compositional gradient BFCO films	109
4.10	Elemental depth profile (ToF-SIMS) of compositional gradient BFCO.	110
4.11	Optical properties of compositional gradient BFCO by SE.	111

4.12	Photo- and ferroelectric properties of compositional gradient BFCO-based PV heterostructures. . .	112
4.13	STEM-EELS analysis of compositional gradient BFCO.	114
A4.1	2D-XRD analysis of all-oxide BFCO10-based heterostructures.	117
A4.2	Optical properties of all-oxide BFCO10-based heterostructures by UV-Vis	118
A4.3	Photoresponse of BFCO10-based PV heterostructures with different ZnO thickness	119
A4.4	Photoresponse of ZnO thin film.	120
A4.5	Macroscopic ferroelectricity of BFCO10 system in top-top configuration.	121
A4.6	Influence of ferroelectric polarization in photogenerated current.	122
A4.7	XPS core level emission lines and VB for energy band alignment determination.	124
A4.8	Methodology to determine the VBM.	125
5.1	Thermal decomposition analysis of LSCO solutions from metal nitrate route.	131
5.2	Thermal profiles for the preparation of LSCO films from metal nitrates.	133
5.3	Surface morphology (SEM) of LSCO thin films.	134
5.4	Crystallinity of LSCO thin films	135
5.5	Optical transmittance of LCO and LSCO on STO.	136
5.6	Electric resistivity vs temperature of LSCO//LAO.	137
5.7	Structural XRD study of LSCO//LAO	138
5.8	Structural defects analysis (STEM) of LSCO//LAO.	139
5.9	STEM-EELS analysis of LCO//LAO and LSCO//LAO.	140
A5.1	Preparation of LSCO from metalorganic route.	145
A5.2	Fine tuning of processing conditions for LSCO thin films.	146
A5.3	SEM-EDX of LSCO from DEA processed in air.	147
A5.4	Crystallinity and phase purity of LSCO thin films.	148
A5.5	Geometrical phase analysis of the LSCO films.	149
A5.6	Influence of thickness-roughness on electrical resistivity of LSCO.	151
A5.7	Fits of electrical resistivity of LSCO to transport models.	152
A5.8	Surface chemical analysis (XPS) of LCO and LSCO.	153
A5.9	C1s core level XPS spectra for LSCO.	154
6.1	Summary of the main results obtained in each Chapter.	158

List of Tables

3.1	Ionic raddi of A and B site cations in BFO-based.	69
3.2	Unit cell parameters and unit cell volume of BFO-based thin films.	73
4.1	Summary of performance of virgin all-oxide BFCO10-based PV heterostructures.	100
4.2	Summary of performance of pre-polarized BFCO10-based PV heterostructures.	102
A4.1	Values extracted for the binding energies for specific core levels, VBM and CBM.	126
5.1	Summary of LSCO solution formulation from metal nitrate route.	130

Bibliography

- [1] IEA. World energy outlook, 2022 (2022). URL <https://www.iea.org/reports/world-energy-outlook-2022>.
- [2] IEA. Renewables 2022 report (2022). URL <https://www.iea.org/reports/renewables-2022>.
- [3] Green, M. A. How did solar cells get so cheap? *Joule* **3**, 631–633 (2019). URL <https://www.sciencedirect.com/science/article/pii/S254243511930090X>.
- [4] Righini, G. C. & Enrichi, F. Chapter one - solar cells' evolution and perspectives: a short review. In Enrichi, F. & Righini, G. C. (eds.) *Solar Cells and Light Management*, 1–32 (Elsevier, 2020). URL <https://www.sciencedirect.com/science/article/pii/B978008102762200001X>.
- [5] Solar photovoltaic tracking report 2022 (2022). URL <https://www.iea.org/reports/world-energy-outlook-2022>.
- [6] IEA. World energy statistics and balances (2022). URL <https://www.iea.org/data-and-statistics/data-product/world-energy-statistics-and-balances#world-energy-statistics>.
- [7] IEA. Share of cumulative power capacity by technology 2010–2027 (2022). URL <https://www.iea.org/data-and-statistics/charts/share-of-cumulative-power-capacity-by-technology-2010-2027>.
- [8] Philipps, S. & Warmuth, W. (2023).
- [9] NREL. Best research-cell efficiency chart (2023). URL <https://www.nrel.gov/pv/cell-efficiency.html>.
- [10] Shockley, W. & Queisser, H. J. Detailed balance limit of efficiency of p-n junction solar cells. *Journal of Applied Physics* **32**, 510–519 (1961). URL <https://doi.org/10.1063/1.1736034>.
- [11] Green, M. A. & Bremner, S. P. Energy conversion approaches and materials for high-efficiency photovoltaics. *Nature Materials* **16**, 23–34 (2016). URL <https://www.nature.com/articles/nmat4676>.
- [12] Nayak, P. K., Mahesh, S., Snaith, H. J. & Cahen, D. Photovoltaic solar cell technologies: analysing the state of the art. *Nature Reviews Materials* **4**, 269–285 (2019). URL <https://doi.org/10.1038/s41578-019-0097-0>.
- [13] Green, M. A. Commercial progress and challenges for photovoltaics. *Nature Energy* **1**, 15015(1–4) (2016). URL <https://doi.org/10.1038/nenergy.2015.15>.
- [14] Kirchartz, T. & Rau, U. What makes a good solar cell? *Advanced Energy Materials* **8**, 1703385 (2018). URL <https://onlinelibrary.wiley.com/doi/abs/10.1002/aenm.201703385>.
- [15] Dimroth, F. & Bächle, S. Fraunhofer ise develops the world's most efficient solar cell with 47.6 % efficiency - fraunhofer ise (2022). URL <https://www.ise.fraunhofer.de/en/press-media/press-releases/2022/fraunhofer-ise-develops-the-worlds-most-efficient-solar-cell-with-47-comma-6-percent-efficiency.html>.
- [16] Jia, X. *et al.* All-silicon tandem solar cells: Practical limits for energy conversion and possible routes for improvement. *Journal of Applied Physics* **119**, 233102 (2016). URL <https://doi.org/10.1063/1.4954003>.
- [17] Polman, A., Knight, M., Garnett, E. C., Ehrler, B. & Sinke, W. C. Photovoltaic materials: Present efficiencies and future challenges. *Science* **352**, aad4424 (2016). URL <https://www.science.org/doi/abs/10.1126/science.aad4424>.
- [18] Kurinec, S. K. *Emerging photovoltaic materials: Silicon and beyond* (Wiley-Scrivener, 2018). URL <https://www.wiley.com/en-us/Emerging+Photovoltaic+Materials%3A+Silicon+and+Beyond-p-9781119407546>.
- [19] Bisquert, J., Qi, Y., Ma, T. & Yan, Y. Advances and obstacles on perovskite solar cell research from material properties to photovoltaic function. *ACS Energy Letters* **2**, 520–523 (2017). URL <https://doi.org/10.1021/acsenerylett.7b00085>.
- [20] Correa-Baena, J.-P. *et al.* Promises and challenges of perovskite solar cells. *Science* **358**, 739–744 (2017). URL <https://www.science.org/doi/abs/10.1126/science.aam6323>.
- [21] Gao, C., Du, D., Ding, D., Qiao, F. & Shen, W. A review on monolithic perovskite/c-si tandem solar cells: progress, challenges, and opportunities. *J. Mater. Chem. A* **10**, 10811–10828 (2022). URL <http://dx.doi.org/10.1039/D2TA01470J>.
- [22] Oreski, G. *et al.* Motivation, benefits, and challenges for new photovoltaic material module developments. *Progress in Energy* **4**, 032003(1–22) (2022).

- [23] Lorenz, M. *et al.* The 2016 oxide electronic materials and oxide interfaces roadmap. *Journal of Physics D: Applied Physics* **49**, 433001 (2016). URL <https://dx.doi.org/10.1088/0022-3727/49/43/433001>.
- [24] Concina, I., Ibupoto, Z. H. & Vomiero, A. Semiconducting metal oxide nanostructures for water splitting and photovoltaics. *Advanced Energy Materials* **7**, 1700706 (2017). URL <https://onlinelibrary.wiley.com/doi/abs/10.1002/aenm.201700706>.
- [25] In Lira-Cantu, M. (ed.) *The Future of Semiconductor Oxides in Next-Generation Solar Cells*, Metal Oxides, 1–568 (Elsevier, 2018). URL <https://www.sciencedirect.com/book/9780128111659/the-future-of-semiconductor-oxides-in-next-generation-solar-cells>.
- [26] Coll, M. *et al.* Towards oxide electronics: a roadmap. *Applied Surface Science* **482**, 1–93 (2019). URL <https://www.sciencedirect.com/science/article/pii/S0169433219309432>. Roadmap for Oxide Electronics, pushed forward by the TO-BE EU Cost action.
- [27] In *Electronic Conduction in Oxides*, vol. 94 of *Springer Series in Solid-State Sciences*, 1–325 (Springer, 1991). URL <https://link.springer.com/book/10.1007/978-3-662-02668-7#book-header>.
- [28] Torrance, J. B., Lacorre, P., Asavaroengchai, C. & Metzger, R. M. Why are some oxides metallic, while most are insulating? *Physica C: Superconductivity* **182**, 351–364 (1991). URL <https://www.sciencedirect.com/science/article/pii/0921453491905346>.
- [29] Woodward, P., Mizoguchi, H., Kim, Y. & Stoltzfus, M. The electronic structure of metal oxides. In J.L.G. F. (ed.) *Metal Oxides: Chemistry and Applications*, 133–190 (Taylor Francis Group, 2006). URL <https://www.sciencedirect.com/science/article/pii/B9780081027622000069>.
- [30] Goldschmidt, V. M. Die gesetze der krystallochemie. *Naturwissenschaften* **14**, 477–485 (1926). URL <https://doi.org/10.1007/BF01507527>.
- [31] Peña, M. A. & Fierro, J. L. G. Chemical structures and performance of perovskite oxides. *Chemical Reviews* **101**, 1981–2018 (2001). URL <https://doi.org/10.1021/cr980129f>. PMID: 11710238.
- [32] Sun, Y., Yang, J., Li, S. & Wang, D. Defect engineering in perovskite oxide thin films. *Chem. Commun.* **57**, 8402–8420 (2021). URL <http://dx.doi.org/10.1039/D1CC02276H>.
- [33] He, H. *et al.* Perovskite oxides as transparent semiconductors: a review. *Nano Convergence* **7**, 32–42 (2020). URL <https://doi.org/10.1186/s40580-020-00242-7>.
- [34] Pérez-Tomás, A., Mingorance, A., Tanenbaum, D. & Lira-Cantú, M. Chapter 8 - metal oxides in photovoltaics: All-oxide, ferroic, and perovskite solar cells. In Lira-Cantu, M. (ed.) *The Future of Semiconductor Oxides in Next-Generation Solar Cells*, Metal Oxides, 267–356 (Elsevier, 2018). URL <https://www.sciencedirect.com/science/article/pii/B9780128111659000089>.
- [35] Yu, X., Marks, T. J. & Facchetti, A. Metal oxides for optoelectronic applications. *Nature Materials* **15**, 383–396 (2016). URL <https://doi.org/10.1038/nmat4599>.
- [36] Wang, F. *et al.* Gradient doped nickel oxide hole selective heterocontact and ultrathin passivation for silicon photovoltaics with efficiencies beyond 20%. *Chemical Engineering Journal* **450**, 138060 (2022). URL <https://www.sciencedirect.com/science/article/pii/S138589472203546X>.
- [37] Bullock, J. *et al.* Efficient silicon solar cells with dopant-free asymmetric heterocontacts. *Nature Energy* **1**, 15031(1–7) (2016). URL <https://doi.org/10.1038/nenergy.2015.31>.
- [38] Bullock, J. *et al.* Stable dopant-free asymmetric heterocontact silicon solar cells with efficiencies above 20%. *ACS Energy Letters* **3**, 508–513 (2018). URL <https://doi.org/10.1021/acsenenergylett.7b01279>.
- [39] Cho, J. *et al.* Performance and thermal stability of an a-si:h/tio_x/yb stack as an electron-selective contact in silicon heterojunction solar cells. *ACS Applied Energy Materials* **2**, 1393–1404 (2019). URL <https://doi.org/10.1021/acsaem.8b01969>.
- [40] Melskens, J. *et al.* Passivating contacts for crystalline silicon solar cells: From concepts and materials to prospects. *IEEE Journal of Photovoltaics* **8**, 373–388 (2018). URL <https://ieeexplore.ieee.org/document/8291156>.
- [41] Gerling, L. G. *et al.* Transition metal oxides as hole-selective contacts in silicon heterojunctions solar cells. *Solar Energy Materials and Solar Cells* **145**, 109–115 (2016). URL <https://www.sciencedirect.com/science/article/pii/S0927024815004225>. Selected papers of the EMRS 2015 Spring meeting – Symposium C on Advanced Inorganic Materials and Structures for Photovoltaics.
- [42] Cao, W. & Xue, J. Recent progress in organic photovoltaics: device architecture and optical design. *Energy Environ. Sci.* **7**, 2123–2144 (2014). URL <http://dx.doi.org/10.1039/C4EE00260A>.
- [43] Becerril-Romero, I. *et al.* Transition-metal oxides for kesterite solar cells developed on transparent substrates. *ACS Applied Materials & Interfaces* **12**, 33656–33669 (2020). URL <https://doi.org/10.1021/acsaami.0c06992>. PMID: 32608962.
- [44] Amrillah, T. *et al.* Environment-friendly copper-based chalcogenide thin film solar cells: status and perspectives. *Mater. Horiz.* **10**, 313–339 (2023). URL <http://dx.doi.org/10.1039/D2MH00983H>.
- [45] Chander, S. & Tripathi, S. K. Recent advancement in efficient metal oxide-based flexible perovskite solar cells: a short review. *Mater. Adv.* **3**, 7198–7211 (2022). URL <http://dx.doi.org/10.1039/D2MA00700B>.

- [46] Shin, S. S., Lee, S. J. & Seok, S. I. Metal oxide charge transport layers for efficient and stable perovskite solar cells. *Advanced Functional Materials* **29**, 1900455 (2019). URL <https://onlinelibrary.wiley.com/doi/abs/10.1002/adfm.201900455>.
- [47] Wang, Y. *et al.* Metal oxide charge transport layers in perovskite solar cells—optimising low temperature processing and improving the interfaces towards low temperature processed, efficient and stable devices. *Journal of Physics: Energy* **3**, 012004 (2020). URL <https://dx.doi.org/10.1088/2515-7655/abc73f>.
- [48] Haque, M. A., Sheikh, A. D., Guan, X. & Wu, T. Metal oxides as efficient charge transporters in perovskite solar cells. *Advanced Energy Materials* **7**, 1602803 (2017). URL <https://onlinelibrary.wiley.com/doi/abs/10.1002/aenm.201602803>.
- [49] Calnan, S. Applications of oxide coatings in photovoltaic devices. *Coatings* **4**, 162–202 (2014). URL <https://www.mdpi.com/2079-6412/4/1/162>.
- [50] Rühle, S. *et al.* All-oxide photovoltaics. *The Journal of Physical Chemistry Letters* **3**, 3755–3764 (2012). URL <https://doi.org/10.1021/jz3017039>. PMID: 26291107.
- [51] Meddeb, H. *et al.* Tunable photovoltaics: Adapting solar cell technologies to versatile applications. *Advanced Energy Materials* **12**, 2200713 (2022). URL <https://onlinelibrary.wiley.com/doi/abs/10.1002/aenm.202200713>.
- [52] Guo, W. *et al.* Recent development of transparent conducting oxide-free flexible thin-film solar cells. *Advanced Functional Materials* **26**, 8855–8884 (2016). URL <https://onlinelibrary.wiley.com/doi/abs/10.1002/adfm.201603378>.
- [53] Li, Y. *et al.* Stacking and twisting of freestanding complex oxide thin films. *Advanced Materials* **34**, 2203187 (2022). URL <https://onlinelibrary.wiley.com/doi/abs/10.1002/adma.202203187>.
- [54] Pesquera, D., Fernández, A., Khestanova, E. & Martin, L. W. Freestanding complex-oxide membranes. *J. Phys.: Condens. Matter* (2022). URL <https://iopscience.iop.org/article/10.1088/1361-648X/ac7dd5>.
- [55] Chiabrera, F. M. *et al.* Freestanding perovskite oxide films: Synthesis, challenges, and properties. *Annalen der Physik* 2200084 (2022). URL <https://onlinelibrary.wiley.com/doi/10.1002/andp.202200084>.
- [56] Salles, P. *et al.* On the role of the $\text{Sr}_{3-x}\text{Ca}_x\text{Al}_2\text{O}_6$ sacrificial layer composition for epitaxial $\text{La}_{0.7}\text{Sr}_{0.3}\text{MnO}_3$ membranes. *Advanced Functional Materials* 2304059 (2023). URL [xx](https://doi.org/10.1002/adfm.202304059).
- [57] Bisquert, J. *The physics of solar cells: Perovskites, organics, and photovoltaic fundamentals* (CRC Press, 2018), 1st edn.
- [58] Fix, T. 2 - oxide and ferroelectric solar cells. In Ginley, D. & Fix, T. (eds.) *Advanced Micro- and Nanomaterials for Photovoltaics*, Micro and Nano Technologies, 19–34 (Elsevier, 2019). URL <https://www.sciencedirect.com/science/article/pii/B9780128145012000025>.
- [59] Mittiga, A., Salza, E., Sarto, F., Tucci, M. & Vasanthi, R. Heterojunction solar cell with 2% efficiency based on a Cu_2O substrate. *Applied Physics Letters* **88**, 163502 (2006). URL <https://doi.org/10.1063/1.2194315>.
- [60] Sullivan, I., Zoellner, B. & Maggard, P. A. Copper(i)-based *p*-type oxides for photoelectrochemical and photovoltaic solar energy conversion. *Chemistry of Materials* **28**, 5999–6016 (2016). URL <https://doi.org/10.1021/acs.chemmater.6b00926>.
- [61] Shibasaki, S. *et al.* Highly transparent Cu_2O absorbing layer for thin film solar cells. *Applied Physics Letters* **119**, 242102 (2021). URL <https://doi.org/10.1063/5.0072310>.
- [62] Kupfer, B. *et al.* Thin film $\text{Co}_3\text{O}_4/\text{TiO}_2$ heterojunction solar cells. *Advanced Energy Materials* **5**, 1401007 (2015). URL <https://onlinelibrary.wiley.com/doi/abs/10.1002/aenm.201401007>.
- [63] Minami, T., Nishi, Y. & Miyata, T. Effect of the thin Ga_2O_3 layer in $\text{n}+\text{ZnO}/\text{n-Ga}_2\text{O}_3/\text{p-Cu}_2\text{O}$ heterojunction solar cells. *Thin Solid Films* **549**, 65–69 (2013). URL <https://www.sciencedirect.com/science/article/pii/S0040609013010894>. The 40th International Conference on Metallurgical Coatings and Thin Films.
- [64] Li, H. *et al.* Photoferroelectric perovskite solar cells: Principles, advances and insights. *Nano Today* **37**, 101062 (2021). URL <https://www.sciencedirect.com/science/article/pii/S1748013220302322>.
- [65] Yang, S. Y. *et al.* Above-bandgap voltages from ferroelectric photovoltaic devices. *Nature Nanotechnology* **5**, 143–147 (2010). URL <https://doi.org/10.1038/nnano.2009.451>.
- [66] Grinberg, I. *et al.* Perovskite oxides for visible-light-absorbing ferroelectric and photovoltaic materials. *Nature* **503**, 509–512 (2013).
- [67] Fan, Z., Sun, K. & Wang, J. Perovskites for photovoltaics: a combined review of organic–inorganic halide perovskites and ferroelectric oxide perovskites. *J. Mater. Chem. A* **3**, 18809–18828 (2015). URL <http://dx.doi.org/10.1039/C5TA04235F>.
- [68] Lopez-Varo, P. *et al.* Physical aspects of ferroelectric semiconductors for photovoltaic solar energy conversion. *Physics Reports* **653**, 1–40 (2016). URL <https://www.sciencedirect.com/science/article/pii/S0370157316301946>. Physical aspects of ferroelectric semiconductors for photovoltaic solar energy conversion.
- [69] Pal, S. *et al.* Giant photovoltaic response in band engineered ferroelectric perovskite. *Chemistry of Materials* **8**, 8005 (1–7) (2018). URL <https://doi.org/10.1038/s41598-018-26205-x>.

- [70] Sturman, B. & Fridkin, V. *Photovoltaic and Photo-refractive Effects in Noncentrosymmetric Materials* (Routledge, 1992), 1st ed. edn. URL <https://www.taylorfrancis.com/books/mono/10.1201/9780203743416/photovoltaic-photo-refractive-effects-noncentrosymmetric-materials-boris-sturman-vladimir-fridkin>.
- [71] Bhatnagar, A., Roy Chaudhuri, A., Heon Kim, Y., Hesse, D. & Marin, A. Role of domain walls in the abnormal photovoltaic effect in bifeo₃. *Nature Communications* **4**, 2835 (2013). URL <https://doi.org/10.1038/ncomms3835>.
- [72] Ji, W., Yao, K. & Liang, Y. C. Evidence of bulk photovoltaic effect and large tensor coefficient in ferroelectric bifeo₃ thin films. *Phys. Rev. B* **84**, 094115 (2011). URL <https://link.aps.org/doi/10.1103/PhysRevB.84.094115>.
- [73] Sheng, Y. *et al.* Bulk photovoltaic effect in hexagonal lumno₃ single crystals. *Phys. Rev. B* **104**, 184116 (2021). URL <https://link.aps.org/doi/10.1103/PhysRevB.104.184116>.
- [74] Pintilie, L. & Alexe, M. Metal-ferroelectric-metal heterostructures with schottky contacts. i. influence of the ferroelectric properties. *Journal of Applied Physics* **98**, 124103 (2005). URL <https://doi.org/10.1063/1.2148622>.
- [75] Lee, D. *et al.* Polarity control of carrier injection at ferroelectric/metal interfaces for electrically switchable diode and photovoltaic effects. *Phys. Rev. B* **84**, 125305 (2011). URL <https://link.aps.org/doi/10.1103/PhysRevB.84.125305>.
- [76] Yang, Y. S. *et al.* Schottky barrier effects in the photocurrent of sol-gel derived lead zirconate titanate thin film capacitors. *Applied Physics Letters* **76**, 774–776 (2000). URL <https://doi.org/10.1063/1.125891>.
- [77] Pintilie, L., Vrejoiu, I., Le Rhun, G. & Alexe, M. Short-circuit photocurrent in epitaxial lead zirconate-titanate thin films. *Journal of Applied Physics* **101**, 064109 (2007). URL <https://doi.org/10.1063/1.2560217>.
- [78] Ji, W., Yao, K. & Liang, Y. C. Bulk photovoltaic effect at visible wavelength in epitaxial ferroelectric bifeo₃ thin films. *Advanced Materials* **22**, 1763–1766 (2010). URL <https://onlinelibrary.wiley.com/doi/abs/10.1002/adma.200902985>.
- [79] Sharma, S., Kumar, M., Laref, A., Siqueiros, J. & Herrera, O. R. Unravelling and controlling hidden imprint fields in ferroelectric capacitors. *Scientific Reports* **6**, 25028(1:7) (2016). URL <https://doi.org/10.1038/srep25028>.
- [80] Sheng, Y., Fina, I., Gospodinov, M. & Fontcuberta, J. Switchable photovoltaic response in hexagonal lumno₃ single crystals. *Applied Physics Letters* **118**, 232902 (2021). URL <https://doi.org/10.1063/5.0053379>.
- [81] Sheng, Y. *et al.* Untwining polar contributions from light-polarization dependent photovoltaic response of lumno₃-based ferroelectric capacitors. *Acta Materialia* **245**, 118601 (2023). URL <https://www.sciencedirect.com/science/article/pii/S1359645422009764>.
- [82] Lin, C. *et al.* Solution epitaxy of polarization-gradient ferroelectric oxide films with colossal photovoltaic current. *Nature Communications* **14**, 2341 (2023).
- [83] Lee, D. *et al.* Giant flexoelectric effect in ferroelectric epitaxial thin films. *Phys. Rev. Lett.* **107**, 057602 (2011). URL <https://link.aps.org/doi/10.1103/PhysRevLett.107.057602>.
- [84] Wang, W. *et al.* Crystal field splitting and optical bandgap of hexagonal lufeo₃ films. *Applied Physics Letters* **101**, 241907 (2012). URL <https://doi.org/10.1063/1.4771601>.
- [85] Han, H. *et al.* Switchable photovoltaic effects in hexagonal manganite thin films having narrow band gaps. *Chemistry of Materials* **27**, 7425–7432 (2015). URL <https://doi.org/10.1021/acs.chemmater.5b03408>.
- [86] Pintilie, L. *et al.* Metal-ferroelectric-metal structures with schottky contacts. ii. analysis of the experimental current-voltage and capacitance-voltage characteristics of pb(zr,ti)o₃ thin films. *Journal of Applied Physics* **98**, 124104 (2005). URL <https://doi.org/10.1063/1.2148623>.
- [87] Huang, Q. *et al.* Significant modulation of ferroelectric photovoltaic behavior by a giant macroscopic flexoelectric effect induced by strain-relaxed epitaxy. *Advanced Electronic Materials* **8**, 2100612 (2022). URL <https://onlinelibrary.wiley.com/doi/abs/10.1002/aelm.202100612>.
- [88] Spanier, J. E. *et al.* Power conversion efficiency exceeding the shockley–queisser limit in a ferroelectric insulator. *Nature Photonics* **10**, 611–616 (2016). URL <https://doi.org/10.1038/nphoton.2016.143>.
- [89] Bai, Y., Tofel, P., Palosaari, J., Jantunen, H. & Juuti, J. A game changer: A multifunctional perovskite exhibiting giant ferroelectricity and narrow bandgap with potential application in a truly monolithic multienergy harvester or sensor. *Advanced Materials* **29**, 1700767 (2017). URL <https://onlinelibrary.wiley.com/doi/abs/10.1002/adma.201700767>.
- [90] Glass, A. M., von der Linde, D. & Negrán, T. J. High-voltage bulk photovoltaic effect and the photorefractive process in linbo₃. *Applied Physics Letters* **25**, 233–235 (1974). URL <https://doi.org/10.1063/1.1655453>.
- [91] Choi, T., Lee, S., Choi, Y. J., Kiryukhin, V. & Cheong, S.-W. Switchable ferroelectric diode and photovoltaic effect in bifeo₃. *Science* **324**, 63–66 (2009).
- [92] Yang, S. Y. *et al.* Photovoltaic effects in bifeo₃. *Applied Physics Letters* **95**, 062909 (2009). URL <https://doi.org/10.1063/1.3204695>.
- [93] Yang, M.-M. ., Luo, Z.-D. ., Kim, D. J. & Alexe, M. Bulk photovoltaic effect in monodomain bifeo₃ thin films. *Applied Physics Letters* **110**, 183902 (2017). URL <https://doi.org/10.1063/1.4983032>.

- [94] Chen, G. *et al.* Bismuth ferrite materials for solar cells: Current status and prospects. *Materials Research Bulletin* **110**, 39–49 (2019). URL <https://www.sciencedirect.com/science/article/pii/S0025540818314818>.
- [95] You, L. *et al.* Revisiting the ferroelectric photovoltaic properties of vertical bifeo₃ capacitors: A comprehensive study. *ACS Applied Materials & Interfaces* **15**, 12070–12077 (2023). URL <https://doi.org/10.1021/acsami.2c23023>. PMID: 36825749.
- [96] Sando, D., Barthélémy, A. & Bibes, M. Bifeo₃ epitaxial thin films and devices: past, present and future. *Journal of Physics: Condensed Matter* **26**, 473201 (2014). URL <https://dx.doi.org/10.1088/0953-8984/26/47/473201>.
- [97] Burns, S. R., Paull, O., Juraszek, J., Nagarajan, V. & Sando, D. The experimentalist’s guide to the cycloid, or noncollinear antiferromagnetism in epitaxial bifeo₃. *Advanced Materials* **32**, 2003711 (2020). URL <https://onlinelibrary.wiley.com/doi/abs/10.1002/adma.202003711>.
- [98] Shannon, R. D. Revised effective ionic radii and systematic studies of interatomic distances in halides and chalcogenides. *Acta Crystallographica Section A* **32**, 751–767 (1976). URL <https://doi.org/10.1107/S0567739476001551>.
- [99] Gebhardt, J. & Rappe, A. M. Doping of bifeo₃: A comprehensive study on substitutional doping. *Phys. Rev. B* **98**, 125202 (2018). URL <https://link.aps.org/doi/10.1103/PhysRevB.98.125202>.
- [100] Chu, Y.-H., Martin, L. W., Holcomb, M. B. & Ramesh, R. Controlling magnetism with multiferroics. *Materials Today* **10**, 16–23 (2007). URL <https://www.sciencedirect.com/science/article/pii/S1369702107702419>.
- [101] Wu, J. & Wang, J. Orientation dependence of ferroelectric behavior of bifeo₃ thin films. *Journal of Applied Physics* **106**, 104111 (2009). URL <https://doi.org/10.1063/1.3261841>.
- [102] Rojac, T. *et al.* Bifeo₃ ceramics: Processing, electrical, and electromechanical properties. *Journal of the American Ceramic Society* **97**, 1993–2011 (2014). URL <https://ceramics.onlinelibrary.wiley.com/doi/abs/10.1111/jace.12982>.
- [103] Yang, J.-C., He, Q., Yu, P. & Chu, Y.-H. Bifeo₃ thin films: A playground for exploring electric-field control of multifunctionalities. *Annual Review of Materials Research* **45**, 249–275 (2015). URL <https://doi.org/10.1146/annurev-matsci-070214-020837>.
- [104] Wang, F. *et al.* Materials design of visible-light ferroelectric photovoltaics from first principles. *Ferroelectrics* **483**, 1–12 (2015). URL <https://doi.org/10.1080/00150193.2015.1058096>.
- [105] Yang, T. *et al.* Design of oxygen vacancy in bifeo₃-based films for higher photovoltaic performance. *Applied Surface Science* **575**, 151713 (2022). URL <https://www.sciencedirect.com/science/article/pii/S0169433221027574>.
- [106] Wang, F., Grinberg, I. & Rappe, A. M. Band gap engineering strategy via polarization rotation in perovskite ferroelectrics. *Applied Physics Letters* **104**, 152903 (2014). URL <https://doi.org/10.1063/1.4871707>.
- [107] Sando, D. *et al.* Revisiting the optical band gap in epitaxial bifeo₃ thin films. *Advanced Optical Materials* **6**, 1700836 (2018). URL <https://onlinelibrary.wiley.com/doi/abs/10.1002/adom.201700836>.
- [108] Nechache, R. *et al.* Bandgap tuning of multiferroic oxide solar cells. *Nature Photonics* **9**, 61–67 (2014).
- [109] Yang, S., Ma, G., Xu, L., Deng, C. & Wang, X. Improved ferroelectric properties and band-gap tuning in bifeo₃ films via substitution of mn. *RSC Adv.* **9**, 29238–29245 (2019). URL <http://dx.doi.org/10.1039/C9RA05914H>.
- [110] Selbach, S. M., Einarsrud, M.-A. & Grande, T. On the thermodynamic stability of bifeo₃. *Chemistry of Materials* **21**, 169–173 (2009).
- [111] Rojac, T. *et al.* Domain-wall conduction in ferroelectric bifeo₃ controlled by accumulation of charged defects. *Nature materials* **16**, 322–327 (2017).
- [112] Schrade, M., Masó, N., Perejón, A., Pérez-Maqueda, L. A. & West, A. R. Defect chemistry and electrical properties of bifeo₃. *J. Mater. Chem. C* **5**, 10077–10086 (2017). URL <http://dx.doi.org/10.1039/C7TC03345A>.
- [113] Schrade, M., Masó, N., Perejón, A., Pérez-Maqueda, L. A. & West, A. R. Defect chemistry and electrical properties of bifeo₃. *J. Mater. Chem. C* **5**, 10077–10086 (2017). URL <http://dx.doi.org/10.1039/C7TC03345A>.
- [114] Shirahata, Y. & Oku, T. Characterization and photovoltaic properties of bifeo₃ thin films. *Coatings* **6** (2016). URL <https://www.mdpi.com/2079-6412/6/4/68>.
- [115] Wu, F. *et al.* Enhanced photovoltaic performance in polycrystalline bifeo₃ thin film/zno nanorod heterojunctions. *The Journal of Physical Chemistry C* **118**, 15200–15206 (2014). URL <https://doi.org/10.1021/jp5059462>.
- [116] Wang, L. *et al.* Electro-photo double modulation on the resistive switching behavior and switchable photoelectric effect in bifeo₃ films. *Applied Physics Letters* **102**, 252907 (2013). URL <https://doi.org/10.1063/1.4812825>.
- [117] Fang, L. *et al.* Switchable photovoltaic response from polarization modulated interfaces in bifeo₃ thin films. *Applied Physics Letters* **104**, 142903 (2014). URL <https://doi.org/10.1063/1.4870972>.
- [118] Azuma, M. *et al.* Rhombohedral–tetragonal phase boundary with high curie temperature in (1-x)bicoo₃–xbifeo₃ solid solution. *Japanese Journal of Applied Physics* **47**, 7579 (2008). URL <https://dx.doi.org/10.1143/JJAP.47.7579>.

- [119] Yasui, S. *et al.* Crystal structure analysis of epitaxial bifeo₃-bicoo₃ solid solution films grown by metalorganic chemical vapor deposition. *Japanese Journal of Applied Physics* **46**, 6948 (2007). URL <https://dx.doi.org/10.1143/JJAP.46.6948>.
- [120] Arti *et al.* Modification in photovoltaic and photocatalytic properties of bismuth ferrites by tailoring band-gap and ferroelectric properties. *Journal of Alloys and Compounds* **908**, 164602 (2022). URL <https://www.sciencedirect.com/science/article/pii/S0925838822009938>.
- [121] Ding, J. *et al.* Switchable ferroelectric photovoltaic in the low bandgap cobalt-substituted bifeo₃ epitaxial thin films. *Applied Surface Science* **606**, 154898 (2022). URL <https://www.sciencedirect.com/science/article/pii/S0169433222024266>.
- [122] Machado, P. *et al.* Band gap tuning of solution-processed ferroelectric perovskite bife_{1-x}co_xo₃ thin films. *Chemistry of Materials* **31**, 947–954 (2019). URL <https://doi.org/10.1021/acs.chemmater.8b04380>. PMID: 30828131.
- [123] Cheng, Z. X. *et al.* Structure, ferroelectric properties, and magnetic properties of the la-doped bismuth ferrite. *Journal of Applied Physics* **103**, 07E507 (2008). URL <https://doi.org/10.1063/1.2839325>.
- [124] Huang, F. *et al.* Effect of nd dopant on magnetic and electric properties of bifeo₃ thin films prepared by metal organic deposition method. *Applied Physics Letters* **89**, 242914 (2006). URL <https://doi.org/10.1063/1.2404942>.
- [125] Das, S. R. *et al.* Structural and multiferroic properties of la-modified bifeo₃ ceramics. *Journal of Applied Physics* **101**, 034104 (2007). URL <https://doi.org/10.1063/1.2432869>.
- [126] You, L. *et al.* Enhancing ferroelectric photovoltaic effect by polar order engineering. *Science Advances* **4** (2018). URL <https://advances.sciencemag.org/content/4/7/eaat3438>.
- [127] Luo, Y.-R. *Comprehensive Handbook of Chemical Bond Energies* (CRC Press, 2007), 1 edn.
- [128] Yang, C.-H., Kan, D., Takeuchi, I., Nagarajan, V. & Seidel, J. Doping bifeo₃: approaches and enhanced functionality. *Phys. Chem. Chem. Phys.* **14** (2012).
- [129] Kan, D. *et al.* Universal behavior and electric-field-induced structural transition in rare-earth-substituted bifeo₃. *Advanced Functional Materials* **20**, 1108–1115 (2010). URL <https://onlinelibrary.wiley.com/doi/abs/10.1002/adfm.200902017>.
- [130] Zhang, L. *et al.* Enhanced switchable photovoltaic response and ferromagnetic of co-doped bifeo₃ based ferroelectric thin films. *Journal of Alloys and Compounds* **742**, 351–355 (2018). URL <https://www.sciencedirect.com/science/article/pii/S0925838818302780>.
- [131] Cheng, X. *et al.* Chemical and interfacial design in the visible-light-absorbing ferroelectric thin films. *Journal of the European Ceramic Society* **43**, 3275–3288 (2023). URL <https://www.sciencedirect.com/science/article/pii/S0955221923001152>.
- [132] Do, D., Kim, J. W., Kim, S. S., Song, R. K. & Kim, M. H. Electrical properties in lanthanides substituted (bi_{0.9a0.1})(fe_{0.975co0.025})o_{3d} (a = la, eu, gd) thin films. *Journal of the Korean Physical Society* **61**, 1409–1412 (2012). URL <https://doi.org/10.3938/jkps.61.1409>.
- [133] Liu, Y. *et al.* Multiferroic properties of la/er/mn/co multi-doped bifeo₃ thin films. *Ceramics International* **45**, 11765–11775 (2019). URL <https://www.sciencedirect.com/science/article/pii/S0272884219305929>.
- [134] Liu, Y. *et al.* Phase transition, leakage conduction mechanism evolution and enhanced ferroelectric properties in multiferroic mn-doped bifeo₃ thin films. *Journal of Materials Science: Materials in Electronics* **27**, 3095–3102 (2016). URL <https://doi.org/10.1007/s10854-015-4135-4>.
- [135] Hwang, J. *et al.* Tuning perovskite oxides by strain: Electronic structure, properties, and functions in (electro)catalysis and ferroelectricity. *Materials Today* **31**, 100–118 (2019). URL <https://www.sciencedirect.com/science/article/pii/S1369702119300185>.
- [136] Sando, D. Strain and orientation engineering in abo₃ perovskite oxide thin films. *Journal of Physics: Condensed Matter* **34**, 153001 (2022). URL <https://dx.doi.org/10.1088/1361-648X/ac4c61>.
- [137] Yang, M.-M., Kim, D. J. & Alexe, M. Flexo-photovoltaic effect. *Science* **360**, 904–907 (2018). URL <https://www.science.org/doi/abs/10.1126/science.aan3256>.
- [138] Park, S. M. *et al.* Selective control of multiple ferroelectric switching pathways using a trailing flexoelectric field. *Nature Nanotechnology* **13**, 366–370 (2018). URL <https://doi.org/10.1038/s41565-018-0083-5>.
- [139] Chu, K. *et al.* Enhancement of the anisotropic photocurrent in ferroelectric oxides by strain gradients. *Nature Nanotechnology* **10**, 972–979 (2015). URL <https://doi.org/10.1038/nnano.2015.191>.
- [140] Guo, R. *et al.* Continuously controllable photoconductance in freestanding bifeo₃ by the macroscopic flexoelectric effect. *Nature Communications* **13**, 2571–2580 (2020). URL <https://doi.org/10.1038/s41467-020-16465-5>.
- [141] Wang, F., Young, S. M., Zheng, F., Grinberg, I. & Rappe, A. M. Substantial bulk photovoltaic effect enhancement via nanolayering. *Nature Communications* **7**, 10419:7 (2016). URL <https://doi.org/10.1038/ncomms10419>.
- [142] Chakrabartty, J. *et al.* Photovoltaic properties of multiferroic bifeo₃/bico₃ heterostructures. *Journal of the American Ceramic Society* **97**, 1837–1840 (2014). URL <https://ceramics.onlinelibrary.wiley.com/doi/abs/10.1111/jace.12837>.

- [143] Nie, C., Zhao, S., Bai, Y. & Lu, Q. The ferroelectric photovoltaic effect of $\text{BiFeO}_3/\text{BiFeO}_3$ bilayer composite films. *Ceramics International* **42**, 14036–14040 (2016). URL <https://www.sciencedirect.com/science/article/pii/S0272884216308410>.
- [144] Sharma, S., Tomar, M., Kumar, A., Puri, N. K. & Gupta, V. Photovoltaic effect in $\text{BiFeO}_3/\text{BaTiO}_3$ multilayer structure fabricated by chemical solution deposition technique. *Journal of Physics and Chemistry of Solids* **93**, 63–67 (2016). URL <https://www.sciencedirect.com/science/article/pii/S0022369716300336>.
- [145] Campoy-Quiles, M. *et al.* Morphology evolution via self-organization and lateral and vertical diffusion in polymer: fullerene solar cell blends. *Nature materials* **7**, 158–164 (2008).
- [146] Andrade-Arvizu, J. *et al.* Rear band gap grading strategies on Sn-Ge -alloyed kesterite solar cells. *ACS Applied Energy Materials* **3**, 10362–10375 (2020). URL <https://doi.org/10.1021/acsaem.0c01146>.
- [147] Witte, W. *et al.* Gallium gradients in $\text{Cu(In,Ga)}\text{Se}_2$ thin-film solar cells. *Progress in Photovoltaics: Research and Applications* **23**, 717–733 (2015). URL <https://onlinelibrary.wiley.com/doi/abs/10.1002/pip.2485>.
- [148] Dalibor, T. *et al.* Towards module efficiencies of 16% with an improved cigsse device design. In *26th European Photovoltaic Solar Energy Conference and Exhibition Hamburg*, 2407–2411 (2011).
- [149] Djordjevic-Reiss, J. *et al.* Optimization of Ga content and grading in the solibro cigs production line. In *2013 IEEE 39th Photovoltaic Specialists Conference (PVSC)*, 1953–1956 (IEEE, 2013).
- [150] Kim, Y. *et al.* Device annealing effect in organic solar cells with blends of regioregular poly (3-hexylthiophene) and soluble fullerene. *Applied Physics Letters* **86**, 063502 (2005).
- [151] Li, G. *et al.* High-efficiency solution processable polymer photovoltaic cells by self-organization of polymer blends. *Nature materials* **4**, 864–868 (2005).
- [152] Yu, G., Gao, J., Hummelen, J. C., Wudl, F. & Heeger, A. J. Polymer photovoltaic cells: enhanced efficiencies via a network of internal donor-acceptor heterojunctions. *Science* **270**, 1789–1791 (1995).
- [153] Li, D.-B. *et al.* 20%-efficient polycrystalline $\text{Cd}(\text{Se,Te})$ thin-film solar cells with compositional gradient near the front junction. *Nature Communications* **13**, 7849 (2022). URL <https://doi.org/10.1038/s41467-022-35442-8>.
- [154] Heo, D., Jang, W. & Kim, S. Recent review of interfacial engineering for perovskite solar cells: effect of functional groups on the stability and efficiency. *Materials Today Chemistry* **26**, 101224 (2022). URL <https://www.sciencedirect.com/science/article/pii/S2468519422004530>.
- [155] Kroemer, H. Nobel lecture: Quasielectric fields and band offsets: teaching electrons new tricks. *Rev. Mod. Phys.* **73**, 783–793 (2001). URL <https://link.aps.org/doi/10.1103/RevModPhys.73.783>.
- [156] Mahmood, K., Sarwar, S. & Mehran, M. T. Current status of electron transport layers in perovskite solar cells: materials and properties. *RSC Adv.* **7**, 17044–17062 (2017). URL <http://dx.doi.org/10.1039/C7RA00002B>.
- [157] Mohamad Noh, M. F. *et al.* The architecture of the electron transport layer for a perovskite solar cell. *J. Mater. Chem. C* **6**, 682–712 (2018). URL <http://dx.doi.org/10.1039/C7TC04649A>.
- [158] Riedl, T. Chapter 5 - metal oxide-based charge extraction and recombination layers for organic solar cells. In Lira-Cantu, M. (ed.) *The Future of Semiconductor Oxides in Next-Generation Solar Cells*, Metal Oxides, 159–181 (Elsevier, 2018). URL <https://www.sciencedirect.com/science/article/pii/B9780128111659000053>.
- [159] Lee, J.-W., Meng, L. & Yang, Y. Chapter 7 - semiconducting metal oxides for high performance perovskite solar cells. In Lira-Cantu, M. (ed.) *The Future of Semiconductor Oxides in Next-Generation Solar Cells*, Metal Oxides, 241–265 (Elsevier, 2018). URL <https://www.sciencedirect.com/science/article/pii/B9780128111659000077>.
- [160] Mirgane, H. A., Nadimetla, D. N., Garole, D. J. & Bhosale, S. V. 7 - metal oxide nanomaterials for organic photovoltaic applications. In Delekar, S. D. (ed.) *Advances in Metal Oxides and Their Composites for Emerging Applications*, Metal Oxides, 239–261 (Elsevier, 2022). URL <https://www.sciencedirect.com/science/article/pii/B9780323857055000075>.
- [161] Battaglia, C. *et al.* Hole selective moo_x contact for silicon solar cells. *Nano Letters* **14**, 967–971 (2014). URL <https://doi.org/10.1021/nl404389u>. PMID: 24397343.
- [162] Ye, S., Liu, Z., Bian, Z. & Huang, C. Chapter 4 - oxide hole transport materials in inverted planar perovskite solar cells. In Lira-Cantu, M. (ed.) *The Future of Semiconductor Oxides in Next-Generation Solar Cells*, Metal Oxides, 117–158 (Elsevier, 2018). URL <https://www.sciencedirect.com/science/article/pii/B9780128111659000041>.
- [163] Fortunato, E., Ginley, D., Hosono, H. & Paine, D. C. Transparent conducting oxides for photovoltaics. *MRS Bulletin* **32**, 242–247 (2007). URL <https://doi.org/10.1557/mrs2007.29>.
- [164] Dalapati, G. K. *et al.* Tin oxide for optoelectronic, photovoltaic and energy storage devices: a review. *J. Mater. Chem. A* **9**, 16621–16684 (2021). URL <http://dx.doi.org/10.1039/D1TA01291F>.
- [165] Van Toan, N., Tuoi, T. T. K., Inomata, N., Toda, M. & Ono, T. Aluminum doped zinc oxide deposited by atomic layer deposition and its applications to micro/nano devices. *Scientific Reports* **11**, 1204–1216 (2021). URL <https://doi.org/10.1038/s41598-020-80880-3>.

- [166] Dong, W. *et al.* Photovoltaic properties of bifeo₃ thin film capacitors by using al-doped zinc oxide as top electrode. *Materials Letters* **91**, 359–361 (2013). URL <https://www.sciencedirect.com/science/article/pii/S0167577X12014632>.
- [167] Tiwari, D., Fermin, D. J., Chaudhuri, T. K. & Ray, A. Solution processed bismuth ferrite thin films for all-oxide solar photovoltaics. *The Journal of Physical Chemistry C* **119**, 5872–5877 (2015). URL <https://doi.org/10.1021/jp512821a>.
- [168] Zhang, Y., Sun, H., Yang, C., Su, H. & Liu, X. Modulating photovoltaic conversion efficiency of bifeo₃-based ferroelectric films by the introduction of electron transport layers. *ACS Applied Energy Materials* **2**, 5540–5546 (2019). URL <https://doi.org/10.1021/acsaem.9b00722>.
- [169] Raj, A. *et al.* Comparative analysis of ‘la’ modified bifeo₃-based perovskite solar cell devices for high conversion efficiency. *Ceramics International* **49**, 1317–1327 (2023). URL <https://www.sciencedirect.com/science/article/pii/S0272884222032904>.
- [170] Mana-ay, H., Zhang, S.-Y., Chen, C.-S., Tu, C.-S. & Chen, P.-Y. Modulating self-biased near-uv photodetection of gd-doped bismuth ferrite ceramics by introducing zinc oxide as electron transport layer. *Ceramics International* **49**, 1646–1656 (2023). URL <https://www.sciencedirect.com/science/article/pii/S0272884222033053>.
- [171] Zhang, F. *et al.* Ferroelectric polarization enhancement of photovoltaic effects in batio₃/bifeo₃/tio₂ heterostructure by introducing double-functional layers. *Journal of Alloys and Compounds* **695**, 3178–3182 (2017). URL <https://www.sciencedirect.com/science/article/pii/S0925838816338026>.
- [172] Fan, Z., Yao, K. & Wang, J. Photovoltaic effect in an indium-tin-oxide/zno/bifeo₃/pt heterostructure. *Applied Physics Letters* **105**, 162903 (2014). URL <https://doi.org/10.1063/1.4899146>.
- [173] Loh, L., Briscoe, J. & Dunn, S. Enhanced performance with bismuth ferrite perovskite in zno nanorod solid state solar cells. *Nanoscale* **6**, 7072–7078 (2014). URL <http://dx.doi.org/10.1039/C4NR00911H>.
- [174] Renuka, H., Joshna, P., Venkataraman, B. H., Ramaswamy, K. & Kundu, S. Understanding the efficacy of electron and hole transport layers in realizing efficient chromium doped bifeo₃ ferroelectric photovoltaic devices. *Solar Energy* **207**, 767–776 (2020). URL <https://www.sciencedirect.com/science/article/pii/S0038092X20307647>.
- [175] Renuka, H. *et al.* Enhanced photovoltaic response in ferroelectric ti-doped bfo heterojunction through interface engineering for building integrated applications. *Solar Energy* **225**, 863–874 (2021). URL <https://www.sciencedirect.com/science/article/pii/S0038092X21006563>.
- [176] Agarwal, R., Sharma, Y., Mendoza, F., Morell, G. & Katiyar, R. S. Photovoltaic effect in ito/rgo/bfo/au heterostructures. *ECS Meeting Abstracts* **MA2016-02**, 1413 (2016). URL <https://dx.doi.org/10.1149/MA2016-02/15/1413>.
- [177] Shi, J., Xu, X., Li, D. & Meng, Q. Interfaces in perovskite solar cells. *Small* **11**, 2472–2486 (2015).
- [178] Sharma, S., Kumar, M., Laref, A., Siqueiros, J. & Herrera, O. R. Recent advances in interfacial engineering and band-gap tuning of perovskite multiferroic heterostructures for high performance photovoltaic applications. *Materials Letters* **331**, 133490 (2023). URL <https://www.sciencedirect.com/science/article/pii/S0167577X22018456>.
- [179] Chakrabartty, J., Harnagea, C., Celikin, M., Rosei, F. & Nechache, R. Improved photovoltaic performance from inorganic perovskite oxide thin films with mixed crystal phases. *Nature Photonics* **12**, 2711–276 (2018). URL <https://doi.org/10.1038/s41566-018-0137-0>.
- [180] Visoly-Fisher, I., Cohen, S., Ruzin, A. & Cahen, D. How polycrystalline devices can outperform single-crystal ones: Thin film cdte/cds solar cells. *Advanced Materials* **16**, 879–883 (2004). URL <https://onlinelibrary.wiley.com/doi/abs/10.1002/adma.200306624>.
- [181] Zhu, J., Luo, W. & Li, Y. Growth and properties of bifeo₃ thin films deposited on lanio₃-buffered sr tio₃(001) and (111) substrates by pld. *Applied Surface Science* **255**, 3466–3469 (2008). URL <https://www.sciencedirect.com/science/article/pii/S0169433208019569>.
- [182] Liu, Z., Liu, H., Du, G., Zhang, J. & Yao, K. Electric properties of bifeo₃ films deposited on lanio₃ by sol-gel process. *Journal of Applied Physics* **100**, 044110 (2006). URL <https://doi.org/10.1063/1.2335399>.
- [183] Jin, L. *et al.* Bifeo₃(001)/lanio₃/si thin films with enhanced polarization: an all-solution approach. *RSC Adv.* **6**, 78629–78635 (2016). URL <http://dx.doi.org/10.1039/C6RA16388B>.
- [184] Wang, C. *et al.* Switchable diode effect and ferroelectric resistive switching in epitaxial bifeo₃ thin films. *Applied Physics Letters* **98**, 192901 (2011). URL <https://doi.org/10.1063/1.3589814>.
- [185] Katiyar, R. K., Misra, P., Sahoo, S., Morell, G. & Katiyar, R. S. Enhanced photoresponse in bifeo₃/srruo₃ heterostructure. *Journal of Alloys and Compounds* **609**, 168–172 (2014). URL <https://www.sciencedirect.com/science/article/pii/S0925838814009128>.
- [186] Zhou, H. *et al.* Interface engineering of highly efficient perovskite solar cells. *Science* **345**, 542–546 (2014). URL <https://www.science.org/doi/abs/10.1126/science.1254050>.
- [187] Dixon, S. C., Scanlon, D. O., Carmalt, C. J. & Parkin, I. P. *n*-type doped transparent conducting binary oxides: an overview. *J. Mater. Chem. C* **4**, 6946–6961 (2016). URL <http://dx.doi.org/10.1039/C6TC01881E>.

- [188] Barquinha, P., Martins, R., Pereira, L. & Fortunato, E. In Barquinha, P. & Fortunato, E. (eds.) *Transparent Oxide Electronics: From Materials to Devices*, Electronic Materials, 1–327 (Wiley, 2012). URL <https://www.wiley.com/en-us/Transparent+Oxide+Electronics%3A+From+Materials+to+Devices-p-9780470683736>.
- [189] Edwards, P. P., Porch, A., Jones, M. O., Morgan, D. V. & Perks, R. M. Basic materials physics of transparent conducting oxides. *Dalton Trans.* 2995–3002 (2004). URL <http://dx.doi.org/10.1039/B408864F>.
- [190] In *Mineral Commodity Summaries 2022*, 80 (USGS (U.S. Geological Survey), 2022). URL <https://pubs.usgs.gov/periodicals/mcs2022/mcs2022.pdf>.
- [191] Zhang, L. *et al.* Correlated metals as transparent conductors. *Nature Materials* **15**, 204–210 (2016). URL <https://doi.org/10.1038/nmat4493>.
- [192] Mirjolet, M., Sánchez, F. & Fontcuberta, J. High carrier mobility, electrical conductivity, and optical transmittance in epitaxial SrVO_3 thin films. *Advanced Functional Materials* **29**, 1808432 (2019). URL <https://onlinelibrary.wiley.com/doi/abs/10.1002/adfm.201808432>.
- [193] Fraga, S., Karwowski, J. & Saxena, K. In *Handbook of atomic data*, vol. 10, 558 (Elsevier Scientific Publishing Company, 1976).
- [194] Kawazoe, H., Yanagi, H., Ueda, K. & Hosono, H. Transparent *p*-type conducting oxides: Design and fabrication of *p-n* heterojunctions. *MRS Bulletin* **25**, 28–36 (2000). URL <https://doi.org/10.1557/mrs2000.148>.
- [195] Zhang, K. H. L., Xi, K., Blamire, M. G. & Egdell, R. G. *P*-type transparent conducting oxides. *Journal of Physics: Condensed Matter* **28**, 383002 (2016). URL <https://doi.org/10.1088>.
- [196] Willis, J. & Scanlon, D. O. Latest directions in *p*-type transparent conductor design. *J. Mater. Chem. C* **9**, 11995–12009 (2021). URL <http://dx.doi.org/10.1039/D1TC02547C>.
- [197] Kawazoe, H. *et al.* *P*-type electrical conduction in transparent thin films of CuAlO_2 . *Nature* **389**, 939–942 (1997). URL <https://doi.org/10.1038/40087>.
- [198] Uekawa, N. & Kaneko, K. Dopant reduction in *p*-type oxide films upon oxygen absorption. *The Journal of Physical Chemistry* **100**, 4193–4198 (1996). URL <https://doi.org/10.1021/jp952784m>.
- [199] Arca, E., Fleischer, K. & Shvets, I. V. Magnesium, nitrogen codoped Cr_2O_3 : A *p*-type transparent conducting oxide. *Applied Physics Letters* **99**, 111910 (2011). URL <https://doi.org/10.1063/1.3638461>.
- [200] Farrell, L. *et al.* Conducting mechanism in the epitaxial *p*-type transparent conducting oxide $\text{Cr}_2\text{O}_3:\text{Mg}$. *Phys. Rev. B* **91**, 125202 (2015). URL <https://link.aps.org/doi/10.1103/PhysRevB.91.125202>.
- [201] Sarma, D. D. *et al.* Investigation of hole-doped insulating $\text{La}_{1-x}\text{Sr}_x\text{CrO}_3$ by soft-x-ray absorption spectroscopy. *Phys. Rev. B* **53**, 13369–13373 (1996). URL <https://link.aps.org/doi/10.1103/PhysRevB.53.13369>.
- [202] Zhang, K. H. L. *et al.* Hole-induced insulator-to-metal transition in $\text{La}_{1-x}\text{Sr}_x\text{CrO}_3$ epitaxial films. *Phys. Rev. B* **91**, 155129 (2015). URL <https://link.aps.org/doi/10.1103/PhysRevB.91.155129>.
- [203] Zhang, K. H. L. *et al.* Perovskite Sr -doped LaCrO_3 as a new *p*-type transparent conducting oxide. *Advanced Materials* **27**, 5191–5195 (2015). URL <https://onlinelibrary.wiley.com/doi/abs/10.1002/adma.201501959>.
- [204] Han, D. *et al.* Giant tuning of electronic and thermoelectric properties by epitaxial strain in *p*-type Sr -doped LaCrO_3 transparent thin films. *ACS Applied Electronic Materials* **3**, 3461–3471 (2021). URL <https://doi.org/10.1021/acsaem.1c00425>.
- [205] ten Elshof, J. E. Chemical solution deposition techniques for epitaxial growth of complex oxides. In Koster, G., Huijben, M. & Rijnders, G. (eds.) *Epitaxial Growth of Complex Metal Oxides*, Woodhead Publishing Series in Electronic and Optical Materials, 69–93 (Woodhead Publishing, 2015).
- [206] Schwartz, R. W. Chemical solution deposition of perovskite thin films. *Materials Science* **9**, 2325–2340 (1997). URL <https://link.aps.org/doi/10.1103/PhysRevB.20.2255>.
- [207] Schwartz, R. W., Schneller, T. & Waser, R. Chemical solution deposition of electronic oxide films. *Comptes Rendus Chimie* **7**, 433–461 (2004). URL <https://www.sciencedirect.com/science/article/pii/S1631074804000852>.
- [208] De Dobbelaere, C. *et al.* Aqueous solutions for low-temperature photoannealing of functional oxide films: Reaching the 400 °C *si*-technology integration barrier. *Journal of the American Chemical Society* **133**, 12922–12925 (2011). URL <https://doi.org/10.1021/ja203553n>. PMID: 21806022.
- [209] Bretos, I. *et al.* Activated solutions enabling low-temperature processing of functional ferroelectric oxides for flexible electronics. *Advanced Materials* **26**, 1405–1409 (2014). URL <https://onlinelibrary.wiley.com/doi/abs/10.1002/adma.201304308>.
- [210] .
- [211] Bretos, I., Jimenez, R., Ricote, J. & Calzada, M. L. Low-temperature crystallization of solution-derived metal oxide thin films assisted by chemical processes. *Chem Soc Rev* **47**, 291–308 (2018). URL <http://xlink.rsc.org/?DOI=C6CS00917D>.
- [212] Bretos, I. *et al.* Low-temperature sol–gel methods for the integration of crystalline metal oxide thin films in flexible electronics. *Journal of Sol-Gel Science and Technology* **81**, xx (2023). URL <https://doi.org/10.1007/s10971-023-06065-2>.

- [213] Carlos, E., Martins, R., Fortunato, E. & Branquinho, R. Solution combustion synthesis: Towards a sustainable approach for metal oxides. *Chem. Eur. J.* **26**, 9099–9125 (2020). URL <https://onlinelibrary.wiley.com/doi/10.1002/chem.202000678>.
- [214] Glynn, C. & O'Dwyer, C. Solution processable metal oxide thin film deposition and material growth for electronic and photonic devices. *Advanced Materials Interfaces* **4**, 1600610 (2017). URL <https://onlinelibrary.wiley.com/doi/abs/10.1002/admi.201600610>.
- [215] Pasquarelli, R. M., Ginley, D. S. & O'Hayre, R. Solution processing of transparent conductors: from flask to film. *Chem. Soc. Rev.* **40**, 5406–5441 (2011). URL <http://dx.doi.org/10.1039/C1CS15065K>.
- [216] Hagendorfer, H. *et al.* Highly transparent and conductive zno: Al thin films from a low temperature aqueous solution approach. *Advanced Materials* **26**, 632–636 (2014). URL <https://onlinelibrary.wiley.com/doi/abs/10.1002/adma.201303186>.
- [217] Xia, N. & Gerhardt, R. A. Fabrication and characterization of highly transparent and conductive indium tin oxide films made with different solution-based methods. *Materials Research Express* **3**, 116408 (2016). URL <https://dx.doi.org/10.1088/2053-1591/3/11/116408>.
- [218] Soler, L. *et al.* Ultrafast transient liquid assisted growth of high current density superconducting films. *Nat. Commun* **11**, 344 (2020). URL <http://www.nature.com/articles/s41467-019-13791-1>.
- [219] Bretos, I. *et al.* Solution-derived $\text{YBa}_2\text{Cu}_3\text{O}_{7-d}$ (YBCO) superconducting films with BaZrO_3 (BZO) nanodots based on reverse micelle stabilized nanoparticles. *J. Mater. Chem. C* **3**, 3971–3979 (2015). URL <http://dx.doi.org/10.1039/C4TC02543A>.
- [220] Park, J.-S. & Kim, Y.-B. Synthesis and characterization of nanoporous strontium-doped lanthanum cobaltite thin film using metal organic chemical solution deposition. *Thin Solid Films* **599**, 174–178 (2016). URL <https://www.sciencedirect.com/science/article/pii/S0040609015012924>.
- [221] Yang, D. *et al.* Epitaxial growth of SrRuO_3 thin films with different orientation by chemical solution deposition. *Journal of Alloys and Compounds* **682**, 154–159 (2016). URL <https://www.sciencedirect.com/science/article/pii/S0925838816312774>.
- [222] Vila-Fungueiriño, J. M. *et al.* Epitaxial $\text{La}_{0.7}\text{Sr}_{0.3}\text{MnO}_3$ thin films on silicon with excellent magnetic and electric properties by combining physical and chemical methods. *Sci Technol Adv Mater* **19**, 702–710 (2018). URL <https://www.tandfonline.com/doi/full/10.1080/14686996.2018.1520590>.
- [223] Godard, N., Grysan, P., Defay, E. & Glinšek, S. Growth of 100-oriented lead zirconate titanate thin films mediated by a safe solvent. *J. Mater. Chem. C* **9**, 281–287 (2021). URL <http://dx.doi.org/10.1039/D0TC04066E>.
- [224] Hosokura, T., Ando, A. & Konoike, T. Orientation-controlled BaTiO_3 thin films fabricated by chemical solution deposition. *RSC Adv.* **5**, 97563–97567 (2015). URL <http://dx.doi.org/10.1039/C5RA22195A>.
- [225] Fei, L., Naeemi, M., Zou, G. & Luo, H. Chemical solution deposition of epitaxial metal-oxide nanocomposite thin films. *The Chemical Record* **13**, 85–101 (2013). URL <https://onlinelibrary.wiley.com/doi/abs/10.1002/tcr.201200022>.
- [226] Schwartz, R. W. Chemical solution deposition of perovskite thin films. *Materials Science* **9**, 2325–2340 (1997). URL <https://link.aps.org/doi/10.1103/PhysRevB.20.2255>.
- [227] Coll, M. *et al.* Integration of atomic layer deposition CeO_2 thin films with functional complex oxides and 3d patterns. *Thin Solid Films* **553**, 7–12 (2014). URL <https://www.sciencedirect.com/science/article/pii/S0040609013015137>. European Materials Research Society (E-MRS) Spring Meeting 2013 Symposium O: Synthesis, processing and characterization of nanoscale multi functional oxide films IV.
- [228] Schneller, T. In Schneller, T., Waser, R., Kosec, M. & Payne, D. (eds.) *Chemical Solution Deposition of Functional Oxide Thin Films*, 1–796 (Springer Vienna, Vienna, 2013). URL https://doi.org/10.1007/978-3-211-99311-8_1.
- [229] Chaudhary, K. T. Thin film deposition: Solution based approach. In Ares, A. E. (ed.) *Thin Films*, chap. 10 (IntechOpen, Rijeka, 2021). URL <https://doi.org/10.5772/intechopen.94455>.
- [230] Griffin, J., Hassan, H. & Spooner, E. Spin coating: Complete guide to theory and techniques. URL <https://www.ossila.com/en-eu/pages/spin-coating#introduction-to-spin-coating>.
- [231] Botsaris, G. D. *et al.* Crystallization. part 1. transport phenomena of nucleation and crystal growth. *Ind. Eng. Chem.* **61**, 86–113 (1969). URL <https://pubs.acs.org/doi/pdf/10.1021/ie50718a009>.
- [232] Cochran, E. A., Woods, K. N., Johnson, D. W., Page, C. J. & Boettcher, S. W. Unique chemistries of metal-nitrate precursors to form metal-oxide thin films from solution: materials for electronic and energy applications. *J. Mater. Chem. A* **7**, 24124–24149 (2019). URL <http://dx.doi.org/10.1039/C9TA07727H>.
- [233] Zhang, Q., Valanoor, N. & Standard, O. Epitaxial (001) BiFeO_3 thin-films with excellent ferroelectric properties by chemical solution deposition-the role of gelation. *J. Mater. Chem. C* **3**, 582–595 (2015). URL <http://dx.doi.org/10.1039/C4TC02371D>.
- [234] Coll, M. & Napari, M. Atomic layer deposition of functional multicomponent oxides. *APL Materials* **7** (2019). URL <https://doi.org/10.1063/1.5113656>. 110901.
- [235] George, S. M. Atomic layer deposition: An overview. *Chemical Reviews* **110**, 111–131 (2010). URL <https://doi.org/10.1021/cr900056b>. PMID: 19947596.

- [236] Coll, M. *et al.* Low temperature stabilization of nanoscale epitaxial spinel ferrite thin films by atomic layer deposition. *Advanced Functional Materials* **24**, 5368–5374 (2014). URL <https://onlinelibrary.wiley.com/doi/abs/10.1002/adfm.201400517>.
- [237] Swann, S. Magnetron sputtering. *Physics in Technology* **19**, 67 (1988). URL <https://dx.doi.org/10.1088/0305-4624/19/2/304>.
- [238] Shi, F. Introductory chapter: Basic theory of magnetron sputtering. In Shi, D. F. (ed.) *Magnetron Sputtering*, chap. 4 (IntechOpen, Rijeka, 2018). URL <https://doi.org/10.5772/intechopen.80550>.
- [239] Wilson, D. I. What is rheology? *Eye* **32**, 179–183 (2018). URL <https://doi.org/10.1038/eye.2017.267>.
- [240] Prime, R. B., Bair, H. E., Vyazovkin, S., Gallagher, P. K. & Riga, A. *Thermogravimetric Analysis (TGA)*, chap. 3, 241–317 (John Wiley Sons, Ltd, 2009). URL <https://onlinelibrary.wiley.com/doi/abs/10.1002/9780470423837.ch3>.
- [241] *Differential Scanning Calorimetry and Thermogravimetric Analysis*, chap. 10, 124–141 (John Wiley Sons, Ltd, 2017). URL <https://onlinelibrary.wiley.com/doi/abs/10.1002/9781119264408.ch10>.
- [242] Harrington, G. F. & Santiso, J. Back-to-basics tutorial: X-ray diffraction of thin films. *Journal of Electroceramics* **47**, 141–163 (2021). URL <https://doi.org/10.1007/s10832-021-00263-6>.
- [243] van der Sluis, P. Determination of strain in epitaxial semiconductor layers by high-resolution x-ray diffraction. *Journal of Physics D: Applied Physics* **26**, A188 (1993). URL <https://dx.doi.org/10.1088/0022-3727/26/4A/039>.
- [244] XII, 762 (Springer New York, NY, 2011). URL <https://link.springer.com/book/10.1007/978-1-4419-7200-2#book-header>.
- [245] Lupini, A. R. *Aberration correction in STEM*. Ph.D. thesis, University of Cambridge (2001). URL <https://www.repository.cam.ac.uk/handle/1810/251789>.
- [246] Du, H. & Jia, C.-L. 13 - high-resolution transmission electron microscopy and spectroscopy of epitaxial metal oxides. In Koster, G., Huijben, M. & Rijnders, G. (eds.) *Epitaxial Growth of Complex Metal Oxides (Second Edition)*, Woodhead Publishing Series in Electronic and Optical Materials, 369–398 (Woodhead Publishing, 2022), second edition edn. URL <https://www.sciencedirect.com/science/article/pii/B9780081029459000149>.
- [247] Vernon-Parry, K. Scanning electron microscopy: an introduction. *III-Vs Review* **13**, 40–44 (2000). URL <https://www.sciencedirect.com/science/article/pii/S096112900080006X>.
- [248] Themes, U. X-ray microanalysis in the scanning electron microscope (2017). URL <https://radiologykey.com/x-ray-microanalysis-in-the-scanning-electron-microscope/>.
- [249] Binnig, G., Quate, C. F. & Gerber, C. Atomic force microscope. *Phys. Rev. Lett.* **56**, 930–933 (1986). URL <https://link.aps.org/doi/10.1103/PhysRevLett.56.930>.
- [250] Bonnell, D. A. *Scanning probe microscopy and spectroscopy: Theory, techniques and applications* (Wiley, 2001).
- [251] Sebastian, A., Gannepalli, A. & Salapaka, M. V. A review of the systems approach to the analysis of dynamic-mode atomic force microscopy. *IEEE Transactions on Control Systems Technology* **15**, 952–959 (2007).
- [252] .
- [253] What is afm? learn about atomic force microscopy. URL <https://www.nanoandmore.com/what-is-atomic-force-microscopy>.
- [254] Mountainsmap® surface analysis software. URL <https://www.digitalsurf.com/software-solutions/profilometry/>.
- [255] *Principles of Spectroscopic Ellipsometry*, chap. 4, 81–146 (John Wiley Sons, Ltd, 2007). URL <https://onlinelibrary.wiley.com/doi/abs/10.1002/9780470060193.ch4>.
- [256] Spectroscopic ellipsometry: Tutorial (2018). URL <https://www.jawoollam.com/resources/ellipsometry-tutorial>.
- [257] Liu, Y., Hsieh, J. & Tung, S. Extraction of optical constants of zinc oxide thin films by ellipsometry with various models. *Thin Solid Films* **510**, 32–38 (2006). URL <https://www.sciencedirect.com/science/article/pii/S0040609006001775>.
- [258] Synowicki, R. Spectroscopic ellipsometry characterization of indium tin oxide film microstructure and optical constants. *Thin Solid Films* **313–314**, 394–397 (1998). URL <https://www.sciencedirect.com/science/article/pii/S0040609097008535>.
- [259] Tauc, J., Grigorovici, R. & Vancu, A. Optical properties and electronic structure of amorphous germanium. *physica status solidi (b)* **15**, 627–637 (1966). URL <https://onlinelibrary.wiley.com/doi/abs/10.1002/pssb.19660150224>.
- [260] Moulder, J. & Chastain, J. *Handbook of X-ray Photoelectron Spectroscopy: A Reference Book of Standard Spectra for Identification and Interpretation of XPS Data* (Physical Electronics Division, Perkin-Elmer Corporation, 1992). URL https://books.google.es/books?id=A_XGQgAACAAJ.
- [261] Chang, C. C. Auger electron spectroscopy. *Surface Science* **25**, 53–79 (1971). URL <https://www.sciencedirect.com/science/article/pii/003960287190210X>.
- [262] Pérez-Dieste, V. *et al.* Near ambient pressure XPS at ALBA. *Journal of Physics: Conference Series* **425**, 072023 (2013).

- [263] Welker, R. W. Chapter 4 - size analysis and identification of particles. In Kohli, R. & Mittal, K. (eds.) *Developments in Surface Contamination and Cleaning*, 179–213 (William Andrew Publishing, Oxford, 2012). URL <https://www.sciencedirect.com/science/article/pii/B9781437778830000043>.
- [264] Richter, S. *et al.* High-resolution structural investigation of passivated interfaces of silicon solar cells. *Solar Energy Materials and Solar Cells* **142**, 128–133 (2015). URL <https://www.sciencedirect.com/science/article/pii/S0927024815003207>. Proceedings of the 5th International Conference on Crystalline Silicon Photovoltaics (SiliconPV 2015).
- [265] de Groot, F. High-resolution x-ray emission and x-ray absorption spectroscopy. *Chemical Reviews* **101**, 1779–1808 (2001). URL <https://doi.org/10.1021/cr9900681>. PMID: 11709999.
- [266] Yano, J. & Yachandra, V. K. X-ray absorption spectroscopy. *Photosynthesis Research* **102**, 241–254 (2009). URL <https://doi.org/10.1007/s11120-009-9473-8>.
- [267] Lidon-Simon, J. *et al.* Low current measurements at alba. *Proceedings of ICALEPCS conference* **361**, 1032–1035 (2011).
- [268] Rodriguez, B. J., Callahan, C., Kalinin, S. V. & Proksch, R. Dual-frequency resonance-tracking atomic force microscopy. *Nanotechnology* **18**, 475504 (2007). URL <https://dx.doi.org/10.1088/0957-4484/18/47/475504>.
- [269] Adler, T., Appel, D. & Kunzmann, M. Physical property measurement system (ppms). URL <https://qd-europe.com/at/en/product/physical-property-measurement-system-ppms/>.
- [270] User manual of tf analyzer 2000.
- [271] Meyer, R., Waser, R., Prume, K., Schmitz, T. & Tiedke, S. Dynamic leakage current compensation in ferroelectric thin-film capacitor structures. *Applied Physics Letters* **86** (2005). URL <https://doi.org/10.1063/1.1897425>. 142907.
- [272] Fina, I. *et al.* Nonferroelectric contributions to the hysteresis cycles in manganite thin films: A comparative study of measurement techniques. *Journal of Applied Physics* **109** (2011). URL <https://doi.org/10.1063/1.3555098>. 074105.
- [273] Tf 2000 e: Aixacct systems (2021). URL <https://www.aixacct.com/en/testsysteme/tf-analyzer-family/tf-analyzer-2000-e/>.
- [274] Wu, J. *et al.* Counter electrodes in dye-sensitized solar cells. *Chem. Soc. Rev.* **46**, 5975–6023 (2017). URL <http://dx.doi.org/10.1039/C6CS00752J>.
- [275] Drivas, C., Botzakaki, M. A., Georga, S. N., Krontiras, C. A. & Kennou, S. Interface band offset determination of ultra-thin oxides grown on tio₂ and zno by x-ray photoelectron spectroscopy. *Journal of Physics D: Applied Physics* **54**, 285301 (2021). URL <https://dx.doi.org/10.1088/1361-6463/abf9db>.
- [276] Sheng, Y. *et al.* Band alignment and photoresponse of lafeo₃-based heterojunctions. *Phys. Rev. Appl.* **19**, 024001 (2023). URL <https://link.aps.org/doi/10.1103/PhysRevApplied.19.024001>.
- [277] Brandt, R. E., Mangan, N. M., Li, J. V., Lee, Y. S. & Buonassisi, T. Determining interface properties limiting open-circuit voltage in heterojunction solar cells. *Journal of Applied Physics* **121**, 185301 (2017). URL <https://doi.org/10.1063/1.4982752>.
- [278] Klein, A. *et al.* Transparent conducting oxides for photovoltaics: Manipulation of fermi level, work function and energy band alignment. *Materials* **3**, 4892–4914 (2010). URL <https://www.mdpi.com/1996-1944/3/11/4892>.
- [279] Walsh, A. *et al.* Nature of the band gap of in₂o₃ revealed by first-principles calculations and x-ray spectroscopy. *Physical review letters* **100**, 167402 (2008).
- [280] Fridkin, V. Bulk photovoltaic effect in noncentrosymmetric crystals. *Crystallography Reports* **46**, 654–658 (2001).
- [281] Alexe, M. & Hesse, D. Tip-enhanced photovoltaic effects in bismuth ferrite. *Nature Communications* **2**, 256–261 (2011).
- [282] De Dobbelaere, C. *et al.* Aqueous solutions for low-temperature photoannealing of functional oxide films: Reaching the 400 °c si-technology integration barrier. *Journal of the American Chemical Society* **133**, 12922–12925 (2011).
- [283] Yang, B. *et al.* Chemical solution route for high-quality multiferroic bifeo₃ thin films. *Small* **17**, 1903663 (2021). URL <https://onlinelibrary.wiley.com/doi/abs/10.1002/smll.201903663>.
- [284] Bein, N. S. *et al.* Electrochemical reduction of undoped and cobalt-doped bifeo₃ induced by water exposure: Quantitative determination of reduction potentials and defect energy levels using photoelectron spectroscopy. *The Journal of Physical Chemistry Letters* **10**, 7071–7076 (2019). URL <https://doi.org/10.1021/acs.jpclett.9b02706>. PMID: 31664832.
- [285] Qi, X., Dho, J., Tomov, R., Blamire, M. G. & MacManus-Driscoll, J. L. Greatly reduced leakage current and conduction mechanism in aliovalent-ion-doped bifeo₃. *Applied Physics Letters* **86**, 062903 (2005). URL <https://doi.org/10.1063/1.1862336>.
- [286] Belik, A. A. *et al.* Neutron powder diffraction study on the crystal and magnetic structures of bicoo₃. *Chemistry of Materials* **18**, 798–803 (2006). URL <https://doi.org/10.1021/cm052334z>.
- [287] Chen, Y., Wei, H., Wu, Y. & Cao, B. Impact of ferroelectric domain structure on bulk photovoltaic effect of epitaxial bife_{1-x}co_xo₃ films. *Advanced Electronic Materials* **8**, 2101043 (2022). URL <https://onlinelibrary.wiley.com/doi/abs/10.1002/aelm.202101043>.

- [288] Gupta, S., Tomar, M., James, A. R. & Gupta, V. Ce-doped bismuth ferrite thin films with improved electrical and functional properties. *Journal of Materials Science* **49**, 5355–5364 (2014).
- [289] Quan, Z. *et al.* Microstructure, electrical and magnetic properties of Ce-doped BiFeO₃ thin films. *Journal of Applied Physics* **104** (2008). URL <https://doi.org/10.1063/1.3000478>. 084106.
- [290] Uchida, H., Ueno, R., Funakubo, H. & Koda, S. Crystal structure and ferroelectric properties of rare-earth substituted bifeo₃ thin films. *Journal of Applied Physics* **100**, 014106 (2006). URL <https://doi.org/10.1063/1.2210167>.
- [291] Pradhan, S. & Roul, B. Electrical behavior of high resistivity ce-doped bifeo₃ multiferroic. *Physica B: Condensed Matter* **407**, 2527–2532 (2012). URL <https://www.sciencedirect.com/science/article/pii/S092145261200350X>.
- [292] Pisarev, R. V., Moskvina, A. S., Kalashnikova, A. M. & Rasing, T. Charge transfer transitions in multiferroic bifeo₃ and related ferrite insulators. *Phys. Rev. B* **79**, 235128 (2009). URL <https://link.aps.org/doi/10.1103/PhysRevB.79.235128>.
- [293] Gujar, T., Shinde, V. & Lokhande, C. Nanocrystalline and highly resistive bismuth ferric oxide thin films by a simple chemical method. *Materials Chemistry and Physics* **103**, 142 – 146 (2007). URL <http://www.sciencedirect.com/science/article/pii/S0254058407000521>.
- [294] Meng, J. *et al.* Charge-transfer-induced interfacial exchange coupling at the Co/bifeo₃ interface. *Phys. Rev. Applied* **12**, 044010 (2019). URL <https://link.aps.org/doi/10.1103/PhysRevApplied.12.044010>.
- [295] Ikeno, H. *et al.* First principles calculation of fe *l*_{2,3}-edge x-ray absorption near edge structures of iron oxides. *Materials Transactions* **45**, 1414–1418 (2004).
- [296] Abbate, M. *et al.* Controlled-valence properties of la_{1-x}sr_xfeo₃ and la_{1-x}sr_xmno₃ studied by soft-x-ray absorption spectroscopy. *Phys. Rev. B* **46**, 4511–4519 (1992). URL <https://link.aps.org/doi/10.1103/PhysRevB.46.4511>.
- [297] Anjum, G. *et al.* NEXAFS studies of la_{0.8}bi_{0.2}fe_{1-x}mn_xo₃ (0.0 ≤ x ≤ 0.4) multiferroic system using x-ray absorption spectroscopy. *Journal of Physics D: Applied Physics* **44**, 075403 (2011).
- [298] Haverkort, M. W. *et al.* Spin state transition in lacoo₃ studied using soft x-ray absorption spectroscopy and magnetic circular dichroism. *Phys. Rev. Lett.* **97**, 176405 (2006). URL <https://link.aps.org/doi/10.1103/PhysRevLett.97.176405>.
- [299] Istomin, S. Y. *et al.* An unusual high-spin ground state of co₃⁺ in octahedral coordination in brownmillerite-type cobalt oxide. *Dalton Trans.* **44**, 10708–10713 (2015). URL <http://dx.doi.org/10.1039/C4DT03670K>.
- [300] Saitoh, T., Bocquet, A. E., Mizokawa, T. & Fujimori, A. Systematic variation of the electronic structure of 3d transition-metal compounds. *Phys. Rev. B* **52**, 7934–7938 (1995). URL <https://link.aps.org/doi/10.1103/PhysRevB.52.7934>.
- [301] Suntivich, J. *et al.* Estimating hybridization of transition metal and oxygen states in perovskites from o k-edge x-ray absorption spectroscopy. *The Journal of Physical Chemistry C* **118**, 1856–1863 (2014). URL <https://doi.org/10.1021/jp410644j>.
- [302] Arima, T., Tokura, Y. & Torrance, J. B. Variation of optical gaps in perovskite-type 3d transition-metal oxides. *Phys. Rev. B* **48**, 17006–17009 (1993). URL <https://link.aps.org/doi/10.1103/PhysRevB.48.17006>.
- [303] Khestanova, E. *et al.* Untangling electrostatic and strain effects on the polarization of ferroelectric superlattices. *Advanced Functional Materials* **26**, 6446–6453 (2016). URL <https://onlinelibrary.wiley.com/doi/abs/10.1002/adfm.201602084>.
- [304] Damodaran, A. R., Breckenfeld, E., Chen, Z., Lee, S. & Martin, L. W. Enhancement of ferroelectric curie temperature in batio₃ films via strain-induced defect dipole alignment. *Advanced Materials* **26**, 6341–6347 (2014). URL <https://onlinelibrary.wiley.com/doi/abs/10.1002/adma.201400254>.
- [305] Yasui, S. *et al.* Crystal structure and electrical properties of 100-oriented epitaxial bicoo₃–bifeo₃ films grown by metalorganic chemical vapor deposition. *Japanese Journal of Applied Physics* **47**, 7582 (2008). URL <https://dx.doi.org/10.1143/JJAP.47.7582>.
- [306] Guan, Z. *et al.* Identifying intrinsic ferroelectricity of thin film with piezoresponse force microscopy. *AIP Advances* **7** (2017). URL <https://doi.org/10.1063/1.4999199>. 095116.
- [307] Kim, S., Seol, D., Lu, X., Alexe, M. & Kim, Y. Electrostatic-free piezoresponse force microscopy. *Scientific Reports* **7**, 41657 (2017). URL <https://doi.org/10.1038/srep41657>.
- [308] Perdew, J. P. *et al.* Understanding band gaps of solids in generalized kohn–sham theory. *Proc. Natl. Acad. Sci. U.S.A.* **114**, 2801–2806 (2017).
- [309] Cazorla, C. & Íñiguez, J. Insights into the phase diagram of bismuth ferrite from quasi-harmonic free-energy calculations. *Phys. Rev. B* **88**, 214430 (2013). URL <https://link.aps.org/doi/10.1103/PhysRevB.88.214430>.
- [310] Hojo, H. *et al.* Development of bismuth ferrite as a piezoelectric and multiferroic material by cobalt substitution. *Advanced Materials* **30**, 1705665 (2018). URL <https://onlinelibrary.wiley.com/doi/abs/10.1002/adma.201705665>.
- [311] Diéguez, O. & Íñiguez, J. First-principles investigation of morphotropic transitions and phase-change functional responses in bifeo₃–bicoo₃ multiferroic solid solutions. *Phys. Rev. Lett.* **107**, 057601 (2011). URL <https://link.aps.org/doi/10.1103/PhysRevLett.107.057601>.

- [312] Gao, B. *et al.* Room-temperature ferrimagnetic multiferroic $\text{BiFe}_{0.5}\text{Co}_{0.5}\text{O}_3$ thin films with giant piezoelectric response. *Phys. Rev. Materials* **2**, 084401 (2018). URL <https://link.aps.org/doi/10.1103/PhysRevMaterials.2.084401>.
- [313] Menéndez, C., Chu, D. & Cazorla, C. Oxygen-vacancy induced magnetic phase transitions in multiferroic thin films. *npj Computational Materials* **6**, 76 (2020).
- [314] Chang, C. F. *et al.* Spin blockade, orbital occupation, and charge ordering in $\text{La}_{1.5}\text{Sr}_{0.5}\text{CoO}_4$. *Phys. Rev. Lett.* **102**, 116401 (2009). URL <https://link.aps.org/doi/10.1103/PhysRevLett.102.116401>.
- [315] Chen, J.-M. *et al.* A complete high-to-low spin state transition of trivalent cobalt ion in octahedral symmetry in $\text{SrCo}_{0.5}\text{Ru}_{0.5}\text{O}_{3-\delta}$, *journal = Journal of the American Chemical Society, volume = 136, number = 4, pages = 1514 – 1519, year = 2014, doi = 10.1021/ja4114006, note = PMID : 24410074, url = https://doi.org/10.1021/ja4114006*.
- [316] Ricken, M., Nölting, J. & Riess, I. Specific heat and phase diagram of nonstoichiometric ceria (CeO_{2-x}). *Journal of Solid State Chemistry* **54**, 89–99 (1984). URL <https://www.sciencedirect.com/science/article/pii/002245968490135X>.
- [317] Ivas, T., Grundy, A., Povoden-Karadeniz, E. & Gauckler, L. Phase diagram of CeO_2 - CoO for nano-sized powders. *Calphad* **36**, 57–64 (2012). URL <https://www.sciencedirect.com/science/article/pii/S0364591611001040>.
- [318] Cayado, P. *et al.* Epitaxial $\text{YBa}_2\text{Cu}_3\text{O}_{7-x}$ nanocomposite thin films from colloidal solutions. *Superconductor Science and Technology* **28**, 124007 (2015). URL <https://dx.doi.org/10.1088/0953-2048/28/12/124007>.
- [319] Uhlmann, D., Chalmers, B. & Jackson, K. Interaction between particles and a solid-liquid interface. *Journal of Applied Physics* **35**, 2986–2993 (1964).
- [320] Shiohara, Y. & Endo, A. Crystal growth of bulk high- T_c superconducting oxide materials. *Materials Science & Engineering R-reports* **19**, 1–86 (1997).
- [321] Kresse, G. & Furthmüller, J. Efficient iterative schemes for ab initio total-energy calculations using a plane-wave basis set. *Phys. Rev. B* **54**, 11169 (1996).
- [322] Perdew, J. P., Burke, K. & Ernzerhof, M. Generalized gradient approximation made simple. *Phys. Rev. Lett.* **77**, 3865 (1996).
- [323] Cazorla, C., Diéguez, O. & Íñiguez, J. Multiple structural transitions driven by spin-phonon couplings in a perovskite oxide. *Sci. Adv.* **3**, e1700288 (2017).
- [324] Blöchl, P. E. Projector augmented-wave method. *Phys. Rev. B* **50**, 17953 (1994).
- [325] Cazorla, C. Lattice effects on the formation of oxygen vacancies in perovskite thin films. *Phys. Rev. Applied* **7**, 044025 (2017). URL <https://link.aps.org/doi/10.1103/PhysRevApplied.7.044025>.
- [326] Janesko, B. G., Henderson, T. M. & Scuseria, G. E. Screened hybrid density functionals for solid-state chemistry and physics. *Phys. Chem. Chem. Phys.* **11**, 443–454 (2009).
- [327] Menéndez, C. & Cazorla, C. Giant thermal enhancement of the electric polarization in ferrimagnetic $\text{BiFe}_{1-x}\text{Co}_x\text{O}_3$ solid solutions near room temperature. *Phys. Rev. Lett.* **125**, 117601 (2020). URL <https://link.aps.org/doi/10.1103/PhysRevLett.125.117601>.
- [328] Cazorla, C. & Stengel, M. Electrostatic engineering of strained ferroelectric perovskites from first principles. *Phys. Rev. B* **92**, 214108 (2015). URL <https://link.aps.org/doi/10.1103/PhysRevB.92.214108>.
- [329] Salles, P. *et al.* Facile chemical route to prepare water soluble epitaxial $\text{Sr}_3\text{Al}_2\text{O}_6$ sacrificial layers for free-standing oxides. *Advanced Materials Interfaces* **8**, 2001643 (1–7) (2021). URL <https://onlinelibrary.wiley.com/doi/abs/10.1002/admi.202001643>.
- [330] Erdem, D. *et al.* CoFe_2O_4 and CoFe_2O_4 - SiO_2 nanoparticle thin films with perpendicular magnetic anisotropy for magnetic and magneto-optical applications. *Advanced Functional Materials* **26**, 1954–1963 (2016). URL <https://onlinelibrary.wiley.com/doi/abs/10.1002/adfm.201504538>.
- [331] Hosseini, M., Amjadi, I., Mohajeri, M. & Mozafari, M. Sol–gel synthesis, physico-chemical and biological characterization of cerium oxide/polyallylamine nanoparticles. *Polymers* **12** (2020). URL <https://www.mdpi.com/2073-4360/12/7/1444>.
- [332] Jimenez, R. *et al.* Processing effects on the microstructure and ferroelectric properties of strontium bismuth tantalate thin films. *Appl. Phys. A* **75**, 607–615 (2002). URL <https://doi.org/10.1007/s003390101072>.
- [333] Qian, M., Fina, I., Sulzbach, M. C., Sanchez, F. & Fontcuberta, J. Synergetic Electronic and Ionic Contributions to Electroresistance in Ferroelectric Capacitors. *Adv. Electron. Mater.* **5**, 1800646 (2019). URL <https://onlinelibrary.wiley.com/doi/abs/10.1002/aelm.201800646>.
- [334] Li, F. & Jen, A. K.-Y. Interface engineering in solution-processed thin-film solar cells. *Accounts of Materials Research* **3**, 272–282 (2022). URL <https://doi.org/10.1021/accountsmr.1c00169>.
- [335] Li, Y., Xie, H., Lim, E. L., Hagfeldt, A. & Bi, D. Recent progress of critical interface engineering for highly efficient and stable perovskite solar cells. *Advanced Energy Materials* **12**, 2102730 (2022). URL <https://onlinelibrary.wiley.com/doi/abs/10.1002/aenm.202102730>.
- [336] Guziewicz, E. *et al.* ZnO grown by atomic layer deposition: A material for transparent electronics and organic heterojunctions. *Journal of Applied Physics* **105**, 122413 (2009). URL <https://doi.org/10.1063/1.3133803>.

- [337] Huang, M., Hameiri, Z., Aberle, A. G. & Mueller, T. Comparative study of amorphous indium tin oxide prepared by pulsed-dc and unbalanced rf magnetron sputtering at low power and low temperature conditions for heterojunction silicon wafer solar cell applications. *Vacuum* **119**, 68–76 (2015). URL <https://www.sciencedirect.com/science/article/pii/S0042207X15001840>.
- [338] Katsidis, C. C. & Siapakas, D. I. General transfer-matrix method for optical multilayer systems with coherent, partially coherent, and incoherent interference. *Appl. Opt.* **41**, 3978–3987 (2002). URL <http://opg.optica.org/ao/abstract.cfm?URI=ao-41-19-3978>.
- [339] Feng, H.-J. *et al.* The origin of enhanced optical absorption of the bifeo₃/zno heterojunction in the visible and terahertz regions. *Phys. Chem. Chem. Phys.* **17**, 26930–26936 (2015). URL <http://dx.doi.org/10.1039/C5CP04389A>.
- [340] Amalathas, A. P. & Alkai, M. M. Effects of film thickness and sputtering power on properties of ito thin films deposited by rf magnetron sputtering without oxygen. *Journal of Materials Science: Materials in Electronics* **27**, 11064–11071 (2016). URL <https://doi.org/10.1007/s10854-016-5223-9>.
- [341] Li, K. *et al.* Modulating light absorption and multiferroic properties of BiFeO₃/sub-based ferroelectric films by the introduction of ZnO layer. *Materials Research Express* **9**, 036402 (2022). URL <https://doi.org/10.1088/2053-1591/ac4328>.
- [342] Abdyldayeva, N. & Beisenkhanov, N. ZnO-ITO multi-layered structure on Si substrate with prospective usage as antireflective covering for solar cells. *Materials Today: Proceedings* **49**, 2516–2520 (2022). URL <https://www.sciencedirect.com/science/article/pii/S221478532040330X>. The 8th International Conference on Nanomaterials and Advanced Energy Storage Systems (INESS-2020).
- [343] Zhang, Q., Dandeneau, C. S., Zhou, X. & Cao, G. ZnO nanostructures for dye-sensitized solar cells. *Advanced Materials* **21**, 4087–4108 (2009). URL <https://onlinelibrary.wiley.com/doi/abs/10.1002/adma.200803827>.
- [344] Xiang, W., Liu, S. F. & Tress, W. A review on the stability of inorganic metal halide perovskites: challenges and opportunities for stable solar cells. *Energy Environ. Sci.* **14**, 2090–2113 (2021). URL <http://dx.doi.org/10.1039/D1EE00157D>.
- [345] Bein, N. S. *The Fermi Level in Bismuth Ferrite*. Master-thesis, TU-Darmstadt, Darmstadt (2018).
- [346] Korte, L., Röckler, R. & Pettenkofer, C. Direct determination of the band offset in atomic layer deposited ZnO/hydrogenated amorphous silicon heterojunctions from X-ray photoelectron spectroscopy valence band spectra. *Journal of Applied Physics* **115** (2014). URL <https://doi.org/10.1063/1.4879915>.
- [347] Siol, S. *et al.* Band alignment engineering at Cu₂O/ZnO heterointerfaces. *ACS Applied Materials & Interfaces* **8**, 21824–21831 (2016). URL <https://doi.org/10.1021/acsami.6b07325>. PMID: 27452037.
- [348] Horiba, K. *et al.* Temperature-dependence of the electronic structure of La_{1-x}Sr_xMnO₃ thin films studied by in situ photoemission spectroscopy. *Journal of Electron Spectroscopy and Related Phenomena* **156–158**, 375–378 (2007).
- [349] Gassenbauer, Y. *et al.* Surface states, surface potentials, and segregation at surfaces of tin-doped In₂O₃. *Physical Review B* **73** (2006).
- [350] Säuberlich, F., Fritsche, J., Hunger, R. & Klein, A. Properties of sputtered ZnO films and its interfaces with Cds. *Thin Solid Films* **431–432**, 378–381 (2003).
- [351] Chen, F., Schafranek, R., Li, S., Wu, W. B. & Klein, A. Energy band alignment between Pb(Zr,Ti)O₃ and high and low work function conducting oxides—from hole to electron injection. *Journal of Physics D: Applied Physics* **43**, 295301 (2010). URL <https://dx.doi.org/10.1088/0022-3727/43/29/295301>.
- [352] Zhang, J. *et al.* Unravelling the role of band-offset landscape on the recombination zone dynamics in perovskite light-emitting diodes. *Nano Select* **2**, 624–631 (2021). URL <https://onlinelibrary.wiley.com/doi/abs/10.1002/nano.202000154>.
- [353] Xu, J., Jia, Z., Zhang, N. & Ren, T. Influence of La and Mn dopants on the current-voltage characteristics of BiFeO₃/ZnO heterojunction. *Journal of Applied Physics* **111**, 074101 (2012). URL <https://doi.org/10.1063/1.3699033>.
- [354] Qi, B. & Wang, J. Open-circuit voltage in organic solar cells. *J. Mater. Chem.* **22**, 24315–24325 (2012). URL <http://dx.doi.org/10.1039/C2JM33719C>.
- [355] Lim, S., Kwon, S. & Kim, H. ZnO thin films prepared by atomic layer deposition and rf sputtering as an active layer for thin film transistor. *Thin Solid Films* **516**, 1523–1528 (2008). URL <https://www.sciencedirect.com/science/article/pii/S0040609007004038>. Proceedings of Symposium R on Advances in Transparent Electronics: from materials to devices EMRS 2006 Conference, Nice, France.
- [356] Liu, J. *et al.* Substantial reduction of leakage currents in La/Er/Zn/Ti multielement-doped BiFeO₃ multiferroic thin films. *Ceramics International* **48**, 17328–17334 (2022). URL <https://www.sciencedirect.com/science/article/pii/S0272884222007313>.
- [357] Singh, S. K., Maruyama, K. & Ishiwara, H. Reduced leakage current in La and Ni codoped BiFeO₃ thin films. *Applied Physics Letters* **91** (2007). URL <https://doi.org/10.1063/1.2784968>.
- [358] Ahn, C. H., Hee Kim, S., Gu Yun, M. & Koun Cho, H. Design of step composition gradient thin film transistor channel layers grown by atomic layer deposition. *Applied Physics Letters* **105** (2014). URL <https://doi.org/10.1063/1.4901732>.
- [359] Cardona, M. Optical properties and band structure of SrTiO₃ and BaTiO₃. *Phys. Rev.* **140**, A651–A655 (1965). URL <https://link.aps.org/doi/10.1103/PhysRev.140.A651>.
- [360] Martino, M. *et al.* La_{0.7}Sr_{0.3}MnO₃ thin films deposited by pulsed laser ablation for spintronic applications. *Physica Status Solidi A, Applications and Materials Science* **208**, 1817–1820 (2011).

- [361] Waldrop, J. R., Grant, R. W., Kowalczyk, S. P. & Kraut, E. A. Measurement of semiconductor heterojunction band discontinuities by x-ray photoemission spectroscopy. *Journal of Vacuum Science & Technology A: Vacuum, Surfaces, and Films* **3**, 835–841 (1985).
- [362] Ellmer, K. Past achievements and future challenges in the development of optically transparent electrodes. *Nature Photonics* **6**, 809–817 (2012). URL <https://doi.org/10.1038/nphoton.2012.282>.
- [363] Lewis, B. G. & Paine, D. C. Applications and processing of transparent conducting oxides. *MRS Bulletin* **25**, 22–27 (2000).
- [364] Ginley, D. S. & Bright, C. Transparent conducting oxides. *MRS Bulletin* **25**, 15–18 (2000).
- [365] Liu, H., Avrutin, V., Izyumskaya, N., Özgür, & Morkoç, H. Transparent conducting oxides for electrode applications in light emitting and absorbing devices. *Superlattices and Microstructures* **48**, 458–484 (2010). URL <https://www.sciencedirect.com/science/article/pii/S0749603610001795>.
- [366] Ramesh, R. & Spaldin, N. A. Multiferroics: progress and prospects in thin films. *Nature Materials* **6**, 21–29 (2007). URL <https://doi.org/10.1038/nmat1805>.
- [367] Reiner, J. W., Walker, F. J. & Ahn, C. H. Atomically engineered oxide interfaces. *Science* **323**, 1018–1019 (2009). URL <https://www.science.org/doi/abs/10.1126/science.1169058>.
- [368] Vaz, C. A. F., Hoffman, J., Ahn, C. H. & Ramesh, R. Magnetoelectric coupling effects in multiferroic complex oxide composite structures. *Advanced Materials* **22**, 2900–2918 (2010). URL <https://onlinelibrary.wiley.com/doi/abs/10.1002/adma.200904326>.
- [369] Olivier, A. *et al.* Indium tin oxide optical access for magnetic tunnel junctions in hybrid spintronic–photonic circuits. *Nanotechnology* **31**, 425302 (2020). URL <https://doi.org/10.1088/1361-6528/ab9c56>.
- [370] Dhole, S., Chen, A., Nie, W., Park, B. & Jia, Q. Strain engineering: A pathway for tunable functionalities of perovskite metal oxide films. *Nanomaterials* **12**, 835, 1–23 (2022). URL <https://www.mdpi.com/2079-4991/12/5/835>.
- [371] Rondinelli, J. M. & Spaldin, N. A. Structure and properties of functional oxide thin films: Insights from electronic-structure calculations. *Advanced Materials* **23**, 3363–3381 (2011). URL <https://onlinelibrary.wiley.com/doi/abs/10.1002/adma.201101152>.
- [372] Catalano, S. *et al.* Rare-earth nickelates $R\text{NiO}_3$: thin films and heterostructures. *Reports on Progress in Physics* **81**, 046501 (2018). URL <https://doi.org/10.1088/1361-6633/aaa37a>.
- [373] Machado, P. *et al.* Enhancement of phase stability and optoelectronic performance of bifeo_3 thin films via cation co-substitution. *J. Mater. Chem. C* **9**, 330–339 (2021). URL <http://dx.doi.org/10.1039/D0TC04304D>.
- [374] Wei, R. *et al.* Solution processing of transparent conducting epitaxial la:basno_3 films with improved electrical mobility. *Applied Physics Letters* **106**, 101906 (1–5) (2015). URL <https://doi.org/10.1063/1.4914972>.
- [375] Wei, R. *et al.* Growth, microstructures, and optoelectronic properties of epitaxial $\text{basn}_{1-x}\text{sb}_x\text{o}_3-\delta$ thin films by chemical solution deposition. *ACS Applied Energy Materials* **1**, 1585–1593 (2018). URL <https://doi.org/10.1021/acsae.8b00003>.
- [376] Wei, R. *et al.* Improved optoelectronic properties in solution-processed epitaxial rare-earth-doped basno_3 thin films via grain size engineering. *Applied Physics Letters* **115**, 162105 (1–5) (2019). URL <https://doi.org/10.1063/1.5115526>.
- [377] He, Y. *et al.* Microstructural engineering of solution-processed epitaxial la-doped basno_3 transparent conducting films. *Crystal Growth & Design* **21**, 5800–5806 (2021). URL <https://doi.org/10.1021/acs.cgd.1c00698>.
- [378] Zhu, X. *et al.* Chemical solution deposition of transparent and metallic $\text{la}_{0.5}\text{sr}_{0.5}\text{tio}_{3+x/2}$ films using topotactic reduction. *Journal of the American Ceramic Society* **92**, 800–804 (2009). URL <https://ceramics.onlinelibrary.wiley.com/doi/abs/10.1111/j.1551-2916.2009.02960.x>.
- [379] Yun, J., Guo, D., Chen, Y. & Zhang, Z. The effect of la doping concentration on optical and electrical properties of $\text{la}_x\text{sr}_{1-x}\text{tio}_3$ thin film fabricated by sol–gel process. *Thin Solid Films* **600**, 1–5 (2016). URL <https://www.sciencedirect.com/science/article/pii/S0040609016000110>.
- [380] Jung, H. S., Lee, J.-K., Young Kim, J. & Hong, K. S. Synthesis of nano-sized mgo particle and thin film from diethanolamine-stabilized magnesium-methoxide. *Journal of Solid State Chemistry* **175**, 278–283 (2003). URL <https://www.sciencedirect.com/science/article/pii/S0022459603002809>.
- [381] Nair, S. & James, C. Evaluation of kinetic parameters for the thermal decomposition of gamma-irradiated strontium nitrate by dynamic thermogravimetry. *Thermochimica Acta* **78**, 357–370 (1984). URL <http://www.sciencedirect.com/science/article/pii/0040603184871622>.
- [382] Hwan-Hwang, Y. *et al.* An ‘aqueous route’ for the fabrication of low-temperature-processable oxide flexible transparent thin-film transistors on plastic substrates. *NPG Asia Materials* **5**, e45 (2013). URL <https://doi.org/10.1038/am.2013.11>.
- [383] Wyrzykowski, D., Hebanowska, E., Nowak-Wicz, G., Makowski, M. & Chmurzyński, L. Thermal behaviour of citric acid and isomeric aconitic acids. *Journal of Thermal Analysis and Calorimetry J Therm Anal Calorim* **104**, 731–735 (2011). URL <https://akjournals.com/view/journals/10973/104/2/article-p731.xml>.
- [384] Datta, A. & Agrawal, D. C. Effect of acetylacetone on the phase formation of bst . *Ferroelectrics* **323**, 57–63 (2005). URL <https://doi.org/10.1080/00150190500308611>.

- [385] Athanasiou, A. *et al.* Thermogravimetric study of the surfactant–diethanolamine–titanium isopropoxide system behavior. *Journal of Thermal Analysis and Calorimetry* **116**, 15–25 (2014). URL <https://doi.org/10.1007/s10973-013-3407-6>.
- [386] De Ávila, S. G., Logli, M. A. & Matos, J. R. Kinetic study of the thermal decomposition of monoethanolamine (mea), diethanolamine (dea), triethanolamine (tea) and methyldiethanolamine (mdea). *International Journal of Greenhouse Gas Control* **42**, 666–671 (2015). URL <https://www.sciencedirect.com/science/article/pii/S1750583615300888>.
- [387] Blake, P. G. & Jackson, G. E. The thermal decomposition of acetic acid. *J. Chem. Soc. B* 1153–1155 (1968). URL <http://dx.doi.org/10.1039/J29680001153>.
- [388] Ding, X., Liu, Y., Gao, L. & Guo, L. Synthesis and characterization of doped LaCoO_3 perovskite prepared by edta–citrate complexing method. *Journal of Alloys and Compounds* **458**, 346–350 (2008). URL <https://www.sciencedirect.com/science/article/pii/S0925838807007475>.
- [389] Liu, D. *et al.* Optimizing the properties of $\text{La}_{0.8}\text{Sr}_{0.2}\text{CoO}_3$ thin films through post-annealing for high-temperature sensing. *Nanomaterials* **11**, 1–11 (2021). URL <https://www.mdpi.com/2079-4991/11/7/1802>.
- [390] Wang, K. *et al.* Epitaxial growth and magnetic/transport properties of $\text{La}_{0.7}\text{Sr}_{0.3}\text{MnO}_3$ thin films grown on SrTiO_3 with optimized growth conditions. *RSC Advances* **7**, 31327–31332 (2017). URL <http://dx.doi.org/10.1039/C7RA04356B>.
- [391] Alaan, U. S. *et al.* Magnetism and transport in transparent high-mobility BaSnO_3 films doped with la, pr, nd, and gd. *Phys. Rev. Mater.* **3**, 124402 (1–12) (2019). URL <https://link.aps.org/doi/10.1103/PhysRevMaterials.3.124402>.
- [392] Biswas, A. *et al.* La doped SrTiO_3 thin films on SrLaO_4 (001) as transparent conductor. *Journal of Applied Physics* **113**, 183711 (1–5) (2013). URL <https://doi.org/10.1063/1.4804664>.
- [393] Obradors, X. *et al.* Nucleation and mesostrain influence on percolating critical currents of solution derived $\text{YBa}_2\text{Cu}_3\text{O}_7$ superconducting thin films. *Physica C: Superconductivity and its Applications* **482**, 58–67 (2012). URL <https://www.sciencedirect.com/science/article/pii/S0921453412002080>. 2011 Centennial superconductivity conference – EUCAS–ISEC–ICMC.
- [394] Mundet, B. *et al.* *An Atomic-Scale Perspective of the Challenging Microstructure of $\text{YBa}_2\text{Cu}_3\text{O}_{7-x}$ Thin Films*, 189–212 (Springer International Publishing, Cham, 2020). URL https://doi.org/10.1007/978-3-030-23303-7_7.
- [395] Gazquez, J. *et al.* Structural defects in trifluoroacetate derived $\text{YBa}_2\text{Cu}_3\text{O}_7$ thin films. *Superconductor Science and Technology* **25**, 065009 (2012). URL <https://doi.org/10.1088/0953-2048/25/6/065009>.
- [396] MacManus-Driscoll, J. L. *et al.* New approaches for achieving more perfect transition metal oxide thin films. *APL Materials* **8**, 040904 (2020). URL <https://doi.org/10.1063/5.0003268>.
- [397] Schlom, D. G. Perspective oxide molecular-beam epitaxy rocks! *APL Materials* **3**, 062403 (2015). URL <https://doi.org/10.1063/1.4919763>.
- [398] Eerenstein, W., Palstra, T. T. M., Hibma, T. & Celotto, S. Origin of the increased resistivity in epitaxial Fe_3O_4 films. *Phys. Rev. B* **66**, 201101 (2002). URL <https://link.aps.org/doi/10.1103/PhysRevB.66.201101>.
- [399] Moreno, C. *New features in solution derived $\text{La}_{0.7}\text{Sr}_{0.3}\text{MnO}_3$ thin films: spontaneous outcropping and nanoscale reversible resistive switching*. Ph.D. thesis, Universitat Autònoma de Barcelona (2010). URL <http://hdl.handle.net/10803/3424>.
- [400] Liao, Z. & Zhang, J. Metal-to-insulator transition in ultrathin manganite heterostructures. *Applied Sciences* **9**, 1–20 (2019).
- [401] Mitterbauer, C. *et al.* Electron energy-loss near-edge structures of 3d transition metal oxides recorded at high-energy resolution. *Ultramicroscopy* **96**, 469–480 (2003). URL <https://www.sciencedirect.com/science/article/pii/S0304399103001098>. Proceedings of the International Workshop on Strategies and Advances in Atomic Level Spectroscopy and Analysis.
- [402] Daulton, T. L. & Little, B. J. Determination of chromium valence over the range cr(0)–cr(vi) by electron energy loss spectroscopy. *Ultramicroscopy* **106**, 561–573 (2006). URL <https://www.sciencedirect.com/science/article/pii/S0304399106000192>.
- [403] Horiba, K. *et al.* In vacuo photoemission study of atomically controlled $\text{La}_{1-x}\text{Sr}_x\text{MnO}_3$ thin films: Composition dependence of the electronic structure. *Phys. Rev. B* **71**, 155420 (2005). URL <https://link.aps.org/doi/10.1103/PhysRevB.71.155420>.
- [404] Fujimori, A. *et al.* Core-level photoemission measurements of the chemical potential shift as a probe of correlated electron systems. *Journal of Electron Spectroscopy and Related Phenomena* **124**, 127–138 (2002). URL <https://www.sciencedirect.com/science/article/pii/S036820480200049X>. Frontiers in photoemission spectroscopy of solids and surfaces.
- [405] Hoene, J. V., Charles, R. G. & Hickam, W. M. Thermal decomposition of metal acetylacetonates: Mass spectrometer studies. *The Journal of Physical Chemistry* **62**, 1098–1101 (1958). URL <https://doi.org/10.1021/j150567a019>.
- [406] Lalancette, R. A., Syzdek, D., Grebowicz, J., Arslan, E. & Bernal, I. The thermal decomposition and analyses of metal tris-acetylacetonates. *Journal of Thermal Analysis and Calorimetry* **135**, 3463–3470 (2019). URL <https://doi.org/10.1007/s10973-018-7598-8>.
- [407] Patil, K. C., Chandrashekar, G. V., George, M. V. & Rao, C. N. R. Infrared spectra and thermal decompositions of metal acetates and dicarboxylates. *Canadian Journal of Chemistry* **46**, 257–265 (1968). URL <https://doi.org/10.1139/v68-040>.
- [408] Duan, Y. *et al.* Thermal investigation of strontium acetate hemihydrate in nitrogen gas. *Journal of Thermal Analysis and Calorimetry* **94**, 169–174 (2008). URL <https://doi.org/10.1007/s10973-007-8711-6>.

- [409] Davoud, J. G. & Hinshellwood, C. N. Thermal decomposition of acetone. *Nature* **144**, 909–910 (1939). URL <https://doi.org/10.1038/144909a0>.
- [410] Schubert, D. W. & Dunkel, T. Spin coating from a molecular point of view: its concentration regimes, influence of molar mass and distribution. *Materials Research Innovations* **7**, 314–321 (2003). URL <https://doi.org/10.1007/s10019-003-0270-2>.
- [411] Kamaruddin, S. A. *et al.* Zinc oxide films prepared by sol–gel spin coating technique. *Applied Physics A* **104**, 263–268 (2011). URL <https://doi.org/10.1007/s00339-010-6121-2>.
- [412] Liang, Y.-C. & Liang, Y.-C. Strain-dependent surface evolution and magneto-transport properties of $\text{La}_{0.7}\text{Sr}_{0.3}\text{MnO}_3$ epilayers on SrTiO_3 substrates. *Journal of Crystal Growth* **304**, 275–280 (2007). URL <https://www.sciencedirect.com/science/article/pii/S0022024807002114>.
- [413] Chambers, S. A. & Droubay, T. Role of oxide ionicity in electronic screening at oxide/metal interfaces. *Phys. Rev. B* **64**, 075410 (2001). URL <https://link.aps.org/doi/10.1103/PhysRevB.64.075410>.
- [414] Qiao, L. *et al.* The impacts of cation stoichiometry and substrate surface quality on nucleation, structure, defect formation, and intermixing in complex oxide heteroepitaxy– LaCoO_3 on $\text{SrTiO}_3(001)$. *Advanced Functional Materials* **23**, 2953–2963 (2013). URL <https://onlinelibrary.wiley.com/doi/abs/10.1002/adfm.201202655>.
- [415] Zhang, K. H. L. *et al.* Reversible nano-structuring of SrCoO_{3-d} through oxidation and reduction at low temperature. *Nature Communications* **5**, 4669 (2014). URL <https://doi.org/10.1038/ncomms5669>.
- [416] Wang, X. *et al.* Activation of surface oxygen sites in a cobalt-based perovskite model catalyst for CO oxidation. *The Journal of Physical Chemistry Letters* **9**, 4146–4154 (2018). URL <https://doi.org/10.1021/acs.jpclett.8b01623>. PMID: 29966086.
- [417] Opitz, A. K. *et al.* The chemical evolution of the $\text{La}_{0.6}\text{Sr}_{0.4}\text{CoO}_{3-d}$ surface under SOFC operating conditions and its implications for electrochemical oxygen exchange activity. *Topics in Catalysis* **61**, 2129–2141 (2018). URL <https://doi.org/10.1007/s11244-018-1068-1>.
- [418] Feng, Z. *et al.* In situ studies of the temperature-dependent surface structure and chemistry of single-crystalline (001)-oriented $\text{La}_{0.8}\text{Sr}_{0.2}\text{CoO}_{3-d}$ perovskite thin films. *The Journal of Physical Chemistry Letters* **4**, 1512–1518 (2013). URL <https://doi.org/10.1021/jz400250t>. PMID: 26282307.
- [419] Sheeraz, M. *et al.* Enhanced ferroelectricity in perovskite oxysulfides. *Phys. Rev. Mater.* **3**, 084405 (2019). URL <https://link.aps.org/doi/10.1103/PhysRevMaterials.3.084405>.
- [420] Ju, M.-G., Dai, J., Ma, L. & Zeng, X. C. Perovskite chalcogenides with optimal bandgap and desired optical absorption for photovoltaic devices. *Advanced Energy Materials* **7**, 1700216 (2017). URL <https://onlinelibrary.wiley.com/doi/abs/10.1002/aenm.201700216>.
- [421] Wu, L., Ji, Y., Dan, H., Bowen, C. R. & Yang, Y. A multifunctional optical-thermal logic gate sensor array based on ferroelectric BiFeO_3 thin films. *InfoMat* **5**, e12414 (2023). URL <https://onlinelibrary.wiley.com/doi/abs/10.1002/inf2.12414>.